The Evolution of Gas in Galaxies

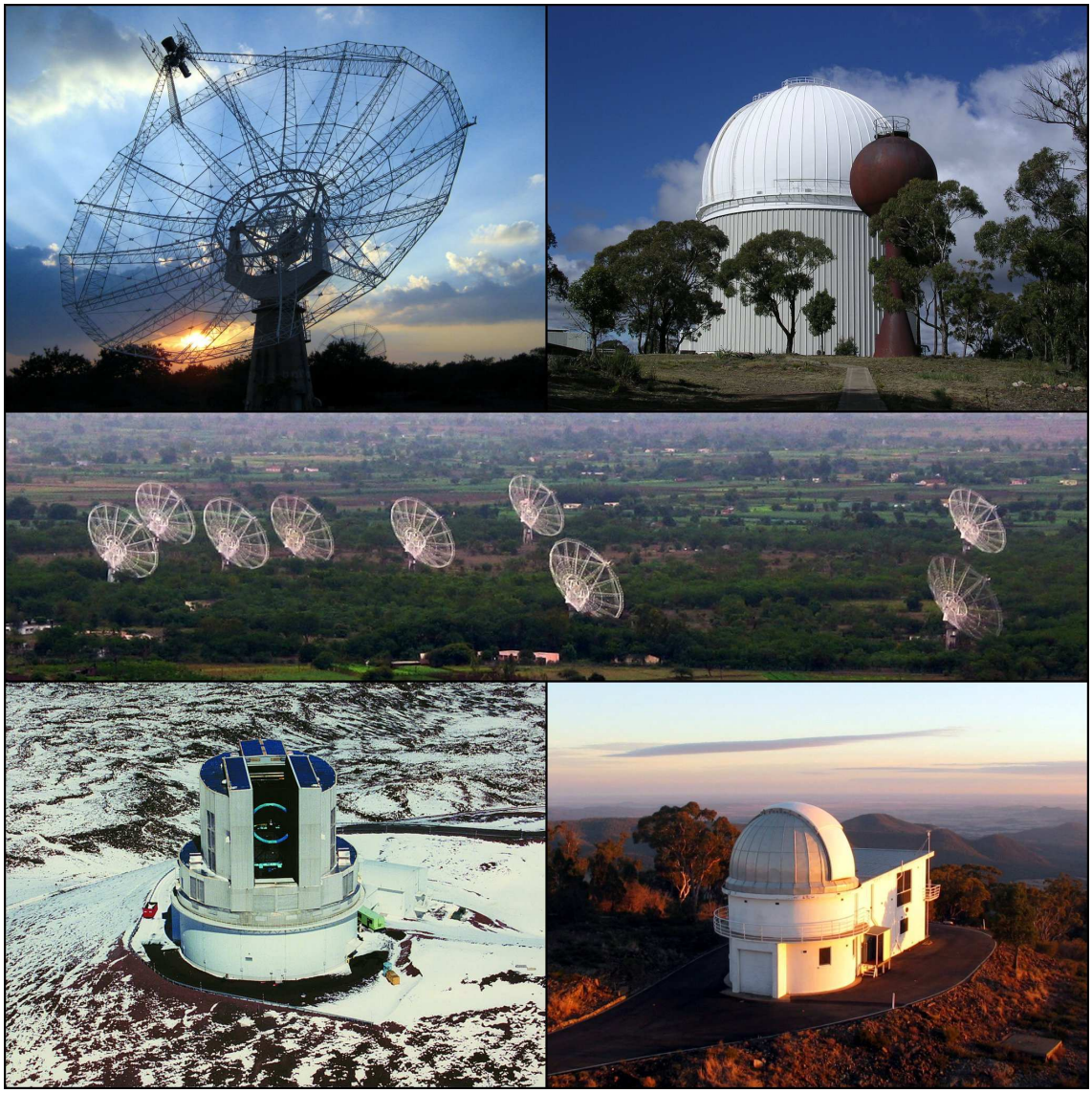

Philip Lah

The Evolution of Gas in Galaxies

by

Philip Lah

A thesis submitted for the degree of

Doctor of Philosophy

of

The Australian National University

Research School of Astronomy & Astrophysics

Submitted: July 2009

Resubmitted With Corrections: May 2010

The fact that we live at the bottom of a deep gravity well, on the surface of a gas covered planet going around a nuclear fireball 90 million miles away and think this to be normal is obviously some indication of how skewed our perspective tends to be.

Douglas Adams

Disclaimer

I hereby declare that the work in this thesis is that of the candidate alone, except where indicated below or in the text of the thesis.

Chapter 2 is based on a paper *The HI content of star-forming galaxies at $z = 0.24$*, by Philip Lah, Jayaram N. Chengalur, Frank H. Briggs, Matthew Colless, Roberto De Propris, Michael B. Pracy, W. J. G. de Blok, Shinobu S. Fujita, Masaru Ajiki, Yasuhiro Shioya, Tohru Nagao, Takashi Murayama, Yoshiaki Taniguchi, Masafumi Yagi and Sadanori Okamura, 2007, MNRAS, 376, 1357. The GMRT observations in this work were observed by Jayaram N. Chengalur and Ayesha Begum before the start of the thesis. The 2dF AAT observations were performed by the candidate, Matthew Colless & Roberto De Propris. Roberto De Propris was responsible for the data reduction of the 2dF data and preliminary redshift identification (both done at the telescope). Further redshift determinations were done with the data by the candidate. Frank H. Briggs used his own code to detemine the errors and correlation matrix for the Hα luminosity Schechter function fit of Fujita et al. (2003).

Chapter 3 is based on the paper *The HI gas content of galaxies around Abell 370, a galaxy cluster at $z = 0.37$*, by Philip Lah, Michael B. Pracy, Jayaram N. Chengalur, Frank H. Briggs, Matthew Colless, Roberto De Propris, Shaun Ferris, Brian P. Schmidt and Bradley E. Tucker. This paper has been accepted by MNRAS on 6 July 2009. The GMRT observations in this work were taken by Jayaram N. Chengalur, again before the start of the thesis. Two sets of telescope observations were taken using the ANU 40 inch for optical imaging of Abell 370, one by Michael B. Pracy, the other by the candidate. The processing of this data was done by Michael B. Pracy with some quality control provided by the candidate. The AAOmega AAT observations of Abell 370 were performed by the candidate, Matthew Colless and Michael B. Pracy. Data reduction of this data was done by Michael B. Pracy and obtaining redshifts from the data was done by Michael B. Pracy and Shaun Ferris. Michael B. Pracy also calculated the star formation rates from the [OII] measurements with some quality control provided by the candidate. A new measure of the velocity disperion of Abell 370 was made by Michael B. Pracy. Substantial aid with the optical K-corrections of the Abell 370 galaxies was provided by Brian P. Schmidt and Bradley E. Tucker. Frank H. Briggs provided the analysis on the relativistic electron hypothesis for the [OII]–radio continuum relationship.

Appendix A is based on part of an early unpublished paper concerning preliminary results of this H I emission work. Section A.2, Analysis of the bias due to threshold-based flagging, is primarily the work of Frank H. Briggs. It has been included here for completeness of our study of threshold flagging which is important to the data reduction of the GMRT observations.

Philip Lah
July 2009

Cover Image: The picture on the cover shows the major telescopes used in this thesis. The top left image shows one of the dishes of the Giant Metrewave Radio Telescope and the central image shows nine of the fifteen dishes of the central array of this telescope as seen from the hill Narayan Godt. Both photos were taken by Philip Lah. The top right image is of the Anglo-Australia Telescope, photo by Tim Rawle. The bottom left image is the Subaru Telescope, photo from the National Astronomical Observatory of Japan. The bottom right images is the Australian National University 40 inch telescope at Siding Spring, photo by Philip Lah.

Acknowledgements

- This PhD thesis is dedicated to my family: Mum and Dad, David, Nicholas, Shai, Catherine and Elizabeth, Opa and Oma, Granny, Aunty Ellice, Aunty Sue, Uncle Bruce, Victoria and Kimberley. I'm finally finished.
- I wish to thank Frank H. Briggs, chair of my PhD Supervisory Panel/Supervisor. I have appreciated his support and patience throughout this work.
- I also wish to thank the rest of my PhD Supervisory Panel: Jayaram N. Chengalur, Matthew Colless, Erwin de Blok and Roberto De Propris. I have benefited from your wisdom and experience.
- Many thanks to Michael B. Pracy for his insight and assistance particularly with the work on Abell 370.
- I am are indebted to Ayesha Begum, Andrew Hopkins, Shaun Ferris, Agris Kalnajs, Nissim Kanekar, Stefan Keller, Wolfgang Kerzendorf, Tony Martin-Jones, Bruce Peterson, Brian Schmidt, Bradley E. Tucker and Eduard Westra for their valuable help.
- I am grateful to the staff and students at Mount Stromlo Observatory for creating such a pleasant working environment.
- Special thanks to the administrative staff at Mount Stromlo Observatory and on ANU main campus who have made dealing with the university bureaucracy easy.
- I want to extend my appreciation to Miss Joan Duffield for setting up the Joan Duffield Research Scholarship.
- I wish to thank the staff of the GMRT for their assistance. The GMRT is run by the National Centre for Radio Astrophysics of the Tata Institute of Fundamental Research.
- I am grateful to the staff of the Anglo Australian Observatory as well as the staff of the Siding Spring Observatory for their assistance.

- This work is based in part on data collected at the Subaru Telescope, which is operated by the National Astronomical Observatory of Japan.
- Thanks goes to the WiggleZ team, particular Michael B. Pracy, and the zCOSMOS team, particularly Simon Lilly.
- This research has made use of the GOLDMine Database.
- This research was supported in part under Australian Research Council's Discovery Projects funding scheme through the grant titled *"Star Formation and Gas Consumption in the High Redshift Galaxies"* (project number 0559688).

Abstract

A new technique has been used to measure in the distant past the gas content of galaxies, the fuel supply for star formation. These results complement the established observations of galaxies that show there has been a ten fold decrease in star formation over the last 8 billion years (from redshift $z \sim 1.0$).

To quantify the atomic neutral hydrogen gas in galaxies their H I 21-cm radio emission has been measured. Instead of trying to observe the weak signal from each galaxy, the H I 21-cm emission signal from multiple galaxies has been coadded together using their known optical positions and redshifts. This coadding technique has been used with radio observations from the Giant Metrewave Radio Telescope (GMRT) and with optical observations from the Anglo-Australian Telescope (AAT) to measure the H I gas content of distant galaxies in a variety of environments from the field to clusters.

Specifically, the average atomic neutral hydrogen (H I) gas content of 121 star-forming galaxies at a look-back time of ∼3 billion years (redshift $z = 0.24$) has been examined, along with the gas content of 324 galaxies around Abell 370, a galaxy cluster at a look-back time of ∼4 billion years (redshift $z = 0.37$). Substantial quantities of H I gas is observed in these distant galaxies and their star formation rate is found to follow the same correlation with their H I gas content as that seen in nearby galaxies. This implies that the star formation mechanisms in these galaxies were not substantially different from those operating today, even though the cosmic star formation rate density was significantly higher at the time.

The H I coadding technique is well suited for use with the next generation of radio telescopes, such as the SKA pathfinder telescopes of ASKAP and MeerKAT. Using the nominal design parameters of these new telescopes, and the properties of galaxies in existing deep optical redshift surveys, estimates of the measurable coadded H I 21-cm radio emission with these telescopes have been made. These estimates show that one can use ASKAP and MeerKAT to measure the H I gas content of galaxies out to a redshift $z = 1.0$. Such observations would provide a full and detailed understanding of the linkage between star formation and gas in galaxies over the last 8 billion years.

Contents

List of Figures

List of Tables

List of Abbreviations

2dF	2 Degree Field system
2MASS	2 Micron All Sky Survey
ΛCDM	Λ Cold Dark Matter (Λ refers to the cosmological constant)
AAOmega	AAT multi-object and integral field spectrograph
AAT	Anglo-Australian Telescope
AGN	active galactic nuclei
AIPS	Astronomical Image Processing System
ANU	Australian National University
arcsec	arcseconds
arcmin	arcminutes
ASCA	Advanced Satellite for Cosmology and Astrophysics
ASKAP	Australian Square Kilometre Array Pathfinder
ASTRON	Netherlands Institute for Radio Astronomy
AUI	Associated Universities, Inc.
CCD	Charge Coupled Device
COSMOS	Cosmological Evolution Survey
Dec.	Declination
DLA	Damped Lyman-α Absoprtion System
ESO	European Southern Observatory
FIRST	Faint Images of the Radio Sky at Twenty-cm
FWHM	full width at half maximum
GALEX	Galaxy Evolution Explorer
GMRT	Giant Metrewave Radio Telescope
Gyr	Gigayear (10^9 years)
GOLDMine	Galaxy On Line Database Milano Network
H I	atomic neutral hydrogen
HIPASS	H I Parkes All Sky Survey
HIRES	High Resolution Echelle Spectrometer
HST	Hubble Space Telescope
IGM	intergalactic medium
IRAF	Image Reduction and Analysis Facility
IRAS	Infrared Astronomical Satellite
ISM	interstellar medium

Jy	Jansky (1 Jy = 10^{-23} erg s^{-1} cm^{-2} Hz^{-1})
$M_\odot$	solar mass (1.9889×10^{33} g)
MERLIN	Multi-Element Radio-Linked Interferometer Network
MeerKAT	'Meer' Karoo Array Telescope ('meer' is Afrikaan for 'more')
NGC	New General Catalogue
NRAO	National Radio Astronomy Observatory
NVSS	NRAO VLA Sky Survey
pc	parsec (1 parsec = 3.0857×10^{16} m, 3.26 light years)
QSO	quasi-stellar object
R.A.	Right Ascension
RCS2	Red Sequence Cluster Survey 2
RFI	radio frequency interference
RMS	root mean square
SDSS	Sloan Digital Sky Survey
SFR	Star Formation Rate
SFRD	Star Formation Rate Density
SKA	Square Kilometer Array
SIS	Solid-state Imaging Spectrometer (on ASCA)
SNR	Signal to Noise Ratio
VIMOS	VIsible MultiObject Spectrograph
VLA	Very Large Array
VLT	Very Large Telescope
WSRT	Westerbork Synthesis Radio Telescope

Chapter 1

Introduction

The most incomprehensible thing about the universe is that it is comprehensible.

Albert Einstein

The aim of this thesis is to examine the amount of neutral atomic hydrogen gas (H I) in galaxies in the distant past. The rate at which new stars are formed in galaxies is known to have been much higher in the past. Around 8 billion years ago (at redshift $z \sim 1$, 60 per cent of the age of the universe ago) the star formation rate density of the universe was ten times higher than it is currently (Lilly et al. 1996; Madau et al. 1996). However the evolution in the gas content of galaxies - the fuel supply for this star formation - is only poorly constrained by observations over this period. Nearby galaxies in the dense environment of galaxy clusters show strong evidence for environmental effects that are reducing their gas content (Haynes, Giovanelli, & Chincarini 1984). Little is known though of the gas content of clusters in the distant past during the era of higher star formation. In this thesis the gas content of galaxies in the era of higher star formation is examined both within the dense environment of clusters and in lower density field environments. This will give a clearer picture of how, when and where stars and their host galaxies form, improving our understanding of our place in the universe, residing in our galaxy, the Milky Way, and orbiting our star, the Sun.

Neutral atomic hydrogen gas (H I) emits a radio signal that can be used to measure the amount of gas present. This radio emission has been used to quantify the H I gas content of nearby galaxies. The H I emission signal from the distant galaxies ($z > 0.1$) is weak making it difficult to detect even with the largest radio telescopes available today. To measure the H I radio emission from distant galaxies the coadding technique (stacking) has been used in this thesis. This involves using optical observations of the position and redshift of a galaxy to identify where one would expect the weak H I signal of the galaxy to be in radio observations. The signal from many galaxies can then be combined to create a measurable signal from which one can quantify the average amount of gas in the combined galaxies. The radio observations for this project were carried out using the Giant Metrewave Radio

Telescope (GMRT) in India. Optical observations came from numerous sources, the most important being the Anglo-Australian Telescope in Australia.

Currently a new era of radio astronomy is beginning. There are a slew of new radio telescopes being built and proposed specifically to address the issue of the evolution of gas in galaxies. The project overshadowing everything else is the proposed Square Kilometre Array (SKA). This telescope will have a collecting area of one square kilometre making it ∼100 times more sensitive than the best present-day instruments. This multi-billion dollar project is proposed to be built over the coming decades by a large international consortium. The SKA will revolutionise the study of gas in galaxies (van der Hulst et al. 2004). The work of this thesis pushes out the limit of what can be done with current telescopes in measuring neutral atomic hydrogen gas (H I), providing results that will influence the design and use of the precursor telescopes to the SKA (the "technology demonstrators") as well as the SKA itself.

This thesis has the following structure. *Chapter 1*, the rest of the current chapter (the Introduction), is given over to background information. This includes: a review of neutral atomic hydrogen gas (H I) and how it is observed, an examination of the evolution of the star formation rate, the stellar mass and the neutral gas content of galaxies, a discussion on galaxy clusters and H I gas in such systems, and finally a brief description of the main radio and optical telescopes used in the thesis. *Chapter 2* of the thesis explores the H I gas content of star-forming galaxies at $z = 0.24$ (∼3 billion years ago) from radio and optical observations. This work has been published in Lah et al. (2007). *Chapter 3* of the thesis examines the H I gas content of galaxies around Abell 370, a galaxy cluster at $z = 0.37$ (∼4 billion years ago) from radio and optical observations. This work has been published in Lah et al. (2009). *Chapter 4* of the thesis presents two unusual radio continuum objects that were found in the radio observations of Abell 370. One is an unusual shaped radio jet that is contained within a small galaxy group that lies in the foreground of Abell 370. The other is a possible radio gravitational arc near the centre of the cluster core of Abell 370. *Chapter 5* of the thesis details the use of the H I coadding technique with the new generation of SKA pathfinder telescopes currently being built. The new telescopes examined are the Australian ASKAP and the South African MeerKAT. The optical surveys consider are WiggleZ and zCOSMOS. *Chapter 6* presents a summary of the thesis work and some conclusions and ideas that came out of the work of the thesis. Additionally some of the challenges encountered and overcome in the thesis are discussed.

Additionally, there are five appendices. *Appendix A* of the thesis details the technique of threshold flagging of radio data used in this work. *Appendix B* of the thesis contains the calculations required to convert a measured 21-cm emission radio signal to the corresponding H I mass that produced the signal. *Appendix C* of the thesis contains a list of spectral lines used in this work. *Appendix D* present some of the problems encountered and overcome during the PhD and the lessons learnt. *Appendix E* provides some insight into the world of AIPS.

Throughout this thesis the consensus cosmological parameters of $\Omega_\lambda = 0.7$, $\Omega_M = 0.3$ and $H_0 = 70\ \mathrm{km\,s^{-1}\,Mpc^{-1}}$ have been adopted.

1.1 Neutral atomic hydrogen gas (H I)

Hydrogen makes up ∼74 per cent of the mass of baryonic matter in the universe, with helium making up ∼24 per cent and heavier elements making up the last ∼2 per cent (Boesgaard & Steigman 1985). As such, hydrogen and to a lesser extent helium are the primary material that form the stars. Hydrogen exists in three main forms in the universe: ionised hydrogen (HII), which is a plasma of free floating protons and electrons, atomic neutral hydrogen (H I), which is a gas of neutral atoms consisting of a single proton with its bound electron, and molecular hydrogen (H_2), which consists of two atoms of hydrogen chemically bonded together. Of these three forms molecular hydrogen (H_2) is the form most frequently encountered on the Earth as the other two forms of hydrogen can only exist for long periods in low density environments such as that found in space.

Since the end of reionisation (after $z \sim 7$, around a billion years after the big bang, Spergel et al. 2007) the majority of hydrogen in the universe has been in ionised form and primarily located in the space between galaxies (Fukugita, Hogan, & Peebles 1998; Nicastro et al. 2005). Only within galaxies are large quantities of non-ionised (neutral) hydrogen found. The hydrogen in galaxies can form gas clouds that are sufficiently dense to survive against the background ionising radiation in the universe. When a neutral atomic hydrogen gas cloud reaches a sufficiently low temperature and high density it can form molecular hydrogen (H_2) and can then collapse further to form stars. As such, neutral atomic hydrogen gas (H I) is the key reservoir of fuel for the formation of new stars in galaxies.

In the ground state of an atom of neutral hydrogen the spins of the proton and electron are anti-parallel. Within H I gas clouds collisions between atoms can excite a hydrogen atom to the slightly higher energy state in which the spins of the proton and electron are parallel. When such an atom decays back to the ground state it emits a photon at a wavelength of 21.106 cm (frequency 1420.406 MHz). A diagram showing this transition can be seen in Fig. 1.1. The half life for this decay is ∼10 million years ($\sim 3 \times 10^{14}$ s). This long timescale would initially make it seem unlikely that one could ever detect such rare events. However 1 $M_\odot$ (1.99×10^{33} g) of atomic hydrogen contains 1.2×10^{57} atoms and galaxies that contain H I gas commonly have between 10^7 to 10^{10} $M_\odot$ (Zwaan et al. 2005). This gives them an H I 21-cm luminosity of between 2×10^{32} to 2×10^{35} ergs s^{-1} which is a sufficiently strong radio signal to be detected using radio telescopes for nearby galaxies (Appendix B contains the details of how one calculates this).

Still as one observes out to greater distances and hence further back in time the detection of this H I 21-cm signal from galaxies becomes increasingly difficult due to the weak flux of the emission. In contrast one can detect optical emission from galaxies out to much greater distances due to their significantly higher luminosities.

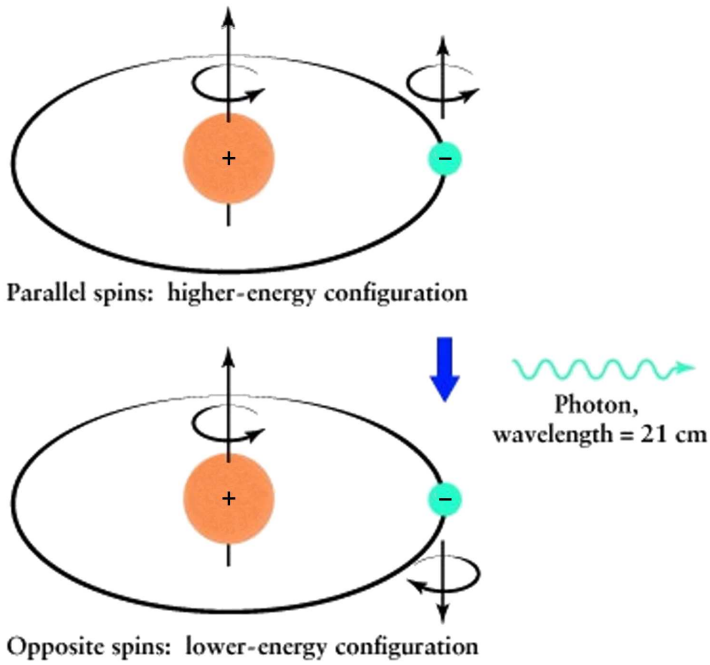

Figure 1.1: This diagram shows the hydrogen atom spin-flip transition that produces H I 21-cm emission. The top panel shows the slightly excited state (higher energy state) of the hydrogen atom where the proton and electron have parallel spin. The bottom panel shows the ground state of the hydrogen atom where the proton and election spins are anti-parallel. When a hydrogen atom decays to the ground state it emits a photon with a wavelength of 21-cm (a frequency of 1420 MHz) as shown in the diagram. (This figure is a modified version of one by Paul Eskridge, Department of Physics & Astronomy, Minnesota State University).

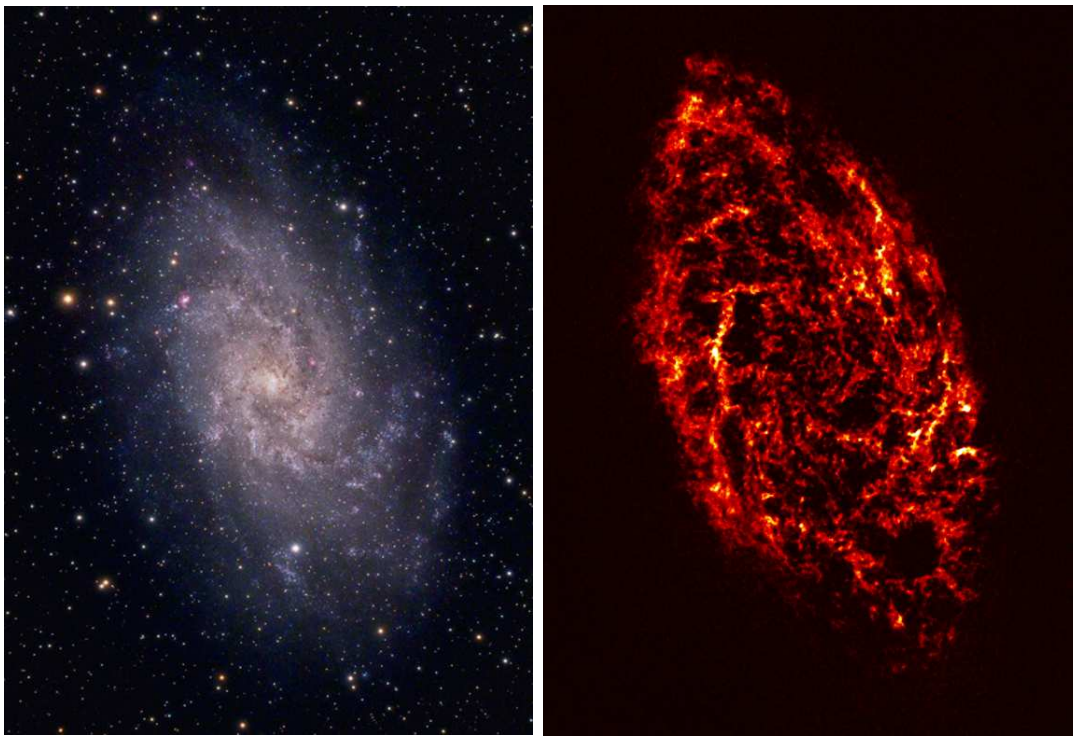

Figure 1.2: This figure shows the Triangulum Galaxy M33. The left panel shows the galaxy as seen in the optical and the right panel as seen in the hydrogen 21-cm emission. The images are ∼1 degree across. (The optical image is courtesy of Walter Koprolin observed with a 4.1" refractor with a digital camera. The H I image is courtesy of NRAO/AUI observed with the VLA.)

For example, the optical spectral line Hα (at 6563 Å) is produced in regions of active star formation of galaxies. The typical luminosity of the Hα emission line for star-forming galaxies ranges commonly from 3×10^{39} to 3×10^{42} ergs s^{-1} (Fujita et al. 2003). So H I 21-cm emission has $\sim 10^7$ times lower power than Hα emission from star-forming galaxies, the galaxies where one expects to find the most neutral hydrogen gas. Other optical spectral lines are similarly luminous.

1.1.1 H I gas in galaxies

Much can be learnt about galaxies by studying both their optical emission and their H I 21-cm emission that traces out their neutral atomic hydrogen gas content. This can be seen in Fig. 1.2 that shows the optical image (left panel) and H I 21-cm emission (right panel) of the nearby Triangulum Galaxy (an Sc galaxy). The optical emission and H I 21-cm emission from the galaxy are distributed differently. The optical emission peaks at the central bulge of the galaxy while the H I 21-cm emission has a local minimum there. The optical brightness tails off smoothly at the outskirts of the galaxy while the H I 21-emission has a relatively sharp truncation

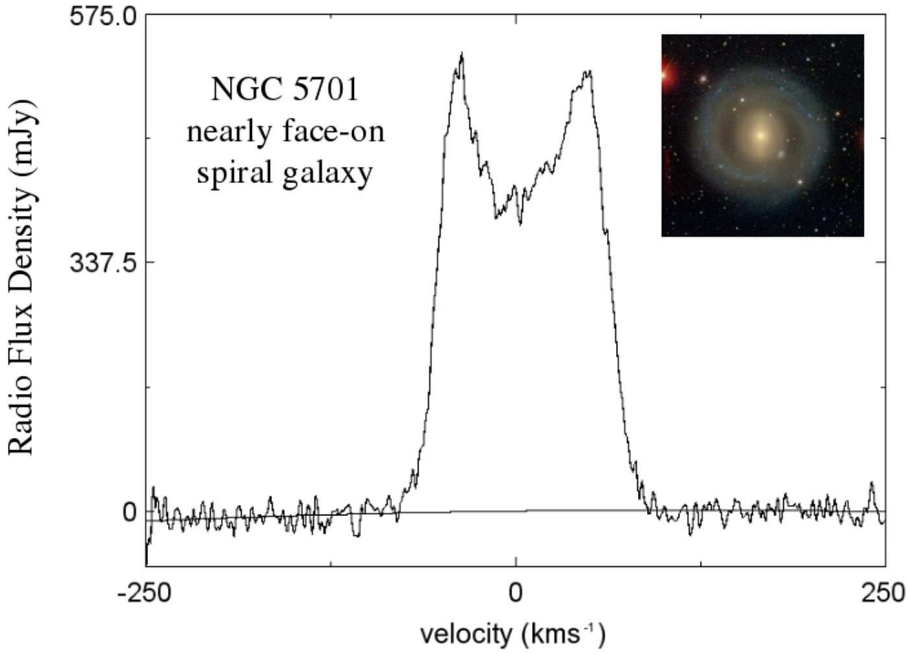

Figure 1.3: The H I emission of spectrum of galaxy NGC 5701 from the (now deactivated) Green Bank 42 m telescope (Haynes et al. 1997). In the top right hand corner is the optical image of the galaxy from the SDSS.

at the galaxy outskirts. Some of the features seen in the optical image such as the spiral arms are also traced out in the H I 21-cm emission.

Radio observations of H I 21-cm emission in a galaxy provide not only a map of the spatial distribution on the sky of the hydrogen gas but also provide measurements of the velocity of the gas from its Doppler Shift. Fig. 1.3 shows the H I 21-cm emission spectrum of the nearby galaxy NGC 5701 (the optical image of the galaxy is in the corner of the figure). This H I spectrum shows the classic double-horn profile which is caused by the hydrogen gas moving with the same velocity at all radii within the disk of the galaxy, i.e. not in Keplerian rotation. That fact that the motion is not Keplernian indicates that there is increasing mass with galaxy radius. The H I gas acts as a tracer for the motion of matter within a galaxy.

Neutral atomic hydrogen gas is the fuel for star formation. This can be seen in the correlation between the star formation rate of a galaxy and the mass of H I gas it contains. Fig. 1.4 shows this correlation with the H I mass of galaxies from HIPASS plotted against their star formation rates from *IRAS* infrared data (Doyle & Drinkwater 2006). This linear fit, taken directly from their figure, is:

$$\log(\text{HI Mass}) = 0.59 \log(\text{SFR}) + 9.55 \tag{1.1}$$

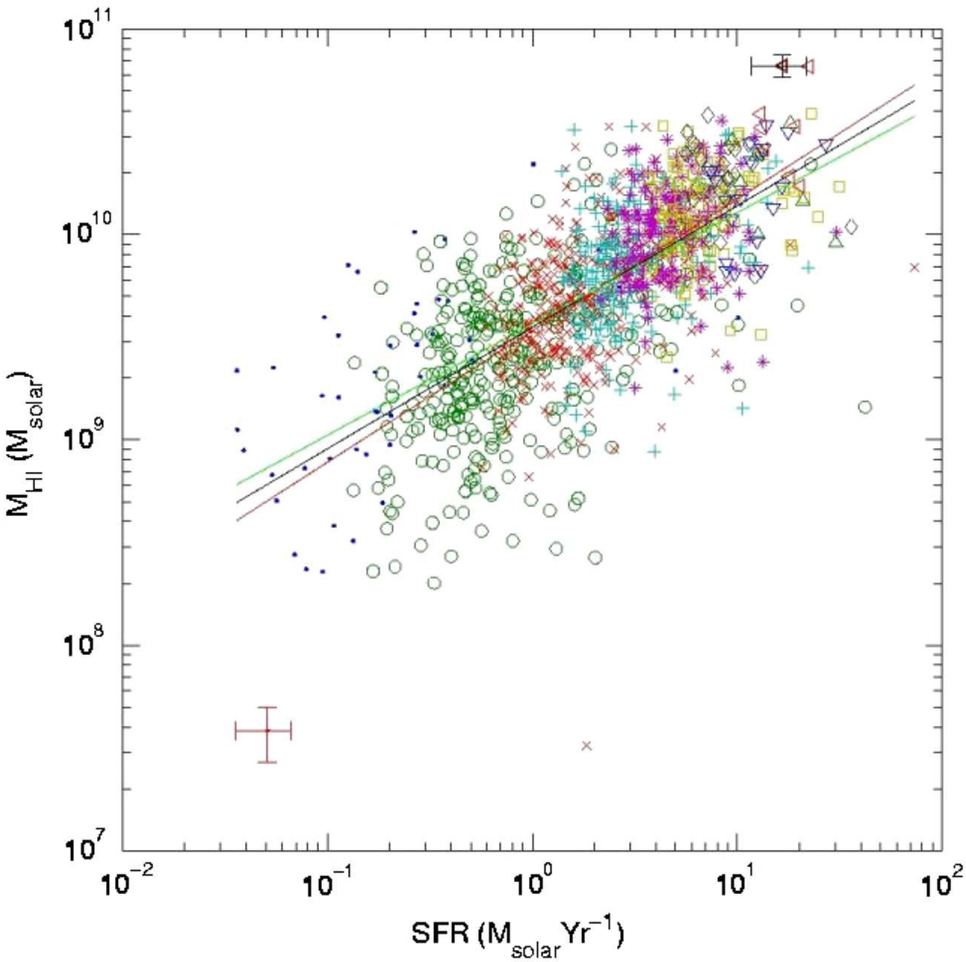

Figure 1.4: This figure shows the H I mass of galaxies from HIPASS plotted against their star formation rates from *IRAS* infrared data as compiled by Doyle & Drinkwater (2006). The least-squares fit to the correlation is shown with the 3σ gradient uncertainty lines.

This relationship between the H I mass and star formation rate of a galaxy does have some real astrophysical scatter. This is probably due to differences in the environment and galaxy structure (morphology) of the galaxies. This relationship is related to but not the same as the Schmidt Law, a relationship between a galaxy's gas surface density and the disc average star formation rate surface density as discussed in Kennicutt (1998b). The above relationship between a galaxy's H I mass and SFR does not have any surface density component to it.

1.2 Galaxy evolution

1.2.1 Evolution in star formation rate and stellar mass of galaxies

Over the last ∼8 billion years (from about $z \sim 1$) the rate at which stars are produced in galaxies has dropped by a factor of 10 (Lilly et al. 1996; Madau et al. 1996). This decrease in the star formation rate density of the universe has been well established by observation as seen in Figure 1.5. The top panel shows the star formation rate density vs. redshift and the bottom panel the same star formation rate data but plotted against look-back time. This data was compiled by Hopkins (2004) from literature values from many different indicators of star formation. These included X-ray, ultraviolet, the optical emission lines of [OII], Hβ & Hα infrared, sub-mm, and radio continuum 1.4 GHz observations. The different indicators of star formation all give good agreement with each other for redshifts less than $z = 2.0$ (∼10 billion years ago).

The growth in the total mass of stars in the universe has also been well constrained observationally as seen in Figure 1.6. The top panel shows the stellar mass density vs. redshift and the bottom panel the stellar mass density vs. look-back time. These data are also compiled from literature values and are primarily derived from near-infrared observations that are combined with optical redshift information to measure the absolute luminosity of the galaxies. This is then converted to a stellar mass by assuming some initial mass function for the stars. From redshift $z \sim 1$ (∼8 billion years ago) to $z = 0$, there has only been a doubling in the stellar mass density due to the decreasing rate of star formation over this period. At higher redshifts, a faster rise in the stellar mass in galaxies is seen corresponding to the higher star formation rate during that period. At some point in time the stellar mass density must reach zero as the universe did not start with stars in it. This point will be reached somewhere above $z = 7.0$. The stellar mass density is a measure of the integrated rate of star formation over time. There is a reasonably good understanding about when the stars in galaxies formed. Nevertheless, to explain why there has been a decrease in the star formation rate density in the universe, one needs to look at the neutral gas content of the galaxies, the fuel for star formation.

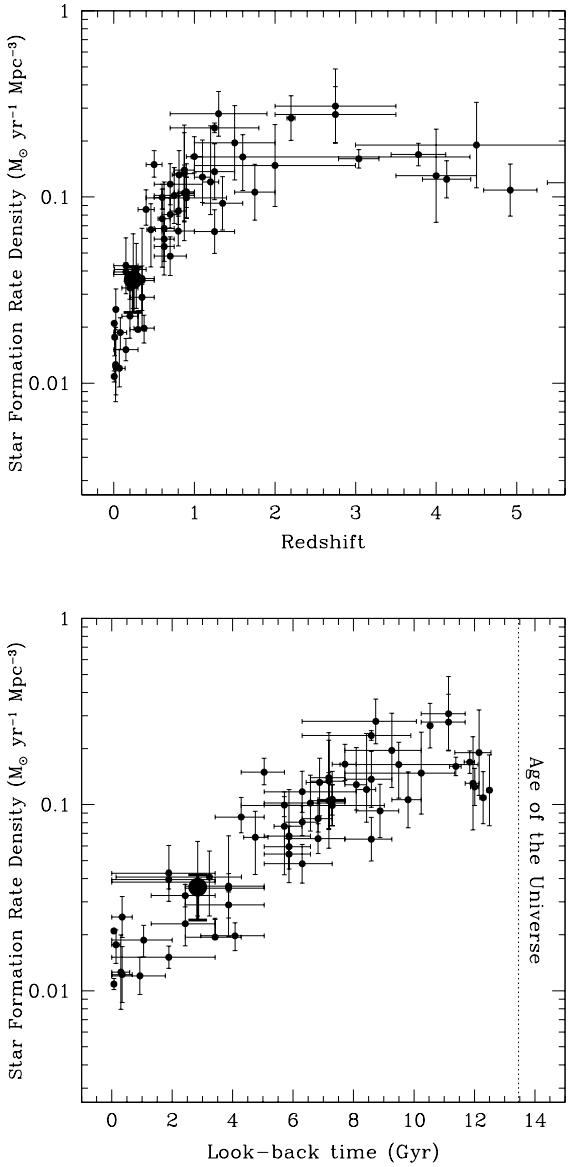

Figure 1.5: The evolution of the rate at which stars are produced in the universe, measured in solar masses per year per megaparsec cubed (the Madau-Lilly Plot). The top panel shows the star formation rate density vs. redshift and the bottom panel the star formation rate density vs. look-back time. The data is a compilation of literature X-ray, ultraviolet, the optical emission lines of [OII], Hβ & Hα infrared, sub-mm, and radio continuum 1.4 GHz observations by Hopkins (2004). The large point at $z = 0.24$ (top panel) and look-back time 2.7 Gyr (bottom panel) is the value from the 'Fujita' galaxies (Fujita et al. 2003) which are examined in in Chapter 2 for H I gas.

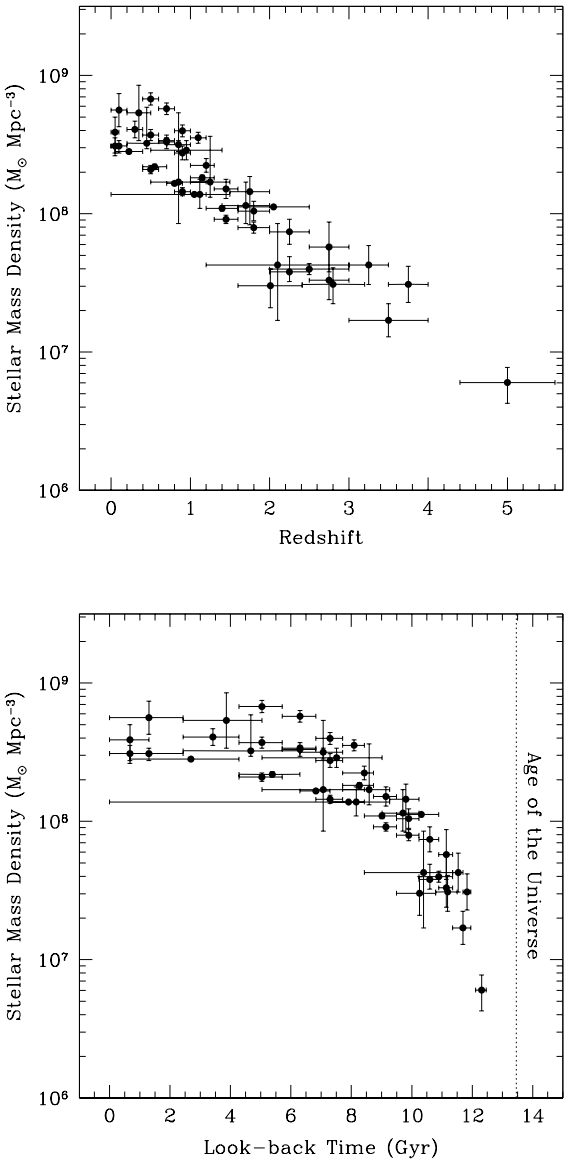

Figure 1.6: The increase with time of the mass in stars in the universe, measured in solar masses per megaparsec cubed. The top panel shows the stellar mass density vs. redshift and the bottom panel the stellar mass density vs. look-back time. The data used comes from Cole et al. (2001), Bell et al. (2003), Dickinson et al. (2003), Rudnick et al. (2003), Sato et al. (2004), Drory et al. (2004), Fontana et al. (2006), Stark et al. (2007), Pozzetti et al. (2007) and Pérez-González et al. (2008).

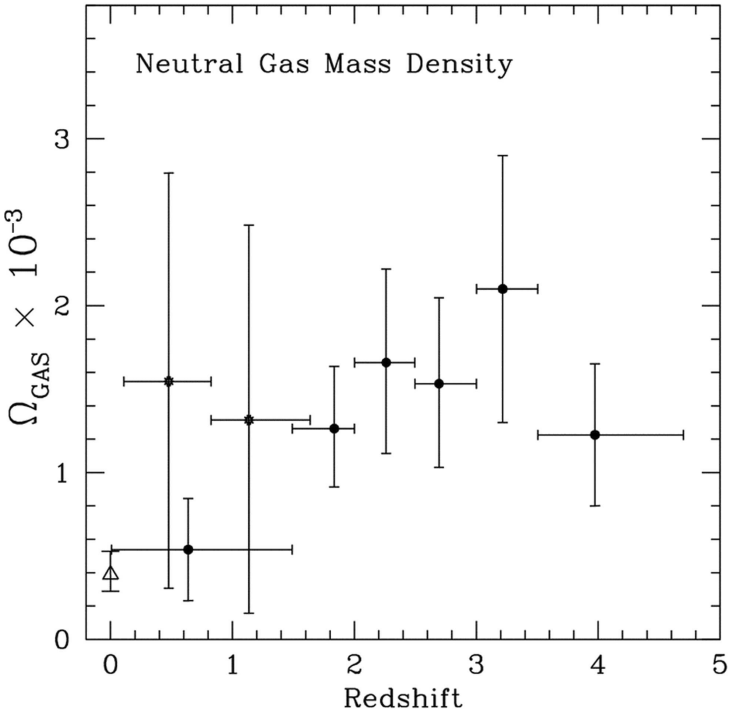

Figure 1.7: The evolution of the neutral gas density of the universe as it was believed to be in 2004 (the start of the thesis). The values have not been adjusted to the then new Λ cosmology. The value Ω_{gas} is the neutral gas density as a fraction of critical density Ω_0. The values here include a correction to the measured hydrogen gas for the expected neutral helium content. The open triangle at $z = 0$ is the HIPASS 21-cm emission measurement from Zwaan et al. (2003). The other values are all damped Lyman-α absorptions systems measurements from Storrie-Lombardi & Wolfe (2000) and Rao & Turnshek (2000).

1.2.2 Evolution in the gas content of galaxies

Back when the work on this thesis began in 2004 the picture of gas evolution in galaxies was somewhat different to the picture now in 2009. The cosmic neutral gas density as a function of redshift is shown in Fig. 1.7 as it was measured at the start of 2004. The value Ω_{gas} is the neutral gas density as a fraction fraction of critical density Ω_0. This has been calculated from measurements of the H I gas with a correction made to include the expected neutral helium content, which is assumed to be 24 per cent by mass of the total neutral gas. No correction for molecular hydrogen gas has been made. The open triangle at $z = 0$ is made from the 1000 galaxies with the highest H I 21-cm peak flux densities in H I Parkes All Sky Survey (HIPASS) by Zwaan et al. (2003). The other values are all damped Lyman-α absorptions systems measurements from Storrie-Lombardi & Wolfe (2000) and Rao & Turnshek (2000) (damped Lyman-α absorptions systems are discussed

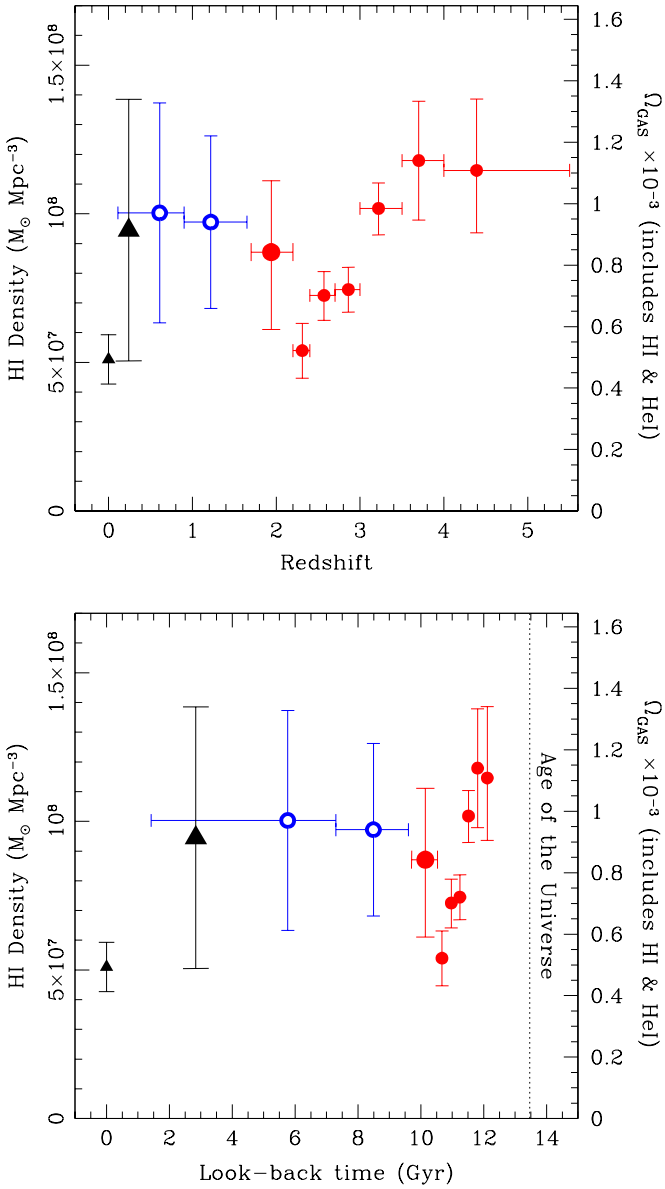

Figure 1.8: The evolution of the neutral gas density of the universe as currently measured. The top panel shows the cosmic neutral gas density vs. redshift and the bottom panel the cosmic density vs. look-back time. All results have been corrected to the same cosmology. The left y-axis shows the cosmic density in terms of H I gas density measured in solar masses per megaparsec cubed. The right y-axis shows the cosmic density measured as a fraction of total critical density Ω_0 and includes the correction for the neutral Helium content. The small triangle at $z = 0$ is the HIPASS 21-cm emission measurement from Zwaan et al. (2005). The small filled circles are damped Lyman-α measurements (Prochaska & Wolfe 2009) as is the larger filled circle (Prochaska, Herbert-Fort, & Wolfe 2005). The open circles are damped Lyman-α measurements from Rao, Turnshek, & Nestor (2006) using HST. The large triangle at $z = 0.24$ is the H I 21-cm emission measurement made in this thesis (see Chapter 2 or Lah et al. 2007)

in detail in below).

Fig. 1.7 shows that the neutral gas density was poorly constrained by observations particularly for redshift below $z = 1.5$. However there appears to be a factor of $\sim$5 increase in the cosmic gas density at the higher redshift values compared to that at $z = 0$, suggesting significant evolution in the gas content of galaxies. Unfortunately this large increase in the gas content was found to be mostly due to the old cosmological parameters used in the calculations. It was only around this time that the Λ-Cold Dark Matter model (ΛCDM) of the universe was becoming the consensus cosmology used by astronomers. The strong results from multiple experiments including the observed brightness of supernovae (Riess et al. 1998; Perlmutter et al. 1999), the observed large scale structure of the universe (Percival et al. 2001) and the variations observed in the microwave background (Spergel et al. 2003) enshrined the ΛCDM model as the preferred cosmological model.

The current best measurements of the cosmic neutral gas density can be seen in Fig. 1.8. These measurements are using ΛCDM and included additional observational results to the previous figure from 2004. The top panel of Fig. 1.8 shows the cosmic neutral gas density vs. redshift and the bottom panel shows the same data vs. look-back time. The left y-axis of these plots shows the cosmic density in terms of the actual measured H I gas density. The right y-axis of these plots shows the cosmic density measured as a fraction of the total critical density Ω_0 and includes the correction for the neutral Helium content (this is the same quantity as plotted in Fig. 1.7). The small triangle at $z = 0$ is made from the 4315 H I 21-cm detected galaxies in HIPASS by Zwaan et al. (2005). The filled circles are damped Lyman-α measurements from Prochaska, Herbert-Fort, & Wolfe (2005) and Prochaska & Wolfe (2009). The open circles are damped Lyman-α measurements from Rao, Turnshek, & Nestor (2006) using the *Hubble Space Telescope* (HST). The large triangle at $z = 0.24$ is the H I 21-cm emission measurement made in this thesis (see Chapter 2 or Lah et al. 2007). The size of the errors in this figure have decreased somewhat from the previous Fig. 1.7 especially at the higher redshifts ($z > 1.5$). However the introduction of the ΛCDM has considerably changed the apparent evolution of neutral atomic hydrogen gas in galaxies. Instead of a factor of $\sim$5 decrease in the gas content of galaxies there now appears to be a factor of only $\sim$2. This is not a large change and calls into question whether there has actually been any significant evolution in the H I gas content of galaxies.

1.3 Measuring the gas content of galaxies in the distant past

1.3.1 Damped Lyman-α absorption systems

In the nearby universe ($z \sim 0$) the quantity of atomic hydrogen gas in galaxies has been measured with good precision using H I 21-cm emission surveys (Briggs 1990; Zwaan et al. 1997; Zwaan et al. 2003; Zwaan et al. 2005). At higher redshifts (large

distances), the weak flux of H I 21-cm emission has made it difficult to measure the gas content of galaxies using this technique. Instead, a different method has been used by astronomers to quantify the neutral hydrogen gas content at these distances. They have studied optically bright, distant objects known as quasars or QSO's (quasi-stellar objects) that can be seen right across the universe. If a hydrogen gas cloud lies somewhere on the path that the light travels from the quasar to us, a Lyman-α absorption feature is seen in the spectrum of the quasar. Large hydrogen gas clouds seen in quasar spectra are known as damped Lyman-α absorption systems due to the characteristic shape of their absorption.

Lyman-α is a spectral line of hydrogen at 1216 Å in the ultraviolet. Lyman-α emission is caused by the decay of the electron in a neutral hydrogen atom from the $n = 2$ orbital level to the $n = 1$ orbital (ground state), where 'n' is the principal quantum number. Lyman-α absorption occurs when neutral atomic hydrogen in its ground state is struck by light at 1216 Å and its electron is excited to the $n = 2$ state. As the light from the quasar is redshifted in its journey to us the observer, many hydrogen clouds at different distances (redshifts) can absorb light from the quasar and be identified in the quasar spectrum. Fig. 1.9 shows diagrammatically how this process forms damped Lyman-α absorption systems.

Fig. 1.10 shows an example of an observed optical spectrum for a quasar that has a damped Lyman-α absorption system (DLA). This is quasar QSO 1425+6039 located at redshift $z = 3.2$ whose spectrum contains a damped Lyman-α absorption system at redshift $z = 2.8$. Besides the large absorption feature of the damped Lyman-α system there are numerous small absorption troughs seen in the spectrum. This is the Lyman-α forest which is caused by hydrogen gas clouds in the intergalactic medium between galaxies. Only a very small fraction of the hydrogen needs to be neutral atoms in these clouds to create these absorption spikes; the vast majority of the gas in such clouds is ionised hydrogen (H II). The broad absorption features of damped Lyman-α systems are expected to be caused by galaxies with their appreciable H I gas content.

Lyman-α absorption is a factor of 10^6 times more sensitive to low column density H I gas than typical H I 21-cm emission observations (Haynes 2008). The flux of emission from an object is reduced by the distance to the object. The strength of an absorption feature, though, does not depend on the distance to the absorber; it depends only on the flux of the object producing the emission against which the absorption is seen. Thus absorption measurements can be made out to extremely high redshifts as long as one can find sufficiently strong sources to measure the absorption against. At redshifts $z > 1.5$ the rest-frame ultraviolet Lyman-α feature has been redshifted to optical wavelengths and so can be observed using ground based telescopes.

By observing many different quasars and quantifying the number, size and position of any observed damped Lyman-α absorption systems, it is possible to measure the average amount of neutral atomic hydrogen gas in the universe as a function of time (see Section 1.2.2). Observations of damped Lyman-α absorption in QSO spectra have proven very effective at measuring the density of atomic hydrogen gas

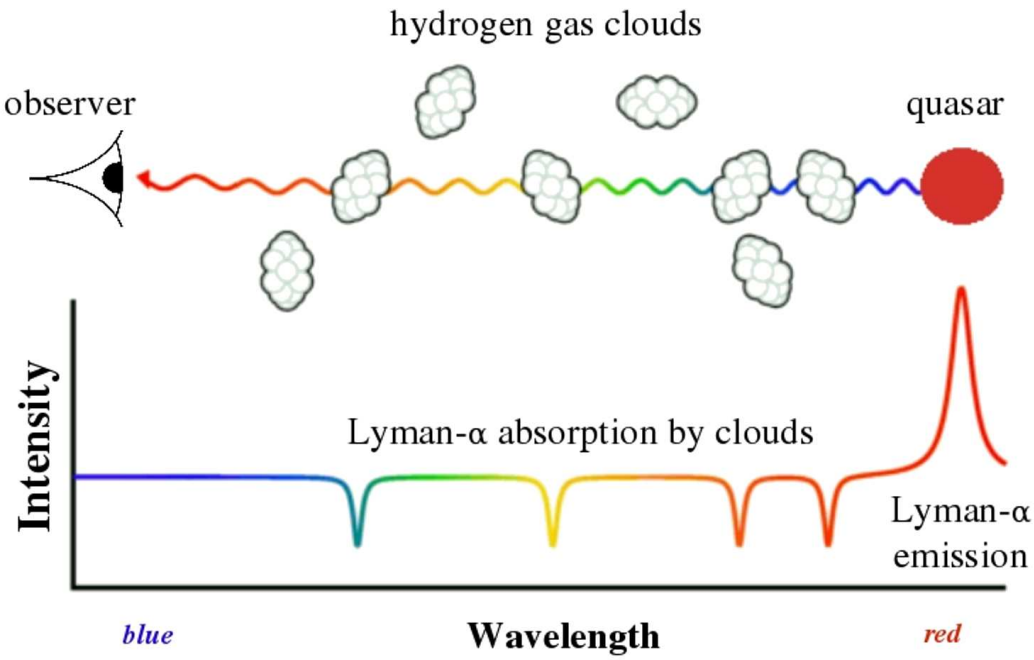

Figure 1.9: This cartoon shows how Lyman-α absorption systems are produced. The light path travelled by the quasar to observer is shown on top with the observed optical spectrum shown below. The light emitted by the quasar is redshifted. This means the Lyman-α emission from the quasar is observed at a much redder wavelength than its rest frame value of 1216 Å (in the ultraviolet). The light from the distant quasar intersects through several hydrogen gas clouds before reaching the observer. The hydrogen gas clouds absorbs light from the quasar at the wavelength of Lyman-α. However by the time the light from the quasar has reached the gas clouds it has been redshifted so that the absorption occurs at different wavelength (the quasar light would originally have been at a bluer wavelength than Lyman-α when it was emitted by the quasar). For each hydrogen gas cloud separate Lyman-α absorption features will be produced in the observed quasar spectrum at different wavelengths that depend on the redshifts (distances) of the clouds (Image modified from that by Edward L. Wright, UCLA Division of Astronomy & Astrophysics).

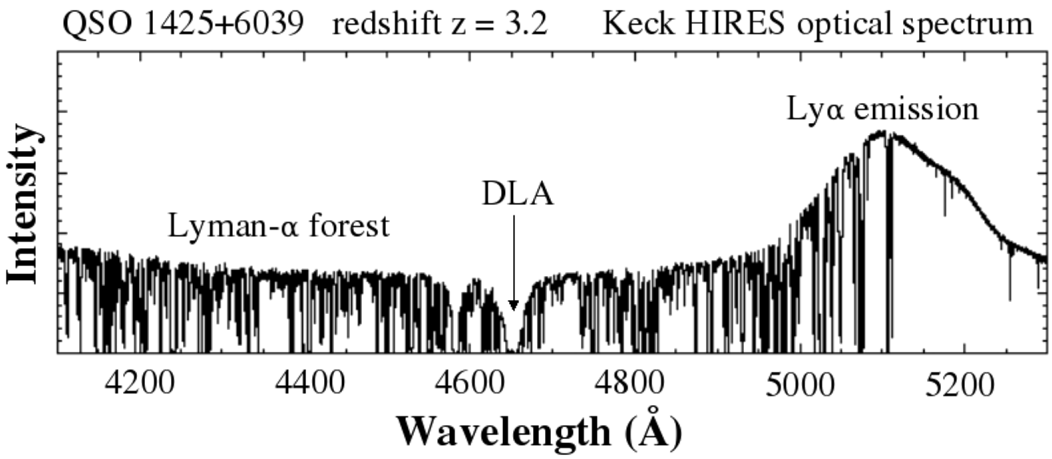

Figure 1.10: This figure shows the optical spectrum for a quasar QSO 1425+6039 located at redshift $z = 3.2$. The redshifted Lyman-α emission from the quasar can be seen at wavelength 5100 Å. Absorption by many different small hydrogen gas clouds can be seen in the Lyman-α forest. At wavelength 4650 Å there is the strong absorption by an optically thick cloud at redshift $z = 2.8$, a damped Lyman-α absorption system. (Spectrum observed with HIRES on the Keck Telescope. Image from Wallace Sargent, Caltech.)

at high redshifts, $z > 1.5$ (Storrie-Lombardi & Wolfe 2000; Prochaska, Herbert-Fort, & Wolfe 2005).

Be that as it may, it is difficult to measure the H I gas density from observations of damped Lyman-α absorbers at intermediate redshifts ($0 < z < 1.5$). The difficulties are: (i) that observations have to be done from space, since at these redshifts the Lyman-α line is still in the ultraviolet and thus not accessible from the ground, and (ii) that the average number of damped Lyman-α absorbers per unit redshift is so low that an accurate estimate of gas density requires impractical amounts of observing time. At lower redshifts ($z < 1.5$), Rao, Turnshek, & Nestor (2006) have made measurements of the neutral gas density using *Hubble Space Telescope* (HST) observations of clouds that were preselected in ground based optical observations to have strong absorption by singly ionised Magnesium (Mg II). Thus this is a potentially biased sample of objects compared to the random lines of sight probed by damped Lyman-α systems at high redshift. A problem inherent in the use of damped Lyman-α measurements is the difficulty in identifying the absorbing system. The faint galaxy which hosts the absorbing hydrogen gas cloud is overwhelmed by the light from the bright QSO, making optical imaging or spectroscopy of that galaxy difficult. For these reasons it would be advantageous to measure the gas content of galaxies at moderate redshifts ($z > 0.1$) using H I 21-cm emission provided adequate levels of sensitivity can be reached.

1.3.2 H I 21-cm emission at moderate redshift

Observations of H I 21-cm emission from galaxies at cosmological distances ($z > 0.1$) have been made despite the difficulty. A single galaxy with H I 21-cm emission was detected in the rich cluster Abell 2218 at $z = 0.18$ using 216 hours with the Westerbork Synthesis Radio Telescope (WSRT) (Zwaan, van Dokkum, & Verheijen 2001). Again only a single galaxy with H I 21-cm emission was detected in the galaxy cluster Abell 2192 at $z = 0.19$ using ∼80 hours with the Very Large Array (VLA) (Verheijen 2004). After an upgrade of the WSRT, a new pilot study was able to detect H I 21-cm emission from 19 galaxies in galaxy cluster Abell 963 at $z = 0.21$ using 240 hours and 23 galaxies in galaxy cluster Abell 2192 at $z = 0.19$ using 180 hours (Verheijen et al. 2007). Additionally, the upgraded Arecibo radio telescope has detected H I 21-cm emission at redshifts between $z = 0.17$ to 0.25 from ∼20 isolated galaxies selected in the optical from the Sloan Digital Sky Survey (Catinella et al. 2008). While the numbers of H I 21-cm emission galaxies directly detected at cosmological distances has been increasing with time, the numbers are still small and limited to the most gas rich systems.

The goal of this thesis was to quantify the gas content of hundreds of galaxies at moderate redshifts by measuring their H I 21-cm emission. Rather than trying to measure the 21-cm signal from the individual galaxies, the signal from multiple galaxies is coadded together to produce a detectable signal (stacking). This is done by observing multiple distant galaxies in the radio usually in a single pointing. The observed optical position and precise optical spectroscopic redshift of each galaxy is used to locate where in the radio observations one would expect to find its H I 21-cm signal. The individual radio signal from a galaxy is below the detection limits of the telescope. However, by combining these measurements, the random noise on each measurement should average systematically towards zero and the combined H I 21-cm emission from the galaxies be measurable. The combined signal can then be used to quantify the average neutral hydrogen gas content of the galaxies.

For a coadded observation one finds the average signal simply by summing the values and dividing by the number as seen below:

$$S_{average} = \frac{S_1 + S_2 + S_3 + \dots}{n} \tag{1.2}$$

where S_1, S_2, S_3, etc. are the individual signal measurements for the different observed galaxies and n is the number of galaxies measured. The average noise (uncertainty) in this average signal is given by:

$$N_{average} = \frac{\sqrt{\sigma_1^2 + \sigma_2^2 + \sigma_3^2 + \dots}}{n\sqrt{t}} \tag{1.3}$$

$$= \frac{\sigma}{\sqrt{n\,t}} \quad \text{if all the errors are equal} \tag{1.4}$$

where σ_1, σ_2, σ_3, etc. are the errors for each signal measurement in some short time interval t_0, and t is the total integration time of observation in units of t_0. The signal to noise ratio (SNR) for the coadded observations is then:

$$SNR = \sqrt{n\,t}\,\frac{S_{average}}{\sigma} \tag{1.5}$$

So as long as the errors for the different observed galaxies are the same, the sensitivity of the observations should increase by the $\sqrt{n}$, where n is the number of galaxies coadded. Thus the coadded measurement of the average H I of 100 galaxies will have a signal to noise 10 times higher than the measurement in the same observations of a single galaxy which has an H I mass equal to that average H I mass. This is equivalent to increasing the integration time by a factor of 100 for the observation of a single galaxy.

The assumption that the error in each galaxies signal is the same does not always hold. If the observed galaxies are scattered all over the primary beam of the telescope then they will be measured with varying sensitivity and hence have widely different uncertainties. In this case it is best to combine the signal using a weighted average such that:

$$S_{average} = \frac{\Sigma\, w_i\, S_i}{\Sigma\, w_i} \tag{1.6}$$

$$= \frac{\Sigma\, \frac{S_i}{\sigma_i^2}}{\Sigma\, \frac{1}{\sigma_i^2}} \tag{1.7}$$

where w_i is the value of the weights with $w_i = \frac{1}{\sigma_i^2}$, with σ_i being the uncertainties, as above, in the ith measurement.

The average noise (uncertainty) in this weighted average signal is given by:

$$N_{average} = \frac{\sqrt{\Sigma\,(w_i\,\sigma_i)^2}}{\sqrt{t}\,\Sigma\, w_i} \tag{1.8}$$

$$= \frac{1}{\sqrt{t\,\Sigma\,\frac{1}{\sigma_i^2}}} \tag{1.9}$$

Thus the final signal to noise ratio for these weighted measurements is:

$$SNR = \frac{\sqrt{t}\;\Sigma\,\frac{S_i}{\sigma_i^2}}{\sqrt{\Sigma\,\frac{1}{\sigma_i^2}}} \tag{1.10}$$

Simply adding in more galaxies may not improve the signal to noise ratio of a coadded measurement for an observed field as one is likely to be adding smaller galaxies with less gas, as one pushes further down the H I mass function. This will have the effect of decreasing the average H I signal. While the average noise level will decrease from the additional coadded galaxies the overall signal to noise may decrease due to this decrease in average signal. Despite these considerations, the improvement in signal to noise ratio using the coadding technique to measure H I 21-cm emission

is considerable. This technique does require substantial optical information for the galaxies (optical imaging for the galaxy position and spectroscopy for the precise redshifts) that must first be obtained. This can be seen as an advantage as it provides a wealth of additional information on the properties of the galaxies which can be compared to their measured H I gas properties.

This coadding technique for measuring H I 21-cm emission has been used by Zwaan (2000) in galaxy cluster Abell 2218 at $z = 0.18$ using 200 hours on Westerbork Synthesis Radio Telescope. Only 45 redshifts were used in the core of Abell 2218 where a coadded signal corresponding to a mass of neutral hydrogen gas of $(5.3 \pm 2.1) \times 10^8\ M_\odot$ was measured. This technique was also used by Chengalur et al. (2001) in observations of the galaxy cluster Abell 3128 at $z = 0.06$ using 39 hours on the Australia Telescope Compact Array (ATCA). Their coadded H I spectrum of 148 galaxies allowed a detection down to $\sim 9 \times 10^8$ $M_\odot$. In this thesis I have used this method to quantify the gas in the Fujita galaxies, star-forming galaxies at $z = 0.24$ (see Chapter 2 or Lah et al. 2007) and galaxies around the galaxy cluster Abell 370 at $z = 0.37$ (see Chapter 3 or Lah et al. 2009).

1.4 Galaxy clusters and their evolution

Galaxy clusters are regions of the universe that contain large overdensities of galaxies. An example of one large cluster can be seen in Fig. 1.11 which shows the optical image of the core of the galaxy cluster Abell 370 (the H I gas content around Abell 370 is examined in Chapter 3). The largest galaxy clusters form at the meeting points of multiple galaxy filaments that make up the large scale structure of the universe.

Galaxy properties, such as morphology and star formation rate, are found to depend on environmental density. In clusters these effects probably originate from a density-dependent quenching of star formation which can come about about via the consumption or removal of the available gas supply in the galaxies. As such, the amount of H I gas available to galaxies to fuel further star formation is likely to be a fundamental parameter in understanding the effect of environment. Galaxies in nearby clusters and their surroundings show strong evidence for environmental effects that are reducing their gas content. At higher redshifts little is known about the gas content of clusters. However there are signs at higher redshifts of galaxy evolution in the optical properties of galaxies.

As the number density of galaxies increases, the rate of star formation in the galaxies is seen to decrease. This star formation-density correlation can be seen locally in that the fraction of blue galaxies decreases with galaxy density (Pimbblet et al. 2002; De Propris et al. 2004). The blue colour seen in galaxies is due primarily to a population of bright, massive young stars that do not live for more than a few million years after their formation. Hence a galaxy with a blue colour is likely to have had recent star formation. Additionally the fraction of galaxies with optical emission lines decreases with galaxy density (Hashimoto et al. 1998; Lewis et al.

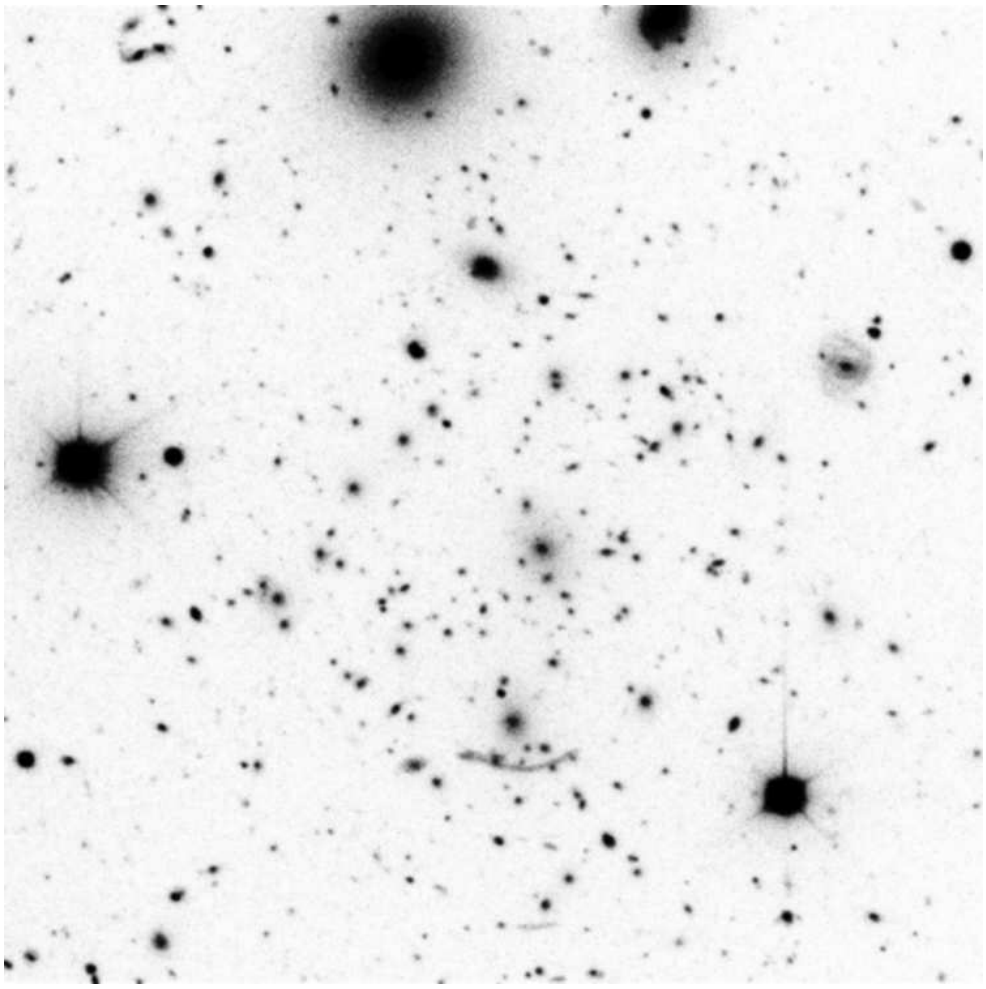

Figure 1.11: Optical image of the core of galaxy cluster Abell 370. The image is ∼3.5 arcmin across which is ∼1.1 Mpc at the redshift of the cluster, $z = 0.37$. One of the cluster's two cD galaxies (extremely luminous galaxies) can be seen as the fuzzy blob near the centre of the image. The other cD galaxy lies almost directly below it just above the bright optical gravitational arc. No galaxy in the cluster are brighter that these two cD galaxies. The objects in the image that appear brighter than these galaxies are either foreground galaxies or stars. (Image courtesy of ESO from the VLT)

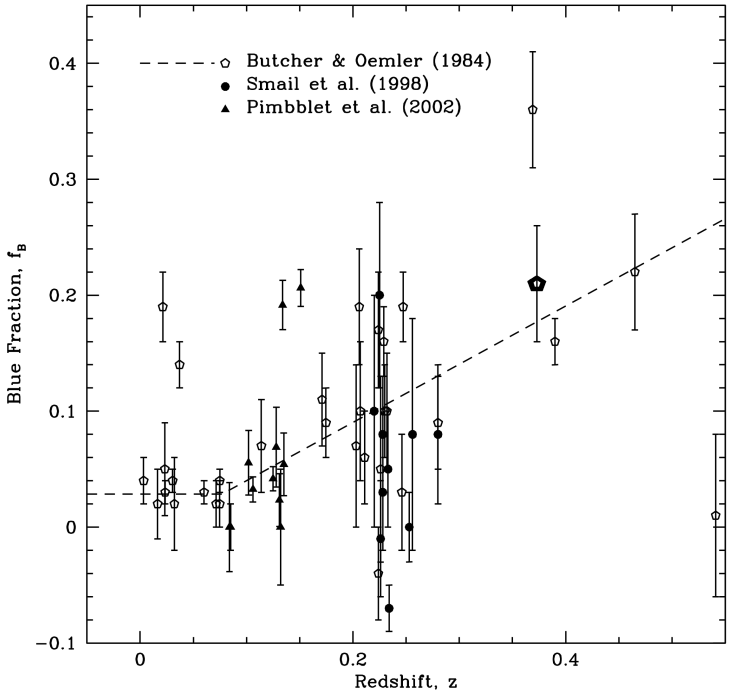

Figure 1.12: The Butcher–Oemler effect. This figure shows the fraction of blue galaxies within clusters at different redshifts. The Butcher–Oemler evolutionary trend is shown as the dotted line. The data includes the original Butcher & Oemler (1984) values as well as more recent values from Smail et al. (1998) and Pimbblet et al. (2002). The larger pentagonal point at $z = 0.37$ is the cluster blue fraction as measured by Butcher & Oemler (1984) for the galaxy cluster Abell 370, which is examined in this thesis (see Chapter 3). (Figure from Pimbblet 2003).

2002; Gómez et al. 2003; Balogh et al. 2004; Kauffmann et al. 2004). Optical emission lines are primarily generated in regions of active star formation from the recombination of hydrogen gas that has been ionised by these same young, massive stars. As such, they are also usually a sign of recent star formation in a galaxy.

The fraction of galaxies that are blue in colour within the dense environment of clusters increases with redshift (Butcher & Oemler 1984). This is known as the Butcher-Oemler effect and was one of the first major pieces of evidence showing evolution in the star formation properties of galaxies. Fig. 1.12 shows the original data of Butcher & Oemler (1984) along with some more recent values. At any particular redshift there is a large variety in the observed blue fractions between different clusters. This is not surprising as clusters span a wide variety of sizes and masses and as such, are likely to have had different histories. There is a visible trend of increasing blue fraction with increasing redshift. Similarly the fraction of galaxies with emission lines in clusters increases with redshift (Couch & Sharples

1987; Balogh et al. 1998; Balogh et al. 1999; Poggianti et al. 1999; Dressler et al. 2004). As noted previously in Section 1.2.1, the amount of star formation in galaxies across the entire universe increases with redshift, so the evolution in clusters can be seen as part of this larger trend. The star formation-density correlation, where cluster galaxies have less star formation that field galaxies, continues to be seen to at least $z \sim 0.8$ (Poggianti et al. 2008), even though the amount of star formation in clusters is seen to be increasing with redshift. However by a reverse of this star formation-density correlation has been noted by Elbaz et al. (2007) at redshifts $z \sim 1.0$. At this epoch they find evidence that star formation is now increasing with environmental density up to a critical galaxy density above which it decreases again.

In the local universe the proportion of galaxies that are ellipticals or S0 galaxies increases with galaxy number density, and there is a corresponding decrease in spirals galaxies (Dressler 1980). This density–morphology relationship also evolves with redshift. While the fraction of elliptical galaxies in dense cluster environments stays reasonably constant, the fraction of S0 galaxies decreases from present values by a factor of 2–3 by $z \sim 0.5$ and there is a proportional increase in the spiral galaxy fraction at the same time (Dressler et al. 1997; Fasano et al. 2000). The suggestion is that the spiral galaxies may have evolved into S0 galaxies once their star formation ends.

The physical mechanisms considered to explain these environmental trends all involve processes that effect the gas content of the galaxies, the fuel supply for star formation. These proposed physical mechanisms include:

i) galaxy mergers and strong gravitational galaxy–galaxy interactions (Toomre & Toomre 1972). These are most efficient when the relative velocities of galaxies are low, i.e. in galaxy groups. The gas in the galaxies involved in such strong interactions is usually used up in a massive burst of star formation.

ii) galaxy harassment, which is the cumulative effect of tidal forces from many weak galaxy encounters (Richstone 1976; Farouki & Shapiro 1981; Moore et al. 1996; Moore, Lake, & Katz 1998). The interactions disturb the gas in the galaxies triggering bursts of star formation until no gas is left. This effect would be important for lower mass galaxies in the dense environment of clusters.

iii) interactions between a galaxy and the intergalactic medium (IGM) (Gunn & Gott 1972; Quilis, Moore, & Bower 2000). The gas is stripped from the galaxy by one of a number of mechanism including ram pressure stripping, viscous stripping and thermal evaporation. These effects will only likely be strong in the centres of clusters, where there are large quantities of hot intracluster gas.

iv) strangulation, which is the removal of any envelope of hot gas surrounding galaxies that was destined to cool and accrete on to the galaxy to fuel further star formation (Larson, Tinsley, & Caldwell 1980; Diaferio et al. 2001). Unlike the other mechanisms which quench star formation relatively quickly ($\sim 10^7$ years), strangulation causes a slow decline in star formation over longer timescales (> 1 Gyr) (Poggianti 2004).

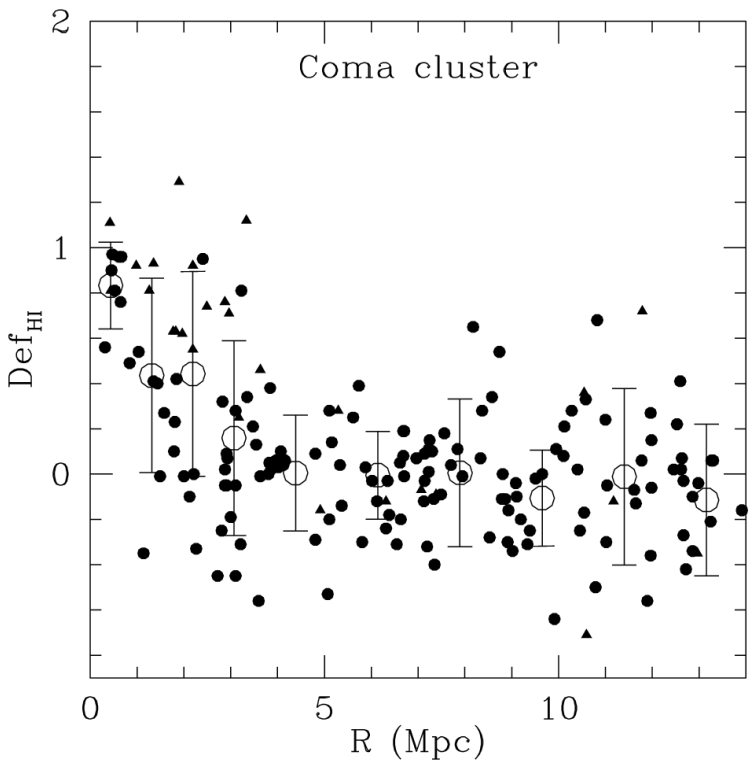

Figure 1.13: This figure shows the H I deficiency in galaxies located in the Coma cluster. The galaxies H I deficiency is plotted against their projected distance from the X-ray centre of the cluster. Galaxies with detected H I emission are the filled dots and undetected galaxies (i.e. upper limits) are triangles. The large open circles are the average H I deficiency in 1 degree bins (Figure from Gavazzi et al. 2006).

The gas content of galaxies in nearby galaxy clusters has been quantified using H I 21-cm emission observations. It has been known for some time that most of the neutral atomic hydrogen gas is contained in spiral galaxies in the local universe. Rao & Briggs (1993), from a comprehensive statistical study of the H I content from various radio surveys, found that 89 per cent of the neutral hydrogen gas in the local universe is found in spiral galaxies. Spirals in the central regions of nearby clusters are seen to be deficient in neutral atomic hydrogen gas compared to similar galaxies in the field (Haynes, Giovanelli, & Chincarini 1984). This effect continues well outside the cluster cores with a gradual change in the H I content of galaxies as the galaxy number density changes (Solanes et al. 2001).

A good example of this H I deficiency trend can be seen in the large nearby Coma cluster. Fig 1.13 shows the H I deficiency of the late-type galaxies as a function of distance from the centre of the Coma cluster Gavazzi et al. (2006). H I deficiency as originally defined by Haynes, Giovanelli, & Chincarini (1984) is:

$$\mathrm{Def_{HI}} = \log\left(\frac{\mathrm{M_{HI\,ref.}}}{\mathrm{M_{HI\,obs.}}}\right) \tag{1.11}$$

where $M_{\mathrm{HI\,ref.}}$ is the H I mass that one would expect the galaxy to have and $M_{\mathrm{HI\,obs.}}$ is the H I mass observed to be present in the galaxy. A $\mathrm{Def_{HI}} = 1$ is 10 per cent of the expected H I mass, while a $\mathrm{Def_{HI}} = 0$ means the galaxy has the expected H I mass. The estimated $M_{\mathrm{HI\,ref.}}$ is based on observations of galaxies in the field and is derived based on the observed optical linear diameter and Hubble type of a cluster galaxy. The H I deficiency in Coma appears to only extend out to ∼2.5 Mpc from the cluster centre.

Galaxies in nearby clusters show evidence of disruption of their H I gas with the presence of unusual asymmetric H I gas distributions, spatial offsets between the H I and optical disks, and tails of H I gas streaming away from the galaxies (Cayatte et al. 1990; Bravo-Alfaro et al. 2000; Chung et al. 2007). Despite these gas depletion trends with galaxy number density in the local universe, the high H I mass galaxies are found to trace the same underlying galaxy population as the optical galaxies (Basilakos et al. 2007). However these authors found that the low H I mass galaxies were preferentially located in regions of lower galaxy density.

In contrast to the wealth of information on the evolution of clusters at optical wavelengths little is known on the evolution of their H I gas content. The substantial changes in the star formation properties of galaxies in clusters suggest that there may have been considerable changes in their gas content as well. At moderate redshifts the angular extent of galaxy clusters is sufficiently small that galaxy environments from the dense cluster core to almost field galaxy densities can be observed in a single radio telescope pointing. For nearby clusters most current H I observations have been limited to targeted observations of individual galaxies, due to the large area on the sky that the clusters span. There have been some observations of the H I 21-cm emission from galaxies in clusters at moderate redshifts, as described above in Section 1.3.2. The small number of galaxies detected in current H I emission observations of distant clusters limits their ability to quantify any changes in the properties of the galaxies that may be a sign of gas evolution. The evolution of gas in clusters is examine using the H I coadding technique on galaxies around the galaxy cluster Abell 370 at $z = 0.37$ in this thesis (see Chapter 3 or Lah et al. 2009).

1.5 The principal telescopes used

1.5.1 Giant Metrewave Radio Telescope

At radio wavelengths it is possible to directly measure the electric field of the electromagnetic radiation. This enables one to coherently combine the radio signal from multiple antennas using radio interferometry. Radio interferometric telescopes can combine the collecting area of many dishes to greatly improve their sensitivity. The angular resolution of radio interferometric telescopes are set by the maximum distance separating the antennas. Their resolution is equivalent to the diffraction limit of a telescope approximately as large as the longest baseline.

The radio interferometric telescope used in this thesis for measuring H I 21-cm

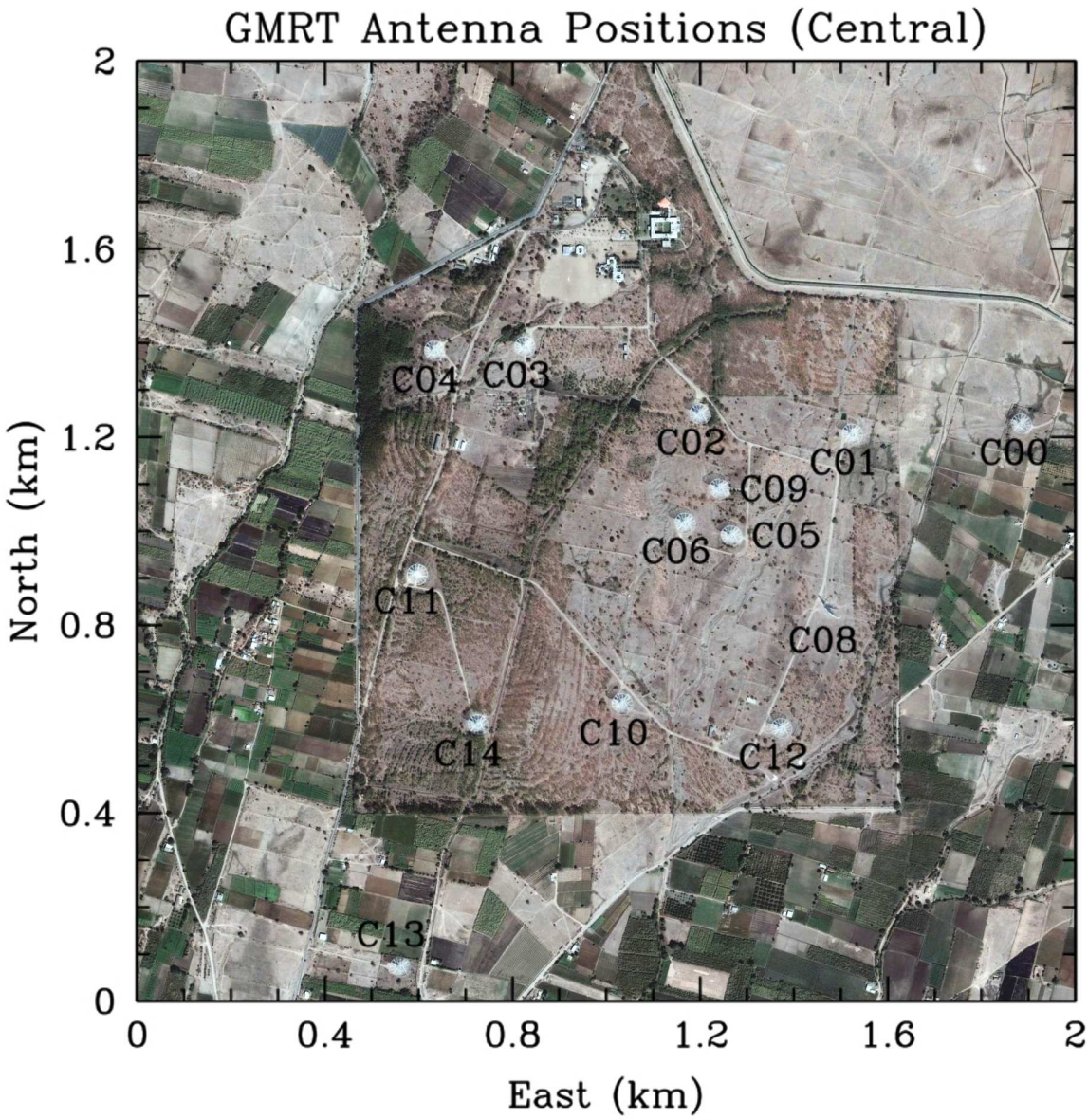

Figure 1.14: The Giant Metrewave Radio Telescope antenna configuration for the 14 antennas of the central array. (Image made using the aid of Google Earth by Philip Lah).

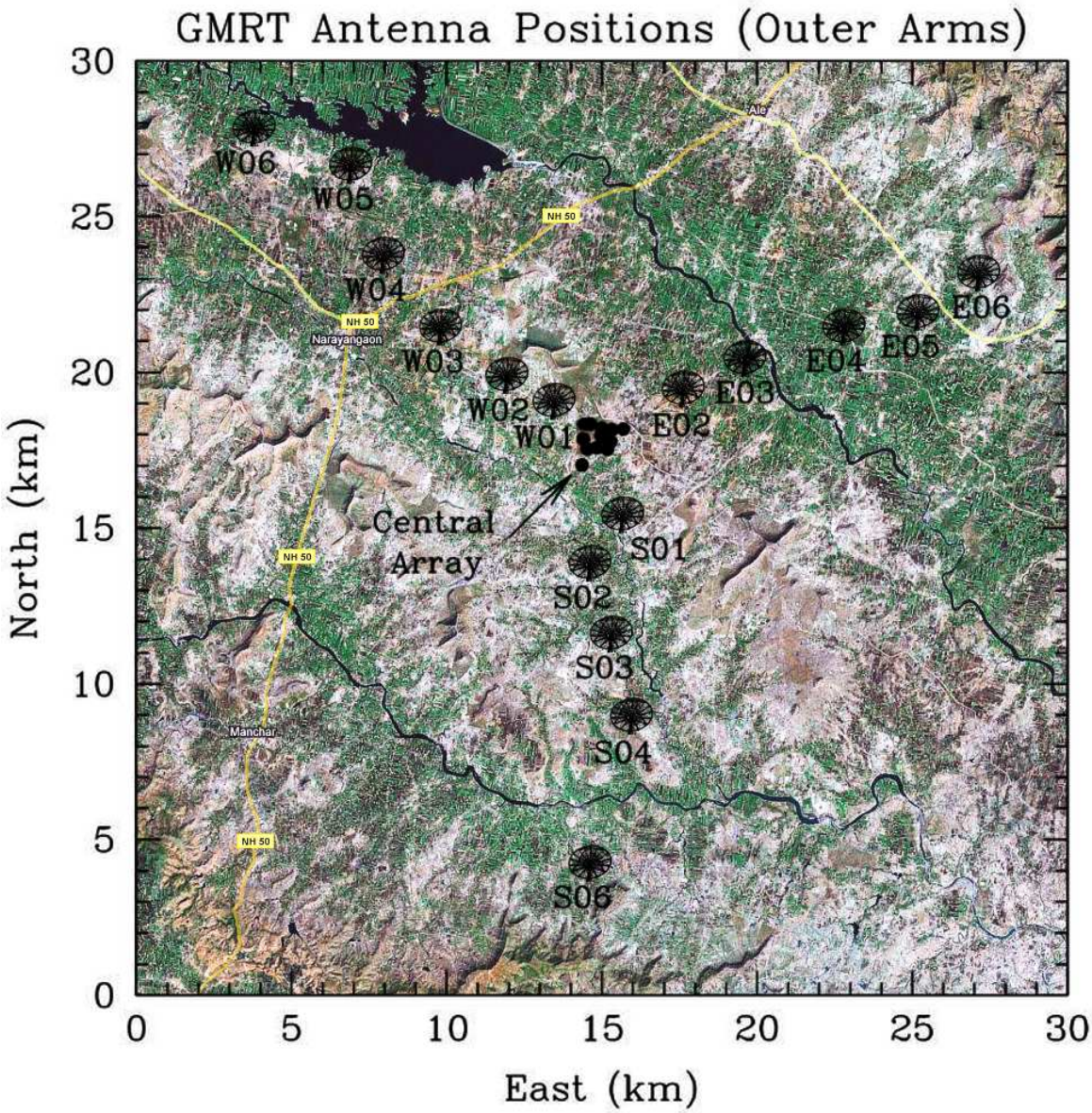

Figure 1.15: The Giant Metrewave Radio Telescope antenna configuration for the outer 'Y' array (Image made using the aid of Google Maps by Philip Lah).

emission from galaxies in the distant past is the Giant Metrewave Radio Telescope (GMRT). The GMRT is located in Khodad, India at latitude $+19°06'$ (N), longitude $74°03'$ (E) and an elevation of 650 m. This is ∼80 km from the city of Pune and ∼110 km from Mumbai (formerly Bombay). The nearest town is Narayangoan, around 15 km from the central array of the telescope. The telescope was built during the 1990s.

The GMRT consists of 30 fully steerable parabolic dishes, each of 45 m in diameter (Swarup et al. 1991). The dishes stand on fixed foundations and have alt-azimuth mounts. The collecting area of the GMRT is over three times that of the Very Large Array (VLA) in New Mexico (27 antennas of 25 m diameter). The antennas are divided into a central array and outer array. The central array consists of 14 antenna scattered over ∼1.5 km in a semi-random pattern as seen in Fig. 1.14. The shortest separation between antenna is 100 m. The central array provides good sensitivity to extended radio surface brightness objects. The outer 16 dishes are configured in an approximate 'Y' configuration as seen in Fig. 1.15. The longest separation between antennas is 26 km. The 'Y' configuration of the antennas allows for good imaging performance for the observation of sources at all Declinations including equatorial sources. The outer array provides high angular resolution to the observations. The dishes can point as low as an elevation of 17.5° which allows a sky coverage for the GMRT of Declinations from $+90°00'$ to $-53°24'$.

The 30 large dishes are covered in light weight, wire mesh that has a spacing 10×10 mm in the central part of the dish and 20×20 mm in the outer parts. As such, the GMRT is designed to operate at low frequencies (metre wavelengths). The current frequency coverage is from a minimum of 150 MHz to a maximum of 1450 MHz (200 cm to 20 cm). For this thesis the observation have been using the L-band system (1000-1450 MHz). At these frequencies the GMRT provides arcsecond resolution (synthesis beam sizes from ∼2 to ∼3 arcsec). The primary beam size (FWHM sensitivity size) at these frequencies has been empirically measured[1] as:

$$\theta_{\rm GMRT} = 26.2 \text{ arcmin} \times \frac{1280 \text{ MHz}}{\rm f_{obs}} \tag{1.12}$$

where $\rm f_{obs}$ is the observing frequency (from 1000-1450 MHz) and θ_{GMRT} is the primary beam size in arcminutes. The GMRT can currently process a maximum frequency bandwidth of 32 MHz, which is divided into two sidebands of 16 MHz bandwidth. Each sideband has 128 channels, giving a 125 kHz channel width when using the maximum frequency bandwidth.

The GMRT was chosen for this work on H I 21-cm emission from distant galaxies because of its frequency coverage. The GMRT large collecting area is advantageous but it is the frequency coverage that is unique. The GMRT can observe in L-band down to 1000 MHz, an H I 21-cm emission redshift of $z = 0.42$. The Westerbork Synthesis Radio Telescope (WSRT) can currently observe in L-band down to 1150 MHz[2], an H I 21-cm emission redshift of $z = 0.23$ (WSRT can observe lower

[1]National Centre for Radio Astrophysics website http://www.ncra.tifr.res.in
[2]ASTRON WSRT website http://www.astron.nl/p/observing.htm

frequencies than this but the receivers have poor sensitivity). The Very Large Array can currently observe in L-band down to 1150 MHz[3] with some loss in sensitivity, an H I 21-cm emission redshift of $z = 0.23$. The Arecibo radio telescope can currently work in L-band down to the 1120 MHz[4], an H I 21-cm emission redshift of $z = 0.27$. As Arecibo is a single dish telescope its resolution is of the order of arcminutes making the separation out of arcsecond size galaxies at moderate redshifts difficult. All the above telescopes including the GMRT work at lower frequencies than that listed here. These frequency regimes are equivalent to H I 21-cm emission at redshifts beyond $z \sim 1.0$ which would require impractical observing times to detect. As such, the GMRT can probe H I 21-cm emission to the highest redshift of those radio telescopes available during the thesis. Combined with its good angular resolution and large collecting area this makes the GMRT the current best radio telescope for observing H I 21-cm emission at moderate redshifts.

An important equation to know when working with a radio interferometric telescope is the noise level for observation of a point source. The noise level in the observation of an unresolved (point) source for a radio interferometric telescope can be calculated using the equation:

$$\Delta S = \frac{\sqrt{2}\, k\, T_{sys}}{\eta_{ap}\, \eta_{corr}\, A_{eff}\, \sqrt{n_{base}\, n_{pol}\, \Delta f\, t_{int}}} \tag{1.13}$$

where k is the Boltzmann constant (1.38×10^{-23} JK^{-1}), T_{sys} is the system temperature, η_{ap} is the aperture efficiency and η_{corr} is the correlator efficiency. A_{eff} is the effective collecting area of an antenna. n_{base} is the number of baselines which is $n_{base} = n_{ant}\,(n_{ant} - 1)/2$ where n_{ant} is the number of antennas in the array. n_{pol} is the number of observed polarisations (usually 2; for the GMRT the right and left circular polarisations, RR and LL). Δf is the frequency width observed and t_{int} is the integration time. For the GMRT the T_{sys} is ~76 K at 1200 MHz, the aperture efficiency is 0.4 at 1200 MHz and the correlator efficiency is 0.8. The telescope has 435 baselines[5]. Equation 1.13 is important not only for the GMRT observations but also for the estimations made in Chapter 5 for the SKA pathfinder telescopes.

1.5.2 Anglo-Australian Telescope

The Anglo-Australian Telescope (AAT) is an optical telescope with a 3.9 m primary mirror[6]. The telescope was commissioned in 1974 to provide large telescope coverage in the Southern Hemisphere that was lacking at that time. It was jointly funded by Australia and the United Kingdom. The AAT is located within Siding Spring Observatory, Australia at latitude $-31°16'\,(S)$, longitude $149°04'\,(E)$ and at an elevation of 1149 m. The AAT was one of the last large telescopes built with an

[3]NRAO VLA website http://www.vla.nrao.edu
[4]Arecibo Observatory website http://www.naic.edu
[5]National Centre for Radio Astrophysics website http://www.gmrt.ncra.tifr.res.in
[6]Anglo-Australian Observatory website http://www.aao.gov.au/

equatorial mount. This resulted in the telescope having a dome the rival of many of the newer 8-m optical telescopes, which use the more compact alt-azimuth mount.

In this work the AAT was used to obtain the optical spectroscopy of the galaxies from which precise redshifts were derived. The redshifts were then used for coadding the H I 21-cm emission signal from the galaxies in the radio data obtained from the GMRT. The Two Degree Field system (2dF) was used in this work with both the old spectrographs and also with the AAOmega upgrade to the system, which was completed in January 2006. The 2dF instrument allows for the spectroscopic observation of hundreds of objects simultaneously over a field 2 degrees across (hence the name). The 2dF instrument sits at the prime focus of the telescope and consist of two field plates. On top of the instrument a robot places magnetic buttons on a field plate at the location of the objects one wishes to observe. A tiny prism on each button reflects the light down into an optic fibre attached to the button. The optic fibre carries the light to the optical spectrographs. Once a field plate is configured, the plate is rotated into the prime focus of the telescope while the other plate is brought back up to the robot. This allows for one field plate to be configured by the robot while the other is used to take observations.

Each fibre accepts light from a region of sky that is 2.0 arcsec in size. For the old 2dF instrument there were 400 fibres. With the AAOmega upgrade this has been reduced 392 fibres to make way for an increase in the number of guide star bundles from 4 to 8 (the guide star bundles are used to align the pointing of the telescope on the observed field). With the old 2dF instrument the spectrographs fed by the fibres were mounted on the telescope and so moved with the telescope. The AAOmega upgrade uses longer optic fibres which lead to a bench mounted spectrograph in a room below the telescope. This increases the long term stability of the system. Unlike the old 2dF spectrograph, the new AAOmega spectrograph is a dual-beam system with separate blue and red arms. The light entering the instrument is split into its blue and red components by a dichroic before reaching two separate diffraction gratings and being recorded on the CCDs.

For ease of analysis the Anglo-Australian Observatory provides pipeline data reduction software called 2DFDR. Additionally, to support the large galaxy redshift surveys performed with the instrument, there exists an interactive software package RUNZ that allows for straightforward redshift determination from the reduce optical spectra. This makes data reduction and analysis of AAT data fairly straightforward.

The Anglo-Australian Telescope with the 2dF instrument is one of the few telescopes that can reliably provide a large number of optical redshifts for galaxies spread across a large field of view. As the AAT is located in the southern hemisphere and the GMRT is located in the northern hemisphere, it was necessary to choose target fields close to the celestial equator (Declination 0°) so that both telescopes could observe the field.

Chapter 2

The H I gas content of star-forming galaxies at z = 0.24

> The diversity of the phenomena of nature is so great, and the treasures hidden in the heavens so rich, precisely in order that the human mind shall never be lacking in fresh nourishment.
>
> Johannes Kepler

2.1 Introductory Summary

Observations with the Giant Metrewave Radio Telescope (GMRT) were used to measure neutral atomic hydrogen (H I) gas content of star-forming galaxies at $z = 0.24$ (a look-back time of ∼3 billion years). At this epoch the cosmic star formation rate is known to be 3 times higher than the present value (see Fig. 1.5). However little was known of the gas content of galaxies in this time period.

The sample of galaxies studied were selected from Hα-emitting field galaxies detected in a narrow-band imaging survey with the Subaru Telescope. The Anglo-Australian Telescope was used to obtain precise optical redshifts for these galaxies. The H I 21-cm emission signal for all the galaxies within the GMRT spectral line data cube was then coadded . From these results a measurement of the cosmic density of neutral gas at $z = 0.24$ was made.

Besides the primary results the correlations between the Hα luminosity and the radio continuum luminosity and between the star formation rate and the H I gas content in star-forming galaxies at $z = 0.24$ were examined. These correlations were compared to the relationships seen in nearby galaxies. The work in this chapter has been published in Lah et al. (2007).

The structure of this chapter is as follows. Section 2.2 details the optical and radio observations and data reduction. Section 2.3 comments on the relationship between the 1.4 GHz radio continuum and Hα luminosities at $z = 0.24$. Section 2.4 details the main results, the H I content of star-forming galaxies at $z = 0.24$. Finally, Section 2.5 presents a brief summary and discussion.

2.2 The data

2.2.1 The optical data

The optical galaxies examined come from a deep narrow-band imaging survey for Hα emission galaxies at $z = 0.24$ (Fujita et al. 2003). This survey was performed using the Subaru Telescope, a 8.2 metre optical telescope run by the National Astronomical Observatory of Japan and located in Mauna Kea Observatory on Hawaii. The instrument used was the imager Suprime-Cam which covers a field 34 arcmin $\times$ 27 arcmin in size. Deep observations were taken of single Suprime-Cam field with broad passband filters B (28 min), R_C (80 min), I_C (56 min), z$'$ (86 min) and a narrow passband filter NB816 (600 min). The filter NB816 is centred at 8150 Å which corresponds to the Hα emission line at $z \sim 0.24$. The Hα emission line be seen through this filter for galaxies at redshifts from approximately $z = 0.22$ to 0.26 (a velocity width of $\sim$12000 km s^{-1}). Fig. 2.1 shows the wavelength covered by these filters. The narrowband filter NB816 lies in a gap in the night sky lines making it an ideal wavelength range to look for emission lines. Fig. 2.2 shows this sky window that NB816 lies in along with the Hα emission line for one of the selected galaxies. Fig. 2.3 shows the field that Fujita et al. (2003) observed.

After applying various selection criteria to remove contaminants, Fujita et al. (2003) found a total of 348 Hα-emitting galaxies with equivalent widths greater than 12 Å (hereafter these galaxies will be referred to as the 'Fujita galaxies'). Thumbnail images of all 348 of these galaxies can be seen in Fig. 2.4. From these galaxies, an extinction-corrected luminosity function for Hα emitting galaxies at $z = 0.24$ was derived. Using this luminosity function, Fujita et al. (2003) computed a star formation rate density of $0.036^{+0.006}_{-0.012}$ M$_\odot$ yr^{-1} Mpc^{-3}. This is a factor of 3 higher than the local star formation rate density (Gallego et al. 1995; Condon, Cotton, & Broderick 2002; Gallego et al. 2002). Their measured star formation rate density is in good agreement with other measurements made at and around $z = 0.24$ (Hogg et al. 1998; Tresse & Maddox 1998; Haarsma et al. 2000; Pascual et al. 2001; Georgakakis et al. 2003). This good agreement indicates that there is nothing particularly unusual about this field; it is not biased by containing an excess or deficiency of galaxies that have unusually high or unusually low star formation rates.

The 348 Fujita galaxies were observed with the 2dF and AAOmega spectrographs at the Anglo Australian Telescope (AAT) to obtain precise spectroscopic redshifts. Observations were carried out with 2dF on 6–10 March 2005, and an additional two hours of AAOmega service time obtained on 20 April 2006. The data were reduced using the Anglo-Australian Observatory's 2DFDR data reduction software[1]. As the targets were selected for Hα emission, the redshifts were confirmed primarily using the emission lines of [OII]λ3727, Hβ, [OIII]λ4959 and [OIII]λ5007. Secure redshifts were obtained for 154 galaxies with redshift range $0.2150 < z < 0.2641$ and a max-

[1]Anglo-Australian Observatory website
http://www.aao.gov.au/AAO/2df/aaomega/aaomega.html

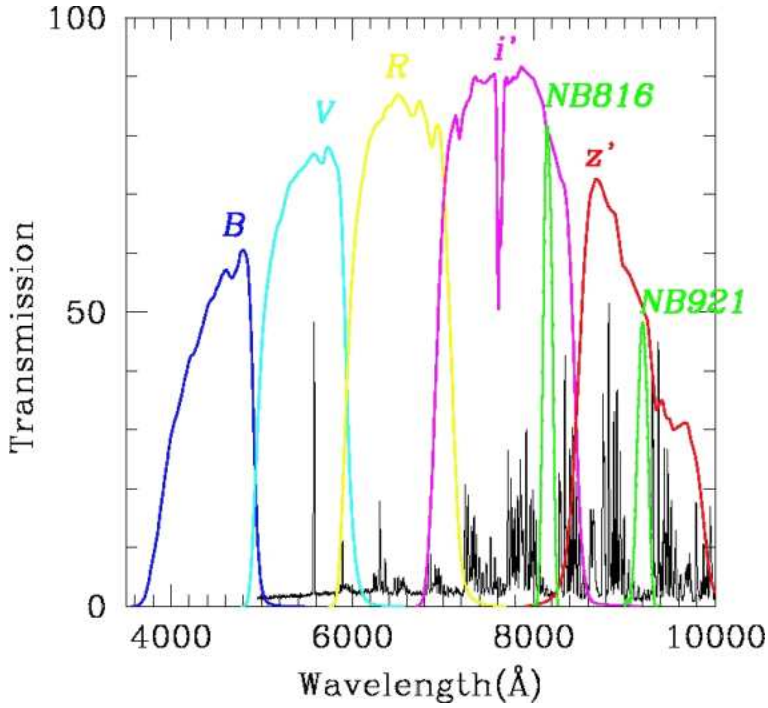

Figure 2.1: The optical filters for Suprime-Cam on Subaru. The narrowband filter NB816 can be used to pick out Hα emission galaxies at z ~0.24. The spectrum shown are the night sky lines. (Figure is from Kashikawa et al. 2004)

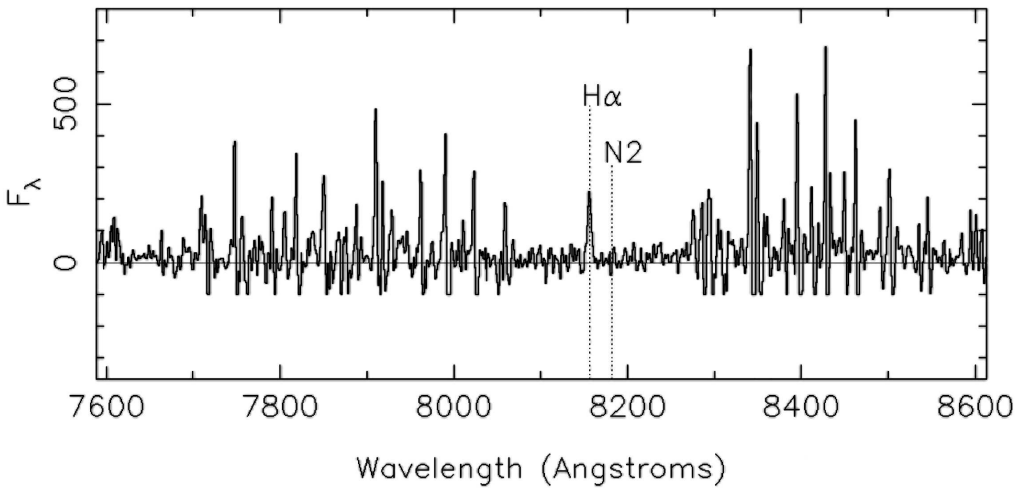

Figure 2.2: Hα emission at z ~0.24 in the sky window at ~8160 Å. The optical spectrum shown is from AAOmega for one of the Fujita galaxies. The residual noise from the strong sky lines can be seen in the region from 7700 Å to 8050 Å and the region 8300 Å onwards. N2 = [NII]6584

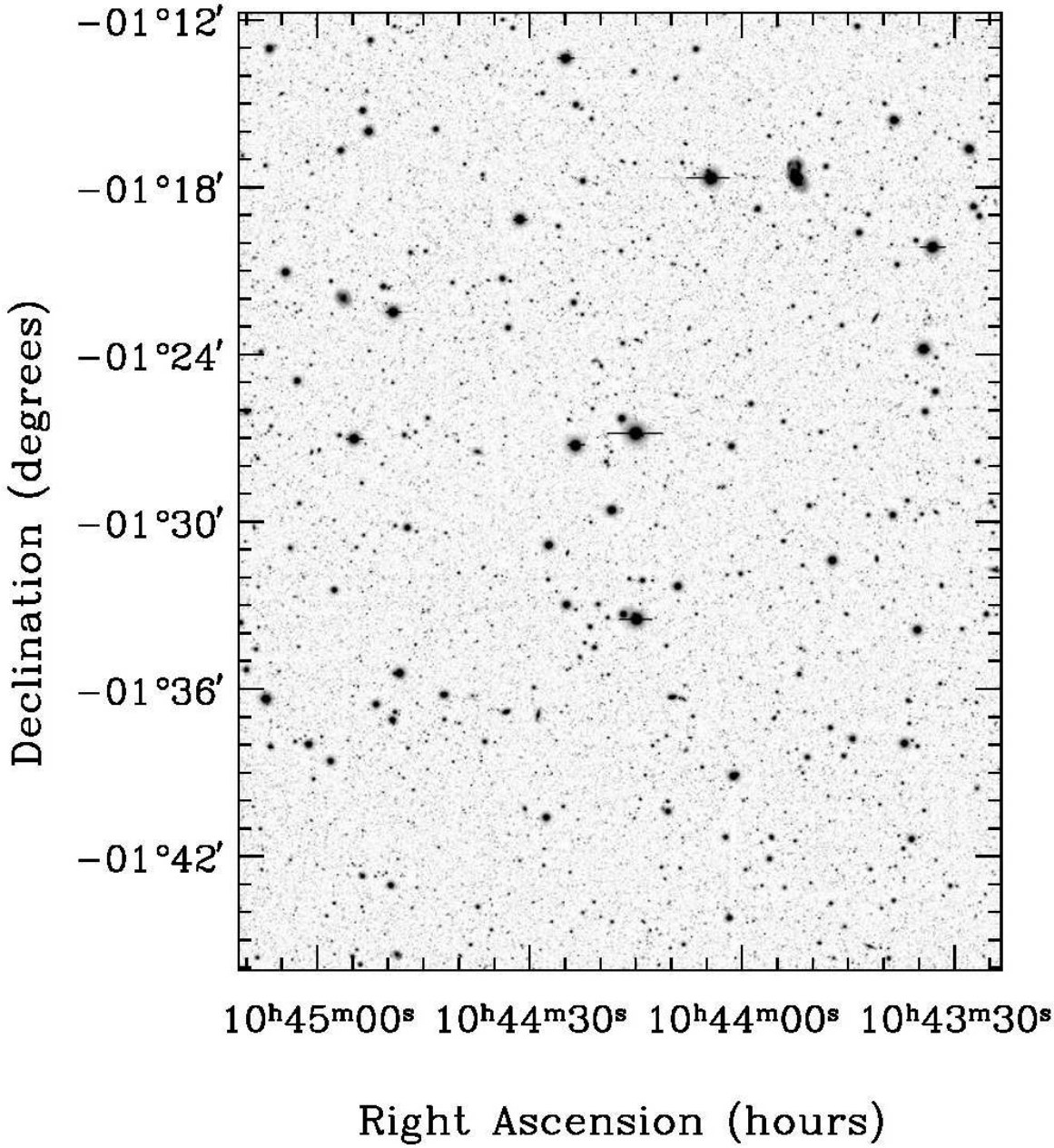

Figure 2.3: The Subaru field that contains the Fujita galaxies. The short side is the Right Ascension and the long side the Declination. This is one Suprime-Cam pointing which covers a field 34 arcmin × 27 arcmin in size. This image is taken through the B filter with an exposure time of 28 minutes.

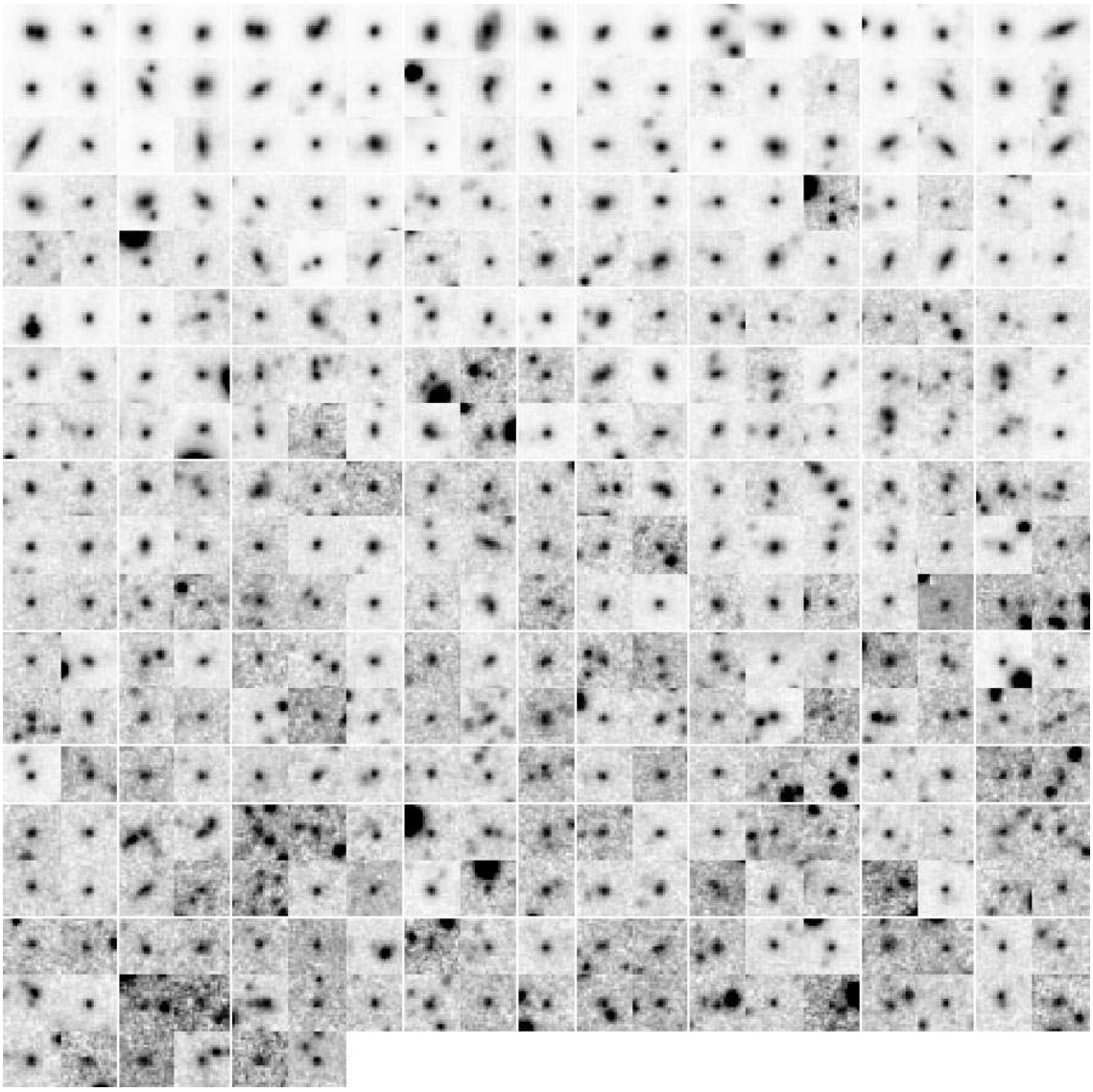

Figure 2.4: Thumbnail images of all 348 Fujita galaxies. These are B band images from the Subaru Telescope. They are ordered by Hα luminosity with the brightest galaxy in the top left, decreasing in luminosity along the rows first and then the columns. The bottom right galaxy is the faintest. The individual images have been all scaled to the same maximum brightest level so that all the galaxies can be seen despite the large contrast between the brightest and faintest galaxies. One can tell the relative brightness of the galaxies by the brightness of the background noise in the thumbnail.

imum error in the redshift of 70 km s^{-1}. The break down of the redshifts obtained by Hα luminosity is: 47 redshifts for the 50 galaxies with L(Hα) > 40.9 log erg s^{-1}, 48 redshifts for the 58 galaxies with 40.4 < L(Hα) $\leq$ 40.9, and 42 redshifts for the 240 galaxies with L(Hα) $\leq$ 40.4.

2.2.2 The radio data

Radio observations of this field were carried out on 26–28 December 2003 and 7–9 & 24–26 January 2004 using the Giant Metrewave Radio Telescope (GMRT) located near Pune in India. A total of 80.5 hours of telescope time was used with ~40 useful hours of on-source integration after accounting for the time slewing, flux and phase calibrator scans, and the flagging of bad data. At most only 28 of the 30 GMRT antennas were providing useful data on any one day. The total observing bandwidth of 32 MHz was split up into two 16 MHz-wide sidebands covering the frequency range from 1034 MHz to 1166 MHz (i.e. a redshift range $0.218 < z < 0.253$ for redshifted H I 21-cm emission). The pointing centre of the observations was R.A. $10^{\rm h}44^{\rm m}33.0^{\rm s}$ Dec. $-01^{\rm d}21^{\rm m}02^{\rm s}$ J2000 (see Fig. 2.5). There were two polarisations and 128 spectral channels per sideband, giving a channel spacing of 0.125 MHz (32.6 km s^{-1}). Primary flux calibration was done using periodic observations of 3C286, which has a flux density at 1150 MHz of 16.24 Jy. Phase calibration was done using scans on the VLA calibrator sources 0943-083 and 1130-148, for which these observations give flux densities of 3.137 ± 0.011 Jy and 5.163 ± 0.044 Jy respectively.

The data reduction was primarily done using AIPS and was partially automated using Perl scripts to interface with AIPS. Each sideband of data was processed separately. The initial assessment of data quality and the preliminary calibration was done using the visibilities in a single channel. Flux and phase calibration was determined using the bandpass calibration task BPASS, and the solution was interpolated to the data. No normalisation was done before determining the solutions. The regular phase calibrator scans throughout the observations allowed for the correction of any time variability in the bandpass shape. Since, over the time span of the observations, there was no significant variation in the measured flux of the phase calibrators, the measured fluxes for each phase calibrator were combined into a single average value. In the final data reduction, this average value was used as the calibrated flux for the phase calibrators.

After a period of testing and refinement, an imaging pixel size of 0.7 arcsec and a robustness value of 0 were adopted. For primary beam correction, a Gaussian beam was assumed with FWHM of 29.2 arcmin at 1150 MHz[2].

The brightest radio continuum source in the field is J104420-011146. It lies ~9.8 arcmin from the phase centre and its measured integrated flux (at 1150 MHz) is 303.66 ± 0.05 mJy. The integrated flux listed in the FIRST radio catalogue

[2]National Centre for Radio Astrophysics website
http://gmrt.ncra.tifr.res.in/gmrt_hpage/Users/Help/help.html

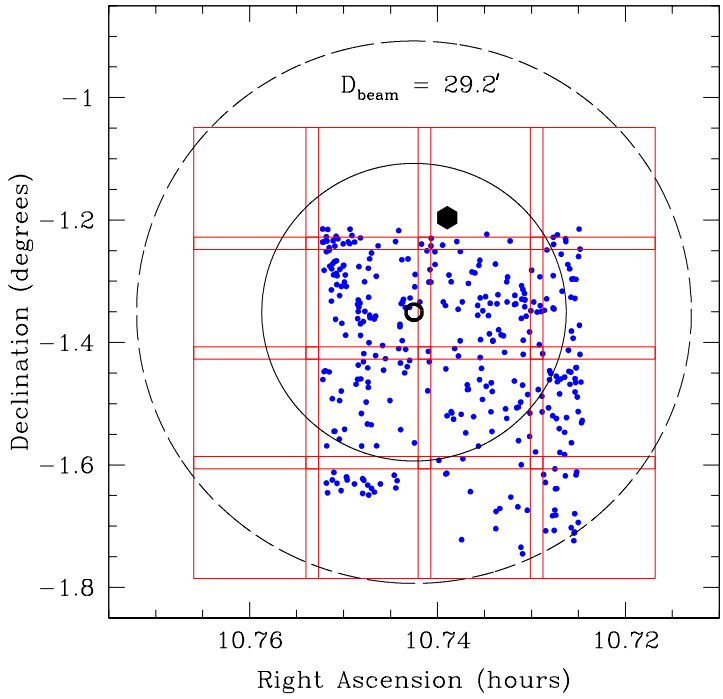

Figure 2.5: This figure shows the positions of the optical galaxies as well as the pointing and beam size of the GMRT observations. The 348 Fujita galaxies are the small points. The large hexagonal point is the strong radio source J104420-011146 on which self calibration was performed. The small, bold, open, central circle is the GMRT pointing of the observations. The unbroken circle is the primary beam diameter (FWHM) of 29.2 arcmin and the broken circle is the 10 per cent level of the beam. The overlapping square grid shows the 16 facets used to tile the sky in the radio imaging. The centre of this grid pattern was created with an offset from the GMRT pointing to ensure that all Fujita galaxies lie within the tiled region.

(at 1.4 GHz) for this source is 276.83 ± 0.15 mJy. J104420-011146 is an order of magnitude brighter than the next brightest radio source in this field. Self-calibration of the data was done using this source.

When making continuum images only channels 11-110 (out of the 128 in each sideband) were used. In order to avoid bandwidth smearing, the visibilities were averaged into a new data set consisting of ten channels, each of which was the average of 10 of the original channels. This new ten channel $u - v$ data file was turned into a single channel continuum image in the AIPS task IMAGR, combining the channels using a frequency-dependent primary beam correction based on the antenna size of 45 m.

The self-calibration of GMRT data sometimes does not converge quickly, probably as a consequence of the GMRT hybrid configuration. Sources that lack coherence

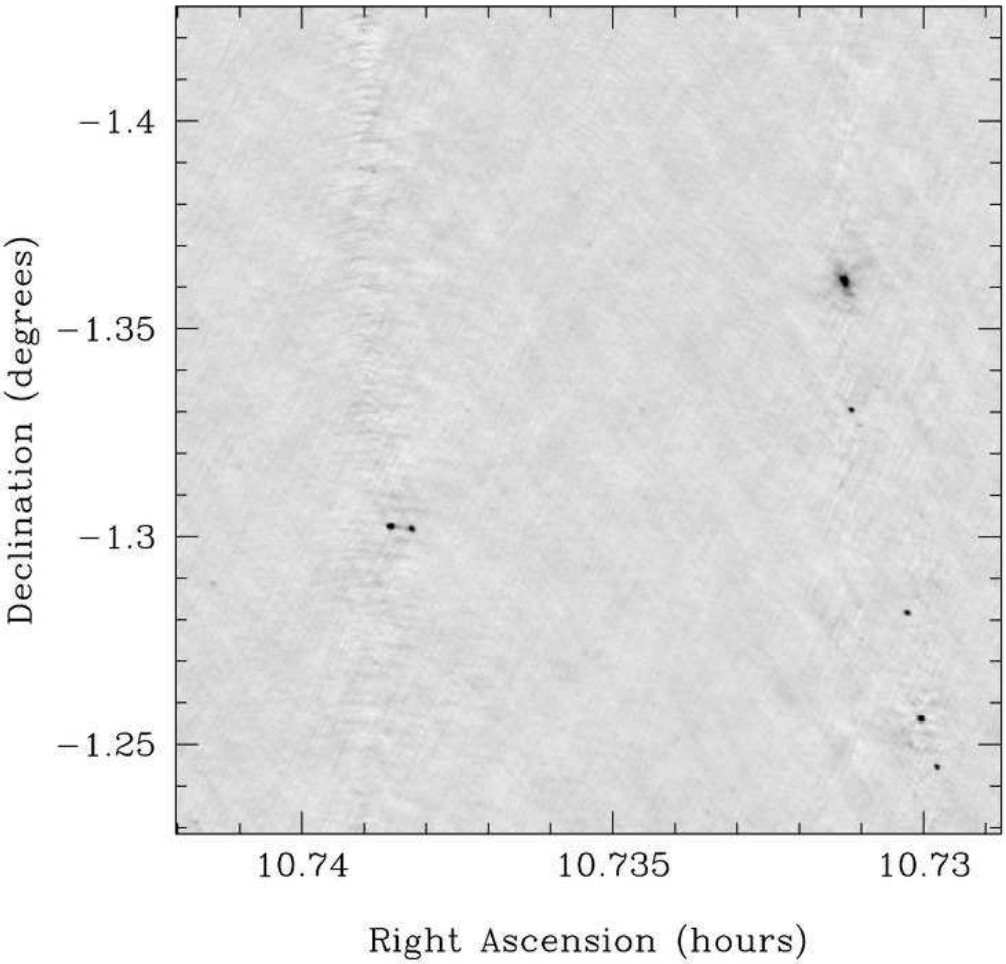

Figure 2.6: This figure shows a grey scale image of one of the radio continuum facets (see the text for details). This facet is just south of the facet with the strong continuum source J104420-011146 (see Fig. 2.5). The residuals from this bright source run north-south and can be seen on the left hand side of the image. The RMS in the continuum images is 15 μJy, but along this strip of residual structure, the RMS increases to $\sim$28 μJy (this is the worst residual remaining in the any of the continuum facets). The grey scale used in the image is a square root scale which varies from $\sim$2.5 mJy for black and $\sim$-120 μJy for white. The brightest source in this image is in the top right hand corner and has extended structure. It been identified as the nearly face-on spiral galaxy, UGC 05849 at $z = 0.026$. The peak flux from the galaxy is 8.76 mJy/beam and the total flux density is 42.3 ± 0.4 mJy, which is spread over a diameter of $\sim$60 arcsec.

in the synthesis image due to phase errors tend to remain defocused. To fix this problem, slightly extended sources were replaced in the first self-calibration loop with point sources with the same centroid and flux density as the original source. Further self-calibration loops were done using the clean components in the traditional manner. Each day's observation was initially self calibrated alone using 4 loops of self-calibration (2 loops of phase calibration and 2 amplitude and phase calibration loops). At this point the bright continuum source J104420-011146 was subtracted from the $u - v$ data, and the data were flagged to exclude any visibility residuals that exceeded a threshold set by the system noise statistics. The bright continuum source was then added back into that day's data.

After this detailed editing process, all the $u - v$ data were combined and self-calibration was repeated on the entire combined data set to ensure consistency between the different days. A large continuum image of the entire field was then made.

The AIPS imaging routine assumes that the sky is flat (it ignores the vertical 'w' term) which is appropriate only for small fields. In order to reduce the distortion over the large field it was necessary to break the image up into 16 facets (see Fig. 2.5). Each of these facets was 11.95 arcmin square (1024 pixels) and each overlapped by 1.2 arcmin. The final total field size was 44.20 arcmin on each side (i.e. large enough to include all the Fujita galaxies). Clean boxes were put around all the significant continuum sources during the imaging process. In this initial continuum image, faint sidelobes from the brightest radio source J104420-011146 remained visible (see Fig. 2.6). To reduce this, all the weaker continuum sources were subtracted from the $u - v$ data, and the data were once again self-calibrated using clean components of the bright source alone. This new model of the bright source was subtracted from the original $u - v$ data, and the weak sources (along with the appropriate calibration for these sources) restored. The final continuum image of the field without the bright source was then made.

The final image has a resolution of $\sim$2.9 arcsec. The RMS at the centre of the final continuum image is 15 μJy. The astrometry of the bright radio continuum sources in the data were checked against their positions in the VLA FIRST survey. A small offset constant across the field of (-0.79 ± 0.30) arcsec in right ascension and (-1.42 ± 0.28) arcsec in declination was found. This offset is believed to have been introduced to the data during the self-calibrating process though the exact origin of the offset is unclear. After correcting for this, several objects could be identified with aligned optical and radio continuum components in the Subaru and GMRT images.

The continuum emission was then subtracted from the original spectral line data using the AIPS task UVSUB. While this removed most of the emission, small residuals of the brighter sources remained. To remove these final traces, a linear fit to the continuum across frequency was subtracted in the image plane using the AIPS task IMLIN. This introduces a small bias, since any line emission from the galaxies would be included in the fit. The correction for this bias is described in Section 2.4.1. In the final data cubes, the median RMS was 123 μJy per channel in

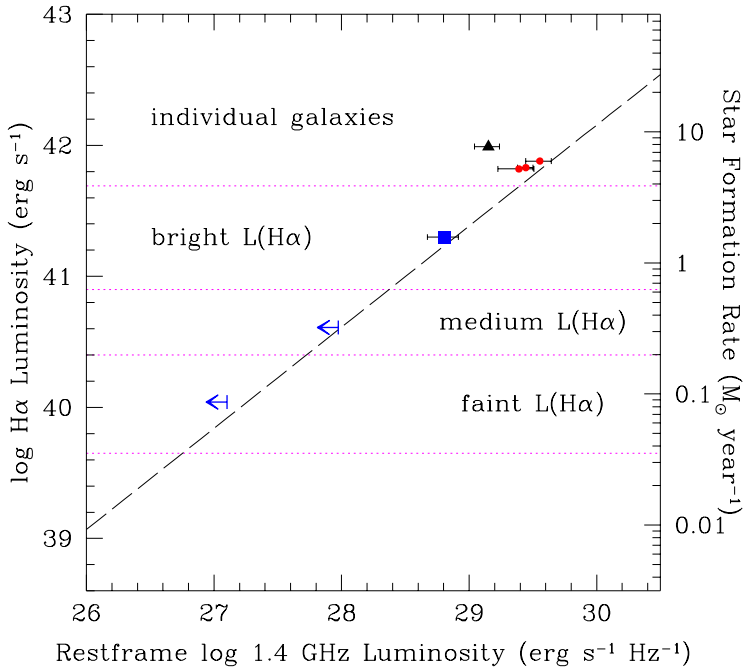

Figure 2.7: Hα emission line luminosity plotted against the restframe 1.4 GHz radio continuum luminosity for galaxies at $z = 0.24$. The line plotted through the data is the observed relationship found at $z = 0$ (Fig. 2 of Sullivan et al. 2001). The 4 points in the 'individual galaxies' region are the brightest Hα-emitting galaxies. The triangle is a merging/interacting system of two galaxies. The square in the 'bright L(Hα)' region is the combined signal from galaxies with bright Hα emission. The two radio continuum 2σ upper limits in the 'medium L(Hα)' and 'faint L(Hα)' regions are from the combined signal of subsamples of Hα-emitting galaxies. The star formation rate shown on the right axis is derived using the Kennicutt (1998a) Hα to SFR relationship.

the lower sideband and 136 μJy per channel in the upper sideband.

2.3 The radio continuum and Hα luminosity correlation

Synchrotron radio emission is generated in areas of active star formation from relativistic electrons accelerated in supernova remnants. Radio emission at 1.4 GHz generated by this process has been used as a measure of the star formation rate for galaxies, and it correlates well with other star formation indicators (Condon 1992; Sullivan et al. 2001). In the radio continuum image, it is possible to measure this emission for some of the Fujita galaxies. Since these galaxies are at a redshift of

$z = 0.24$ and they were observed at 1150 MHz, the rest frequency of their radio continuum emission in the data is 1.4 GHz. Thus it is possible to directly compare the relationship in star-forming galaxies between Hα line emission luminosity and 1.4 GHz radio continuum luminosity at $z = 0.24$ and $z \sim 0$. These measurements are shown in Fig. 2.7. Also shown in Fig. 2.7 is the linear relationship found by Sullivan et al. (2001) from comparing the Hα emission against 1.4 GHz luminosity for 17 galaxies at $z \sim 0$. The uncertainties and the standard errors in the means for the Hα measurements in Fig. 2.7 are all smaller than the size of the points.

The integral flux densities of the radio continuum sources were measured using the AIPS task JMFIT which fits a 2D Gaussian to the source. The radio continuum for the 4 brightest Hα-emitting galaxies each have individual measurable radio continuum fluxes (from $\sim$100 to $\sim$300 μJy). These are the points shown in the 'individual galaxies' region of Fig. 2.7. The three galaxies with circular points show reasonable agreement with the Sullivan et al. (2001) line. The triangle point is a merging/interacting system of two galaxies within 3 arcsec ($\sim$11 kpc) of each other (see Fig. 2.8). The galaxies were observed to be at the same redshift of $z = 0.2470$ and have overlapping optical profiles. Both galaxies show strong Hα emission but only the galaxy with brighter Hα emission shows any signs of radio emission. Interestingly, this galaxy, although brighter in Hα, appears to be less massive than its companion (it is $\sim$5 times more luminous in Hα than its companion but is $\sim$0.6 times as luminous in the 'z' band filter). The reason why this galaxy's radio continuum luminosity lies away from the Sullivan et al. (2001) line may have to do with it being a merging system.

At lower Hα luminosities the radio continuum signal from multiple galaxies has been combined to improve the signal to noise ratio. Of the remaining 344 Fujita galaxies, 4 have been excluded as they have contamination by bright radio continuum sources within 10 arcsec that do not appear to be connected to the galaxy. Another 2 galaxies were excluded because they lie within regions of artifacts in the synthesis images. Finally, excluded is a galaxy with a very strong radio continuum flux (2336$\pm$ 67 μJy, which is brighter than any other Fujita galaxy by an order of magnitude) but has a relatively low Hα luminosity (39.82 ± 0.10 log erg s^{-1}). The source of such a strong radio flux is more likely to be an active galactic nucleus than star formation. Unfortunately this galaxy does not have an observed redshift.

The galaxies have been divided up into three subsamples for the purpose of combining the radio continuum. In these subsamples are: 45 bright galaxies with $40.9 < \mathrm{L(H\alpha)} \leq 41.69$ log erg s^{-1}, 55 medium galaxies with $40.4 < \mathrm{L(H\alpha)} \leq 40.9$ and 236 faint galaxies with $39.65 \leq \mathrm{L(H\alpha)} \leq 40.4$. Nearly all of the bright L(Hα) galaxies and most of the medium L(Hα) galaxies have optical redshifts, but the vast majority of the faint L(Hα) galaxies do not. The radio continuum signal of the galaxies are combined using a weighted average, with the weight being the individual noise level in the radio image for that galaxy. The further a galaxy is from the centre of the GMRT observations the greater the beam correction to its flux density; this results in a higher noise level and thus a lower weight in the sum.

The square in Fig. 2.7 is the average signal for the bright L(Hα) galaxies. This

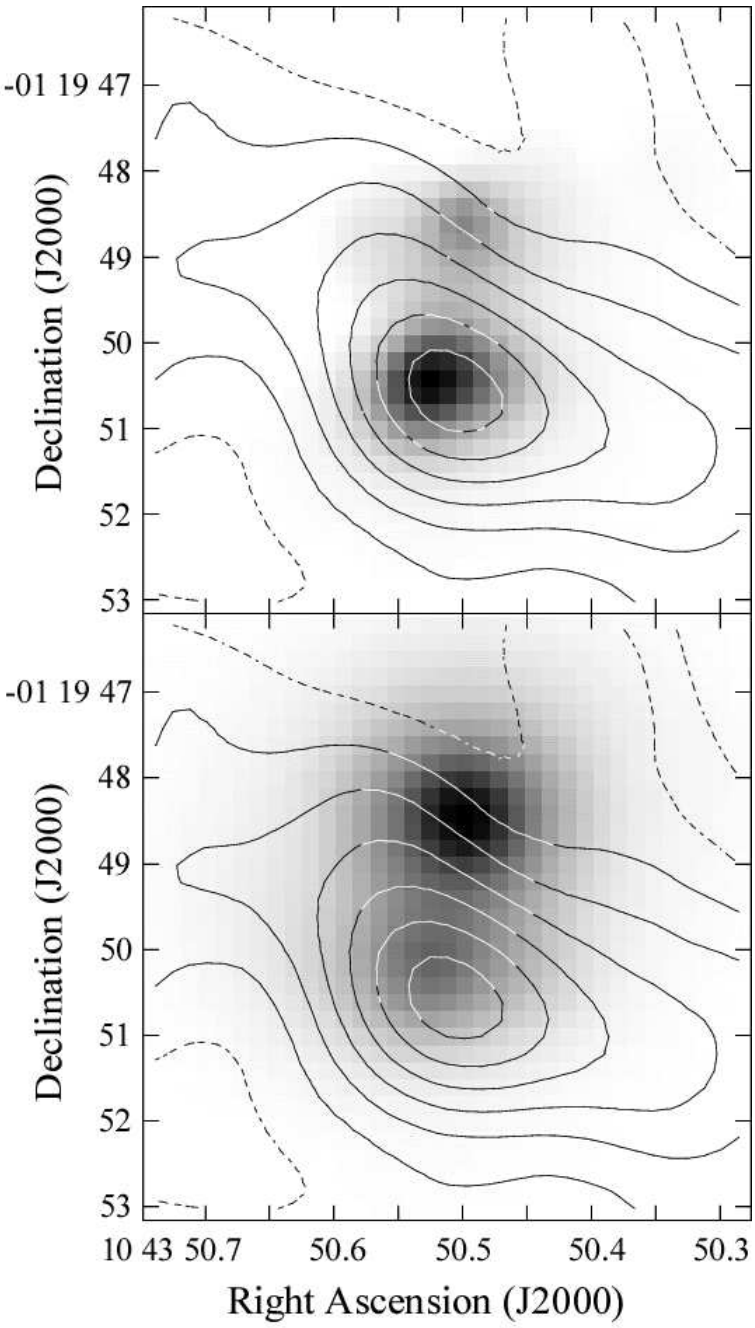

Figure 2.8: The top figure shows the Hα emission greyscale and radio continuum contours of the pair of merging/interacting galaxies mentioned in the text. The same pair of galaxies are shown in the bottom figure with the same radio continuum contours and the '*Iz continuum*' (the '*Iz continuum*' is the combination of the Suprime-Cam I_C and z' images, the continuum level around the Hα line; see Fujita et al. 2003 for details). The radio continuum contour levels are -40, -20, 0, 20, 40, 60, 80, 100 μJy. The images are both 7 arcsec on a side.

value shows good agreement with the Sullivan et al. (2001) line. For the medium L(Hα) and faint L(Hα) galaxies there was no detection of radio continuum flux, meaning that only upper limits can be determined. The 2σ upper limits for these regions are plotted on Fig. 2.7. When determining these upper limits, it was assumed that the galaxies were not resolved by the GMRT synthesised beam. Both of these upper limits lie just to the left of the Sullivan et al. (2001) line, suggesting that the linear relationship might not hold at low luminosities. Indeed, Sullivan et al. (2001) state that there is some evidence that the Hα–radio continuum relationship may not be perfectly linear for galaxies with low star formation rates. They suggest that a fraction of the cosmic rays accelerated in supernovae remnants may escape from the lower mass galaxies. This would reduce the radio continuum emission relative to the galaxy's Hα luminosity. This effect would explain the positions of the two lower limits without requiring a change in the star formation mechanism at $z = 0.24$. Bell (2003) have explicitly quantified this correlation for low mass galaxies.

Overall, Fig. 2.7 shows that at $z = 0.24$ the relationship between radio continuum luminosity at 1.4 GHz and Hα emission luminosity for galaxies is consistent with that found at $z = 0$. This suggests that there has been no significant change in the star formation mechanism over the last 3 Gyrs.

2.4 H I results

2.4.1 The H I 21-cm emission signal

The first step in measuring the coadded H I signal of the Fujita galaxies is to use the optical redshifts to determine the expected frequency of the 21-cm H I emission. Of the 154 optical galaxy redshifts obtained, 121 lie within the usable regions of the radio data cube (see Fig. 2.9). The reasons the remaining 33 galaxies are unusable are either: (i) their redshifted H I frequency lies outside the frequency range covered by the GMRT data, (ii) their redshift lies close to the boundary of the two sidebands where the data quality is poor, or (iii) their redshift lies within 5 channels of strong radio interference in the lower sideband (this strong radio interference is at $\sim$1137 MHz, covering $\sim$0.625 MHz). For the purposes of defining a spectral window for coadding the H I signal, an average H I profile for the galaxies of the order of $\sim$300 km s^{-1} (Doyle et al. 2005) is assumed. A velocity window width of 500 km s^{-1} should contain all the significant H I emission after factoring in the uncertainty in the optical redshifts ($\sim$70 km s^{-1}).

In the data, the H I signals from individual galaxies are mostly below reasonable detection limits. Using the H I mass function at $z \sim 0$ (Zwaan et al. 2005), it is estimated that there is only a $\sim$15 per cent chance of a direct detection (5σ) of the H I flux from an individual galaxy within the volume probed by these GMRT observations. There is probably more H I mass in galaxies at $z = 0.24$ than at $z \sim 0$, making a direct detection more likely, however detecting significant numbers of galaxies is still unlikely. For this reason the choice was made to coadd the H I sig-

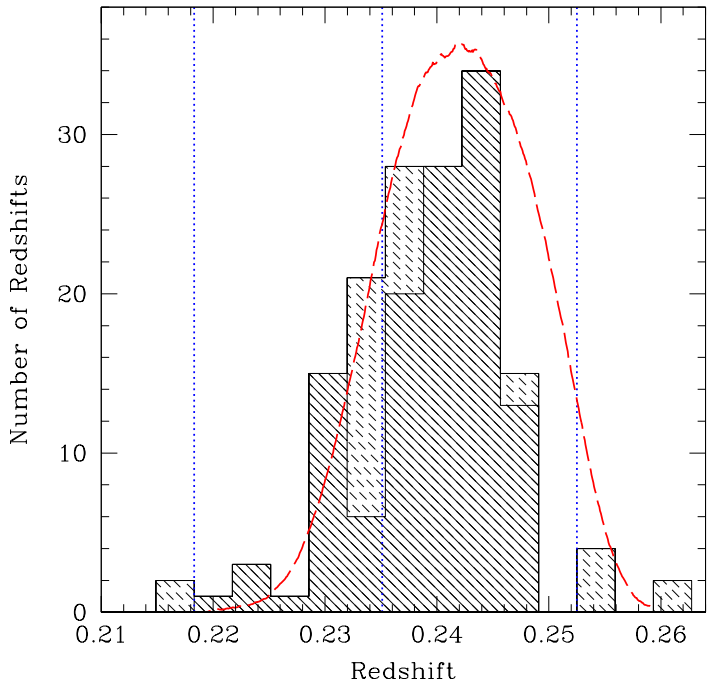

Figure 2.9: The distribution of the measured redshifts for the Fujita galaxies. There are 154 redshifts in total. The dashed line is the shape of the Suprime-Cam narrow-band filter NB816 after converting the filter wavelength to the equivalent redshift of the Hα line. The vertical dotted lines are the GMRT frequency limits converted to H I redshift; the central line is the boundary between the upper and lower sidebands of the GMRT data. The histogram shaded with the unbroken line shows the distribution of the 121 redshifts usable for H I coadding. The histogram shaded with the broken line shows the distribution of the 33 unusable redshifts (see text for details).

nal from multiple galaxies to dramatically increase the signal to noise ratio of the measurement of the H I gas content of the galaxies.

As the H I in the galaxies is not individually detectable in the GMRT data, it is impossible to take into account any structure their H I gas may have when determining their H I flux density. However, the peak specific intensity of an unresolved source in a radio synthesis image is equal to the total flux density of that source. This means, that if a galaxy is unresolved by the GMRT beam, one can take the value of the specific intensity at the optical position of the galaxy as a measure of the galaxy's total H I flux density.

The GMRT synthesised beam has a FWHM ∼2.9 arcsec which corresponds to ∼11 kpc (1 arcsec corresponds to 3.8 kpc at $z = 0.24$). All but the smallest of the galaxies in the sample are at least partially resolved by this beam size. To solve this problem the radio data were smoothed to larger beam sizes of 5.3 arcsec (∼20 kpc) and 8.0 arcsec (∼30 kpc). The larger galaxies should be unresolved in these larger beam size data. Gaussian smoothing in the image plane is equivalent to tapering (multiplying by a Gaussian) in the $u - v$ plane. This effectively reduces the weight of the outer antennas in the image plane, and hence decreases the signal to noise ratio for unresolved sources. However the measured H I flux increases for galaxies that are now unresolved in the smoothed data.

A rough estimate of the H I size of each individual galaxy was made using a correlation between optical and H I size found by Broeils & Rhee (1997). From their data, a relationship between the diameter of the optical isophote corresponding to a surface brightness of 25 mag arcsec^{-2} in B ($\mathrm{D}_{25}^{\mathrm{b,i}}$) and the diameter within which half the H I mass of the galaxy is contained ($\mathrm{D}_{\mathrm{eff}}$) was derived. This relationship is:

$$\log(\mathrm{D}_{\mathrm{eff}}) = (0.978 \pm 0.035)\log(\mathrm{D}_{25}^{\mathrm{b,i}}) \; + \; (0.041 \pm 0.046) \tag{2.1}$$

where $\mathrm{D}_{25}^{\mathrm{b,i}}$ and $\mathrm{D}_{\mathrm{eff}}$ are measured in kpc.

The IRAF task *ellipse* was used to measure the 25 mag arcsec^{-2} isophotal level in the Subaru B images, taking into account the cosmological surface brightness dimming and a k-correction taken from Norberg et al. (2002). From this an estimate of the H I diameter is made. If a galaxy has $2\,\mathrm{D}_{\mathrm{eff}} < \mathrm{D}_{\mathrm{mid}}$, where $\mathrm{D}_{\mathrm{mid}}$ is the midpoint between two beam smoothing levels, then it was assumed to be unresolved in the smaller beam data. Fig. 2.10 shows the distribution of the estimated effective H I diameter and the grouping of the galaxies into the three different beam sized radio data sets.

When making the final data cube, a linear fit to the spectrum through each sky pixel was subtracted to remove the residuals left from the continuum sources (see the discussion on IMLIN above). Any spectral line features are included in the calculation of this linear fit across frequency. Such features would create an over-estimation of the continuum, creating a bias in the measured H I spectrum. To correct for this effect, each galaxy H I spectrum has a new linear fit made across all channels except those channels corresponding to a 500 km s^{-1} velocity width around the galaxy at its redshift (these should be the channels that contain any H I signal).

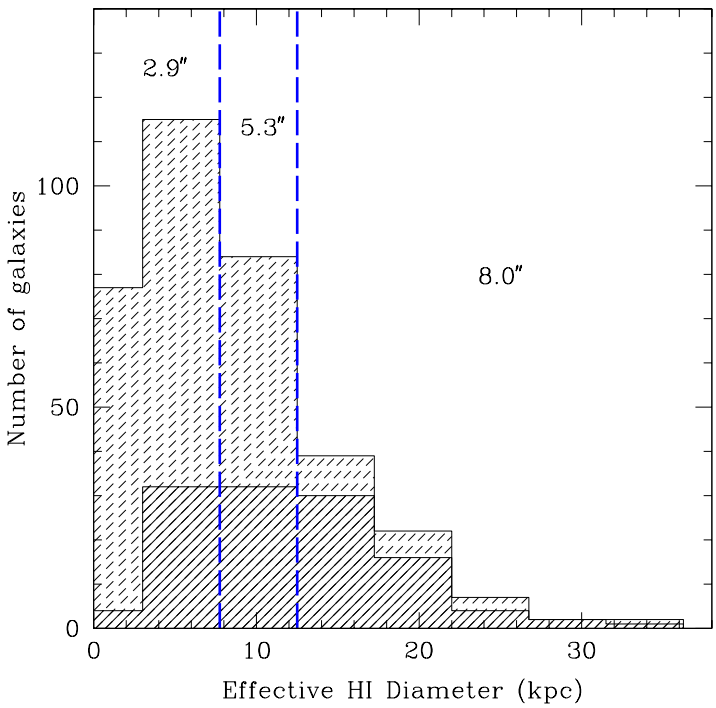

Figure 2.10: This figure shows the histogram of the estimated effective H I diameter of the Fujita galaxies. This was derived from the diameter of the galaxy at the optical B magnitude 25 mag arcsec^{-2} isophote and the correlation from Broeils & Rhee (1997). The histogram shaded with the dashed line shows the distribution for all 348 Fujita galaxies; the histogram shaded with the solid line shows the distribution for galaxies with measured optical redshifts. The vertical dashed lines show the boundaries used in sorting galaxies into the three different synthesised beam subsamples with beam FWHM of 2.9 arcsec (11 kpc), 5.3 arcsec (15 kpc) and 8.0 arcsec (20 kpc).

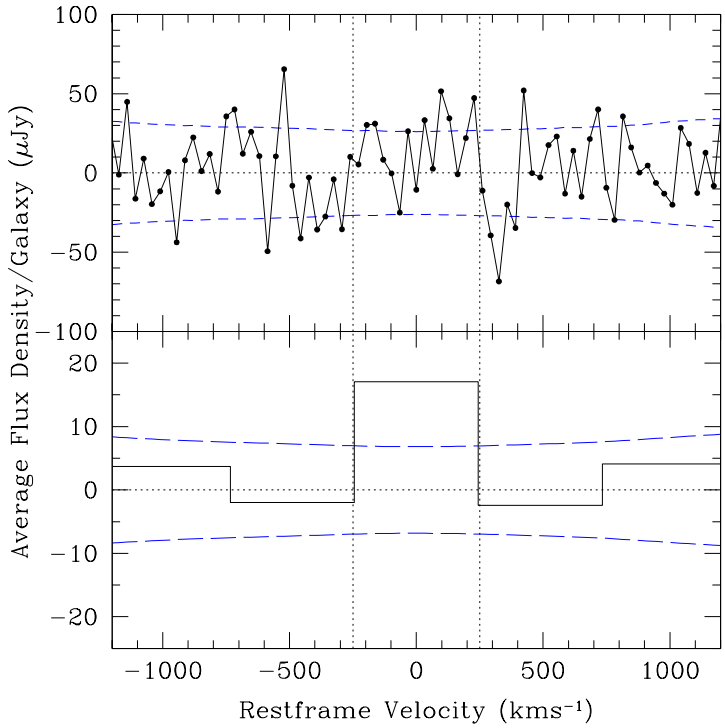

Figure 2.11: The average H I galaxy spectrum created from coadding the signal of all 121 galaxies with known optical redshifts. The top spectrum has no smoothing or binning and has a velocity step size of 32.6 km s^{-1}. The bottom spectrum has been binned to ∼500 km s^{-1}. This is the velocity width that the combined H I signal of the galaxies is expected to span. For both spectra the 1σ error is shown as dashed lines above and below zero.

This new fit is then subtracted from the data, correcting for any bias created by IMLIN. This correction to the H I flux for the combined galaxy spectrum increases the measured flux by ∼25 per cent.

When coadding the separate H I spectra, each measured flux value carries a statistical weight that is inversely proportional to the square of its uncertainty (the RMS noise level). This noise value is calculated from the known RMS per frequency channel in the radio data cube, factoring in the increase in the noise from the beam correction for galaxies away from the centre of the GMRT beam. As regions are being probed far from the GMRT beam centre, uncertainties in the beam shape could be a significant factor. However as the coadded H I signal from individual galaxies is weighted by their noise, any errors in the assumed Gaussian shape in the outskirts of the beam are heavily attenuated by the weight factor.

The weighted average H I spectrum from coadding all 121 galaxies can be seen in Fig. 2.11. To measure the error in the H I spectrum, a series of artificial galaxies with random positions and H I redshifts were used to create coadded spectra. From

many such artificial spectra a good estimate of the noise level in the final real spectrum can be determined. As seen in Fig. 2.11, the noise level increases with increasing velocity offset from the centre of the coadded spectrum. This is because some galaxies lie at redshifts near the edges of the data cube and when adding the spectra of these galaxies to the total, there is no data for channels that lie off the edge of the data cube. These channels with no data are given zero weight in the coadded sum resulting in a higher noise level at these velocities in the final coadded spectrum.

In Fig. 2.11 the total H I flux density within a central velocity width of 500 km s^{-1} is 8.9±3.4 mJy km s^{-1}, a signal to noise ratio of 2.6. The level of this flux is not highly dependent on the choice of the velocity width; choosing various velocity widths from ∼400 to ∼600 km s^{-1} gives total fluxes that are similar within the errors.

H I emission flux can be converted to the mass of atomic hydrogen that produced the signal by the following relation:

$$\mathrm{M_{HI}} = \frac{236}{(\,1+z\,)}\left(\frac{S_v}{\mathrm{mJy}}\right)\left(\frac{d_L}{\mathrm{Mpc}}\right)^2\left(\frac{\Delta V}{\mathrm{km\,s^{-1}}}\right) \tag{2.2}$$

where S_v is the H I emission flux averaged across the velocity width ΔV and $\mathrm{d_L}$ is the luminosity distance to the source (see Appendix B for the derivation of this equation). No correction for H I self absorption has been made. H I self-absorption may cause an underestimation of the H I flux by as much as 15 per cent. However this value is extremely uncertain (Zwaan et al. 1997). For the H I mass calculation a value of $\Delta V = 500$ km s^{-1}, mean $z = 0.235$ and $d_L = 1177$ Mpc were used. This gives an average H I galaxy mass for all 121 galaxies of $(2.26 \pm 0.90) \times 10^9$ $\mathrm{M_\odot}$ (Note: $\mathrm{M^*_{HI}} = 6.3 \times 10^9$ $\mathrm{M_\odot}$ at $z = 0$, Zwaan et al. 2005).

2.4.2 The cosmic neutral gas density, Ω_{gas}

The conversion of the H I mass of the galaxies to the cosmic density of neutral gas requires a measure of the number density of the galaxies. This information is available from the Fujita et al. (2003) Hα luminosity function at $z = 0.24$ which was created from these galaxies.

The narrow-band filter used to select the Fujita galaxies is not square but has an almost Gaussian-like profile (see Fig. 2.9). This means that galaxies with strong Hα emission can be detected in the wings of the filter but will have their measured Hα luminosity underestimated. There is a strong luminosity bias in the spectroscopic redshifts obtained due to this effect. Bright galaxies that have Hα emission lines in the wings of the filter will be easier to obtain redshifts for than faint galaxies at the centre of the filter. The distribution of redshifts appears to be slightly biased towards lower redshifts. This small bias is probably caused by the [NII]6584 emission line contributing more to the narrow-band flux at the lower redshifts, giving rise to more detections. Near $z \sim 0.225$, the emission from the [NII]6584 line and the [SII] doublet both come through simultaneously at opposite ends of the narrow-band filter. This could explain the tail at low redshift seen in the redshift distribution.

Galaxy Subsample	Number of galaxies	L(Hα) Limits (log erg s^{-1})	Average L(Hα) (log erg s^{-1})	Average SFR (M$_\odot$ yr^{-1})	Average H I Mass (10^9 M$_\odot$)	Average Volume per galaxy (Mpc^3)	Subsample $\Omega_{\rm gas}$ (10^{-3})
all galaxies	121	–	41.0	0.79	2.26 ± 0.90	–	–
bright L(Hα)	42	L(Hα) > 40.9	41.4	1.98	4.1 ± 2.2	105 ± 38	0.38 ± 0.24
medium L(Hα)	42	$40.4 <$ L(Hα) ≤ 40.9	40.6	0.31	2.9 ± 1.5	76 ± 28	0.37 ± 0.23
faint L(Hα)	37	$40.0 \leq$ L(Hα) ≤ 40.4	40.2	0.13	0.9 ± 1.4	53 ± 27	0.16 ± 0.26

Table 2.1: The table shows the properties of all the galaxies coadded together and the three Hα luminosity subsamples. For each subsample the average Hα luminosity, average star formation rate (SFR) and average H I mass is listed. Also listed is the average volume per galaxy which is the average volume one would need to probe in order find a single galaxy belonging to that luminosity subsample. The reciprocal of this volume is the number density of such galaxies per Mpc^3. The cosmological neutral gas density for each galaxy subsample is listed in the last column. Combining these values gives the total cosmic neutral gas density. The star formation rate listed is derived using the Kennicutt (1998a) Hα to SFR relationship.

Fujita et al. (2003) applied a statistical correction for the effect of the filter shape when creating their Hα luminosity function. This could be done because they have reasonably well-understood selection criteria for Hα emission detection. This is not the case for the subsample of Fujita galaxies for which redshifts were obtained. Different galaxies were observed for different amounts of time, as it was not possible to configure the fibres in 2dF on all the galaxy targets simultaneously. Some galaxies also had small errors in their astrometry (the positions of the galaxies as measured off the optical imaging) that reduced the amount of light down the optic fibre obtained for that galaxy (these astrometric errors have since been corrected). This uncertainty in the detection success rate for the galaxy redshifts is the reason the Fujita et al. (2003) Hα luminosity function was used to determine the number density of the galaxies.

For calculating the number density of the galaxies, the Fujita galaxies with redshifts have been divided into three subsamples based on their Hα luminosity. In order to divide the galaxies accurately into subsamples, it is necessary to correct the Hα luminosity for the effect of the filter shape. This is done in order to separate genuine faint galaxies from brighter galaxies seen through the wings of the narrow-band filter. Without this correction, the faintest Hα emission galaxies are measured to have more atomic hydrogen gas than galaxies with stronger Hα emission.

An estimate of the necessary Hα luminosity correction can be made using the precise redshifts of the galaxies and the known shape of the narrow-band filter with wavelength[3]. The measured Hα luminosity is adjusted by the relative decrease in the filter transmission at the redshifted wavelength of the Hα line compared to the filter centre[4].

Using the corrected Hα luminosities the galaxies are separated into three subsamples: bright, medium and faint. The details for each of the Hα subsamples can be seen in Table 2.1. The average H I mass for the galaxies in each subsample is measured as described in Section 2.4.1.

An estimate of the average number density for galaxies belonging to each subsample is determined using the Fujita et al. (2003) luminosity function. This is done by integrating the Hα luminosity function over the Hα limits for each subsample to obtain the number density of such galaxies. The galaxy number density for each subsample is expressed in Table 2.1 as the average volume one would need to probe in order to find a single galaxy belonging to that Hα luminosity subsample (the

[3]National Astronomical Observatory of Japan website
http://subarutelescope.org/Observing/Instruments/SCam/

[4]This Hα correction was not used in the comparison of the Hα and radio continuum observations in Section 2.3. Corrections cannot be done for all the galaxies included in that analysis as not all have redshifts. The correction is only necessary in the work above because of the bias in the galaxies for which spectroscopic redshifts were obtained. The much larger sample of faint galaxies in Section 2.3, most of which do not have redshifts, is dominated by genuine faint galaxies rather than bright galaxies seen through the edge of the narrow-band filter. It is these bright galaxies that need the correction. The number of these bright galaxies misclassified as faint galaxies should be small compared to the large number of actual faint galaxies in that analysis, so that any correction should not be statistically significant.

reciprocal of the number density). The errors in the calculated volumes are derived by considering the effect of the errors in the Fujita et al. (2003) Schechter luminosity function parameters.

The cosmic density of H I gas for each subsample can be calculated using:

$$\rho_{HI} = \frac{\overline{M}_{HI}}{\overline{V}_{gal}} \tag{2.3}$$

where $\rho_{\rm HI}$ is the cosmic density of H I gas, $\overline{\rm M}_{\rm HI}$ is the average H I mass per galaxy and $\overline{\rm V}_{\rm gal}$ is the average volume per galaxy. To compare with other values in the literature, it is necessary to convert this value of the H I gas density to the density of neutral gas. This is done by adding a correction for the neutral helium content, which is assumed to be 24 per cent by mass of the total neutral gas. This neutral gas density is converted to units of the total cosmic mass density using:

$$\Omega_{\rm gas} = \frac{8\,\pi\,{\rm G}\,\rho_{\rm gas}}{3\,{\rm H}_0^2} \tag{2.4}$$

After combining the neutral gas density values for each subsample a total cosmic density of neutral gas in star-forming galaxies at $z = 0.24$ of $\Omega_{\rm gas} = (0.91 \pm 0.42) \times 10^{-3}$ was obtained (an H I density $= (9.5 \pm 4.4) \times 10^7$ ${\rm M}_\odot\,{\rm Mpc}^{-3}$). This value is shown in comparison to other literature values in Fig. 2.12.

Fig. 2.12 shows the neutral gas density of the universe as a function of both redshift and look-back time. There is a large uncertainty in the cosmic neutral gas density in the redshift range $z = 0.1$–1.5, which corresponds to two thirds of the age of the universe. This measured value of $\Omega_{\rm gas}$ is comparable to that from previous damped Lyman-α measurements at intermediate redshifts (Rao, Turnshek, & Nestor 2006). While the trend of the measurements is to indicate a sharp rise in H I content with redshift, both studies suffer from large statistical uncertainty. However, this new measurement has the advantage that it applies to a narrow range of redshifts $z \sim 0.24$.

Strictly speaking, this measured cosmic neutral gas density is only a lower limit, as it includes only the gas from galaxies that show star formation. The star formation–H I mass correlation found in low-redshift H I-selected galaxies (Doyle & Drinkwater 2006), shows that galaxies with little or no star formation contain no significant quantities of neutral gas. This relationship appears to hold at $z = 0.24$ (see Section 2.4.3). Since the sample includes galaxies with Hα luminosities at $\sim$1 per cent of ${\rm L}_*$ no significant reservoirs of H I gas should be missed.

In this work no attempt has been made to separate the Hα emitting galaxies into those that are genuine active star-forming galaxies from those that are actually active galactic nuclei (AGN). When calculating their star-formation density for this field at $z = 0.24$, Fujita et al. (2003) included a 15 per cent correction for the luminosity contribution of AGN (taken from Pascual et al. 2001). No similar correction exists for the atomic hydrogen gas content of AGN. However, the ratio of H I mass to Hα luminosity for AGN is likely to be lower than for star-forming galaxies, as AGN

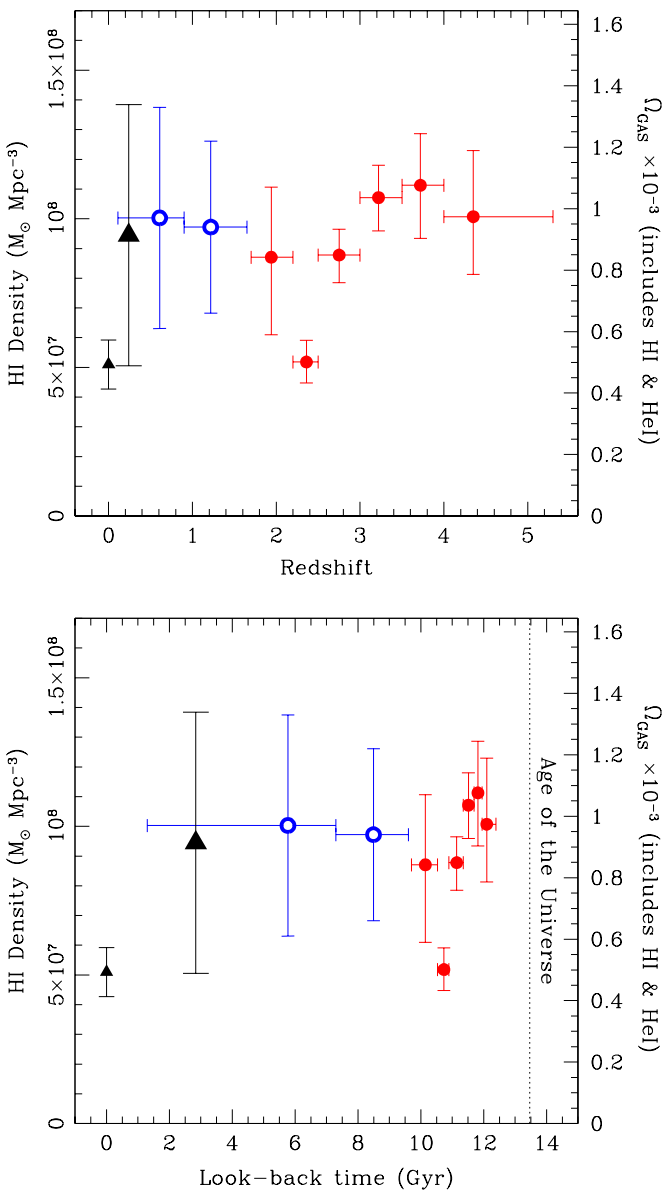

Figure 2.12: The evolution of the neutral gas density of the universe as measured in 2007. The top panel shows the cosmic neutral gas density vs. redshift and the bottom panel the cosmic density vs. look-back time. All results have been corrected to the same cosmology. The left y-axis shows the cosmic density in terms of H I gas density measured in solar masses per megaparsec cubed. The right y-axis shows the cosmic density measured as a fraction of the total cosmic mass density $\Omega_{\rm M}$ and includes the correction for the neutral Helium content. The small triangle at $z = 0$ is the HIPASS 21-cm emission measurement from Zwaan et al. (2005). The filled circles are damped Lyman-α measurements from Prochaska, Herbert-Fort, & Wolfe (2005). The open circles are damped Lyman-α measurements from Rao, Turnshek, & Nestor (2006) using HST. The large triangle at $z = 0.24$ is the H I 21-cm emission measurement made in this chapter.

preferentially reside in early-type galaxies (Schade et al. 2001). Including AGN in the sample may cause a small underestimation in the density of neutral gas for star-forming galaxies, however it will bring the result closer to the true total cosmic neutral gas density of all galaxies by including another galaxy type in the measurement.

The volume probed by Fujita et al. (2003) for their Hα luminosity function (and used here for the calculation of the number density of galaxies) is $\sim$4000 Mpc and is a rectangular strip with a depth $\sim$110 Mpc. The cosmic variance in the number of galaxies in a field of this volume and shape at $z = 0.24$ is approximately 40 per cent. This estimate is based on a calculation using the Eisenstein & Hu (1998) fitting function for the matter power spectrum function and is confirmed by an examination of the galaxy distribution in the Millennium Simulation at $z = 0.24$ (Springel et al. 2005; Croton et al. 2006). Treating this as a random error (rather than a systematic offset), the final error in $\Omega_{\rm gas}$ would increase by $\sim$15 per cent. However, the star formation rate measured for this field places it close to the mean, or perhaps slightly higher, compared to other values in the literature (see Section 2.2.1). This suggests that this field has close to the average number of galaxies despite the large possible cosmic variation, and that the measured neutral gas density measured in this field is close to, or slightly higher than, the true cosmic gas density, $\Omega_{\rm gas}$.

2.4.3 The star formation rate–H I mass galaxy correlation

In the local universe there is a known correlation between the star formation rate in a galaxy and the mass of H I in that galaxy. For a recent study using H I-selected galaxies from HIPASS, see Doyle & Drinkwater (2006). In Table 2.1 the average H I galaxy mass for the different Hα luminosity subsamples is listed. For each subsample, one can derive the average star formation rate per galaxy from the average Hα luminosity and the SFR conversion of Kennicutt (1998a). This comparison of star formation rate and galaxy H I mass is shown in Fig. 2.13. Plotted on this figure is the linear relationship from Fig. 3 of Doyle & Drinkwater (2006), where they compared individual galaxies' H I masses from HIPASS to their star formation rate derived from *IRAS* infrared data. The linear fit, taken directly from their figure, is:

$$\log(\text{HI Mass}) = 0.59 \log(\text{SFR}) + 9.55 \tag{2.5}$$

From Fig. 2.13, it is clear that the values found at $z = 0.24$ are consistent with the correlation found at $z = 0$. This suggests that there has been no significant change in the star formation mechanisms in field galaxies 3 Gyrs ago; that the same amount of atomic hydrogen gas in a galaxy gives the same measurable star formation rate.

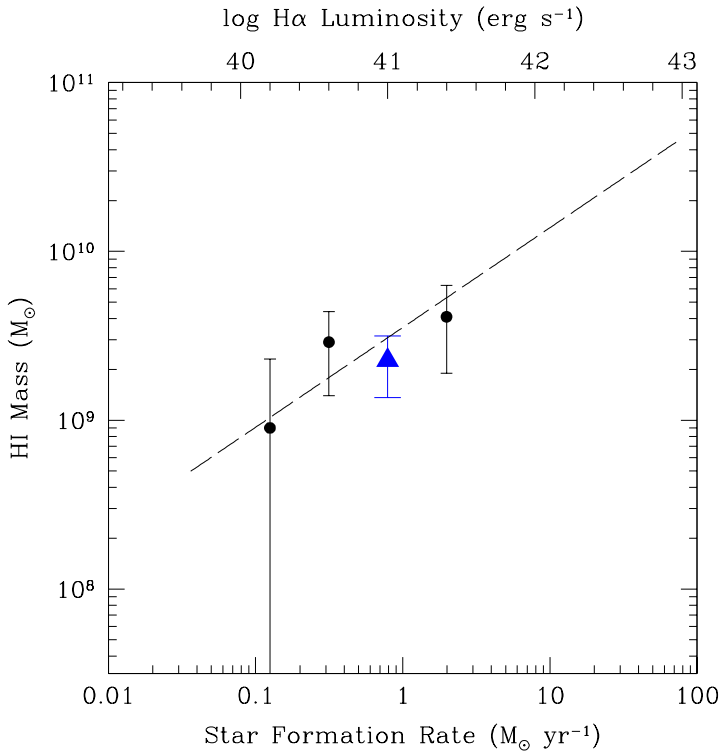

Figure 2.13: The average galaxy atomic hydrogen gas mass plotted against the average galaxy star formation rate. The circular points are the average values for the bright, medium and faint L(Hα) subsamples (see Table 2.1). The triangle is the value for the average of all galaxies. The line is from Doyle & Drinkwater (2006) for $z \sim 0$ galaxies.

2.5 Conclusion

It has been demonstrated that is possible to measure, in reasonable observing times, the average amount of atomic hydrogen gas in galaxies from their H I 21-cm emission at intermediate redshifts. This is done by coadding the H I signal from multiple galaxies with known positions and optical redshifts. The measurement in this work of H I 21-cm emission from galaxies corresponds to a cosmic density of neutral gas that is consistent with previous measurements of the neutral gas density from damped Lyman-α measurements at a similar redshift.

The relationship between Hα luminosity and the restframe 1.4 GHz radio continuum emission in star-forming galaxies at $z = 0.24$ has been shown to be consistent with the correlation found at $z = 0$, as is the relationship between galaxy star formation rate and galaxy H I mass. These two results suggest that the process of star formation in field galaxies is not significantly different 3 Gyr ago from the present day.

Chapter 3

The H I gas content of galaxies around Abell 370 at z = 0.37

> Science is built up of facts, as a house is built of stones; but an accumulation of facts is no more a science than a heap of stones is a house.
>
> Henri Poincaré

3.1 Introductory Summary

Observations with the Giant Metrewave Radio Telescope (GMRT) were used to measure the neutral atomic hydrogen (H I) gas content of 324 galaxies around the galaxy cluster Abell 370 at a redshift of $z = 0.37$ (a look-back time of ∼4 billion years). The H I 21-cm emission from these galaxies was measured by coadding their signals using precise optical redshifts obtained with the Anglo-Australian Telescope.

The goal of this work is to quantify the evolution of the H I gas in galaxies in a variety of environments from the field to dense cluster cores (see Section 1.4 for more on galaxy clusters). At moderate redshifts the angular extent of galaxy clusters is sufficiently small enough that galaxy environments from the dense cluster core to almost field galaxy densities can be observed in a single radio telescope pointing. The cluster studied, Abell 370, is a large galaxy cluster, similar in size and mass to the nearby Coma cluster. The H I gas content of galaxies at different distances from the Abell 370 cluster core are examined, in particular that of galaxies inside and outside the extent of the hot, X-ray emitting, intracluster gas as well as that of galaxies inside and outside the cluster R_{200} radius (the radius at which the galaxy density is 200 times the general field).

Significant quantities of gas were found around Abell 370, suggesting that there has been substantial evolution in the gas content of galaxy clusters since redshift $z = 0.37$. The total amount of atomic hydrogen gas found around Abell 370 is many times more than that seen around the Coma cluster. Despite this higher gas content, Abell 370 shows the same trend as nearby clusters, that galaxies close to the cluster core have lower H I gas content than galaxies further away where the galaxy

Telescope	Type of Observation	Date of Observations	Duration of Observations
GMRT	radio spectroscopy	10–17 August 2003	63 hours
ANU 40 inch	optical imaging	1–2 November 2005	2 nights
ANU 40 inch	optical imaging	19–24 September 2006	5 nights
Anglo-Australian Telescope	optical spectroscopy	11–14 October 2006	4 nights

Table 3.1: List of telescope observations used in this chapter.

density is lower. The optically blue galaxies contain the majority of the H I gas surrounding the cluster. However, there is evidence that the optically red galaxies contain appreciable quantities of H I gas within their central regions. The Abell 370 galaxies have H I mass to optical light ratios similar to local galaxy samples and have the same correlation between their star formation rate and H I mass as found in nearby galaxies. The average star formation rate derived from [OII] emission and from de-redshifted 1.4 GHz radio continuum for the Abell 370 galaxies also follows the correlation found in the local universe. The large amounts of H I gas found around the cluster can easily be consumed entirely by the observed star formation rate in the galaxies over the ∼4 billion years (from $z = 0.37$) to the present day. Abell 370 appears set to evolve into a gas poor system similar to galaxy clusters observed in the local universe.

In this chapter, the cluster centre of Abell 370 has been set as the mid point between the two cD galaxies which is at right ascension (R.A.) $02^{\rm h}39^{\rm m}52.90^{\rm s}$ declination (Dec.) $-01°34'37.5''$ J2000. This value is close to the centre determined from X-ray measurements (Ota & Mitsuda 2004) and a good match to the velocity and surface density distribution of the galaxy data used in this chapter. The redshift of the cluster centre has been set as $z = 0.373$ based on the galaxy redshift distribution that was observed. The observations used in this paper are listed in Table 3.1. The work in this chapter has been published in Lah et al. (2009).

The structure of this chapter is as follows. Section 3.2 details the optical imaging and optical spectroscopy of the Abell 370 galaxies. Section 3.3 details the radio observations and data reduction. Section 3.4 presents the measurement of the H I 21-cm emission signal from all the Abell 370 galaxies with usable redshifts. Section 3.5 presents the H I signal from different subsamples of these galaxies. Section 3.6 details the comparison of the H I results for Abell 370 with various literature measurements. Section 3.7 elaborates on the star formation properties of the Abell 370 galaxies. Finally, Section 3.8 presents a summary and discussion of the results.

3.2 The Optical Data

3.2.1 The optical imaging and galaxy target selection

Wide-field and moderately deep imaging of the galaxy cluster Abell 370 and its surroundings were obtained using the Wide Field Imager (WFI) on the Australian

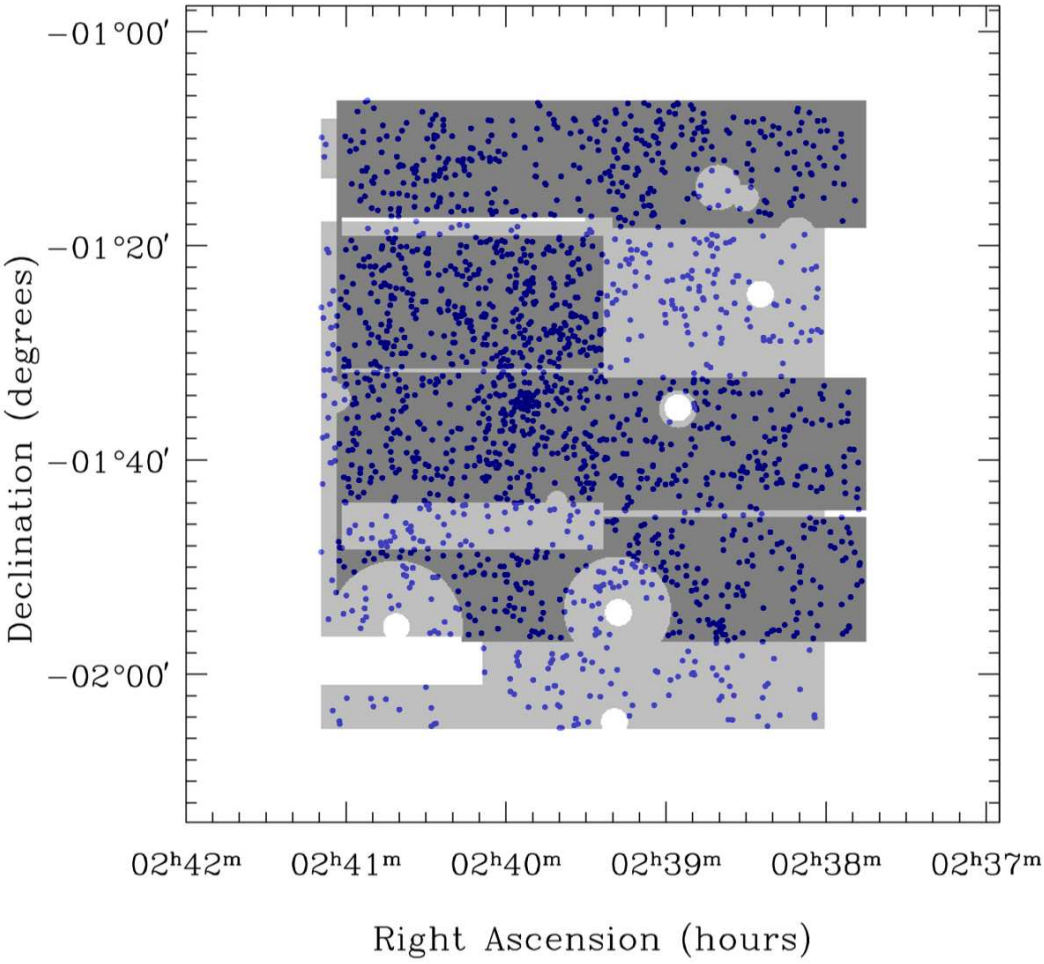

Figure 3.1: This figure shows the extent of the optical imaging taken with the ANU 40 inch telescope. The dark grey areas were observed in 2005 November; the light grey areas are the additional areas covered in 2006 September. The circles are the regions around bright stars where galaxy identification could not be made. The circles are larger in the 2005 November observations as the better seeing caused the brightest stars to saturate the CCD. The small points are the 1877 objects for which redshifts were obtained during the AAOmega run in 2006 October.

National University (ANU) 40 inch telescope at Siding Spring Observatory. There were two separate observing runs: the first in 2005 November 1–2, and the second in 2006 September 19–24. Both sets of observations were taken through the standard broad passband filters V, R and I.

The Wide Field Imager has a 52 by 52 arcmin field-of-view which is sampled by a mosaic of 8 2k×4k CCDs. One of these detectors was not functioning leaving a 12 arcmin by 24 arcmin gap in the imaged field. In 2005 November only a single WFI pointing was observed, leaving in a gap in the imaging due to the missing CCD. The conditions during this run were close to photometric and the seeing in the final combined imaging was ∼2.1 arcsec. The average 3σ surface brightness limit of this imaging was 25.5 mag arcsec^{-2} in V, 25.3 in R and 24.2 in I. The 2006 September WFI observations consisted of two pointings that filled in the gap from the missing WFI detector and extended the imaged region. The observing conditions were poor during this run with the seeing in the final combined images being ∼2.8 arcsec. The average 3σ surface brightness limit of this later imaging was 24.1 mag arcsec^{-2} in V, 23.8 in R and 22.7 in I. The extent of the WFI imaging from both runs is shown in Fig. 3.1. The total imaged area was ∼51 by ∼59 arcmin.

Targets were selected from the WFI imaging for optical spectroscopic follow up. Initial target selection was done on the I band images with confirmation of the targets in the R and V bands. There were many spurious object detections around bright stars, diffraction spikes and chip defects. To remove these a series of rectangular and circular exclusion regions were defined around the problem areas as seen in Fig. 3.1.

Objects brighter than a V band total magnitude of 19.2 were removed from the list of targets for spectroscopic follow up. This limit is 0.6 magnitudes fainter than the cD galaxies in Abell 370 and no other cluster members are expected to be this luminous (Note: the two cD were included for spectroscopic follow up as additional targets). Objects brighter than V band total magnitude of 21.7 were used for target selection. A small number of objects were removed from the target list that were substantially redder than galaxies belonging to the red sequence of Abell 370 and hence likely to be stars or distant background galaxies.

Aperture magnitudes were measured using 3 arcsec diameter apertures. Total magnitudes were measured using the *best* magnitude parameter of SExtractor. All magnitudes were calibrated on the Vega system. Comparisons between the total and aperture magnitudes were used to remove stars from the galaxy sample. The optical magnitudes of the galaxies were corrected for the foreground extinction from the Galaxy using the Schlegel–Finkbeiner–Davis Galactic reddening map (Schlegel, Finkbeiner, & Davis 1998). No correction was done for the internal extinction of the galaxies and it is assumed that any correction would have minimal effect on the results. Separate lists of targets were made from each set of the WFI imaging. Only after applying all the above selection criteria were the target catalogues merged. The photometry is consistent for objects that appear in both catalogues.

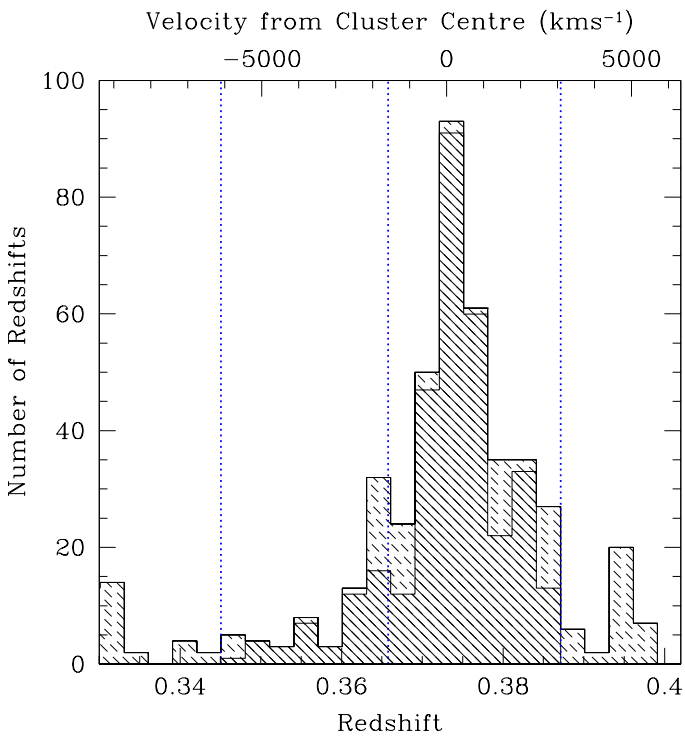

Figure 3.2: This figure shows the distribution of the 450 redshifts around the galaxy cluster Abell 370. The vertical dotted lines are the GMRT frequency limits converted to their H I redshift; the central dotted line is the boundary between the upper and lower sidebands of the GMRT radio data. The histogram shaded with the unbroken line is the distribution of the 324 redshifts used in H I coadding. The histogram shaded with the broken line is the distribution of the unusable redshifts (see Section 3.4 for details). The top x-axis shows the velocity from the cluster centre, giving an indication of the peculiar motion of the galaxies within the cluster. The cluster centre is at $z_{cl} = 0.373$ and the listed velocity includes the cosmological correction (i.e. it is divided by $1 + z_{cl}$).

3.2.2 The optical spectroscopic data

Over 4 nights from 2006 October 11–14, the targets were observed with AAOmega, the fibre-fed, dual-beam spectrograph on the Anglo-Australian Telescope. Eleven fibre configurations were observed for 2 hours each. Optical spectra were obtained for a total of 2347 unique targets. The combination of the blue and red arms of the spectrograph provided continuous wavelength coverage from ∼3700 Å to ∼8800 Å. At the redshift of the cluster ($z = 0.37$) this covers the rest frame wavelength region from ∼2700 Å to ∼6400 Å which includes the emission lines of [OII]λ3727, Hβ, [OIII]λ4959 and [OIII]λ5007 (but not Hα) as well as the absorption features Ca H&K, Na, Mg, Hδ, G–band and Hγ.

The data were reduced using the Anglo-Australian Observatory's 2DFDR data

reduction pipeline[1] and the redshift determination was done with the interactive software package RUNZ. In total there were 1877 objects with secure redshifts (includes both galaxies and some foreground stars), a redshift completeness of 80 per cent. The objects range in redshift from $z \sim 0$ to 1.2 and the error in the redshifts is $\sim$70 km s^{-1}. There are 450 galaxies with redshifts between $z = 0.33$ and $z = 0.40$ (see Fig. 3.2 for the redshift distribution); 324 of these galaxies were usable for H I coadding (see Section 3.4 for details on this selection). Thumbnail images of all 324 Abell 370 galaxies used in the H I coadding can be seen in Fig. 3.3.

3.2.3 The optical properties of the Abell 370 galaxies

Fig. 3.4 shows the 324 galaxies used in the H I coadding plotted as projected distance in Mpc from the galaxy cluster centre. Plotted on this figure is the extent of the hot intracluster gas, the X-ray significance radius. This is the radius from the cluster centre where the X-ray emission surface brightness has fallen to three times the background sky level (the 3σ extent of the X-ray gas). For the cluster Abell 370 this radius is at 1.45 Mpc (4.7 arcmin) (Ota & Mitsuda 2004). Also plotted on this figure is the R_{200} radius, the radius at which the cluster is 200 times denser than the general field (Carlberg et al. 1997). For Abell 370 this is $R_{200} = 2.57$ Mpc which was derived from the cluster velocity dispersion of 1263 km s^{-1}. The cluster velocity dispersion of Abell 370 was measured from the redshifts obtained in this work (Pracy et al. 2009).

The optical magnitudes of the galaxies near the redshift of the cluster at $z = 0.37$ were K-corrected to rest frame values. Instead of K-correcting the magnitudes to the same optical filter, the observed R band magnitudes were K-corrected to rest frame B band and the observed I band magnitudes to rest frame V band following the methodology of Kim, Goobar, & Perlmutter (1996) and Schmidt et al. (1998). At redshift $z = 0.37$ the deredshifted peak transmission of the Johnson-Cousins R band is at 4369 Å and for the V band at 5880 Å. These values are closer to the wavelength centres of the Johnson-Cousins B and V band (4207 Å and 5283 Å) than the rest frame peak transmissions of the R and I band (5985 Å and 8056 Å respectively, Bessell 1990). This method minimises the variation in the K-correction value between the red and blue galaxies as one is extrapolating over a smaller wavelength range.

For these galaxies the variation in K-corrections from the bluest to reddest galaxies was $\sim$1.9 when correcting the observed V band to rest frame V band, $\sim$0.6 for the R band to R band correction and $\sim$0.28 for the I band to I band. In contrast the range in K-correction values when correcting the observed R band to rest frame B band was only $\sim$0.26 and correcting the observed I band to rest frame V band was only $\sim$0.18. Beside minimising the range in the K-corrections, correcting to the rest frame B and V magnitudes is useful for comparisons of the galaxies to literature

[1] Anglo-Australian Observatory website
http://www.aao.gov.au/AAO/2df/aaomega/aaomega.html

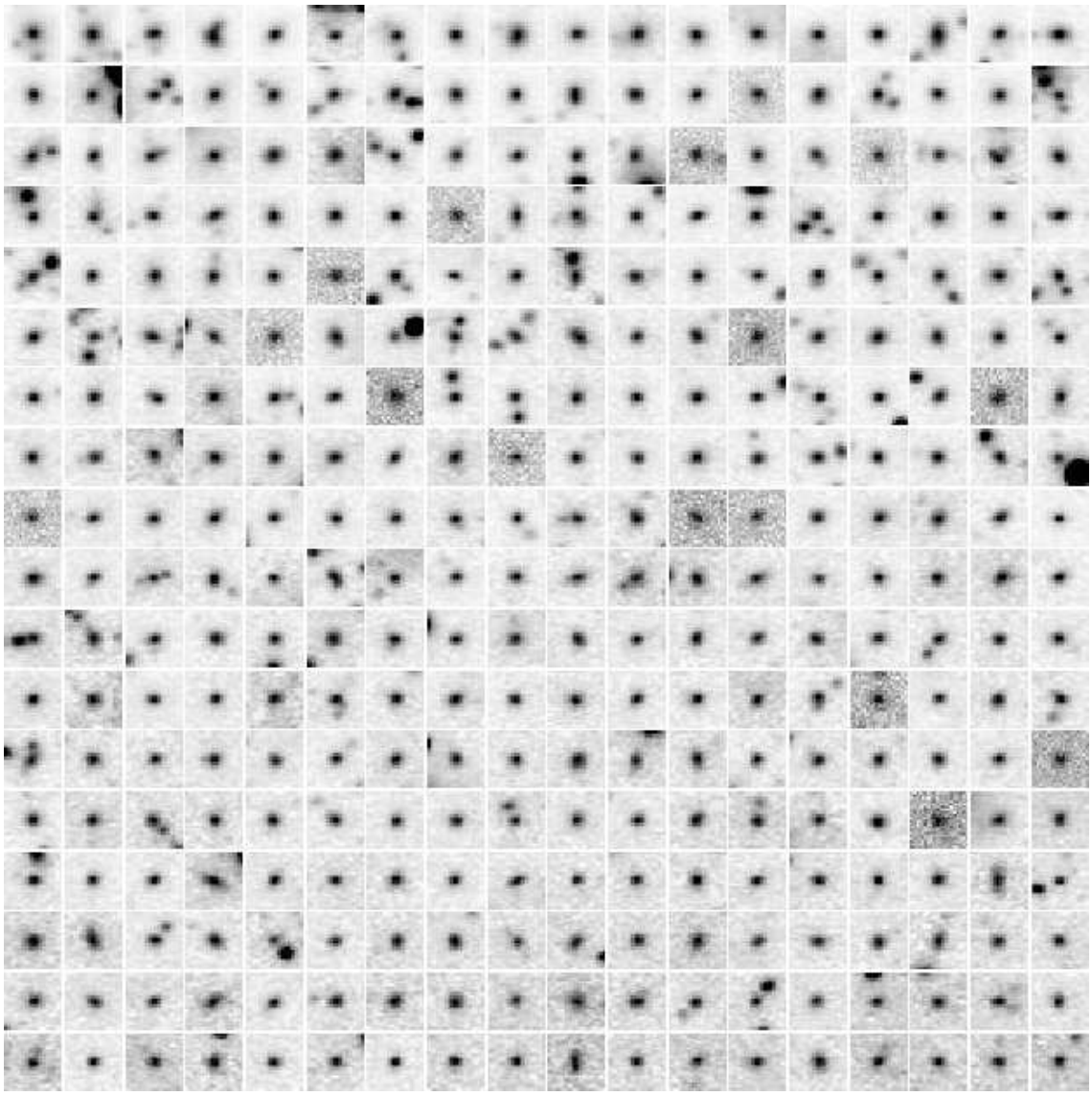

Figure 3.3: Thumbnail images of all 324 Abell 370 galaxies used in the H I coadding. These are R band images from the ANU 40 inch telescope. They are ordered by apparent R magnitude with the brightest galaxy in the top left, decreasing in luminosity along the rows first then columns with the bottom right galaxy being the faintest. The individual images have been all scaled to the same maximum brightest level so that all the galaxies can be seen despite the large contrast between the brightest and faintest galaxies. One can tell the relative brightness of the galaxies by the brightness of the background noise in the thumbnail. Several galaxies appear to have higher noise levels than their magnitudes would suggest. These are galaxies found only in the lower quality September 2006 imaging.

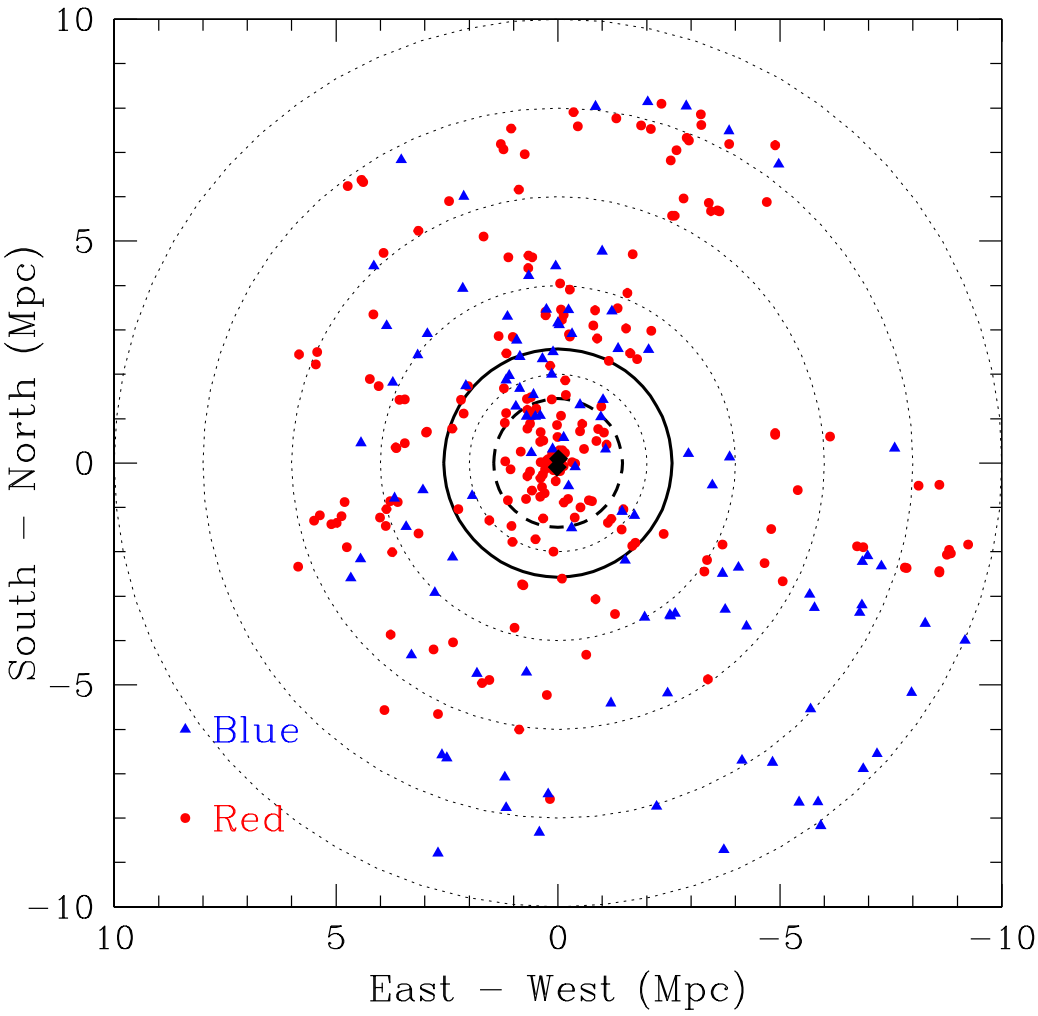

Figure 3.4: This figure shows the 324 galaxies used in the H I coadding plotted as projected distance in Mpc from the galaxy cluster centre. The triangular points are the blue galaxies and the circular points are the red galaxies. The two diamond points near the centre are the two cD galaxies. The dashed circle is the 3σ extent of the X-ray gas (Ota & Mitsuda 2004) and is at a radius of 1.45 Mpc. The solid circle is the R_{200} radius of 2.57 Mpc. The faint, dotted circles are at radii of 2, 4, 6, 8 & 10 Mpc from the cluster centre.

samples. In particular the Butcher–Omeler blue galaxy classification is defined in K-corrected $B - V$ colour.

When performing the K-corrections the magnitudes were corrected for the change in the shape of the filter as well as the change in the zero points of the Vega magnitude system for the different filters. Five flux calibrated template spectra were used in the K-corrections: an elliptical, S0, Sa, Sb and Sc galaxy spectra. For determining the K-correction values, $V - I$ colours were generated for a variety of combinations of the template spectra at the redshift of the galaxy. The template combinations that had generated $V - I$ colours that matched the observed $V - I$ colour of the galaxy within 0.1 magnitudes were then used to calculate a K-correction value (the photometric uncertainty was ∼0.1 magnitudes). Usually multiple template combinations matched a galaxy's observed $V - I$ colour, so all the calculated K-correction values were averaged. The variation in the K-corrections from the different template combinations varied minimally suggesting that this is robust method for determining the required K-correction. The $V - I$ colour was chosen for the template matching because the deredshifted peak transmission of the V band is at 3856 Å at $z = 0.37$, putting it blue-ward of the 4000 Å break. The greatest difference between the template spectra occurred around the 4000 Å break with the ellipticals having a strong decrease in flux blue-ward of the break while the Sa spectral template actually increases in brightness past this point.

The $B - V$ colour vs. B band magnitude diagram for all the 324 galaxies used in the H I coadding can be seen in the top panel of Fig. 3.5 and for those galaxies within 1.45 Mpc of the galaxy cluster centre (the X-ray significance radius) in the bottom panel. A least absolute deviation regression fit was made to the cluster ridge-line in the colour–magnitude diagram containing those galaxies within 1.45 Mpc of the cluster centre. The slope of this linear fit was close to zero, so a fixed colour term for the ridge-line of $B - V = 0.77$ was used. This almost zero slope is probably due to the limited magnitude range used and the relatively large errors in the optical magnitudes (∼0.1 mag). The galaxies were divided into blue and red galaxies using the Butcher–Oemler condition, i.e. the blue galaxies are those at least 0.2 magnitudes bluer than the cluster ridge-line (Butcher & Oemler 1984). This sets the division at $B - V = 0.57$. In Fig. 3.4, which shows the projected distance distribution of the galaxies, the blue and red galaxies are plotted using different symbols. Near the cluster core the red galaxies dominate. Away from the cluster centre the number of blue galaxies increases though a large number of these outer galaxies are red. The blue fraction of galaxies in the cluster using the Butcher–Oemler criteria is 0.132 ± 0.003 within the measured R_{30} radius of 0.669 Mpc (2.17 arcmin). (R_{30} is defined as the radius containing 30 per cent of the projected galaxies that lie within 3 Mpc of the cluster centre.) The blue fraction found in the majority of nearby clusters is ∼0.03 (Butcher & Oemler 1984), substantially lower than that found in Abell 370.

The equivalent width of the [OII]λ3727 emission line was measured from the AAOmega optical spectra using the standard flux-summing technique. The galaxies were divided into an [OII] emission and non-[OII] emission samples at an equivalent

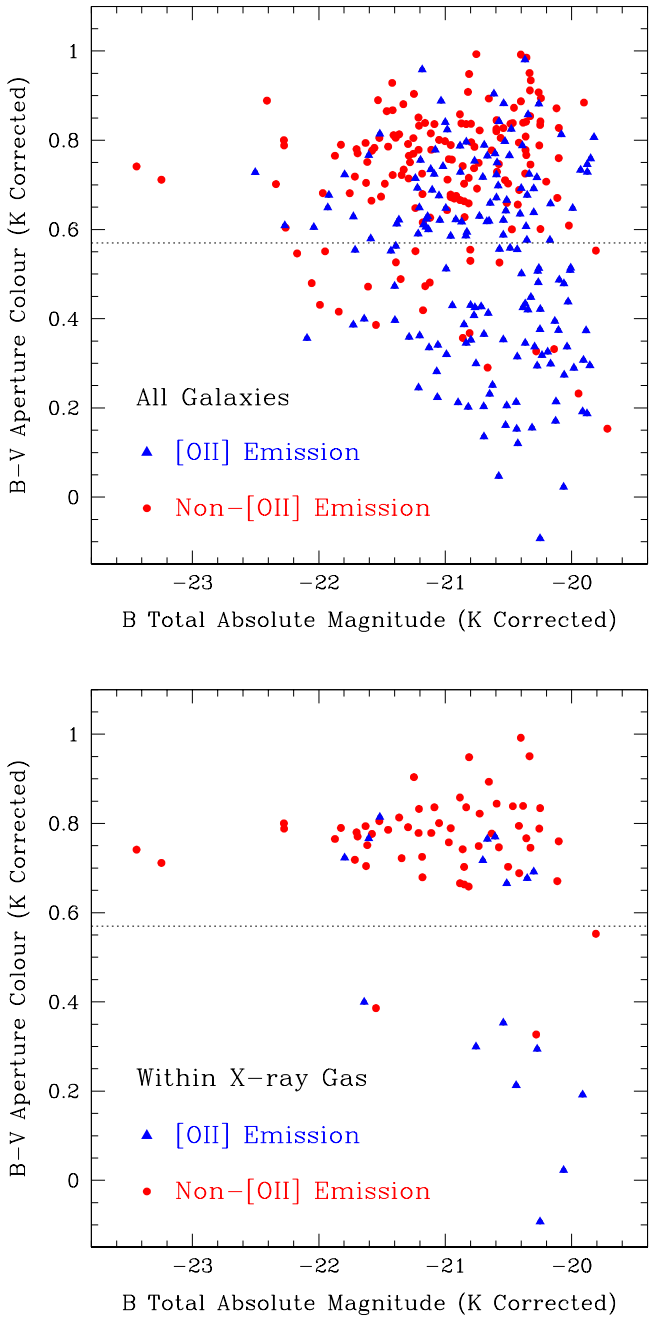

Figure 3.5: In the top panel is the $B - V$ aperture colour vs. B band total absolute magnitude for the 324 galaxies used in the H I coadding. The bottom panel shows the same for the 75 galaxies close to the galaxy cluster centre (within a projected distance from the cluster centre of 1.45 Mpc, the 3σ extent of the X-ray gas). The triangular points are galaxies with measured [OII] equivalent widths > 5 Å and the circular points are those with [OII] equivalent widths ≤ 5 Å. The dotted line is the dividing line used to separate the blue and red galaxies at $B - V = 0.57$.

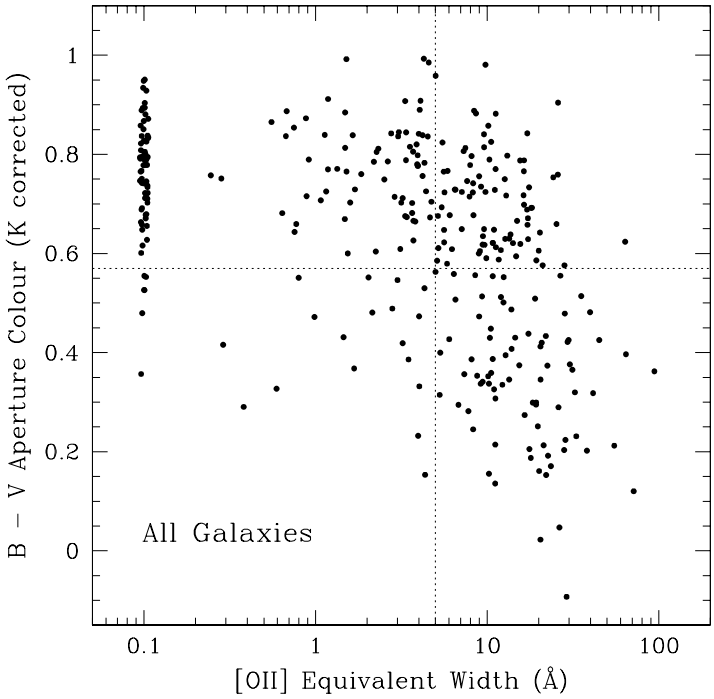

Figure 3.6: This figure shows the $B - V$ aperture colour vs. [OII] equivalent width for all the 324 galaxies used in the H I coadding. The 68 galaxies that have measured [OII] equivalent widths equal to or less than zero have been given a value of ∼0.1 Å so that they can be plotted on the log scale used here. The dashed vertical line is the [OII] cut used to separate emission from non-emission galaxies (at 5 Å) and the horizontal line is the colour cut used to separate blue and red galaxies (at 0.57 mag).

width of 5 Å. This is roughly the 2σ limit for the equivalent width measurements. It was not possible to identify the active galactic nuclei (AGN) in this sample as the optical spectra at $z = 0.37$ did not include the Hα and [NII] lines, which are required for the standard AGN diagnostic test (Baldwin, Phillips, & Terlevich 1981). In the colour–magnitude diagrams of Fig. 3.5 the [OII] emission and non-[OII] emission galaxies are plotted using different symbols. Around the cluster centre (the bottom panel of Fig. 3.5) there are few [OII] emission galaxies. For all 324 galaxies (the top panel of Fig. 3.5) the majority of the blue galaxies have [OII] emission but the red galaxies are almost evenly split between emission and non-emission galaxies. The $B - V$ colour vs. [OII] equivalent width for all the 324 galaxies used in the H I coadding can be seen in the Fig. 3.6. A trend is seen with bluer galaxies having a larger [OII] equivalent width. However there is a large amount of scatter in this relationship which is mostly due to real astrophysics variation, i.e. not due to random statistical errors.

The star formation rate for the galaxies at redshifts near Abell 370 was calculated

from the [OII]λ3727 emission line. The [OII] line flux for the galaxies was estimated using the measured equivalent width from the optical spectra and the broad-band photometry from the optical imaging. A correction for internal dust extinction in the galaxies was made to the [OII] line flux by assuming the canonical 1 mag extinction at Hα (Kennicutt 1983; Niklas, Klein, & Wielebinski 1997). This was converted to an extinction at the wavelength of [OII]λ3727 using the extinction relation of Calzetti (1997). This correction increases the [OII] flux by a factor of 5.15. The [OII] line luminosity was converted to a star formation rate using Equation (4) of Kewley, Geller, & Jansen (2004). The errors in the derived star formation rates are based on a combination of the statistical errors in the spectral line fits, the intrinsic error in the conversion from [OII] luminosity to star formation rate, and the scatter in the internal dust extinction correction which is of order 50 per cent (Kennicutt 1983). The dust correction dominates the error and limits the precision for the measured star formation rate of individual galaxies to a percentage error of at best 55 per cent. However, the average star formation rate of the galaxies can be derived with significantly higher precision, assuming the error is purely random, i.e. there are no systematic offsets.

For extended detail on the optical data reduction and analysis see Pracy et al. (2009).

3.2.4 The comparison of the properties of galaxy subsamples

In this work the Abell 370 galaxies have been broken up into a number of subsamples based on their optical colour, spectroscopic properties and location in the cluster (their galaxy environment). The galaxies are divided into optically blue and red galaxy subsamples at $B - V = 0.57$, as discussed above. Out of the 324 galaxies used in the H I coadding, there are 219 red galaxies and 105 blue galaxies. The galaxies are divided into [OII] emission and [OII] non-emission galaxy subsamples at [OII] equivalent width of 5 Å, as outlined above. Out of the 324 galaxies used in the H I coadding, there are 156 non-[OII] emission galaxies and 168 [OII] emission galaxies. An inner subsample of galaxies were selected that lay within a projected distance of 2.57 Mpc (the R_{200} radius) of the cluster centre. To remove a handful of galaxies that were clearly foreground to the cluster, galaxies in this subsample were also required to lie within 4 times the velocity dispersion of 1263 km s^{-1} of the cluster centre ($z_{cl} = 0.373$), a redshift range of $z = 0.356$ to 0.390. Using these criteria there are 110 galaxies in the inner subsample, leaving 214 galaxies in an outer subsample, distant from the cluster centre in redshift and/or projected distance.

These subsamples will be important in Section 3.5, where the H I content of each galaxy subsample is considered. Each of the Abell 370 subsamples share a number of galaxies in common. Understanding the overlap between the subsamples is critical to interpreting the different H I measurements made. The distribution of various properties for each of the subsamples is shown in Fig. 3.7.

The top panels of Fig. 3.7 shows distribution of the B band total absolute magnitude of the galaxies broken up into colour, emission type and cluster location in

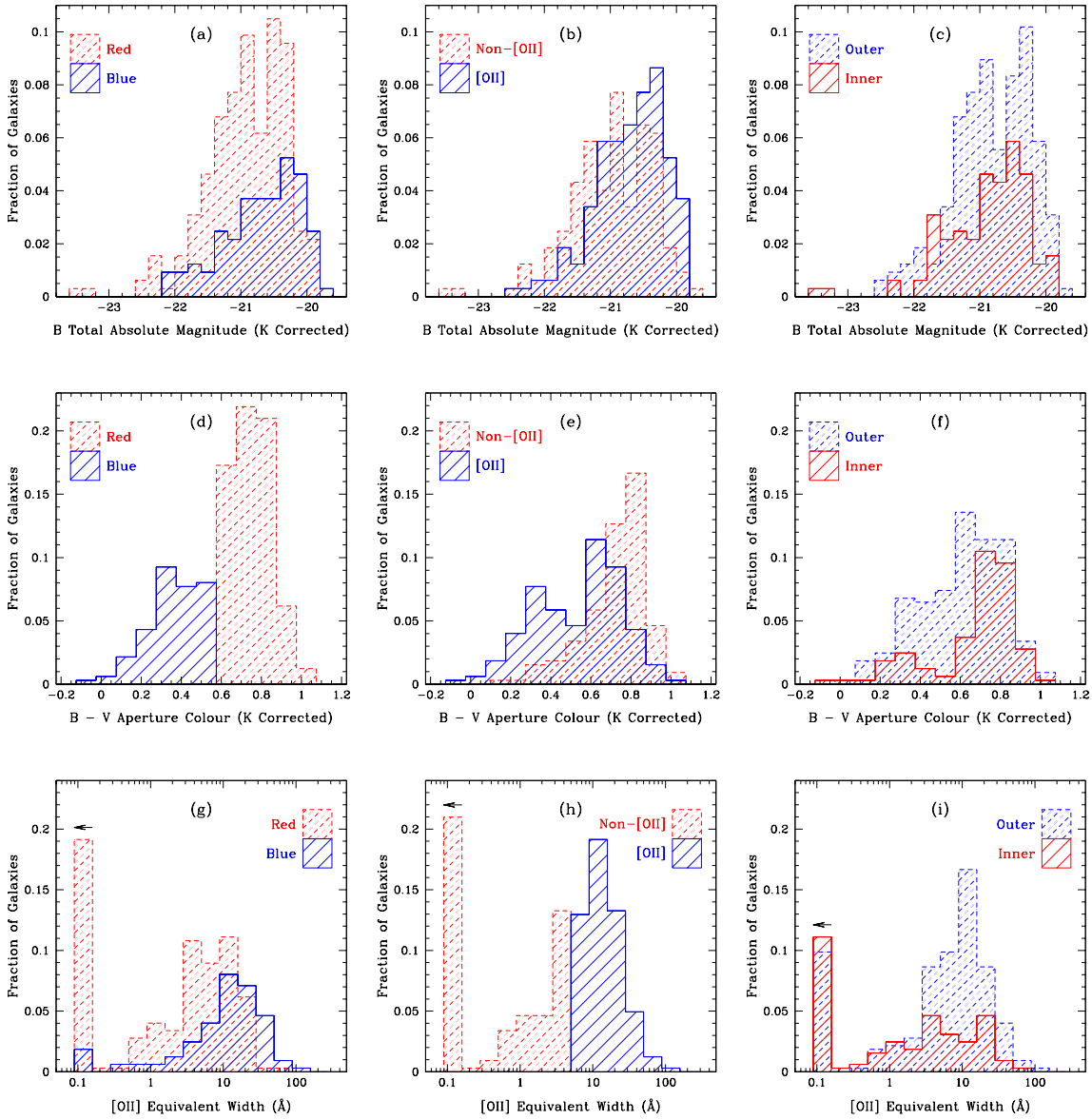

Figure 3.7: This figure shows the distribution in various parameters of the galaxies within the examined subsamples. The distributions are given as the fraction of the total number of galaxies (324). The parameters considered are the B band total absolute magnitude (top panels), the $B-V$ colour (middle panels) and [OII] equivalent width (bottom panels). The subsamples are the red and blue galaxies (left panels), [OII] and non-[OII] emission galaxies (centre panels), and the inner and outer cluster galaxies (right panels). In the bottom panels, galaxies with [OII] equivalent widths that are zero or negative have been given a value of 0.1 Å to allow them to be plotted on the log scale used. In the [OII] equivalent width histograms, these galaxies are in the last bin which is marked with an arrow on top.

the left, middle and right panels respectively. The blue galaxies, on average, tend to be slightly fainter than the red galaxies. The [OII] and non-[OII] emission galaxies span similar ranges in absolute magnitude as do the outer and inner subsamples. In this comparison the two red cD galaxies that are both brighter than -23 B band total absolute magnitude have been ignored.

The middle panels of Fig. 3.7 show the distribution of the $B - V$ colour for the galaxies broken into the different subsamples. In panel (d), which breaks the galaxies into blue and red colour, the $B - V$ colour shows only that there are considerably more red galaxies than blue galaxies. Panel (e), which displays the emission subsamples, shows that the [OII] emission galaxies span the complete colour range from blue to red. The non-[OII] emission galaxies are much more tightly grouped, with most being red in colour with only a small tail of blue galaxies. Panel (f) shows the colour distribution of the inner and outer cluster galaxies. Not surprisingly the inner sample is dominated by red galaxies while the outer galaxies have a more even distribution of colours, though there are still more red galaxies than blue galaxies (136 red to 84 blue) in the outer sample.

The bottom panels of Fig. 3.7 shows the distribution of the [OII] equivalent width of the galaxies broken into the different subsamples. Panel (g) shows the [OII] equivalent width distribution for the blue and red galaxies. While the galaxies with the very largest equivalent widths are dominated by the blue galaxies, there is a fair amount of overlap between the red and blue galaxies in the intermediate equivalent width values. Below 5 Å (the cutoff used in the [OII] samples) the galaxies are dominated by the red galaxies with the blue galaxies tailing off. Of the 168 galaxies above the 5 Å cutoff there are 87 red galaxies and 81 blue galaxies; below the cutoff there are 132 red galaxies and only 24 blue galaxies. In panel (h) the [OII] equivalent width is broken up into the [OII] emission and non-[OII] emission samples at the 5 Å value. The most common equivalent width value for galaxies with [OII] emission lies around 15 Å. Panel (i) shows the distribution of the [OII] equivalent width for the outer and inner cluster galaxies. There is a greater fraction of [OII] emission galaxies in the less dense region away from the cluster centre. This agrees with the star formation–density relationship found by Balogh et al. (1998) in clusters from $0.18 < z < 0.55$ using [OII] emission.

3.3 The Radio Data

Radio observations of the galaxy cluster Abell 370 were carried out in 2003 August 10–17 using the Giant Metrewave Radio Telescope (GMRT) in India. A total of 63 hours of telescope time was used, with 34 hours of on-source integration after the removal of the slewing time, flux and phase calibrator scans. After flagging, ∼63 per cent of the visibilities for the lower sideband and ∼50 per cent of the visibilities for the upper sideband of this on-source data remained (50 per cent of the total GMRT visibilities provides an equivalent sensitivity as an integration with ∼21 of the 30 GMRT antennas working perfectly for the entire time).

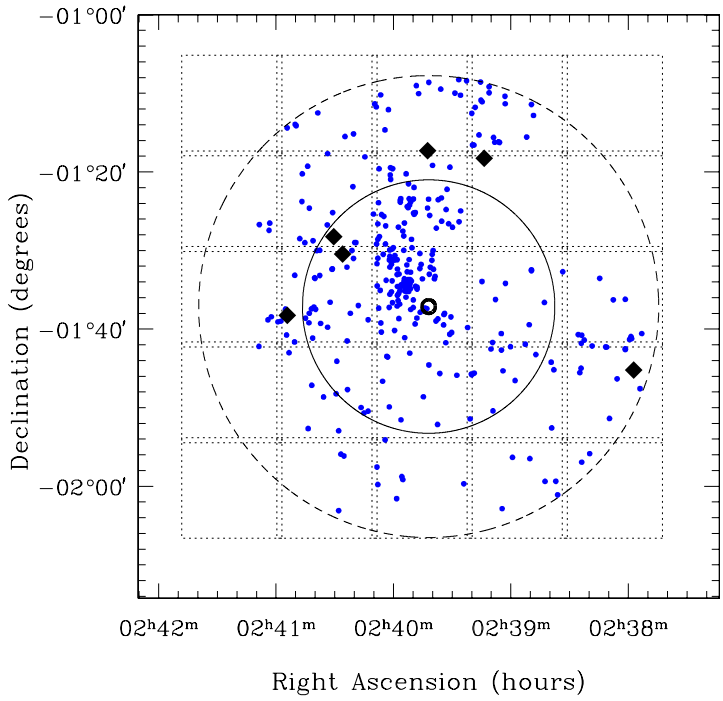

Figure 3.8: This figure shows the pointing and primary beam size of the GMRT observations with the 324 optical galaxies used in the H I coadding (the small points). The large diamond points are the radio continuum sources on which self calibration was performed. The small, bold circle is the centre of the GMRT pointing. The unbroken circle is the primary beam FWHM diameter of 32.2 arcmin and the dashed circle is the 10 per cent primary beam level with diameter of 58.8 arcmin. The dotted, overlapping, square grid shows the 25 facets used to tile the sky in the radio imaging. The centre of this grid pattern was created slightly offset from the GMRT pointing to ensure that the all of the 10 per cent level of the primary beam lay within the tiled region.

The total observing bandwidth of 32 MHz was split into two 16 MHz-wide sidebands covering the frequency range from 1024 MHz to 1056 MHz which is a redshift range $0.345 < z < 0.387$ for H I 21-cm emission. The pointing centre of the GMRT observations was R.A. $2^{\rm h}39^{\rm m}42.0^{\rm s}$ Dec. $-01°37'08''$ J2000 (see Fig. 3.8). This is 3.7 arcmin from the cluster centre. The reason for the offset was to bring the strong radio continuum source 4C -02.13 closer to centre of the GMRT primary beam and out of the sidelobes of the primary beam. The data has two polarisations and 128 spectral channels per sideband, giving a channel spacing of 0.125 MHz (36.0 km s^{-1}). Primary flux calibration was done using periodic observations of 3C48, which has a flux density at 1040 MHz of 20.18 Jy. Phase calibration was done using scans on the VLA calibrator source 0323+055 for which the observations give a flux density of 3.723 ± 0.061 Jy.

The data reduction was primarily done using AIPS. Each sideband of data was processed separately. Flux and phase calibration was determined using the bandpass calibration task BPASS, and the solution was interpolated to the data from the calibrator scans. No normalisation was done before determining the solutions. The regular phase calibrator scans throughout the observations allow one to correct for any time variability of the bandpass shape. An imaging pixel size of 0.75 arcsec and an imaging robustness value of 0 have been used. The synthesised beam size (resolution) of the data is ∼3.3 arcsec. For primary beam correction, a Gaussian beam with FWHM of 32.2 arcmin at 1040 MHz[2] was assumed.

When making continuum images only channels 11-110 (out of the 128 in each sideband) were used. In order to avoid bandwidth smearing, the visibilities were averaged into a new data set consisting of 10 channels, each of which was the average of 10 of the original channels. This new 10 channel $u - v$ data file was made into a single channel continuum image using the AIPS task IMAGR, which combined the channels using a frequency-dependent primary beam correction based on the effective antenna diameter of 37.5 m. This correction assumes that the primary beam is a uniformly illuminated disk of the specified diameter. The value of this diameter was estimated using the known GMRT primary beam size.

Self-calibration of the data was done using the 6 brightest radio continuum sources in the field. These sources have raw flux density values (not corrected for the primary beam shape) ranging from 18 mJy to 80 mJy. The self-calibration of GMRT data sometimes does not converge quickly, probably as a consequence of the GMRT hybrid configuration. Radio continuum sources that lack coherence in the synthesis image due to phase errors tend to remain defocused during self calibration. To fix this problem, slightly extended sources were replaced in the first self-calibration loop with point sources with the same centroid and flux density as the original source. Further self-calibration loops were done using the clean components in the traditional manner. The observational data for each day were initially self calibrated alone using 4 loops of self-calibration (2 loops of phase calibration and 2 amplitude and phase calibration loops). At this point the six brightest continuum source were subtracted from the $u - v$ data, and the data were flagged to exclude any visibility residuals that exceeded a threshold set by the system noise statistics. The continuum sources were then added back into that day's data.

After this detailed editing process, all the $u - v$ data were combined and self-calibration was repeated on the entire combined data set to ensure consistency between the observations on the different days. A large continuum image of the entire field was then made. The AIPS imaging routine assumes that the sky is flat (it ignores the vertical 'w' term). This is an appropriate assumption only for small fields. In order to reduce the distortion over the large field it was necessary to break the image up into 25 facets (see Fig. 3.8). Each of these square facets was 12.8 arcmin on a side (1024 pixels) and each overlapped by 38.4 arcsec. The total

[2]National Centre for Radio Astrophysics website
http://gmrt.ncra.tifr.res.in/gmrt_hpage/Users/Help/help.html

combined field size was 61.4 arcmin on each side. These overlapping facets cover the region within the 10 per cent primary beam level (58.8 arcmin in diameter). Clean boxes were put around all the discernible continuum sources during the imaging process.

In this initial continuum image, faint sidelobes from the brighter radio sources remained visible which took the form of narrow strips running north-south from the continuum sources. These are residuals from the dirty synthesised beam for the equatorial field that have not been fully removed in the cleaning process. In order to improve the quality of the image a process of peeling was used to remove the bright sources and these artifacts from the data. This involved removing all continuum sources from the $u - v$ data except for one of the bright sources. A full round of self calibration was then performed on this new set of $u - v$ data on the single bright source alone. The new calibration derived from the self calibration (its AIPS SN table) was then applied to the original $u - v$ data (the data with all the continuum sources still in it). The new model of the bright source was then subtracted from this $u - v$ data. Finally the effect of the new calibration was removed from the $u - v$ data to restore it to its previous calibration by applying the inverse SN table created using the AIPS task CLINV. This process was done for each of the six brightest sources in turn, working from east to west across the field, removing the sources from the $u - v$ data.

The final continuum image was made from this new $u - v$ data set. This image has an RMS of 20 μJy. The astrometry of the radio continuum sources in the data were checked against their positions in the VLA FIRST survey (Becker, White, & Helfand 1995). They show good astrometric agreement of -0.27 ± 0.11 arcsec in Right Ascension and 0.24 ± 0.31 arcsec in Declination. Several objects showed good alignment between their optical and radio continuum components suggesting that the optical and radio astrometry are in good agreement.

The remaining radio continuum sources were subtracted from the $u - v$ data using the AIPS task UVSUB. The final spectral data cube was made from this $u - v$ data set. While UVSUB removed most of the continuum emission, some small residuals remained. To remove these final traces, a linear fit to the continuum across frequency was subtracted in the final data cube using the AIPS task IMLIN. This introduces a small bias to the data cube, since any line emission from the galaxies would be included in the fit. The correction for this bias is described in Section 3.4. In the final data cubes, the median RMS was 152 μJy per channel in the lower sideband and 174 μJy per channel in the upper sideband.

3.4 Measuring the H I 21-cm emission signal from the Abell 370 galaxies

Directly detecting the H I 21-cm emission from even the most gas rich galaxy in the observed radio data for Abell 370 is unlikely. For a galaxy to be directly detected at 5σ significance it would need to have an H I mass of at least $M_{HI} = \sim 5 \times 10^{10}$ $M_{\odot}$, have

a velocity width of 300 km s^{-1}and the signal to be all contained within a diameter of ∼3.3 arcsec (17 kpc at $z = 0.37$). In the volume probed by the observations it is unlikely to find a galaxy with such a large H I mass. Additionally the H I gas in such a galaxy would likely extend out to a much greater diameter, making it even harder to detect in the data. A search of the radio data cube for H I direct detections was made using the DUCHAMP software developed by Matthew Whiting of the Australia Telescope National Facility. Nothing of significance was found as expected.

Instead of direct detection, the H I 21-cm emission signal from multiple galaxies has been coadded to increase the signal to noise of the measurement. This stacked signal can then be used to quantify the total H I gas content of the galaxies. The galaxies are located in the radio data using their measured optical positions and redshifts.

The expected frequency of the H I 21-cm emission from each galaxy is determined from their optical redshift. Of the 1877 optical redshifts obtained 324 are usable for H I coadding. The optical redshift distribution for galaxies around the cluster at $z = 0.37$ can be seen in Fig. 3.2. Only redshifts that lay within the H I frequency range covered by the radio data of $z = 0.3451$ to 0.3871 could be used in the coadding. The galaxies used for coadding were also limited to those inside the 10 per cent GMRT primary beam level. Redshifts that lie within 7 channels (0.875 MHz) of the boundary between the two radio sidebands (this is $z \sim 0.3658$) were also excluded. Finally redshifts that lay in the 9 channels (1.125 MHz) surrounding some strong radio interference in the lower sideband were excluded from the coadding. This strong radio interference is located at ∼1030 MHz (H I redshift $z = 0.379$).

The H I 21-cm emission signal of a galaxy is spread over a velocity width (frequency width) determined by the motion of the H I gas within the galaxy. If the gas in the galaxy is rotating in a disk, then the inclination of the disk to the observer will have a substantial effect on the observed velocity width. A rotating disk galaxy will have its largest velocity width when its disk is viewed edge on by an observer and its smallest velocity width when its disk is viewed face on. Assuming minimal H I self-absorption, galaxies with the same H I mass but different disk inclinations should have the same integrated H I flux. However the peak H I flux of these galaxies will vary greatly depending on their disk inclinations. The peak flux will be a maximum when its disk is face on, i.e. when the velocity width is at a minimum.

Assuming a random distribution of disk orientations, 50 per cent of disk galaxies will have inclinations to the observer of greater than 60° (edge on) and only 13 per cent galaxies will have inclinations less than 30° (face on). By selecting the galaxies in the optical, a higher proportion of the disk galaxies in the sample will be edge on compared to H I selected samples. This is due to a combination of this preferred orientation and because edge on galaxies have higher optical surface brightnesses making them easier to detect than face on systems. As a result of this selection effect, the galaxies in the sample with the most H I gas (the spiral disk galaxies) are likely to have large H I velocity widths. Unfortunately it is not possible to measure the inclination of the disk galaxies in the sample due to the combination of the poor seeing in the optical imaging and the small angular size of the galaxies

at redshift of $z = 0.37$.

As the H I 21-cm emission from individual galaxies is not detected, their individual galaxy velocity widths cannot be measured. Instead some reasonable assumptions are made and a velocity width is defined for the galaxies which should encompass all their coadded H I 21-cm emission signal. From the HIPASS survey (Meyer et al. 2004), a galaxy with $M_{HI} = \sim 10^9$ $M_\odot$ has a maximum velocity width of $\sim$250 km s^{-1} and a galaxy with $M_{HI} = \sim 10^{10}$ $M_\odot$ has a maximum velocity width of $\sim$400 km s^{-1}(w_{50}). Galaxies with low disk inclinations can have markedly narrower velocity widths than these maxima. Using the optical Tully-Fisher relationship from McGaugh et al. (2000) and assuming no inclination correction, the median estimated velocity width (W_{20}) based on the B band absolute magnitudes of the Abell 370 galaxies is $\sim$320 km s^{-1}.

The statistical uncertainty in the optical redshifts obtained for Abell 370 is $\sim$70 km s^{-1}. When coadding the galaxies this redshift uncertainty will broaden the resulting H I emission signal. This redshift broadening is taken into account by increasing the H I velocity width used by $\pm 2\sigma$ (280 km s^{-1}). To ensure that all the H I signal from all the combined galaxies is measured a velocity width of 600 km s^{-1} was used. This velocity width takes into account the width of the larger galaxies in the sample as well as the effect of the redshift broadening. The uncertainty due to noise in the measured coadded H I 21-cm emission signal is approximately proportional to the square root of the velocity width used. A narrower velocity width will have a smaller estimated error but will likely miss some of the H I signal.

When making the final data cube, a linear fit to the spectrum through each sky pixel was subtracted to remove the residuals left from the continuum sources (see the discussion on IMLIN in Section 3.3). Any H I signal would be included in the calculation of this linear fit across frequency and this would create an overestimation in the continuum fit, creating a bias in the final H I spectrum. To remove this bias, the H I spectrum for each galaxy has a new linear fit made across all frequency channels except those corresponding to a 600 km s^{-1} velocity width around the galaxy at its redshift (these should be the channels that would contain any H I signal). This fit is then subtracted from the data, removing any bias created by IMLIN. This correction increases the H I flux density measured in the coadded spectra of different subsample of galaxies from anywhere from 20 to 40 per cent.

Variance weighting is used when coadding the separate H I spectra. The variance is calculated from the known RMS per frequency channel in the radio data cube, factoring in the primary beam correction for galaxies away from the beam centre. Variance weighting provides the optimal signal to noise for the coadded H I signal. However it does introduce a potential bias since those galaxies located near the cluster centre are given higher weight as they are close to the GMRT pointing centre. The measured H I 21-cm emission flux density can be converted to the mass of atomic hydrogen that produced the signal by the following relation:

$$M_{HI} = \frac{236}{(\,1+z\,)} \left(\frac{S_v}{\mathrm{mJy}}\right) \left(\frac{d_L}{\mathrm{Mpc}}\right)^2 \left(\frac{\Delta V}{\mathrm{km\,s^{-1}}}\right) \tag{3.1}$$

where S_v is the H I emission flux density averaged across the velocity width ΔV and d_L is the luminosity distance to the source. This equation assumes that the cloud of atomic hydrogen gas has a spin temperature well above the cosmic background temperature, that collisional excitation is the dominant process, and that the cloud is optically thin (Wieringa, de Bruyn, & Katgert 1992). No correction for H I self absorption has been made to any of the measurements. H I self-absorption may cause an underestimation of the H I flux by as much as 15 per cent. However this value is extremely uncertain (Zwaan et al. 1997). In this analysis the galaxies were all assumed to be at the distance of the cluster centre at $z_{cl} = 0.373$, a luminosity distance of $d_L = 2000$ Mpc.

It is not possible to measure the projected extent of the H I gas on the sky for the galaxies, as their individual H I 21-cm emission is not detected. In synthesis images the peak specific intensity of a point source is equal to the total flux density of that source. This means, that if a galaxy is unresolved by the GMRT synthesised beam, one can take the value of the specific intensity at the optical position of the galaxy as a measure of the total H I flux density of the galaxy. The GMRT synthesised beam has a FWHM ∼3.3 arcsec at 1040 MHz which corresponds to ∼17 kpc at $z = 0.37$. Unfortunately all but the very smallest of the galaxies in the sample are likely to be resolved by this synthesised beam size. The solution to this problem is to smooth the radio data to larger synthesised beam sizes until the galaxies are unresolved and then measure their H I signal.

Gaussian smoothing in the image plane is equivalent to tapering (multiplying by a Gaussian) in the $u - v$ plane. This effectively reduces the weight of the longer GMRT baselines in the image plane. Thus smoothing to larger synthesised beam sizes increases the RMS noise in the radio data. However, the measured H I flux density increases for galaxies that are now unresolved in the new smoothed data. From the initial radio data with synthesised beam size ∼3.3 arcsec (∼17 kpc at $z = 0.373$), smoothed data sets were created with circular synthesised beam sizes in 10 kpc steps, i.e. equal to 30, 40, 50, 60, 70, 80, 90 and 100 kpc (5.8, 7.8, 9.7, 11.7, 13.6, 15.5, 17.5 and 19.4 arcsec). The smoothing was done with the AIPS task SMOTH. The RMS per channel in the radio data increases from ∼160 μJy at a synthesised beam size of 17 kpc (∼3.3 arcsec), to ∼280 μJy at 50 kpc (9.7 arcsec), and to ∼550 μJy at 100 kpc (19.4 arcsec).

The coadded H I 21-cm flux density for all 324 galaxies in the sample was measured in each set of smoothed data and converted to the equivalent average H I mass as seen in Fig. 3.9. In this figure the measured H I mass can be seen to rise with increasing synthesised beam size. This indicates that the H I gas extends beyond the inner regions of the galaxies that is probed by the smaller synthesised beam sizes. As the synthesised beam size increases, the error also increases making it difficult to precisely define the extent of the H I signal.

An estimate of the projected size of the H I gas in a galaxy can be used to determine the minimum synthesised beam size that would leave the galaxy unresolved. This enables a definite measurement of the total H I gas as well as reducing the error introduced by smoothing the data. An estimate of the H I size of a galaxy can

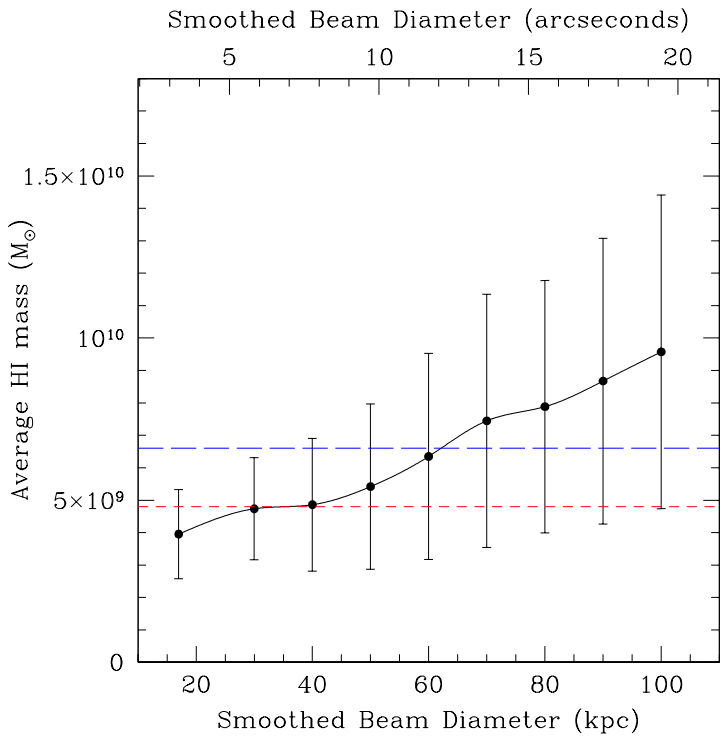

Figure 3.9: This figure shows the average H I mass for all 324 Abell 370 galaxies measured in the different smoothed synthesised beam size data. The short dashed line shows the H I mass for the mid-smoothing measurement and the long dashed line shows the H I mass for the large smoothing measurement (see text for details).

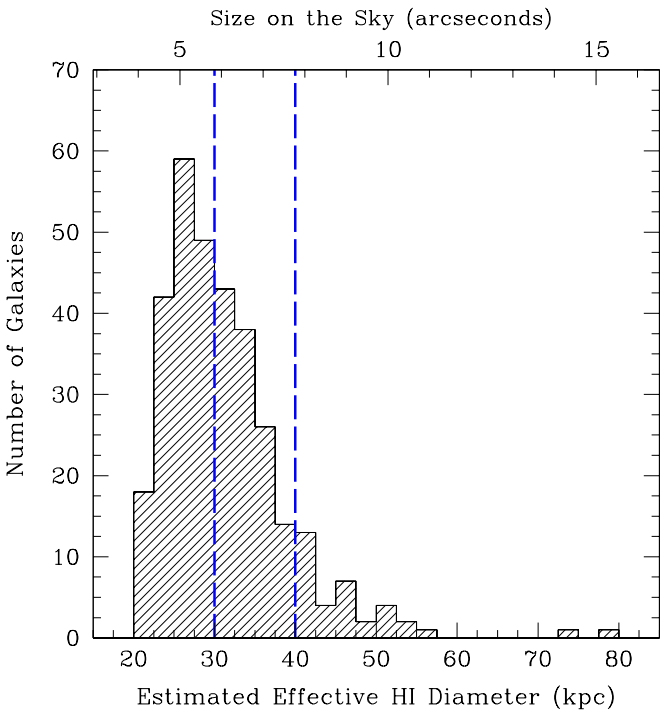

Figure 3.10: This figure shows the estimated H I effective diameter (the diameter within which half the H I mass is contained) for the 324 galaxies that are used in the H I coadding. The diameter was derived from the relationship between H I size and optical magnitude found for spiral and irregular galaxies in the field (Broeils & Rhee 1997). The dashed lines mark the values used to split the galaxies into the small, medium and large categories. The top x-axis displays the size the galaxies would appear on the sky at the redshift of the cluster ($z_{cl} = 0.373$).

be made using the correlation found between the optical B band magnitude and H I size of spiral and irregular galaxies in the field at low redshift (Broeils & Rhee 1997). This relationship is:

$$\log(D_{eff}) = -\ (0.1588 \pm 0.011)\ B_{abs}\ -\ (1.827 \pm 0.22). \tag{3.2}$$

where D_{eff} is the diameter within which half the H I mass of the galaxy is contained and is measured in kpc. Fig. 3.10 shows the distribution of the estimated effective H I diameter for the 324 galaxies around Abell 370. The galaxies are broken up into three groups based on their estimated D_{eff}. Small galaxies are defined as those with $D_{eff} \leq 30$ kpc, medium galaxies as those with 30 kpc $< D_{eff} \leq 40$ kpc and large galaxies as those with $D_{eff} > 40$ kpc. The 30 kpc value corresponds to an absolute B band magnitude of -20.8 and the 40 kpc value to -21.6. There are 168 small galaxies, 121 medium sized galaxies and 35 large galaxies in the sample.

Galaxies that have $2 \times D_{eff}$ = synthesised beam size have peak specific intensity values that are ∼90 per cent of their total flux density (assuming a Gaussian shape

to the H I gas spatial distribution). In previous coadding H I work looking at star-forming field galaxies at $z = 0.24$ (Lah et al. 2007) this was the criterion used with the estimated D_{eff} to determine the maximum synthesised beam size in which a galaxy would be unresolved. However, the relationship found by Broeils & Rhee (1997) was for spiral and irregular galaxies in the field, while the galaxies in Abell 370 are a mixture of early and late-type galaxies in a variety of environments. This criterion will likely over estimate the true extent of the H I gas for many of the galaxies.

Three different measurements of the average H I gas mass are made to reflect this uncertainty in the H I extent of the galaxies. The first coadded H I mass measurement is made by measuring the specific intensity at the optical positions of the galaxy in the original unsmoothed GMRT radio data (synthesised beam size of 17 kpc, ∼3.3 arcsec). For all 324 galaxies the measured average H I mass in this unsmoothed measurement is $(4.0 \pm 1.4) \times 10^9$ $M_\odot$. The second coadded H I mass measurement is made by first breaking the galaxies into their small, medium and large size groups based on their estimated D_{eff}. The H I flux density for each group of galaxies is then measured in the radio data that has $D_{eff} \leq$ the smoothed synthesised beam size (30, 40 and 50 kpc beam sizes). The three measured values are then combined to give a single average H I flux density. For all 324 galaxies the measured average H I mass in this mid-smoothed measurement is $(4.8 \pm 1.8) \times 10^9$ $M_\odot$. A third measurement is made similarly, except each group of galaxies is measured in the radio data that has $2 \times D_{eff} \leq$ the smoothed synthesised beam size (60, 80 and 100 kpc beams sizes). This large smoothing measurement should give an accurate reflection of the total H I gas mass for the galaxies that have similar H I extents to the field spiral and irregular galaxies observed by Broeils & Rhee (1997). For all 324 galaxies the measured average H I mass in this large smoothed measurement is $(6.6 \pm 3.5) \times 10^9$ $M_\odot$.

The top panel in Fig. 3.11 shows the weighted average H I spectrum from coadding the signal from all 324 galaxies using the large smoothing criteria. To estimate the error in the H I measurements, a series of artificial galaxies with random positions and random H I redshifts were used to create coadded random spectra. From many such artificial spectra a good estimate of the noise level in the measured real H I spectrum could be determined. As seen in Fig. 3.11, the noise level increases with increasing velocity offset from the centre of the coadded spectrum. This is because some galaxies lie at redshifts (frequencies) near the edges of the radio data cube. When adding the spectra of these galaxies to the total, there is no data for velocities that correspond to frequencies that lie off the edge of the data cube. These velocities with no data are given zero weight in the coadded sum resulting in a higher noise level at these velocities in the final coadded spectrum.

The bottom panel in Fig. 3.11 shows the coadded H I image for all galaxies after averaging the frequency channels across the velocity width of 600 $\mathrm{km\,s^{-1}}$. The radio data used for this image was that smoothed to a synthesised beam size of 30 kpc (5.8 arcsec), i.e. the galaxies have not been broken up into the groups of small, medium and large. As such, the signal to noise is not the maximum measured.

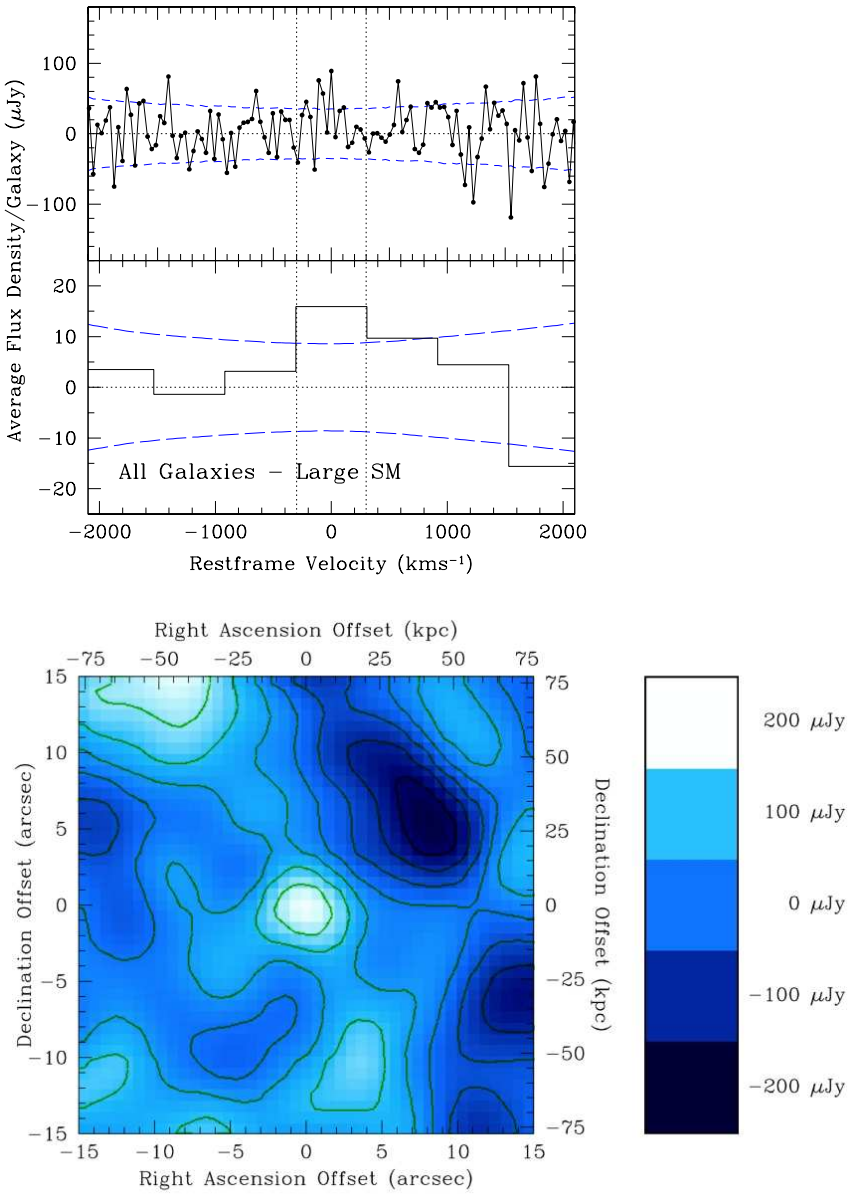

Figure 3.11: The top panel shows the average H I galaxy spectrum created from coadding the signal of all 324 galaxies using the large spatial smoothing. The top spectrum has no smoothing or binning and has a velocity step size of 36.0 km s^{-1}. The bottom spectrum has been binned to 600 km s^{-1}. This is the velocity width that the combined H I signal of the galaxies is expected to span. For both spectra the 1σ error is shown as dashed lines above and below zero. The bottom panel shows the average H I image made by coadding the data cube around each of the 324 galaxy and binning across 17 spectral channels (600 km s^{-1}). The radio data used for this image is that smoothed to a synthesised beam size of 5.8 arcsec (30 kpc at $z = 0.373$). The image size is shown in both arcsec and in kpc on opposite axes. The contour levels are -150, -100, -50, 0, 50, 100 and 150 μJy.

3.5 The H I 21-cm emission signal from subsamples of galaxies

The 324 Abell 370 galaxies used in the H I coadding are a mixture of early and late-type galaxies in a variety of environments. It is interesting to examine the average H I content of subsamples of galaxies selected by their optical colour, spectroscopic properties or location in the cluster (their galaxy environment). The definition of the major galaxy subsamples considered can be found in Section 3.2.4, which also details the overlap in their optical properties. The H I mass measurements for various subsamples of the Abell 370 galaxies can be seen in Table 3.2. The table lists three average H I masses for each subsample; these measurements are the same as used previously for all the galaxies, i.e. unsmoothed, mid-smoothed and large smoothed measurements. These average H I mass measurements are displayed in Fig. 3.12. From this figure it can be seen that there are differences not only in the quantity of the H I gas between the subsamples but also differences in where the H I gas is located within the galaxies.

3.5.1 The blue and red subsamples

The separation of the Abell 370 galaxies into optically blue and red subsamples was done using the Butcher–Oemler criterion, i.e. the blue galaxies in Abell 370 have $B - V$ colour ≤ 0.57 (see Section 3.2.3).

In the coadded signal from the 219 red galaxies the unsmoothed average H I mass measurement is $(2.8\pm1.6)\times10^9$ $M_\odot$. Measurements made using the higher smoothing criteria show no increase in the average H I mass and the higher noise in these measurements overwhelms any signal as can be seen in Fig. 3.12. These results suggest that any substantial quantities of H I gas in the red galaxies must lie within the central regions of the galaxies, i.e. closer than 8.5 kpc to the centre of the galaxies based on the unsmoothed measurement. It is likely that a fair number of these red galaxies have no H I gas. An examination of the data shows that there is no immediately obvious handful of galaxies that have the majority of this H I signal.

In contrast to the red galaxies, coadding the blue galaxies gives rise to a strong detection of H I 21-cm emission with the observed signal increasing appreciable in the higher smoothing measurements (see Fig. 3.12). This is similar to the trend seen in H I rich galaxies in the local universe, which contain large amounts of H I gas that extend beyond their visible stellar discs (Broeils & Rhee 1997). The average H I mass measured for the 105 blue galaxies using the large smoothing criteria is $(19.0\pm6.5)\times10^9$ $M_\odot$. The large smoothing criteria, which is based on the H I galaxy sizes of spiral and irregular galaxies in the field, appears to be a good fit to H I gas content of the blue galaxies.

Galaxy Sample	Selection Criteria	Number of Galaxies	HI Mass Unsmoothed (10^9 $M_\odot$)	HI Mass Mid-Smoothing (10^9 $M_\odot$)	HI Mass Large Smoothing (10^9 $M_\odot$)
All	–	324	4.0 ± 1.4 (2.9σ)	4.8 ± 1.8 (2.7σ)	6.6 ± 3.5 (1.9σ)
Red	$B - V > 0.57$	219	2.8 ± 1.6 (1.8σ)	2.6 ± 2.1 (1.2σ)	1.4 ± 4.2 (0.3σ)
Blue	$B - V \leq 0.57$	105	7.1 ± 2.7 (2.6σ)	10.0 ± 3.3 (3.0σ)	19.0 ± 6.5 (2.9σ)
Blue, Outside X-ray Gas	$B - V \leq 0.57$ & $d_{cl} > 1.45$ Mpc	94	8.0 ± 3.2 (2.5σ)	11.1 ± 3.9 (2.8σ)	23.0 ± 7.7 (3.0σ)
Non-[OII] Emission	[OII] ≤ 5 Å	156	4.3 ± 1.8 (2.4σ)	5.2 ± 2.4 (2.2σ)	2.3 ± 4.8 (0.5σ)
[OII] Emission	[OII] > 5 Å	168	3.6 ± 2.1 (1.7σ)	4.3 ± 2.6 (1.7σ)	11.4 ± 5.2 (2.2σ)
Inner	$d_{cl} \leq R_{200}$ & $z \leq 0.357$	110	3.6 ± 1.7 (2.2σ)	3.9 ± 2.2 (1.8σ)	3.3 ± 4.4 (0.8σ)
Outer	$d_{cl} > R_{200}$ or z > 0.357	214	4.6 ± 2.4 (1.9σ)	6.4 ± 3.1 (2.1σ)	12.1 ± 6.1 (2.0σ)
Within 8 Mpc	$d_{cl} \leq 8$ Mpc	220	3.6 ± 1.4 (2.6σ)	4.3 ± 1.9 (2.3σ)	5.1 ± 3.7 (1.4σ)
Blue, Within 8 Mpc	$B - V \leq 0.57$ & $d_{cl} \leq 8$ Mpc	58	8.5 ± 3.0 (2.8σ)	11.6 ± 3.7 (3.1σ)	17.5 ± 7.3 (2.4σ)

Table 3.2: This table lists the average galaxy H I mass for subsamples of the Abell 370 galaxies measured using the three different smoothed radio data combinations. The 'H I Mass Unsmoothed' is the measurement made using only the original GMRT resolution radio data. The 'H I Mass Mid-Smoothing' measurements are made by coadding different smoothed radio data such that the galaxies have estimated $D_{eff} \leq$ smoothed synthesised beam size and the 'H I Mass Large Smoothing' using $2 \times D_{eff} \leq$ smoothed synthesised beam size. In brackets next to each value is the signal to noise of the measurement. d_{cl} is the projected distance in Mpc from the cluster centre and R_{200} is 2.57 Mpc for Abell 370. The two measurements 'Within 8 Mpc' subsamples are for comparison with the Coma cluster in Section 3.6. The selection for these subsamples is more complicated than that listed above (see Fig. 3.18). See the text for further details on the subsample selection and smoothing size.

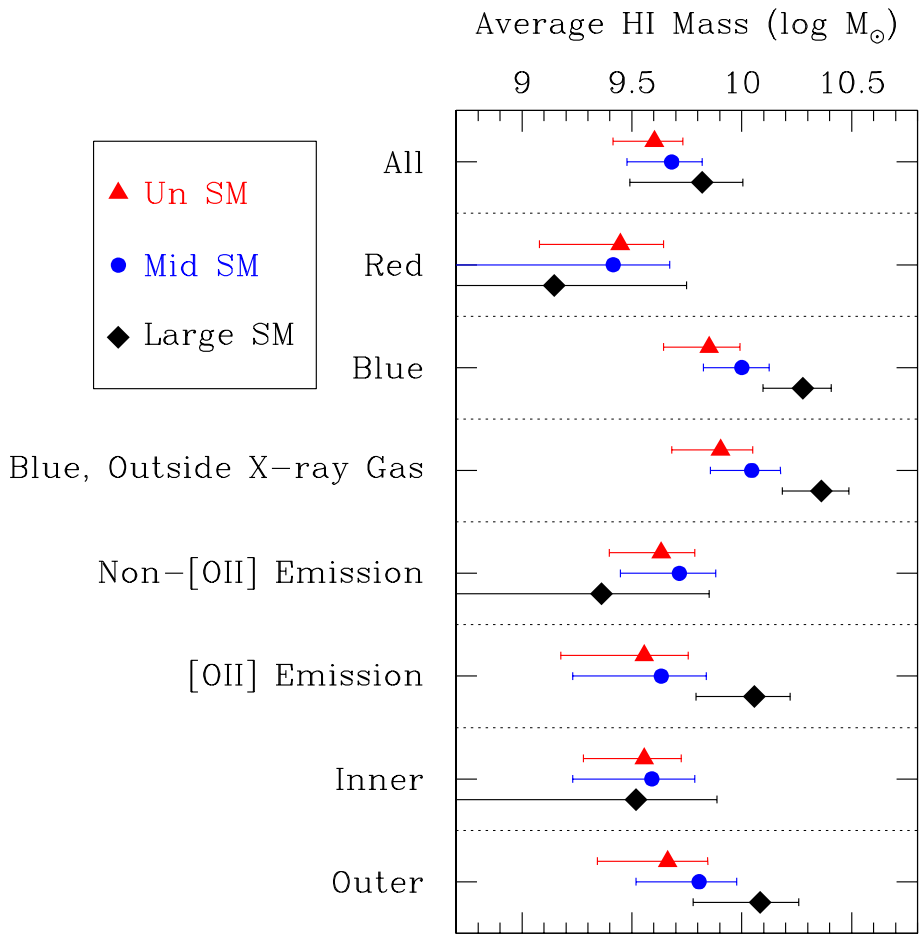

Figure 3.12: This figure displays the average galaxy H I mass for the different subsamples of galaxies measured using the different smoothed data combinations. The 'Un SM' are the Unsmoothed values, 'Mid SM' the Mid-Smoothing values and the 'Large SM' are the Large Smoothing values.

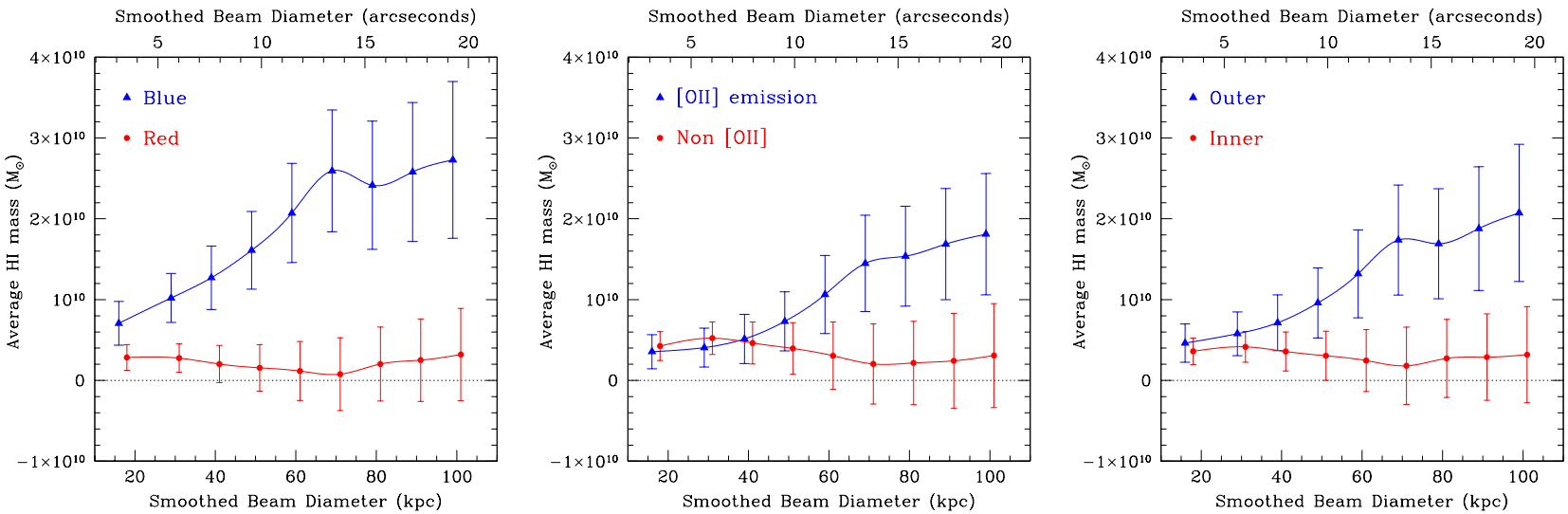

Figure 3.13: This figure shows the average H I mass as measured in the different smoothed synthesised beam size data for various galaxy subsamples. The left panel shows the blue and red subsamples, the middle panel the [OII] emission and non-[OII] emission subsamples and the right panel the inner and outer subsamples. The points in each panel for the two subsamples have been slightly offset in the x-direction to prevent obscuration by overlapping values.

The very different way the H I gas is distributed in the blue and red galaxies can be seen in greater detail in the left panel of Fig. 3.13. This figure traces the change in H I mass as a function of smoothed synthesised beam size for the blue and red galaxies, i.e. not using the galaxy size groupings. The blue galaxies show steady increase in H I gas with smoothing size until it appears to end ∼70 kpc. The red galaxies show some H I signal at the lowest smoothing sizes but the higher beam sizes appear to just add noise obscuring any signal. The coadded H I spectrum for the blue galaxies using the large smoothing criteria can be seen in panel (a) of Fig. 3.14 and the coadded H I spectrum for the red galaxies using the unsmoothed criteria in panel (d) of this figure.

In the central regions of nearby clusters, late-type galaxies are found to be H I deficient compared to similar galaxies in the field (Haynes, Giovanelli, & Chincarini 1984). One would like to see if this trend is seen in the late-type galaxies inside the hot intracluster medium of the cluster core of Abell 370 at $z = 0.37$. Assuming that blue galaxies are a representative sample of the late-type galaxies, then there are 11 such galaxies within the 3σ extent of the X-ray gas (1.45 Mpc from the cluster centre, see Section 3.2.3). Unfortunately this is an insufficient number of galaxies to coadded to enable a meaningful measurement of the gas depletion of the galaxies. The best that one can do is consider the subsample of blue galaxies outside the X-ray significance radius of which there are 94. For this subsample the average H I mass is $(23.0 \pm 7.7) \times 10^9$ $M_\odot$ using the large smoothing criteria. This is slightly larger than that found for the blue subsample as a whole and is the highest significance detection of H I 21-cm emission found in this work. The difference between this subsample and the subsample of all blue galaxies seems to be greatest in the large smoothing H I measurements; there is only a small increase in the unsmoothed and mid-smoothing values (see Table 3.2). This suggests that the blue galaxies inside the hot intracluster gas have lost H I gas in their outer regions. This is consistent with how most of the various environment mechanisms would remove the gas in galaxies (see Section 1.4). This difference in average H I mass for all 105 blue galaxies and the 94 blue galaxies outside the X-ray gas is not statistically significant but it does follow the expected trend of H I deficiency found in late-type galaxies within nearby clusters.

The top panel in Fig. 3.15 shows the weighted average H I spectrum from blue galaxies outside the X-ray gas using the large smoothing criteria. The bottom panel in Fig. 3.15 shows the coadded H I image for the same galaxies after averaging the frequency channels across the velocity width of 600 $\mathrm{km\,s^{-1}}$. This image was made using the same method as discussed in Section 3.4 for the image of all galaxies (seen in Fig. 3.11) except that data from the larger smoothed synthesised beam of 50 kpc (9.7 arcsec) was used. This was done to highlight the signal from the outskirts of the coadded galaxies which are difficult to see in the smaller beam sized data. The centre of the H I image appears ∼2 arcsec different from the centre of the optical galaxies. This is not a real astrometric difference between the radio and optical data. Instead it is an effect of the large smoothed synthesised beam size used and the contribution of a slight positive noise spike (less than 1σ) that is located away

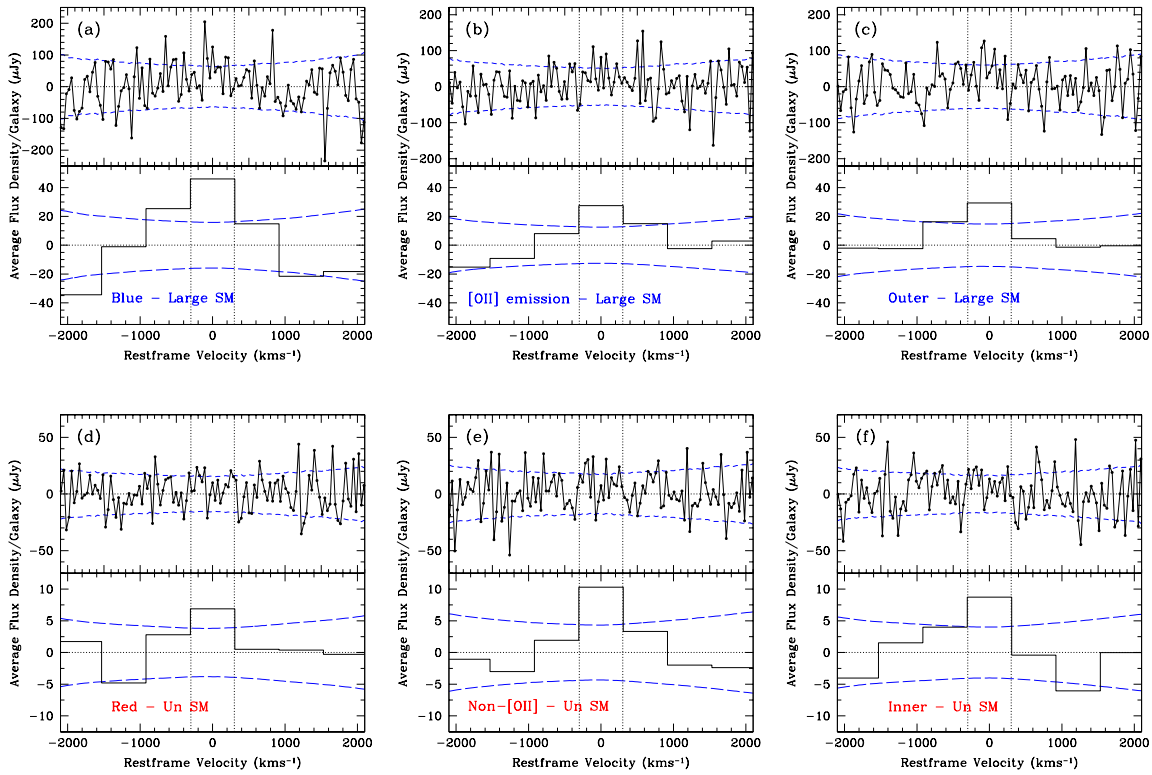

Figure 3.14: The average H I galaxy spectrum created from coadding the signal of galaxies in different subsamples. The top panels use the large smoothing criterion; the bottom panels the unsmoothed criterion. Panel (a) is for the 105 blue galaxies, panel (b) is for the 168 [OII] emission galaxies and the panel (c) is for those 214 outer galaxies (those away from the cluster centre). Panel (d) is for the 219 red galaxies, panel (e) for the 156 non-[OII] emission galaxies and panel (f) is for the 110 inner galaxies (those close to the cluster centre). In each sub-window the top spectrum has no smoothing or binning and has a velocity step size of 36.0 $\mathrm{km\,s^{-1}}$. The bottom spectrum in each sub-window has been binned to 600 $\mathrm{km\,s^{-1}}$. This is the velocity width that the combined H I signal of the galaxies is expected to span. For both spectra the 1σ error is shown as dashed lines above and below zero. Note that the y-axis scale for the top and bottom panels are substantially different.

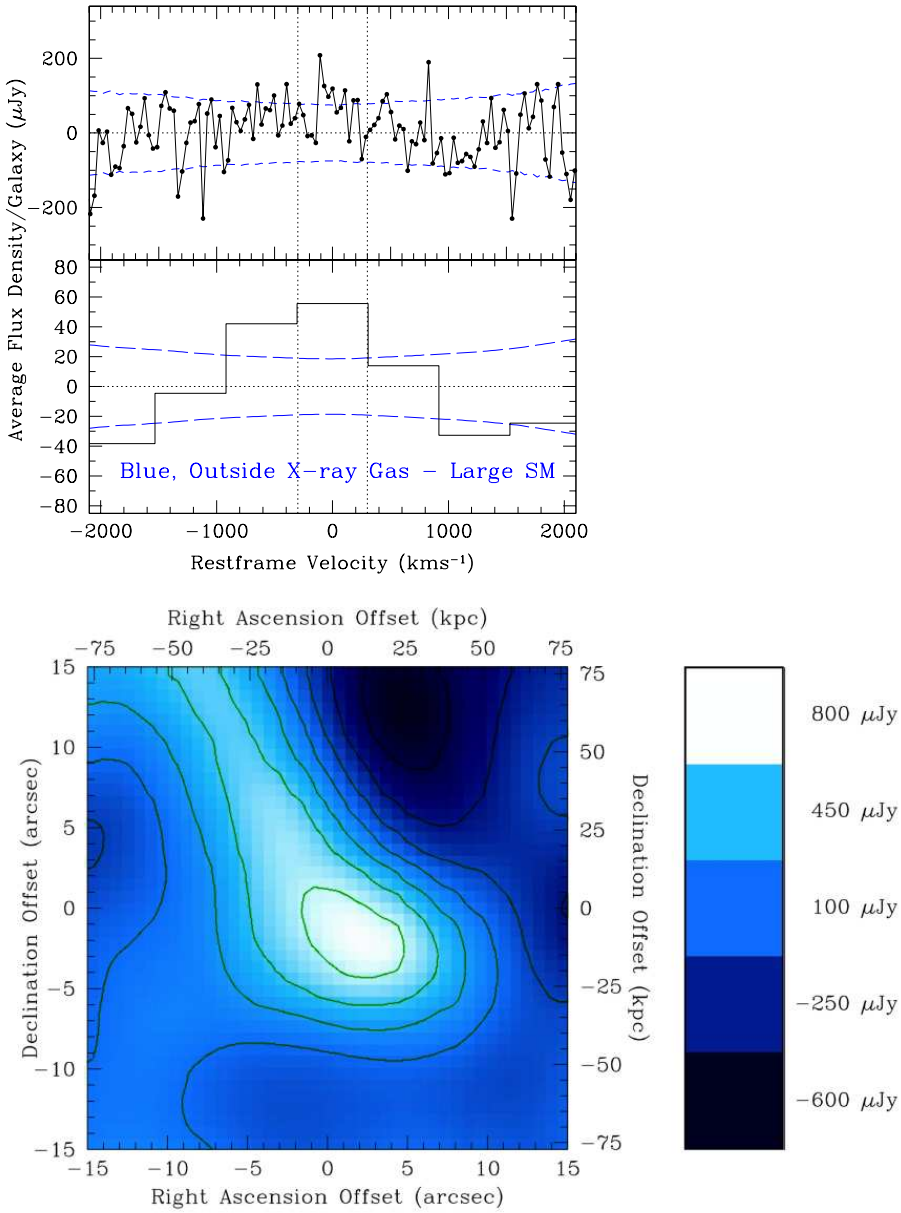

Figure 3.15: The top panel shows the average H I galaxy spectrum created from coadding the signal of the 94 blue galaxies outside the intracluster, X-ray gas using the large smoothing criteria. The top spectrum has no smoothing or binning and has a velocity step size of 36.0 km s^{-1}. The bottom spectrum has been binned to 600 km s^{-1}. This is the velocity width that the combined H I signal of the galaxies is expected to span. For both spectra the 1σ error is shown as dashed lines above and below zero. The bottom panel shows the average H I image made by coadding the data cube around each of the blue galaxies outside the intracluster, X-ray gas and binned across 17 spectral channels (600 km s^{-1}). The radio data used has been smoothed to a synthesised beam size of 9.7 arcsec (50 kpc at $z = 0.373$). The contour levels are -500, -300, -100, 100, 300, 500 & 700 μJy.

from the centre of the image. The good alignment between the optical and radio data can be seen in images made using the smallest synthesised beam size where only the H I signal from the very central regions of the galaxies is noticeable.

3.5.2 The [OII] and non-[OII] emission subsamples

Subsamples of the Abell 370 galaxies were made based on the presence or lack of the [OII]λ3727 optical emission line in their spectra. A measured [OII] equivalent width of 5 Å was used as the cut off between the emission and non–emission subsamples (see Section 3.2.3). Multiple H I mass measurements for each subsample were made, as previously, and the results are shown in Fig. 3.12. Unlike the red and blue galaxies, these two subsamples seem to have similar average H I gas masses in the inner regions of the galaxies. It is in measurements including the outer regions that a difference between the two subsamples can be seen. For the large smoothing with the [OII] emission subsample shows an increase in the average H I gas content while the non-[OII] emission subsample measurement is consistent with no increase in H I gas. The 168 [OII] emission galaxies have an average H I mass of $(11.4 \pm 5.2) \times 10^9$ $M_\odot$ using the large smoothing criteria while 156 non-[OII] emission galaxies have only $(4.3 \pm 1.8) \times 10^9$ using the unsmoothed criteria. The H I spectrum for the [OII] emission galaxies using the large smoothing criteria can be seen in panel (b) of Fig. 3.14 and the H I spectrum for the non-[OII] emission galaxies using the unsmoothed criteria in panel (e) of this figure.

The H I gas distribution in these subsamples can be seen in greater detail in the middle panel of Fig. 3.13. This figure shows the change in H I mass as a function of smoothed synthesised beam size for the [OII] emission and non-[OII] emission subsamples of galaxies. The two subsamples start out with similar average H I masses within the smaller synthesised beams, until they diverge at $\sim$50 kpc beam size. The measurements for the non-[OII] emission subsample are consistent with no increase in H I content factoring in the increasing size of the measurement errors. The [OII] emission subsample shows an increase in the H I gas content in the outskirts of the galaxies (an increase in signal in the higher beam measurements) that is similar to that seen in the blue galaxy subsample.

This similarity brings up the obvious question of how much overlap there is between the blue galaxy subsample and the [OII] emission galaxy subsample. In the [OII] emission subsample of 168 galaxies roughly half are blue and the other half red (81 blue galaxies vs. 87 red galaxies). This is the majority of the blue galaxies (there are only 24 blue galaxies in the non-[OII] emission subsample) but less than half of the total red galaxies. This shows that the [OII] subsamples are a substantially different grouping of galaxies than the blue/red galaxy subsamples (for more on the overlap of the subsamples see Section 3.2.4).

The [OII] emission galaxies were broken up further into their blue and red galaxy subsamples and the average H I mass with smoothed synthesised beam size measured as seen in the top panel of Fig. 3.16. Although this is pushing the data to its limit, a clear difference can be seen. In general the blue [OII] emission galaxies

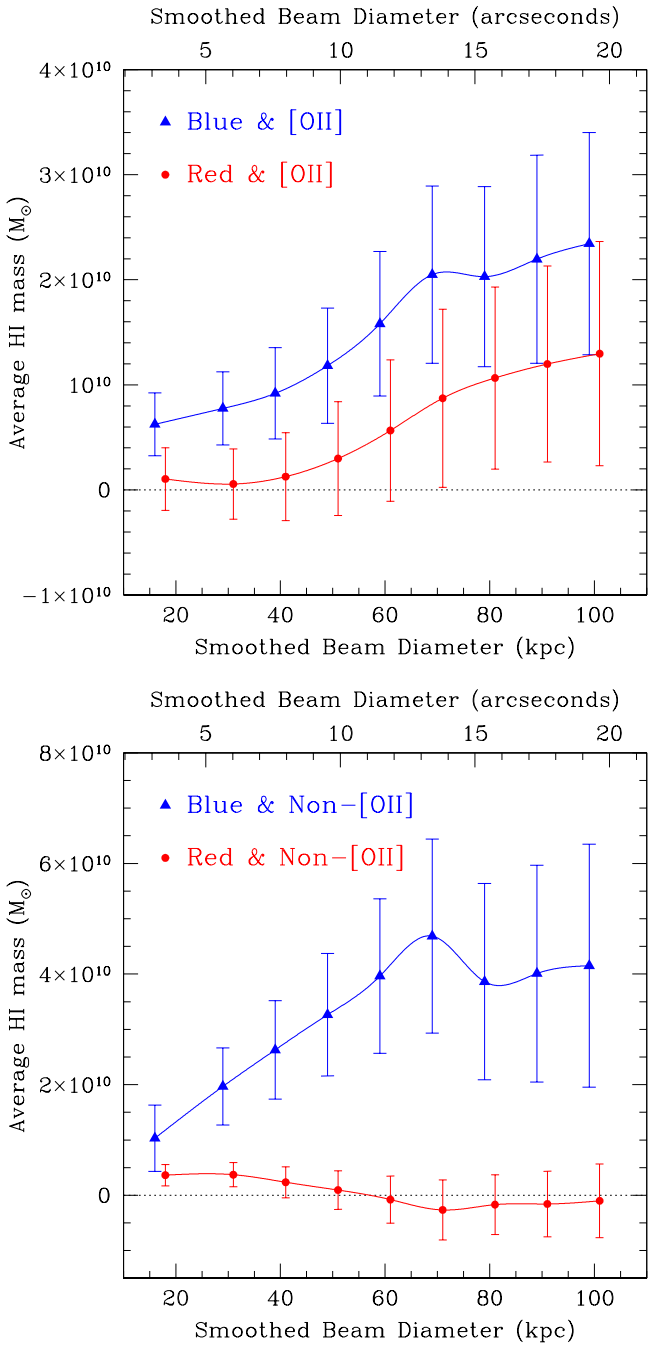

Figure 3.16: This figure shows the average H I mass measured in the different smoothed synthesised beam size data for the [OII] emission and non-[OII] emission subsamples split further into their constituent red and blue galaxies. The top panel shows the 168 [OII] emission galaxies split up into the 87 red galaxies and 81 blue galaxies. The bottom panel shows the 156 non-[OII] emission galaxies split into the 132 red galaxies and 24 blue galaxies. The points in each panel for the two subsamples have been slightly offset in the x-direction to prevent obscuration by overlapping values. Note that y-axis scale is substantially different between the two panels.

have an average H I gas content higher than the red [OII] emission galaxies. The measured H I content of both subsamples increases with increasing synthesised beam sizes. However, the red galaxies have H I gas values consistent with zero H I gas in their inner regions (the lower synthesised beam measurements). It is only as one moves to the higher synthesised beam measurements that any H I signal appears (at low significance). From this data, one could suggest that the red [OII] emission subsample are galaxies that have a large, optically bright, red bulge with little or no gas surrounded by optically faint disk containing some gas, i.e. similar to Hubble type 'Sa' galaxies. The resolution of the optical imaging is not sufficient to confirm this large bulge, small disk model for these galaxies. 'Sa' galaxies in the nearby universe have median $B - V$ colour of 0.78 (Roberts & Haynes 1994), which is consistent with the colour value for the red [OII] emission galaxies (see Fig. 3.7, the middle, centre panel).

Similarly the non-[OII] emission galaxies have been divided into their blue and red galaxies. Of the 156 non-[OII] emission galaxies, there are 132 red galaxies and only 24 blue galaxies. The average H I mass with smoothed synthesised beam size has been measured for these subsamples of galaxies as seen in the bottom panel of Fig. 3.16. The blue non-[OII] emission galaxies appear to contain substantial amounts of H I gas with an average $\sim 40 \times 10^9$ $M_\odot$, twice that found in the blue galaxies as a whole. This result should be judged with caution as this is a subsample of only 24 galaxies with large measurement errors. No single galaxy or small subgroup of galaxies in this sample dominates the measured HI signal. Of these blue non-emission galaxies only 3 lie within the R_{200} radius of the cluster. These galaxies span the complete spread of the B band total absolute magnitudes of all blue galaxies in the sample (from -22.8 to -19.9). The [OII] emission line in these galaxies could be present at a very weak level, i.e. below 5 Å. It is unlikely though, that the line is obscured completely by dust extinction internal to the galaxies. If this was the case the galaxies would show a redder colour. These galaxies could be similar to E+A galaxies that have no O and B stars to create the emission lines in HII regions but contain sufficient A and F stars to give the galaxies a blue colour. Unfortunately, for these galaxies the optical spectra is not of sufficient quality to use the Hδ and Hγ absorption features to identify whether they are E+A galaxies. The lack of [OII] emission lines suggests that the galaxies currently lack strong internal ionising radiation. Without this radiation HII gas in the galaxies could recombine to give the higher H I content. This HII gas could be gas ionised in the previous star formation period (possibly during a star-burst) or could be gas currently infalling onto the galaxy.

Although the blue non-[OII] emission galaxies appear to have a strong H I signal when considered alone, they do not dominate the total H I signal of all non-[OII] emission galaxies. The red non-[OII] emission galaxies dominate the average H I signal from all the non-[OII] emission galaxies due to their large number and their higher weight in the coadded signal, as many are located near the cluster centre and hence close to the GMRT pointing centre. In the bottom panel of Fig. 3.16, the red non-[OII] emission measurements are actually quite similar to the values found for

both the red galaxies and the non-[OII] emission galaxies as a whole (see the left and middle panels of Fig. 3.13). The red non-[OII] emission sample has a measured average H I mass of $(3.6 \pm 1.9) \times 10^9$ $M_\odot$ in the unsmoothed data, not dissimilar to both the total red subsample and total non-[OII] emission sample values (see Table 3.2).

3.5.3 The inner and outer cluster subsamples

Subsamples of the Abell 370 galaxies were made based on their location relative to the centre of the cluster. An inner subsample was formed from galaxies that fell within a projected distance of 2.57 Mpc (the R_{200} radius) of the cluster centre and in the redshift range $z = 0.356$ to 0.390 around the cluster redshift centre (see Section 3.2.4). Galaxies outside these criteria make up the outer galaxy subsample.

For these subsamples H I measurements were made as previously and the results are shown in Fig. 3.12. The inner subsample of galaxies have an average H I mass similar to the red galaxy subsample; any H I gas content they have is located in the central regions of the galaxies. The 110 inner galaxies have an unsmoothed average H I mass measurement of $(3.6 \pm 1.7) \times 10^9$ $M_\odot$. The similarity with the red galaxies is not surprising as the inner sample is dominated by red galaxies (87 out of 110 galaxies). The H I measurements for the outer subsample are similar to that seen for the blue galaxies. There is a definite H I signal from the central regions of the galaxies with an increased H I signal when including the outskirts of the galaxies. The 219 outer galaxies have an average H I mass of $(12.1 \pm 6.1) \times 10^9$ $M_\odot$ using the large smoothing criteria. The outer sample is made up of 132 red galaxies and 82 blue galaxies (this is ~80 per cent of all the blue galaxies around Abell 370). Around two thirds of the outer subsample H I signal is due to the blue galaxies with the final third coming from the outer red galaxies.

The galaxies within the inner regions of the cluster Abell 370 at $z = 0.37$ have a lower average H I mass than galaxies outside this region, following the environmental trend seen in nearby clusters. The difference in the way the H I gas is distributed in the inner and outer galaxies can be seen in greater detail in the right panel of Fig. 3.13 which traces the change in H I mass as a function of smoothed synthesised beam size for these subsamples. The H I spectrum for the outer galaxies using the large smoothing criterion can be seen in panel (c) of Fig. 3.14 and the H I spectrum for the inner galaxies using the unsmoothed criterion in panel (f) of this figure.

Any H I gas located in the inner galaxy subsample seems to be concentrated in the centre of the galaxies. The central region of a galaxy is the place where H I gas could survive for longer. Only a small percentage of the interstellar medium in a galaxy needs to be neutral to greatly reduce the ionising flux that reaches the central regions of the galaxy. Gas in the central regions would be packed into a small volume giving rise to higher gas densities. This would allow for the H I gas to recombine faster after being ionised, extending its lifetime. Additionally, H I gas in the centre of a galaxy would also be less affected by ram pressure stripping and galaxy harassment lying deep in the gravitational well of the galaxy. In fact galaxy harassment may

Galaxy Cluster	Redshift	Luminosity Distance (Mpc)	X-ray gas Temperature kT_X (eV)	Velocity Dispersion ($km\,s^{-1}$)	R_{200} (Mpc)
Abell 370	0.373	2000	7.13 ± 1.05	1263^{+99}_{-99}	$2.57^{+0.20}_{-0.20}$
Coma cluster	0.023	96.0	8.38 ± 0.34	1010^{+51}_{-49}	$2.47^{+0.12}_{-0.12}$
Abell 1367	0.022	91.3	3.50 ± 0.18	822^{+69}_{-55}	$2.01^{+0.17}_{-0.13}$
Virgo cluster	0.0036	17.0	2.20 ± 0.69	673^{+48}_{-40}	$1.66^{+0.12}_{-0.10}$

Table 3.3: The cluster properties of Abell 370 and some nearby clusters. The cluster velocity dispersion of Abell 370 is measured from the redshifts obtain in this work (Pracy et al. 2009). The luminosity distance for Abell 370 and Abell 1367 has been calculated from their redshift. For the Coma and Virgo clusters the luminosity distance is the value found in the GOLDMine database (Gavazzi et al. 2003). The X-ray temperature data and other velocity dispersion measurements are from the compilation by Wu, Xue, & Fang (1999). The R_{200} values are calculated from the velocity dispersions.

actually encourage gas in the outskirts of a galaxy to move towards the centre of the galaxy. In the simulations of Moore et al. (1996), galaxy harassment had the effect of stripping ∼10 per cent of a galaxy's gas content while the other 90 per cent of the gas sank to the inner few hundred parsecs. Such an effect could be important in creating the H I gas distribution seen in the Abell 370 galaxies.

3.6 Comparison of the H I measurements with the literature

Abell 370 is a large galaxy cluster with a velocity dispersion of 1263 ± 99 $km\,s^{-1}$. In the nearby universe, there are few galaxy clusters of this size, which limits the available literature H I 21-cm emission observations for direct comparison. Table 3.3 lists the cluster properties of Abell 370 and three nearby clusters that have extensive H I observations. Abell 370 and the nearby Coma cluster have similar cluster velocity dispersions and similar X-ray gas temperatures for the hot intracluster gas in their cores. This indicates that the two clusters have similar total masses, assuming that they are both dynamically relaxed. Coma and Abell 370 are also similar in that they both have two cD galaxies rather than the usual one seen in rich clusters. Abell 370 is substantially more massive than the two other clusters listed in the table, Abell 1367 (also known as the Leo cluster) and the Virgo cluster. Detailed comparisons of the H I gas content in Abell 370 and these clusters are discussed below.

3.6.1 H I density

It is necessary to compare the H I measurements of the galaxies in Abell 370 with local samples in order to quantify any evolution in the H I gas over the past ∼4 billion

years (since $z = 0.37$). One way to quantify the gas evolution in Abell 370 is to compare the H I density around the cluster with values from the literature. The H I densities calculated for a variety of subsamples and volumes around Abell 370 along with various literature values can be found in Table 3.4 and can be seen plotted in Fig. 3.17. The H I density in a volume can be calculated using:

$$\rho_{\,\mathrm{HI}} = \frac{n_{gal}\,\overline{\mathrm{M}}_{\mathrm{HI}}}{V}, \tag{3.3}$$

where $\rho_{\,\mathrm{HI}}$ is the H I density, n_{gal} is the number of galaxies being considered, $\overline{\mathrm{M}}_{\mathrm{HI}}$ is the average H I mass measured for these galaxies, and V is the volume in which these galaxies are contained. The comoving volume containing all 324 Abell 370 galaxies was calculated from the extent of the optical imaging (see Fig. 3.1) and the redshift range spanned by the galaxies. The total area on the sky of the optical imaging after accounting for the removal of the exclusion regions (see Fig. 3.1) is 0.776 deg^2. Not all this area has uniform optical sampling which may cause a slight underestimate of the H I densities measured. Taking into account the limits placed by the GMRT 10 per cent beam level, the area on the sky containing the galaxies with H I measurements is 0.668 deg^2. The H I frequency range of the GMRT observations spans from $z = 0.345$ to 0.387. Using these values, the total comoving volume of the Abell 370 H I measurements is 62300 Mpc^3. The volume is much longer in the redshift direction than in projected distance on the sky (at most ∼15 Mpc across compared to 148 Mpc deep).

Using this volume, an H I density of $(0.034 \pm 0.018) \times 10^9$ M$_\odot$ Mpc^{-3} is found using all 324 Abell 370 galaxies. The H I density in this volume due to just the 105 blue galaxies is $(0.032 \pm 0.011) \times 10^9$ M$_\odot$ Mpc^{-3}. This almost equals the density calculated for all the galaxies, indicating that most of the H I gas around the cluster is located in the blue galaxies. In contrast, the H I density due to just the 219 red galaxies is $(0.0098 \pm 0.0056) \times 10^9$ M$_\odot$ Mpc^{-3}. The blue and red galaxy values do not sum exactly to give the H I density from all galaxies due to the weighting schemes used when measuring the H I gas. The H I density measured using only the 168 [OII] emission galaxies is $(0.031 \pm 0.014) \times 10^9$ M$_\odot$ Mpc^{-3}. This is similar to that found for the blue galaxies, which shows that this sample also selects the majority of the H I gas in galaxies within this volume.

The H I density measurements listed above only include the H I gas contained in the known Abell 370 galaxies; they do not take into account the many 'missing', optically fainter galaxies in the volume that may contain H I gas. As such, these measurement are only lower limits on the total H I density in the volume. These previous measured values have been scaled up to an estimate of the total H I density in the volume. This is done by assuming that the optical luminosity density of the galaxies is proportional to their H I density. The optical luminosity density in the B band for the galaxies in each Abell 370 galaxy sample was measured. For each of the galaxy samples a Schechter function fit using χ^2 minimisation was made to their magnitude distribution. In this function fitting, the faint end slope of the luminosity function, α, was set at 1.35 ± 0.10 because the Abell 370 B band magnitudes do not

Galaxy Sample	H I Gas Density (10^9 $M_\odot$ Mpc^{-3})	Volume (Mpc^3)	Number of Galaxies
Abell 370 Samples			
All Galaxies	0.034 ± 0.018	62300	324
Blue Galaxies	0.032 ± 0.011	62300	105
[OII] Emission Galaxies	0.031 ± 0.014	62300	168
Red Galaxies	0.0098 ± 0.0056	62300	219
All Galaxies - *Extrapolated* ($\times 2.18 \pm 0.58$)	0.075 ± 0.044	62300	324+
Blue galaxies - *Extrapolated* ($\times 2.13 \pm 0.61$)	0.068 ± 0.030	62300	105+
Inner Galaxies	5.6 ± 2.6	71	110
Galaxies within 8 Mpc	0.53 ± 0.38	2140	220
Blue Galaxies within 8 Mpc	0.47 ± 0.20	2140	58
Literature Samples			
Cosmic Density z = 0: H I 21-cm (Zwaan et al. 2005)	0.0510 ± 0.0083	-	4315
Cosmic Density z = 0.24: H I 21-cm (Lah et al. 2007)	0.095 ± 0.044	-	121
Cosmic Density z $\sim$ 0.6: DLAs (Rao, Turnshek, & Nestor 2006)	0.100 ± 0.037	-	18
Cosmic Density z $\sim$ 3.7: DLAs (Prochaska, Herbert-Fort, & Wolfe 2005)	0.111 ± 0.018	-	89
Virgo cluster within 2.5 Mpc (GOLDMine)	2.23 -	65	252
Abell 1367 within 2.5 Mpc (Cortese et al. 2008)	1.066 ± 0.019	65	36
Coma cluster within 2.5 Mpc (GOLDMine)	0.74 -	65	22
Coma cluster within 8 Mpc (GOLDMine)	0.066 -	2140	42

Table 3.4: This table lists the H I gas density measured in different subsamples of galaxies around Abell 370, including extrapolations to the total H I density. Included in the table are also a number of literature values for the cosmic H I gas density at a few different redshifts and the H I gas density found in nearby galaxy clusters. The volume for which the H I density is measured is listed where relevant.

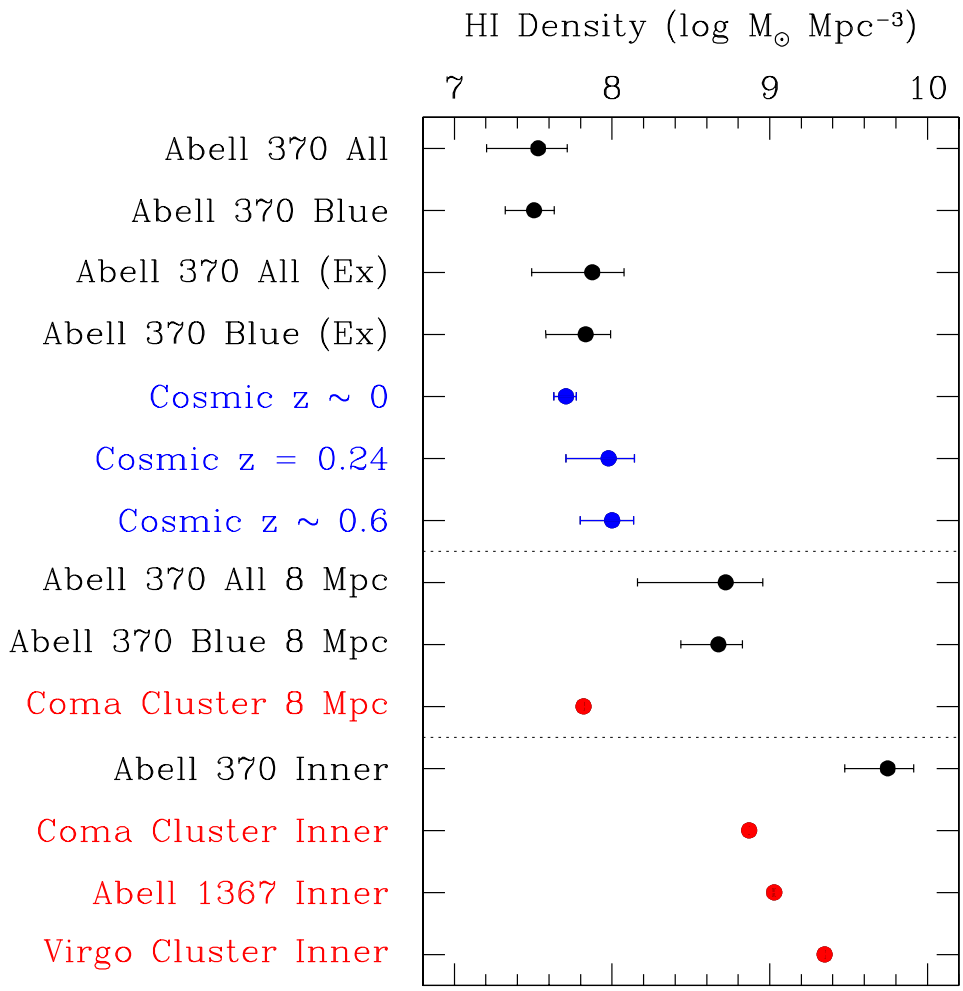

Figure 3.17: This figure shows the measured H I gas density around Abell 370 for various subsamples and that found in a variety of literature samples. The figure is divided into three parts by faint dashed lines. The top part shows measurements made from the total volume sampled around Abell 370 in this work. It includes the H I density measured from just the known Abell 370 galaxies as well as extrapolations to the total H I density in the volume (the 'Ex' values). Also shown in the top part are cosmic H I density values at variety of redshifts. The middle part shows the H I density within 8 Mpc of the cluster centre of Abell 370 and a similar sized volume around the nearby Coma cluster. The bottom part shows the H I density within ~2.5 Mpc of the cluster centre of Abell 370 and in similar volumes within nearby galaxy clusters.

extend faint enough to allow an accurate determination of this parameter. This α value is based on literature results for H I galaxies in HIPASS (Zwaan et al. 2005) and optical cluster galaxies in the 2dFGRS (De Propris et al. 2003). The fitted Schechter functions were integrated over all magnitudes to create an estimate of the total optical luminosity density of the galaxies. The H I density for each galaxy sample was then scaled up by the ratio of this total optical luminosity density to the optical luminosity density measured from just the galaxies in the sample. These total H I density estimates are the extrapolated values listed in Table 3.4 and are shown in Fig. 3.17. The value of this ratio is listed in brackets in the table, next to the sample name.

Also measured was the H I density for the 110 inner galaxies in Abell 370, i.e. the H I density within the cluster core. When calculating the inner density the average H I mass from the unsmoothed measurement was used because this has the highest precision and appears to contain the total H I signal for these galaxies (see Section 3.5.3). The galaxies in this inner subsample span a projected distance on the sky of R_{200}= 2.57 Mpc from the cluster centre and a redshift range of $z = 0.357$ to 0.387, a cosmological distance of 106 Mpc. However, these galaxies close to the cluster core have large peculiar motions. As such, the majority of these galaxies are likely to span a much smaller distance in the redshift direction than that indicated by this direct cosmological distance conversion. A reasonable assumed distance that the majority of the inner galaxies would span in the redshift direction would be 2.57 Mpc, i.e. similiar to the galaxies projected distance on the sky. This is the physical volume spanned by the galaxies which should remain unchanged with time in this gravitationally bound region. Using this value, the volume probed is 71 Mpc^3, which makes the H I density in this region $(5.6 \pm 2.6) \times 10^9$ $M_\odot$ Mpc^{-3}.

The H I density measured for the inner subsample is substantially greater (more than 50 times higher) than even the extrapolated H I densities measured for the other galaxy samples in Abell 370. Even though the galaxies in the cluster core may have lower H I gas content than similar galaxies in the field, they are packed into a very small volume, dramatically raising the H I density measured there. Galaxies in field environments may have more H I gas per galaxy but they are spread over larger volumes reducing the H I density found there.

In order to make a comparison with the nearby galaxy cluster of Coma, a sample of galaxies within 8 Mpc of the cluster centre of Abell 370 was selected. Fig. 3.18 shows the redshifts of the Abell 370 galaxies plotted against their projected distance from the cluster centre. Galaxies close to the cluster core have larger peculiar velocities than those further out. Using this fact, an envelope was drawn on the figure consisting of smoothly varying curves that is the locus boundary for those galaxies likely to lie within 8 Mpc of the cluster centre; these are the 220 circular points in Fig. 3.18. These galaxies are assumed to all lie within the 8 Mpc radius sphere centred on the cluster core with physical volume 2140 Mpc^3 (again the volume spanned by these galaxies should remain relatively unchanged with time in this gravitationally bound region). The average H I mass measured for these galaxies is listed in Table 3.2, as is the value for the subsample of 58 blue galaxies within

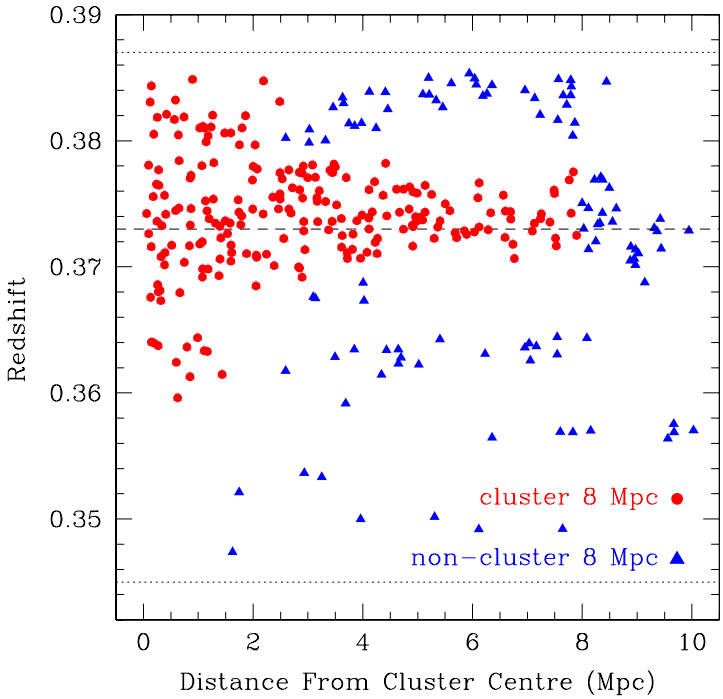

Figure 3.18: This figure shows the redshift vs. projected distance from the cluster centre for all 324 galaxies used in the H I coadding. The circular points are those galaxies expected to lie within 8 Mpc of the cluster centre both in projected distance and in the redshift direction after taking into account the galaxies peculiar motion. The triangular points are those galaxies expected to lie further away than 8 Mpc. The two dotted lines are the frequency limits of the GMRT and the dashed line is the redshift of the cluster centre.

this selection. Using the large smoothing average H I mass measurement of all 220 galaxies, an H I density of $(0.53 \pm 0.38) \times 10^9$ $M_\odot$ Mpc^{-3} is found (this is the value plotted in Fig. 3.17 and listed in Table 3.4). Using the unsmoothed average H I mass measurement, an H I density of $(0.37 \pm 0.14) \times 10^9$ $M_\odot$ Mpc^{-3} is found, which has substantially higher signal to noise. If one considers only the 58 blue galaxies in this region, using their average H I mass large smoothing measurement, an H I density of $(0.47 \pm 0.20) \times 10^9$ $M_\odot$ Mpc^{-3} is found. This is comparable to that measured for all 220 galaxies in the selection 8 Mpc radius region which suggests that again it is the blue galaxies that contain the majority of the H I gas within this volume.

The first set of literature values listed in Table 3.4 are H I gas cosmic density values at a variety of redshifts. These values were all converted to H I densities; some were published as neutral gas densities and included a correction for the neutral helium content. The first value listed is the $z = 0$ cosmic H I density as measured in the HIPASS survey (Zwaan et al. 2005) using H I 21-cm emission from a large sample of galaxies across the entire southern sky. The second value is the H I density

measured in a sample of star-forming galaxies at $z = 0.24$ using coadded H I 21-cm emission (Lah et al. 2007). The other two values are from damped Lyman-α measurements, looking at the H I absorption in quasar spectra in the rest-frame ultraviolet. The lower redshift value is from damped Lyman-α absorbers at redshifts $z \sim 0.6$ (redshift range $z = 0.1$ to 0.9) that have been optically selected to have MgII absorption, before being followed up in the ultraviolet with the *Hubble Space Telescope* (Rao, Turnshek, & Nestor 2006). The $z \sim 3.7$ (redshift range $z = 3.5$ to 4.0) value has been measured from optical spectra of quasars primarily from the Sloan Digital Sky Survey (the Lyman-α absorption is redshifted into the optical at these redshifts) (Prochaska, Herbert-Fort, & Wolfe 2005).

The listed cosmic H I density values beyond redshift $z = 0$ are similar. They are all around 0.10×10^9 $M_\odot\,Mpc^{-3}$, which is twice the H I density at $z = 0$. The $z = 0.24$ and $z \sim 0.6$ value are the cosmic density measurements which are closest in redshift to Abell 370 at $z = 0.37$. They are plotted with the $z = 0$ in the top part of Fig. 3.17. The $z \sim 3.7$ DLA value is the highest H I cosmic density value as currently measured. The H I density measured in the larger volume samples of Abell 370 galaxies are slightly less than the H I cosmic density found at $z = 0$ (see the top part of Fig. 3.17). However the extrapolated H I density values are comparable to the H I cosmic density found at $z = 0.24$ and $z \sim 0.6$. The errors in these measurements make it difficult to determine if there has been any substantial evolution in the H I gas in galaxies from these values. Indeed it is probably not fair to compare the H I density found in this large volume around Abell 370 to the cosmic density as the volume considered is unusual in the universe with a considerably higher galaxy density than the average. Additionally the extrapolation used to scale up the H I gas density is highly uncertain particularly in the inner regions of the cluster where the high galaxy density would probably effect the smaller galaxies gas content more significantly than the larger galaxies. To do a fair test for evolution it is necessary to compare the measured H I density around Abell 370 to nearby volumes with similarly high galaxy densities.

The second set of literature values listed in Table 3.4 are derived from H I density values for three nearby galaxy clusters. The first value is for the Virgo cluster which has H I observations from Gavazzi et al. (2005) which are available from the GOLDMine database (Gavazzi et al. 2003). These include targeted observations of all late–type galaxies with $m_p \leq 18.0$ magnitude, which at the distance of the cluster is more than 6 magnitudes fainter than the Abell 370 observations. There are 252 galaxies with H I measurements within a radius 2.5 Mpc in the inner regions of the Virgo cluster. For this volume, an H I density of 2.23×10^9 $M_\odot\,Mpc^{-3}$ was measured. This measurement is a lower limit as it does not include a correction for any missing galaxies. However it is likely to be close to the total H I density as it contains the majority of the galaxies with significant H I gas content.

The second galaxy cluster considered is Abell 1367 which has H I observations from the Arecibo Galaxy Environment Survey (AGES), a blind H I survey (Cortese et al. 2008). Using this data, the H I density within a radius 2.5 Mpc around the cluster centre was measured. Galaxies were included in this volume if they lay with

the 2.5 Mpc projected distance of the sky of the cluster centre and had redshifts between 4000 km s^{-1} and 9000 km s^{-1}. There are 36 galaxies with H I measurements not contaminated by RFI in this region which gives an H I density of $(1.066 \pm 0.0192) \times 10^9$ M$_\odot$ Mpc^{-3}.

The third galaxy cluster considered is the Coma cluster. The H I observations came from Gavazzi et al. (2006) and are compiled with optical data in the GOLDMine database (Gavazzi et al. 2003). The H I observations include 94 per cent of all late–type galaxies with apparent magnitude $m_p \leq 15.7$ mag in the Coma supercluster (a much larger region surrounding the Coma cluster). This magnitude limit is equivalent to B band absolute magnitude of $\sim$−19.2 at the distance of Coma cluster (the faintest Abell 370 galaxy is -19.7). The H I density was measured around the Coma cluster centre out to a radius of 2.5 Mpc and 8 Mpc. A radius of 8 Mpc is the maximum projected distance from the Coma cluster with good observations (there were insufficient H I observations to make similar 8 Mpc measurements for Abell 1367 and the Virgo cluster). The inner 2.5 Mpc radius region of the Coma cluster has an H I density of 0.74×10^9 M$_\odot$ Mpc^{-3} from 22 H I galaxies. The larger 8 Mpc radius region of the Coma cluster has an H I density of 0.066×10^9 M$_\odot$ Mpc^{-3} from 42 H I galaxies.

The inner values for Abell 370 and the three literature clusters are shown together in the bottom part of Fig. 3.17. These inner samples all come from similar sized volumes, spheres with radii $\sim$2.5 Mpc. The R$_{200}$ radii for Coma and Abell 370 are close to this value but Abell 1367 has an R$_{200}$ radius of $2.01^{+0.17}_{-0.13}$ Mpc and the Virgo cluster of $1.66^{+0.12}_{-0.10}$ Mpc (see Table 3.3). The H I density within the R$_{200}$ radii for these two smaller clusters is almost twice as high in both cases. As can be seen in bottom part of Fig. 3.17 in the nearby cluster values, the H I density increases with decreasing cluster size. The H I density in the inner Coma region is 3 times smaller than that found in the smaller irregular Virgo cluster, with the H I density of Abell 1367 in between. This clearly shows the known trend in the nearby universe, that H I gas in galaxies is lower in high galaxy density environments. The H I density found for Abell 370 is 3 ± 1 times higher than that found in Virgo and 8 ± 4 times higher than that found in Coma, a similar sized cluster. This is not evidence against the trend of H I gas in galaxies being lower in high galaxy density environments. This trend is seen for the Abell 370 galaxies when comparing the inner and outer subsamples (see Section 3.5.3). Rather this high H I density value found in the inner regions of Abell 370 compared to nearby clusters is an indication that there has likely been substantial evolution in the gas content of galaxies in clusters over the last $\sim$4 billion years since $z = 0.37$.

Similarly, the region within 8 Mpc of the centre of Abell 370 has an H I density that is 8 ± 6 times higher than the similar size region around Coma or 7 ± 2 times higher considering only the Abell 370, blue galaxies in this region. This is a statistically significant difference as can be seen in the middle part of Fig. 3.17 (the Coma value has no discernible random error). As Coma and Abell 370 are galaxy clusters of similar size, this is again evidence of substantial evolution in the gas content of cluster galaxies between redshift $z = 0.37$ and the present.

In order to ensure that the striking differences between the H I densities found for the Coma cluster and Abell 370 are real one must ensure that there is no significant biases on the measurements that could be distorting the result. The Coma H I gas measurements come from targeted observations rather than a blind H I search of the cluster. As such, it is not impossible that an appreciable fraction of the H I gas in galaxies within the cluster has been missed. This is unlikely though, as all the optically bright late-type galaxies have been observed and these are likely to be the dominate contributors to the H I density. Even if including the missing low H I mass galaxies raises the H I density in Coma by a factor of two there is still considerably more gas found around Abell 370. The unaccounted for gas due to these smaller galaxies is unlikely to be anywhere near as substantially as this particular as these galaxies with lower total galaxy masses will have a harder time holding onto their gas against the high density environmental mechanisms such as ram pressure stripping. Additionally it is likely that appreciable amounts of the H I gas is missing in the Abell 370 volumes due to the relatively bright optical magnitude limit of this galaxy sample.

The optical imaging of Abell 370 does not extend fully out to a projected radius of 8 Mpc in all directions as seen in Fig. 3.4. This will result in missing some galaxies within this volume causing a small underestimation of the H I density in this volume. To select the Coma and Virgo galaxies the distances in the GOLDMine database were used. These distances have had the effect of the peculiar velocities of the galaxies removed, allowing one to select the galaxies close to the cluster centres. If these distances are incorrect for a large number of galaxies, then this could result in an underestimation of the true H I densities in these clusters. However, this is unlikely as the distances appear quite reasonable based on their redshift and spatial distribution on the sky. The literature values for the clusters included H I flux upper limits for a number of galaxies. These galaxies were considered to have no gas when doing the density calculations. They are unlikely to contain sufficient gas to significantly effect the results.

Ideally one would want deep H I blind observations of a number of large galaxy cluster at low redshift to compare with the Abell 370 observations. Such published data do not exist as yet. Due to the uncertainties on the current galaxy samples of both Abell 370 and the low redshift clusters it is difficult to say with precision the amount of difference in the H I densities. However, from the measurements it is clear that Abell 370 has considerably more gas than local clusters suggesting there has been substantial evolution in the gas content in clusters over the last 4 billion years.

The H I density of Abell 370 is markedly larger than that found in the Coma cluster in the regions considered. The H I gas density in Abell 370 is up to 8 times higher than in Coma. The increase in the cosmic H I density from $z = 0$ to the largest known values at higher redshifts is at most a factor of two (see Table 3.4). If Abell 370 were to evolve into a gas poor system like Coma in $\sim$4 billion years, then the rate of decrease in the gas would be considerably faster than the rate of decrease seen in the field. This higher rate of decrease in gas content could be

caused by the combination of the higher rate of galaxy-galaxy interactions in the cluster environment and the interactions between the interstellar medium (ISM) of the galaxies with the intergalactic medium (IGM) of the cluster which is denser than the IGM of the field.

3.6.2 Average H I mass comparisons with the Coma cluster

Comparing the H I measurements of the galaxies in Abell 370 directly with local samples is difficult, primarily due to the unusual way in which the Abell 370 measurements were made, i.e. by coadding the H I 21-cm emission signal from multiple galaxies. One way of doing this comparison is to make similar coadded average H I mass measurements in nearby clusters using literature H I 21-cm emission values. To do this one needs a complete sample of the optical galaxies in a nearby cluster down to the magnitude limits of the Abell 370 galaxy sample. Additionally one needs to know the H I mass for each of these optical galaxies. Each galaxy in the Abell 370 sample can then be randomly matched to a literature galaxy in the nearby cluster with similar absolute optical magnitude. The average H I mass of this randomly matched sample of literature galaxies can then be calculated. This can be repeated multiple times, each time taking different randomly matched samples. The different random samples are then combined to give a robust measure of the average H I mass for a sample of galaxies with similar optical magnitude distributions to the Abell 370 galaxies. The variation between the different random samplings provides an estimate on the error in this measurement.

This comparison was done using galaxies in the nearby Coma cluster as the GOLDMine database contains both optical and H I observations for the galaxies (Gavazzi et al. 2003) (See above for details on this galaxy sample). Each galaxy in the Abell 370 sample was matched to a random Coma galaxy with B band absolute magnitude within 0.25 mag.

The Coma data was used to make average H I mass measurements to compare with the Abell 370 measurements for all 324 galaxies, for the inner subsample and for the outer subsample. Galaxies that lay within 8.0 Mpc of the cluster centre of Coma were chosen to match against all 324 Abell 370 galaxies. In this Coma cluster sample there were 113 galaxies within the magnitude range spanned by the 324 Abell 370 galaxies. Of these 24 per cent had detected H I masses. The galaxies within a radius of 2.5 Mpc of the cluster centre of Coma were matched with the inner subsample of the Abell 370 galaxies. In this Coma inner sample there were 67 galaxies within the magnitude range of the galaxies in the Abell 370 inner sample. Of these 19 per cent had measured H I masses. The galaxies more than 2.5 Mpc from the cluster centre of Coma but less than 8.0 Mpc from the centre were chosen to compare with the Abell 370 outer subsample. In this Coma outer sample there are 37 galaxies within the magnitude range of the galaxies in the Abell 370 outer sample. Of these 35 per cent had measured H I masses. The number of Coma galaxies in each subsamples is smaller than the number of Abell 370 galaxies. As such, the matched samples will contain repeats of the Coma galaxies which may introduce a

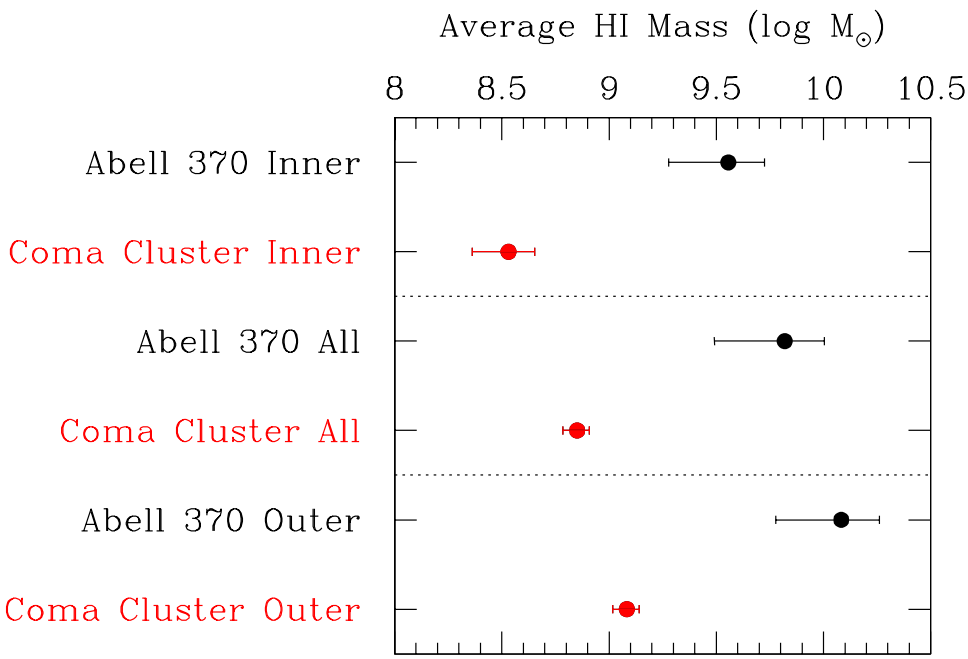

Figure 3.19: This figure shows the average H I mass for selected galaxy subsamples from Abell 370 and similar measurements made using literature values for the Coma cluster. The Coma average H I mass measurements are made from randomly selected samples of galaxies with similar B band absolute magnitudes to the Abell 370 galaxies (see text for details).

bias. However a larger sample of nearby cluster galaxies will likely have a similar distribution so that the effect of any bias will likely be small.

The measured average H I mass for the Abell 370 subsamples and the similar Coma measurements can be seen in Fig. 3.19. There is a similar trend in both Coma and Abell 370, that the galaxies in the outer regions of both clusters have average H I masses that are ∼3.5 times higher than that found in their inner galaxies. This is the well known trend, that galaxies within dense cluster cores generally have less H I gas content than galaxies in lower density environments (Haynes, Giovanelli, & Chincarini 1984). This is true in nearby clusters and appears to be true at $z = 0.37$, ∼4 billion years in the past. The similar ratio between the inner and outer measurements in the two clusters could suggest that the mechanism for creating this H I gas reduction is of similar strength in both clusters.

Despite this trend with galaxy density seen in both clusters, the amount of H I gas content of the galaxies is substantially different between the two clusters. In all three measurements the average H I mass in the Abell 370 galaxies is ∼10 times larger than that found in the Coma samples of optical galaxies with similar magnitudes. This higher H I gas content is likely due to the optically bright, blue galaxies that

exist around Abell 370 that have been shown to have large quantities of H I gas. Similar galaxies do not exist in Coma. This is seen in the difference in Butcher–Oemler blue fraction between the clusters; Abell 370 has a blue fraction of ∼0.13 while Coma has a blue fraction of ∼0.03 (Butcher & Oemler 1984), a factor of ∼4 less. The blue galaxies in Coma have had an extra ∼4 billion years of evolution to remove their H I gas through star formation or interactions in the dense galaxy environment. The young, blue stars in such galaxies would have died out in timescales less than ∼4 billion years. Without more H I gas to supply the fuel for additional star formation, the galaxies would have dimmed and evolved to a redder colour. The passive evolution of the galaxies in Abell 370 over ∼4 billion years would decrease their B band magnitudes by up to 1 magnitude (Poggianti 1997). Decreasing the optical brightness of the galaxies in Abell 370 by ∼1 magnitude creates a reasonable match to the B band magnitude distribution of the Coma galaxies.

Similar average H I mass comparison with either Abell 1367 or the Virgo cluster are not practical as there are insufficient galaxies optically bright enough to match to the Abell 370 galaxies.

3.6.3 H I mass to light ratios

In the previous literature comparisons it has been shown that the Abell 370 galaxies have higher H I gas content than galaxies in nearby clusters. This raises the question whether the Abell 370 galaxies have unusual H I gas properties compared to nearby galaxies. One way of assessing this is to measure the H I mass to optical light ratios seen for the Abell 370 galaxy subsamples and compare these to 'normal' galaxy values. The average ratio of H I mass to the B band luminosity for a variety of Abell 370 subsamples are shown in Fig. 3.20.

For each of the Abell 370 galaxy subsamples the average rest frame B band luminosity in units of the solar luminosity was calculated using an absolute B band magnitude for the sun of 5.46 (Bessell, Castelli, & Plez 1998). When combining the individual galaxy B band luminosities, weights were used equal to those used in the average H I mass measurements to ensure that similar quantities were measured. The weighted average and the non-weighted average B band luminosities are very similar for the subsamples considered (for all 324 galaxies the difference in values was ∼7 per cent). This suggests that the weighting scheme used in H I mass measurements does not create a bias in the results. Using this average B band luminosity and the average H I mass for a subsample, the H I mass to light ratio can be calculated.

The literature H I mass to blue light ratios considered are for samples of galaxies with different morphological types (Roberts & Haynes 1994). The morphologies move along the Hubble sequence starting with the early-type galaxies of ellipticals and S0s, moving across the variety of late-type galaxies in the direction of increasing spiral structure (moving from Sa to Sd galaxies), and finally reaching the irregular galaxies. The H I mass to light ratio increases fairly regularly along this sequence. These literature measurements are the median values from two catalogues, the Up-

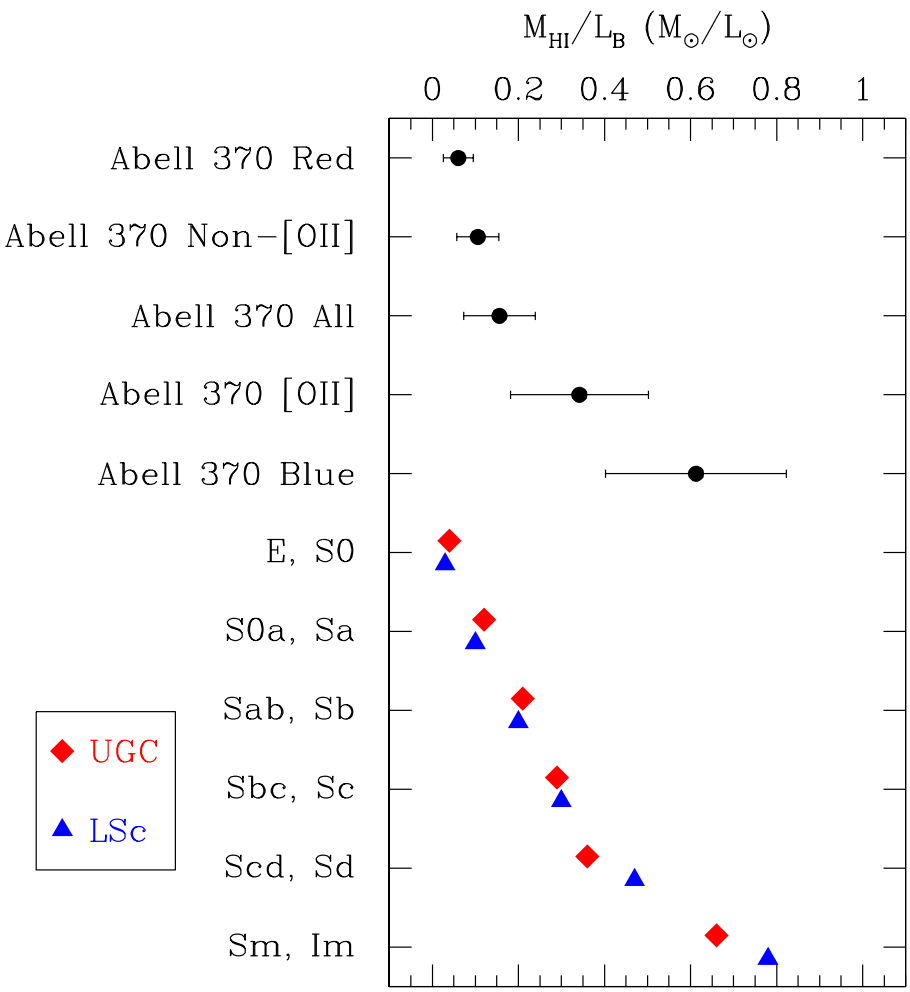

Figure 3.20: This figure shows the average ratio of H I mass to optical B band light ratio for various subsamples of the Abell 370 galaxies. Also plotted for comparison are the median H I mass to light ratios for different morphological type galaxies from the Uppsala General Catalogue (UGC) and the Local Super Cluster (LSc) (Roberts & Haynes 1994).

psala General Catalogue (UGC) and the Local Super Cluster sample (LSc).

In Fig. 3.20 the values for the galaxy subsamples of Abell 370 are plotted in order of increasing H I mass to light ratio. The red galaxy subsample has the lowest H I mass to light ratio while the blue galaxies have the highest. Below these are plotted the literature values from both the Uppsala General Catalogue (UGC) and the Local Super Cluster sample (LSc). The red galaxy subsample has an H I mass to light ratio similar to that for the ellipticals and S0 galaxies of the literature samples and the blue galaxy subsample has a ratio similar to those literature galaxies with the most spiral structure or which are irregular. Unfortunately deriving morphologies for the galaxies in Abell 370 is not possible due to the poor seeing in the optical imaging combined with the small size of galaxies at a redshift of $z = 0.37$. However, it is clear from this comparison that galaxies in Abell 370 seem to follow similar trends in H I mass to light ratios as nearby, 'normal' galaxies and even have similar H I mass to light ratios for galaxies of roughly similar types (the red and blue galaxies). With time, the galaxies in Abell 370 will undergo passive evolution, and their optical brightness will decrease. In order for the galaxies still to have 'normal' H I mass to light ratios their H I gas content will need to decrease similarly during this evolution.

3.7 Star Formation Rate Results

3.7.1 The SFR–H I mass correlation for the galaxies

In the local universe, there is a reasonably strong correlation between the star formation rate in a galaxy and the mass of H I gas in that galaxy. This relationship can be seen in Fig. 3 of Doyle & Drinkwater (2006), where they compared the H I masses of individual galaxies from HIPASS to their star formation rate derived from *IRAS* infrared data. This correlation between galaxy H I mass and star formation rate can be examined in the galaxies around Abell 370. The star formation rate for the Abell 370 galaxies was derived from their [OII] luminosity as described in Section 3.2.3. In Fig. 3.21, the large circular point shows the comparison of the average [OII] star formation rate against the average H I for the Abell 370 galaxies with [OII] equivalent width greater than 5 Å (the 168 galaxies of the [OII] emission subsample). When calculating the average [OII] star formation rate the same weighting scheme was used as in the average H I mass measurement. The difference between this weighted average star formation rate and the standard average is small (less than 1 per cent).

Plotted on Fig. 3.21 is the linear fit to the SFR–H I correlation for the local sample of galaxies (Doyle & Drinkwater 2006). The average value for the Abell 370 [OII] emission galaxies lies almost on this line. This indicates that the galaxies around Abell 370 have normal galaxy properties, in that their higher H I gas contents leads naturally to higher star formation rates. The same SFR–H I correlation relationship was found to hold at $z = 0.24$ in a field sample of star-forming galaxies (see Lah et al. 2007 and Fig. 2.13). These two results at $z = 0.24$ and $z = 0.37$ suggest that the

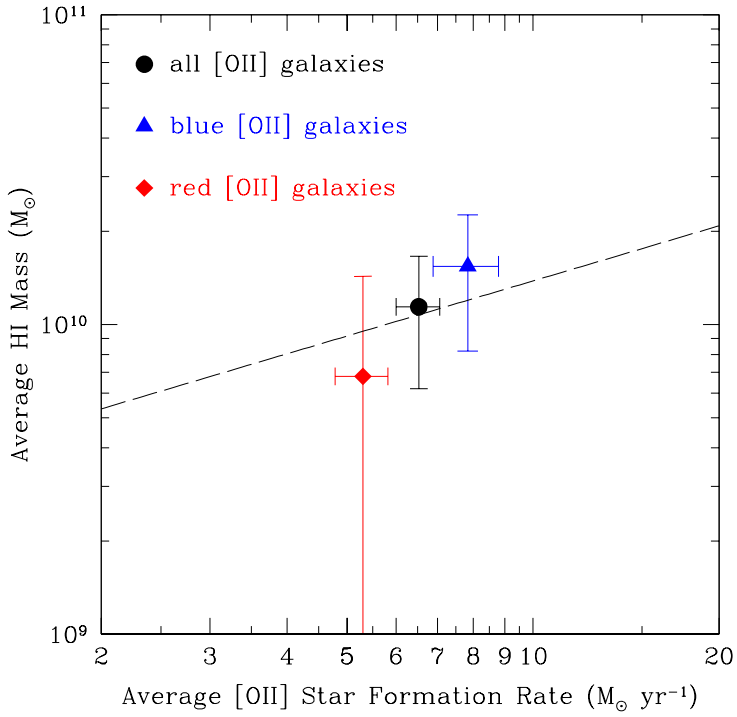

Figure 3.21: This figure shows the comparison of the average galaxy [OII] star formation rates with their average H I mass. The dashed line is the relationship seen in $z \sim 0$ galaxies (Doyle & Drinkwater 2006). The large circular point is the average for all 168 galaxies with [OII] emission. The triangle point is the average for the 81 blue galaxies with [OII] emission. The diamond point is the average of the 87 red galaxies with [OII] emission.

increase in star formation rate densities seen at moderate redshifts are simply due to higher H I gas content in the galaxies. The good SFR–H I correlation agreement for the Abell 370 galaxies also indicates that the assumptions and corrections made when calculating the [OII] star formation rate were reasonable.

Also shown in Fig. 3.21 are the values for the average galaxy [OII] star formation rates and average galaxy H I masses for the 81 galaxies that have [OII] emission and blue colours (the triangular point) as well as for the 87 galaxies that have [OII] emission but have red colours (the diamond point). Both of these measurements agree with the (Doyle & Drinkwater) line. The expected trend that the blue [OII] galaxies have higher star formation rates and higher H I masses compared to red [OII] galaxies is seen.

From the measured star formation rate, it would take ∼1.7 billion years for the [OII] emission galaxies to turn all their H I gas into stars. This assumes: that the conversions from H I gas to stars is 100 per cent efficient, that there is no change in the star formation rate as the H I gas decreases, that there is no significant amounts of molecular hydrogen gas, that galaxy harassment or H I stripping have minimal

effect on the gas, that there is no recycling of gas, and that there is no gas accretion onto the galaxies. None of these assumptions are reasonable. However, this rough time frame does show that it is possible for the H I gas in the Abell 370 galaxies to be depleted in the ∼4 billion years from $z = 0.37$ to the current epoch. Abell 370 can easily evolve into an H I gas poor galaxy cluster based entirely on the star formation rate seen in its galaxies.

3.7.2 The SFR–radio continuum correlation

Synchrotron radio emission is generated in areas of active star formation from relativistic electrons accelerated in supernova remnants. The luminosity of this radiation has a good correlation with other galaxy star formation rate indicators. This radiation in nearby galaxies is often measured using 1.4 GHz observations and compared to star formation rates measured using other indicators (Sullivan et al. 2001; Bell 2003). The GMRT data also provided measurements of the radio continuum emission at 1040 MHz for objects surrounding Abell 370. Since the Abell 370 galaxies are at a redshift of $z = 0.37$, their de-redshifted radio continuum emission in the GMRT data has a frequency of 1.4 GHz. It is therefore possible to directly measure the 1.4 GHz radio continuum emission from the Abell 370 galaxies and compare it to their measured [OII] star formation rate to see if the correlations found in the nearby universe hold at $z = 0.37$.

Despite the low radio continuum RMS of only 20 μJy, only a handful of the 168 Abell 370 galaxies with [OII] emission have radio continuum flux densities at or above the 5σ level. To increase the number of galaxies studied, the signal from all 168 galaxies was coadded using their known optical position to measure their average radio continuum flux density. This coadding was done using a similar weighted average as used in the H I measurements, to take into account the variation in noise due to the GMRT primary beam shape. Using this method, the 168 galaxies with [OII] emission have a measured average flux density of 25.7 ± 2.8 μJy. The coadded radio continuum image appeared to be unresolved with no extended emission. Therefore the central specific intensity value was used as a measure of the total flux density. Converting from flux density to luminosity density using the cosmological distance and de-redshifting the radio continuum emission from $z = 0.37$, gives an average 1.4 GHz radio continuum luminosity density of $(8.96 \pm 0.96) \times 10^{28}$ ergs s^{-1} Hz^{-1} for the [OII] emission galaxies. This measurement is the large circular point in Fig. 3.22.

The dashed line in Fig. 3.22 is the 1.4 GHz radio continuum conversion to star formation rate (Bell 2003). There is a change in the slope of this conversion at a star formation rate of ∼3.5 M$_\odot$ yr^{-1}. This is due to galaxies of lower mass not being able to retain all their cosmic rays accelerated in supernovae remnants and so reducing the radio continuum emission produced relative to other star formation indicators. The value for the [OII] emission subsample lies $\sim 1\sigma$ below this conversion line, showing reasonable agreement. The result shown here does not depend on a handful of galaxies with high radio continuum luminosity (i.e. the few individually detectable sources) but is a general result from all the galaxies in the subsample.

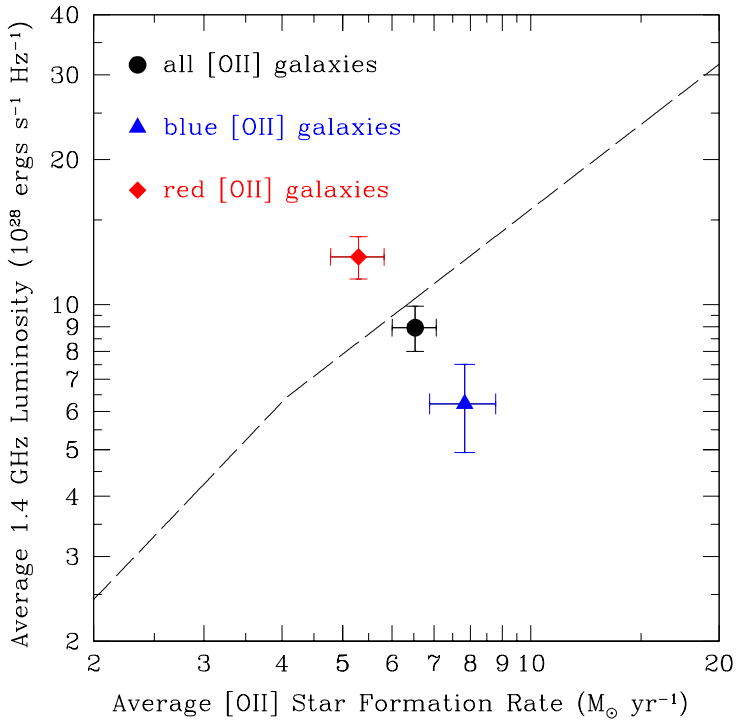

Figure 3.22: This figure shows the comparison of the average galaxy star formation rates measured from the [OII] emission line luminosity and the de-redshifted 1.4 GHz radio continuum luminosity. The dashed line is the conversion from 1.4 GHz radio continuum to star formation rate Bell (2003). The large circular point is the average for all 168 galaxies with [OII] emission. The triangle point is the average for the 81 blue galaxies with [OII] emission. The diamond point is the average of the 87 red galaxies with [OII] emission.

There is some intrinsic scatter (i.e. not purely random error) around the star formation rate correlation between different indicators. The galaxies studied in the Abell 370 analysis have been selected based on their [OII] equivalent widths. This will create a selection bias such that those galaxies that have low [OII] luminosities but higher radio continuum that exist within the general scatter of the correlation may be missed. If these galaxies were included in the sample the average [OII] star formation rate would slightly decrease and average radio continuum luminosity increase. This would bring the average point in Fig. 3.22 closer to the line derived by Bell (2003).

Many of the individual galaxies in the [OII] emission subsample will have radio continuum luminosities below the point were the SFR correlation changes slope. As individual measures of the radio continuum luminosity for these galaxies cannot be done, it is not possible to correct for this. If this could be corrected, the star formation rate determined from the average radio continuum of the galaxies would

increase slightly, which will improve the agreement between the [OII] and radio continuum star formation rate.

It has been found that active galactic nuclei (AGN) dominate the radio continuum sources above 1.4 GHz luminosities of 10^{30} ergs s^{-1} Hz^{-1} and star formation below this value (Condon, Cotton, & Broderick 2002). The highest individually measurable radio continuum luminosity for a galaxy in the Abell 370 [OII] emission subsample is $(0.884 \pm 0.080) \times 10^{30}$ ergs s^{-1} Hz^{-1}. This brightest radio continuum source in the [OII] emission subsample falls below this transition value with the majority of galaxies having appreciably lower radio continuum luminosities. Thus it is likely that the AGN contamination of the sample is small with a minimal effect on the measured average radio continuum luminosity.

The [OII] emission galaxies were split into the 81 blue and 87 red galaxies and the average radio continuum luminosity and average [OII] star formation rates for these subsamples were measured. In Fig. 3.22 the average values for the blue [OII] emission subsample is the triangular point and the average values for the red [OII] emission subsample is the diamond point. An unexpected relationship is seen, with the red galaxies showing a higher radio continuum luminosity compared to the blue galaxies even though the red galaxies have a lower [OII] star formation rate. It is not known what is causing this relationship. It is not due to the effect of a small handful of galaxies in the red and blue subsamples; it is a general trend across both subsamples. No simple systematic effect such as AGN contamination on the radio continuum, or metallicity and/or dust extinction effects on the [OII] star formation rate are able to explain this trend. Since the [OII] star formation–H I mass correlation seems to agree with expectations (see in Section 3.7.1), it is likely that the radio continuum is the cause of this unusual relationship.

A working hypothesis to explain this effect is the different timescale responsible for the production of the [OII] and radio continuum emission in galaxies. The weak radio continuum observed in normal galaxies is emitted by an ensemble of relativistic electrons that are produced in supernova remnants. Lifetimes of these relativistic particles can exceed the timescale associated with star bursts. The lifetime, $t_{\rm life}$, of synchrotron emitting particles capable of emitting a characteristic frequency can be expressed as:

$$t_{\rm life} \sim 3{\times}10^4\, B^{-\frac{3}{2}}\, \nu_c^{-\frac{1}{2}} \text{ yrs} \tag{3.4}$$

where B is the magnetic field strength of the galaxy (in gauss), ν_c is the characteristic frequency of emission and can be expressed as $\nu_c \sim 4 \times 10^6\, B\gamma^2$ Hz, and γ is the electron Lorentz factor (Rybicki & Lightman 1986). For frequencies of 1 GHz, $t_{\rm life} \sim B^{-\frac{3}{2}}$ yrs, which ranges from $3{\times}10^7$ to 10^9 years for the dilute magnetic fields (1 to 10 μgauss) in an ageing disk galaxy.

Thus it is suggested that red [OII] galaxies are older galaxies coming out of a burst of star formation. They have some residual [OII] emission as well as supernovae remnants that have produced a large reservoir of decaying, relativistic electrons in the galaxies. The blue [OII] galaxies are younger systems, which are only currently

seen to be building their stellar populations and their relativistic electron distributions. The hypothesis is that this difference in relativistic electron distributions between the red [OII] and blue [OII] galaxies is the cause of the difference in their radio continuum measurements.

3.8 Conclusion

The result from the measurement of the average H I mass for a large sample of galaxies around the galaxy cluster Abell 370 at a redshift of $z = 0.37$, a look-back time of ∼4 billion years, have been presented in this chapter. The average H I mass measured for all 324 galaxies is $(6.6 \pm 3.5) \times 10^9$ $M_\odot$ while the average H I mass measured for the 105 optically blue galaxies is $(19.0 \pm 6.5) \times 10^9$ $M_\odot$. The H I gas content of the galaxies is found to be markedly higher than that found in nearby clusters. Abell 370 has considerably more H I gas than Coma, a cluster of similar size. The average galaxy H I mass measurements in Abell 370 are ∼10 times higher than similar measurements made from galaxies in Coma. The measured H I density around the galaxy cluster Abell 370 is ∼8 times higher than in Coma. These results show there has been substantial evolution in the gas content of clusters over the past ∼4 billion years.

Despite the appreciable H I gas content in the Abell 370 galaxies, there is evidence that environmental effects reduce the gas content of galaxies, similar to what is seen in nearby clusters. The galaxies in the inner regions of the cluster (within the R_{200} radius) have average H I masses smaller by a factor of ∼3.5 than galaxies outside this region. The optically blue galaxies outside the hot, intracluster medium of the cluster core have a higher average H I gas mass than found from the complete sample of blue galaxies in Abell 370. This shows that the late-type galaxies close to the cluster core in Abell 370 are H I deficient like those seen in nearby clusters (Haynes, Giovanelli, & Chincarini 1984).

Although the galaxies in Abell 370 have high H I gas contents, they have similar galaxy properties to present day galaxies: the Abell 370 galaxies have normal H I mass to optical light ratios and have a similar correlation between their star formation rate and H I mass as found in nearby galaxies. The average star formation rate derived from [OII] emission and from de-redshifted 1.4 GHz radio continuum for the Abell 370 galaxies follows the correlation found in the local universe. However, there is an unexpected relationship where the red [OII] emission galaxies have a higher average radio continuum luminosity than the blue [OII] emission galaxies despite having a lower average [OII] star formation rate. This effect is the reverse of what is expected and is currently unexplained.

The data suggests that the red galaxies in Abell 370 may have discernible amounts of H I gas contained within their central regions unlike nearby galaxies. Additionally the blue galaxy population with no appreciable [OII] emission appear to contain large amounts of H I gas. Both of these results merit further investigation in future more sensitive observations.

The current rate of star formation in the Abell 370 galaxies can easily exhaust their H I gas in the ∼4 billion years to the present epoch. Abell 370 seems set to evolve into a gas poor system like nearby galaxy clusters, especially when one considers the other physical mechanisms besides star formation that may reduce the gas content of the galaxies in the dense galaxy environment. Such a rapid rate of decrease in H I gas in the volume around Abell 370 would be significantly faster than the rate of decrease seen in field environments.

The final evolved state of the galaxy cluster Abell 370 has not been considered. This is a complex problem involving looking at the effect of the current measured star formation rates in the galaxies, the effect of passive evolution on the stellar population of the galaxies, the possible growth in the cluster core mass, the motion of the galaxies in the cluster potential and the precise effects of the environment on each galaxy which will change with time as the galaxies move within the cluster.

Chapter 4

Two Unusual Radio Continuum Objects Near Abell 370

> A scientist must also be absolutely like a child. If he sees a thing, he must say that he sees it, whether it was what he thought he was going to see or not. See first, think later, then test. But always see first. Otherwise you will only see what you were expecting. Most scientists forget that.
>
> Douglas Adams

In the radio continuum images produced from the GMRT observations of Abell 370 (see Section 3.3) there were found two unusual sources that were worth further investigation. One object was a very unusually shaped radio continuum source that I have been calling the 'DP Structure'. The other is a possible radio gravitational arc near the centre of the galaxy cluster of Abell 370. This chapter presents results on these two objects. Further research on these objects may prove productive.

4.1 The DP Structure

4.1.1 The observational data

When looking through the radio continuum images from GMRT observations of Abell 370, I found a very unusual object which I have been calling the 'DP Structure' (NVSS J023943-012754). The grey-scale image of the object can be seen in left panel of Fig. 4.1. The radio continuum objects that one commonly finds in the data are unresolved sources that appear as circular objects with the diameter of the synthesised beam. These often appear as double sources – the two lobes of a radio galaxy. Occasionally there are more extended blob like objects. This strange wiggly shaped object immediately caught my eye, so I investigated further.

This radio continuum image has a synthesised beam size (resolution) of ∼3.3 arcsec and an RMS noise of 20 μJy. The DP Structure is a reasonably bright radio source. At the observed frequency of 1040 MHz, the peak flux of the structure is

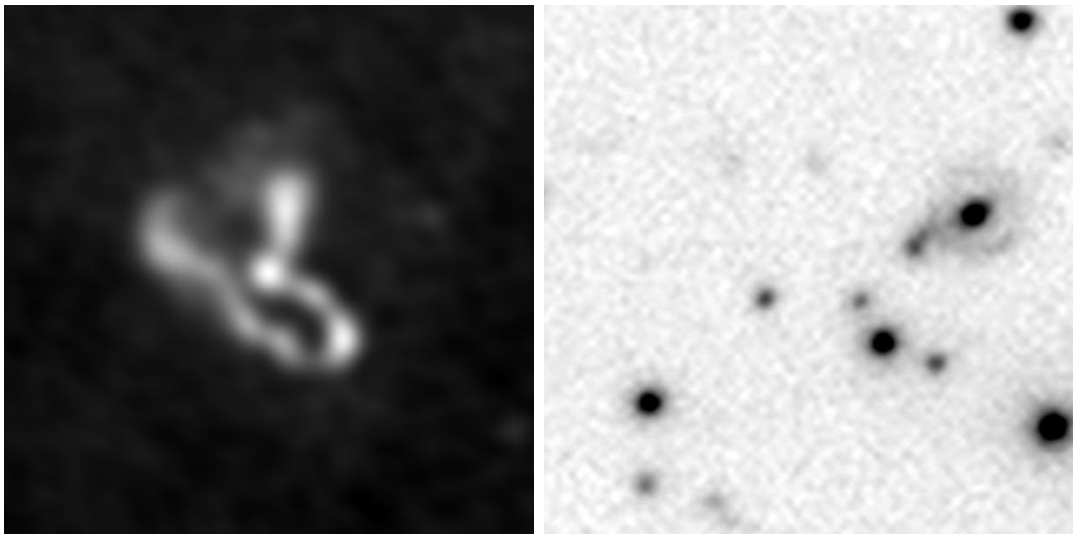

Figure 4.1: The left panel shows the grey-scale, GMRT radio continuum image of the DP Structure (the lighter the grey-scale the brighter the radio continuum). This image has a synthesised beam size (resolution) of ∼3.3 arcsec. The peak flux of the object is 1.29 mJy/Beam and the RMS noise is 20 μJy. The right panel shows the same region of the sky in the optical from the V band image from the ANU 40 inch observations (in this case the darker the grey-scale the brighter the optical light). The optical seeing in this image is ∼2.1 arcsec. Both images are 60 arcsec on a side. This is a projected distance of ∼282 kpc at the redshift of the object ($z = 0.326$, see later in this section).

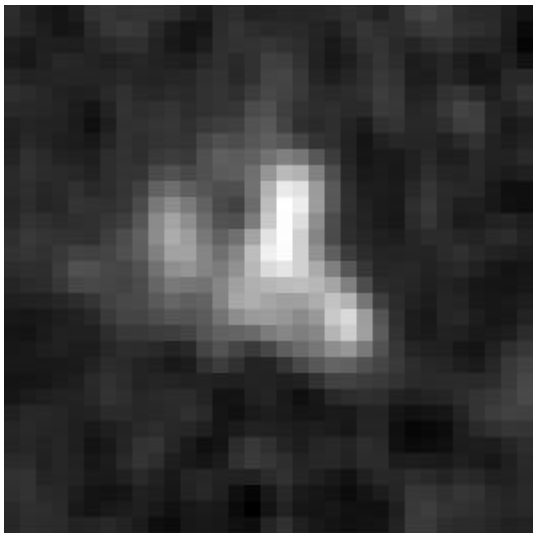

Figure 4.2: This figure shows the DP Structure as it appears in the 1.4 GHz radio continuum VLA FIRST survey (Becker, White, & Helfand 1995). This image has a synthesised beam size (resolution) of ∼5 arcsec and the image is 60 arcsec on a side, the same size as the images in Fig. 4.1.

1.29 mJy/Beam and is located at R.A. $02^{h}39^{m}43.5^{s}$ Dec. $-01°27'54''$ J2000. The total flux density of the entire structure is 23.28 ± 0.19 mJy. The object appears in the 1.4 GHz radio continuum survey of FIRST (Becker, White, & Helfand 1995) and the FIRST image of the structure can be seen in Fig 4.2. This image has a synthesised beam size (resolution) of ∼5 arcsec and the image is 60 arcsec on a side, the same size as the images in Fig. 4.1. The details of the structure are not clear in the FIRST image. This is primarily due to the longer telescope baselines used in the GMRT observations and the significantly better $u - v$ coverage of the GMRT imaging (the FIRST image was made with only 3 minutes of observation). Some of the components of the structure can be identified in the FIRST image using the GMRT image as a guide. The total flux density of the structure at 1.4 GHz in the FIRST survey is 25.25 ± 0.30 mJy.

The right panel of Fig. 4.1 shows the same region of the sky in the optical from the V band image from the ANU 40 inch observations. This image is the same size as the radio image (60 arcsec on a side). With only a first look at the optical imaging one might wonder if it is the same region of the sky. There appears to be nothing directly corresponding to the bulk of the radio continuum structure and no optical counterpart to the bright central part of the DP Structure. However further investigation shows there to be a deep relationship between the optical and radio observations.

In the top panel of Fig. 4.3 is shown the grey-scale optical image overlaid with the radio continuum as contours. One can see that three optical objects (probably galaxies) underlie the structure with one located directly under the bright radio spot at lower bottom right of the structure. The large spiral galaxy in the middle right of the image, away from the structure, has faint radio continuum emission (single contour) showing that there is good alignment of the radio and optical astrometry. This is real radio emission as the first contour level is at 150 μJy and the RMS noise in the image is 20 μJy. In the radio continuum grey-scale image (Figure 4.1) one can see fuzzy emission around the end of the tail which is pointing up. From the contour plot one can see that this emission is real, being at least 150 μJy, the level of the first contour.

The radio contour image is quite complex making it difficult to understand optical-radio relationship. So I have included the bottom panel of Fig. 4.3 which shows the radio emission in grey-scale and the optical in contours. This makes it much easier to see the alignment of the objects between the radio and optical. One can clearly see that the three optical objects have a very good alignment to parts of the radio continuum structure. In particular the optical object underlying the bottom right end of the structure looks like the source of the radio emission with two wiggly jets of radio emission leaving from it. The smaller optical object slightly above and to the left corresponds to a small local peak in the radio continuum emission. The last optical object that lies further to the left actually corresponds to a region where the radio emission decreases; one can see this in the pinching in the radio continuum contours at this location in the top panel of Fig. 4.3. It is possible that the source of the radio emission is interacting with these two smaller optical

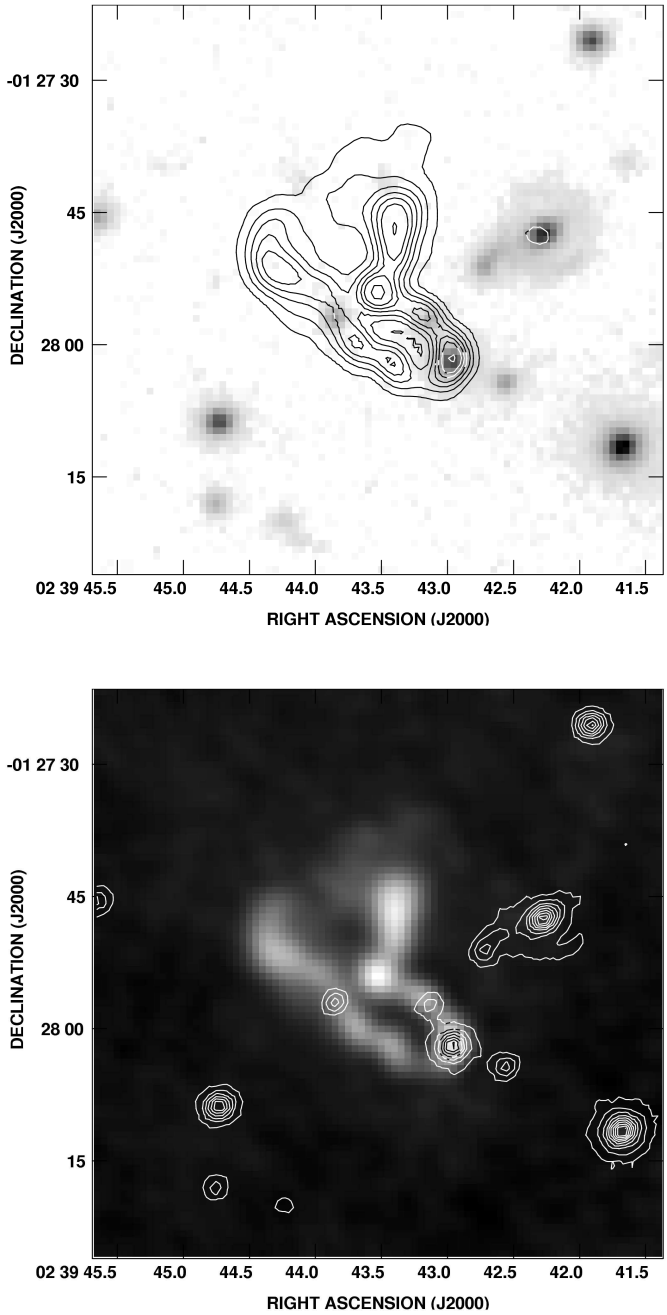

Figure 4.3: The top panel shows the DP Structure with the optical V band as a grey-scale and the GMRT radio continuum image as contours. The radio contour levels are 150, 300, 450, 600, 750, 900, 1150 μJy/beam. The darker the optical grey-scale the brighter the object. The bottom panel shows the same image except that now the radio is the grey-scale and the optical is shown as contours. In this case the lighter the grey-scale the brighter the radio continuum. Both images are 60 arcsec on a side.

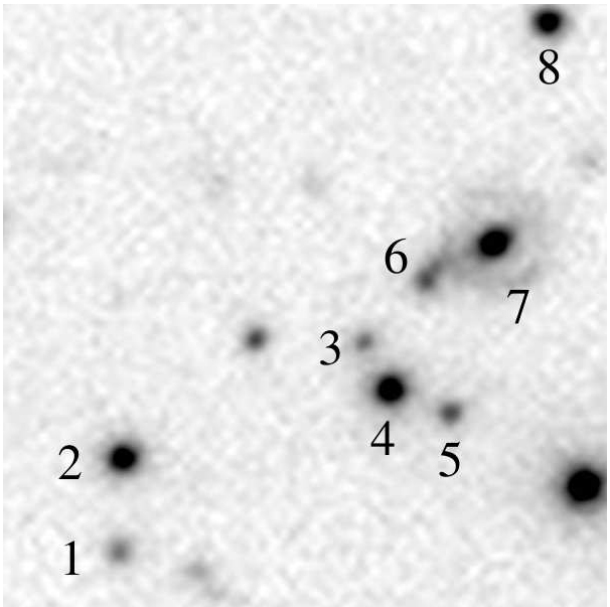

Figure 4.4: This figure shows the same optical image as Fig. 4.1 but those galaxies that have a measured redshift are labelled with a number. The properties of these galaxies are listed in Table 4.1 below.

objects creating these features in the radio.

The DP Structure is ∼7.0 arcmin on the sky from the centre of the large cluster Abell 370 (cluster centre at R.A. $02^{\rm h}39^{\rm m}52.90^{\rm s}$ Dec. $-01°34'37.5''$ J2000). This puts it 7.1 arcmin away from the cluster core but close enough that many of the optical objects in the region around the structure were sampled in the spectroscopic AAOmega observation with the Anglo-Australian Telescope (see Section 3.2.1). The eight galaxies in the 60 arcsec optical image for which redshifts were obtained are numbered in Fig. 4.4 and the properties of these galaxies are listed in Table 4.1. Galaxy 4 is the optical object that appears to be the source of the DP Structure and Galaxy 3 one of the two other optical objects that could possibly be interacting with the structure. The final optical object that could be interacting with the radio emission does not have an observed redshift. All these eight galaxies have redshifts that are quite near each other in value. This can be seen most clearly by looking in the column of Table 4.1 labelled 'Velocity Difference'. This is the difference between the redshift of each galaxy and galaxy 4 (the apparent source of the DP Structure) converted to a velocity. None of the galaxies are more than 1000 $\rm km\,s^{-1}$ from galaxy 4, suggesting that they form a galaxy group or small cluster (I have been calling this the DP Group). If the galaxies are in a group they likely all lie at the same distance and the variation in their redshifts would then be due to their different peculiar motions within the galaxy group. The listed 'Velocity Differences' are estimates of the galaxies peculiar motion as it includes a cosmological correction, i.e. divide by $(1 + z_{group})$, where $z_{group} = 0.326$ is the redshift of the galaxy group.

Galaxy Number	R.A. (J2000)	Dec. (J2000)	Redshift	Velocity Difference	V mag	Spectral Type
1	02 39 44.76	-01 28 18.0	0.32723	195 $\mathrm{km\,s^{-1}}$	19.9	abs
2	02 39 44.71	-01 28 08.9	0.32492	-328 $\mathrm{km\,s^{-1}}$	19.4	abs
3	02 39 43.13	-01 27 57.2	0.32622	-34 $\mathrm{km\,s^{-1}}$	20.5	abs
4	**02 39 42.96**	**-01 28 02.2**	**0.32637**	**0 $\mathrm{km\,s^{-1}}$**	**19.3**	**abs**
5	02 39 42.70	-01 27 50.6	0.32369	-606 $\mathrm{km\,s^{-1}}$	19.8	abs
6	02 39 42.58	-01 28 04.2	0.32680	97 $\mathrm{km\,s^{-1}}$	20.0	abs
7	02 39 42.26	-01 27 47.5	0.32786	337 $\mathrm{km\,s^{-1}}$	19.0	em
8	02 39 41.90	-01 27 25.4	0.32584	-120 $\mathrm{km\,s^{-1}}$	20.2	em

Table 4.1: The properties of the galaxies that are near the DP Structure on the sky and that have measured redshifts. The 'Galaxy Number' is the number used to label the galaxies in Fig. 4.4. The 'Velocity Difference' is the difference in redshift between the galaxy and galaxy 4 (the apparent source of the DP Structure) converted to a velocity. The 'V mag' are the observed V band total magnitudes from the ANU 40 Inch observations calibrated on the Vega system (see Section 3.2.1). The 'Spectral Type' is a rough classification of the optical spectrum. 'abs' indicates that galaxy spectrum was dominated by absorption features; 'em' indicates that the galaxy spectrum was dominated by emission features. (Note: the redshift of Abell 370 is $z = 0.37$).

In Table 4.1 is listed a rough 'Spectral Type' for the galaxies. The optical spectrum of a galaxy was either dominated by absorption features, making it likely that the galaxy was an early-type galaxy, or the optical spectrum was dominated by emission features, making it likely that galaxy is a late-type galaxy with active star formation or possibly an Active Galaxy Nucleus (AGN). The majority of the galaxies (6 out of 8) are absorption galaxies which is what one would expect for the central regions of a galaxy group. Galaxy 7, which is one of the two emission galaxies in the sample, can be clearly be identified as a normal spiral galaxy from the optical imaging. A clear optical disk around a central bulge can be seen, with the disk appearing almost face on.

The eight galaxies with redshifts in the 60 arcsec optical image are not the only galaxies identified in the Anglo-Australian Telescope observations that belong to this group. This can be seen in Fig. 4.5 which plots all the redshifts obtained in these observations between redshifts $z = 0.3$ and 0.4 against their Right Ascension. The galaxy cluster, Abell 370 (the main target of these observations) is the large collection of galaxies centred at redshift $z \sim 0.37$, R.A. $\sim 02^{\mathrm{h}}40^{\mathrm{m}}00^{\mathrm{s}}$. The DP Group is the smaller collection of galaxies that lies foreground to the cluster at redshift $z \sim 0.325$, R.A. $02^{\mathrm{h}}39^{\mathrm{m}}40^{\mathrm{s}}$. One can clearly see that there is an overdensity of galaxies at this location though it is nowhere near the size of the overdensity that is the large galaxy cluster, Abell 370. The DP Group is not connected to the galaxy cluster, Abell 370; it is a foreground object that by chance happens to lie a small angular distance away. Abell 370 is at $z = 0.373$ while the DP Group is located at $z = 0.326$. This is $\sim$14,000 $\mathrm{km\,s^{-1}}$ velocity difference which is too large to be due to peculiar motion. This redshift difference corresponds to a 167 Mpc comoving

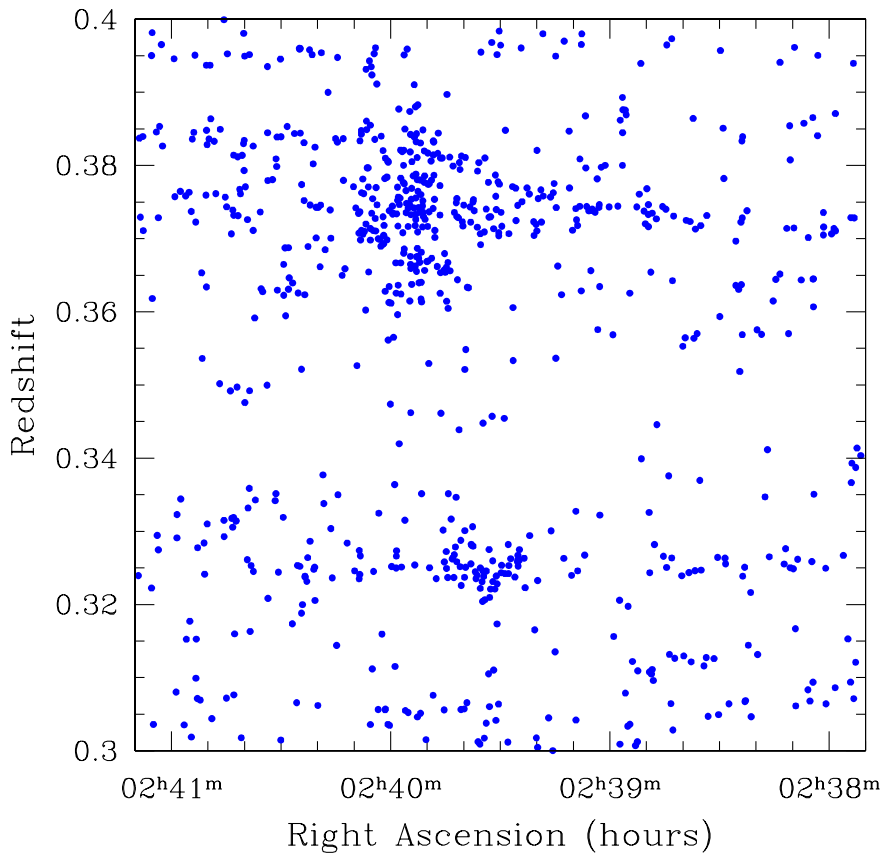

Figure 4.5: This figure shows the location of the galaxy cluster Abell 370 and the galaxy group around the DP Structure (the DP Group). The figure displays the Right Ascension and redshifts of the galaxies with redshifts from the AAOmega observations of Abell 370. The galaxy cluster, Abell 370 is the large collection of galaxies centred at redshift $z \sim 0.37$, R.A. $\sim 02^{\rm h}40^{\rm m}00^{\rm s}$. The DP Group is the smaller collection of galaxies that lies foreground to the cluster at redshift $z \sim 0.325$, R.A. $02^{\rm h}39^{\rm m}40^{\rm s}$.

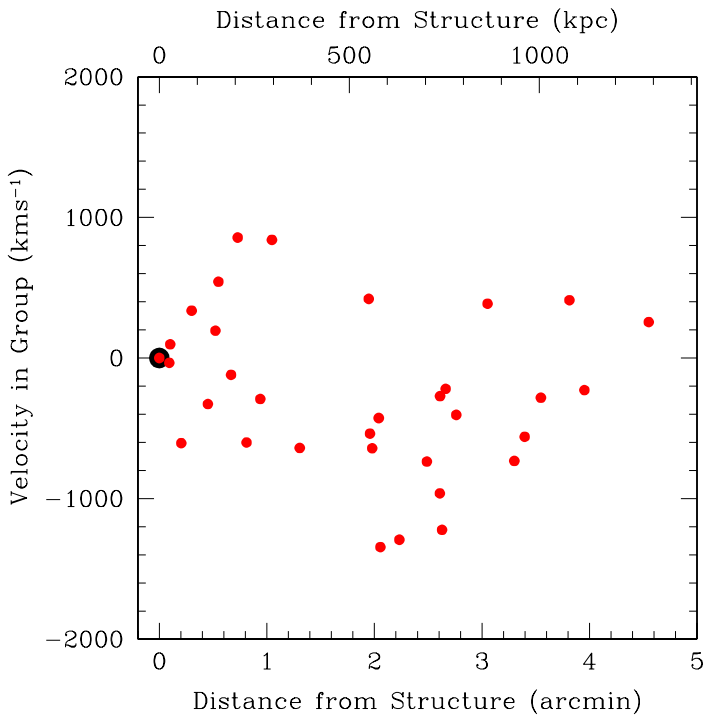

Figure 4.6: This figure shows the location of the galaxies within the DP Group. The figure displays the velocity of the galaxies and their projected distance on the sky from the centre of the group (in arcminutes on the lower x-axis and kpc on the upper x-axis). Galaxy 4, the source of the DP Structure has been assumed to be the centre of the group. It is the larger point at zero velocity, zero distance. The velocities of the galaxies include the cosmological correction, i.e. they are divided by $(1+z_{group})$, where $z_{group} = 0.326$, the assumed galaxy group redshift.

distance difference which is also too large to make the group and cluster spatially connected. The cluster and group are separated in look-back time by 0.4 Gyr. (Note: the redshift of the DP Group puts it well outside the H I redshift range that can be measured with the GMRT observations which are centred on the cluster Abell 370).

To identify the galaxies that lie within the DP Group the redshift difference and projected distance on the sky from galaxy 4 were considered. Galaxy 4 (the source of the DP Structure) is assumed to be the centre of the group. The redshift difference and projected distance are plotted in Fig. 4.6. The velocities of the galaxies includes the cosmological correction, i.e. they are divided by $(1+z_{group})$, where $z_{group} = 0.326$, the assumed group redshift. The projected distance on the sky is listed in both arcminutes and physical distance in kpc. The physical distance is defined at the redshift of the group, $z_{group} = 0.326$ where 1 arcsec on the sky corresponds to 4.717 kpc. The galaxy with the next closest redshift that lies within the projected distance on the sky shown in Fig. 4.6 is $\sim$4600 km s^{-1}away. This suggests that the

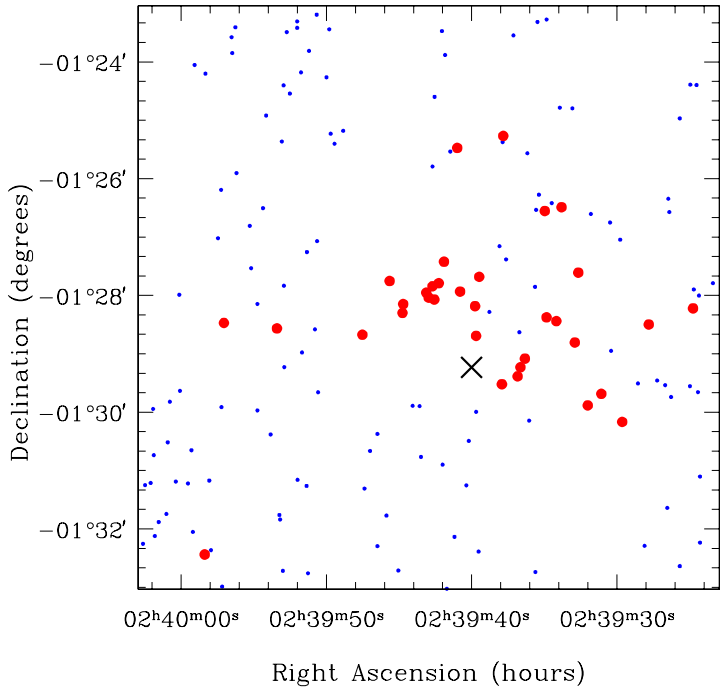

Figure 4.7: This figure shows the position of the DP Group on the sky. The figure covers 10 arcminutes on each side and is centred on galaxy 4, the source of the DP Structure. The larger points are the galaxies located in the DP Group, the same galaxies shown in Fig. 4.6. The smaller points are other galaxies that have measured redshifts that are either foreground or background to the group. The cross is the location of the literature group NSCS J023940-012914.

velocity range used in this figure contains all the major galaxies with a measured redshift in the DP Group. The velocity dispersion of this group/cluster is ∼600 km s^{-1}.

The location of these DP Group galaxies on sky has been shown in Fig. 4.7 as the large points. The other smaller points in this figure are the other galaxies that have measured redshifts that are either foreground or background to the group. The galaxy group can be clearly seen as a relatively compact structure on the sky with galaxy 4 (the centre of the figure) likely to be close to the centre of the galaxy group. There are a few additional galaxies at the redshift of the group that lie outside the 5 arcmin (∼1.4 Mpc) radius plotted here. However they are widely distributed on the sky making it unlikely that they are related to the group. In the literature there is an optically identified galaxy cluster/group NSCS J023940-012914 at R.A. 02^{h}39^{m}39.7^{s} Dec. −01°29′14″ J2000. This was selected from an overdensity of galaxies in the digitised Second Palomar Observatory Sky Survey (Lopes et al. 2004) and was found to have a photometric redshift of ∼0.37. These coordinates are

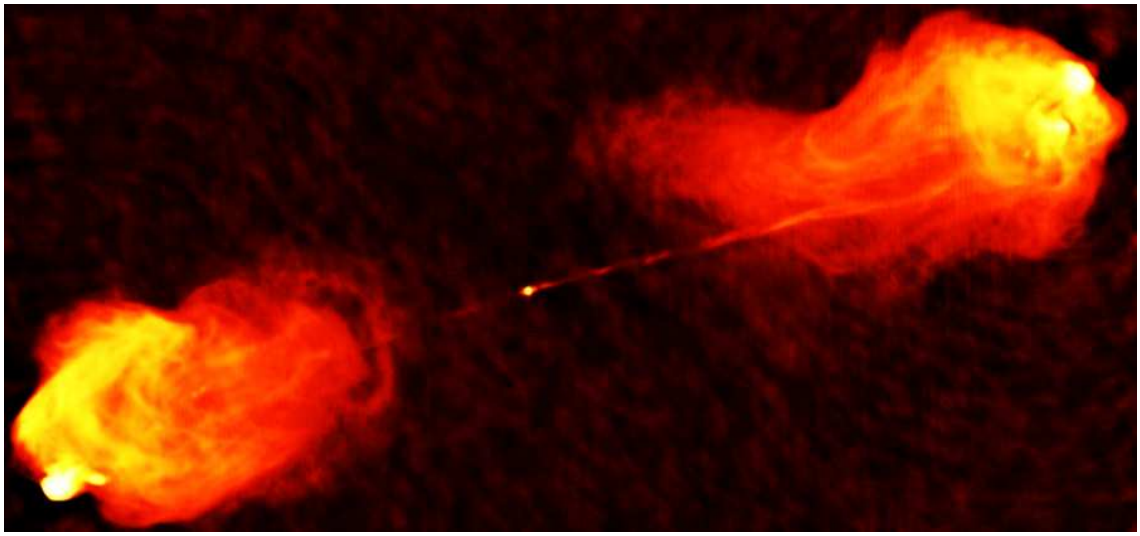

Figure 4.8: Cygnus A, one of the brighter radio continuum objects in the sky. This image was observed at 5 GHz and is 2.3×1.3 arcmin in size with a resolution of 0.5 arcsec (image courtesy of NRAO/AUI and Perley, Dreher, & Cowan 1984).

slightly away from where our data places the group but sufficiently close to likely be the same structure. The deeper optical imaging and the use of spectroscopic redshifts allow one to make a better identification of the location of the group. There are no sufficiently deep X-ray observations of this region in the literature to identify the hot intragroup gas that would likely be present at the heart of the galaxy group.

If the DP Structure is at redshift of the group ($z_{group} = 0.326$), then the ~25 arcsec across the structure corresponds to a projected distance of ~118 kpc wide. At the speed of light this distance would take ~395,000 years to cross which is quite a short period of time relative to the cosmological timescales I am used to dealing with.

4.1.2 Explaining the structure

With the data in hand it is possible to explain what the DP Structure is likely to be. The radio emission is likely to be caused by jets of relativistic particles that originate at galaxy 4. At the centre of this early-type galaxy is likely to be a supermassive black hole accreting gas and producing a pair of jets of relativistic plasma directed in opposite directions. The relativistic particles in these jets spiral around the magnetic field lines producing synchrotron radiation which is observed as radio continuum emission.

Such galaxies with radio jets are relatively common. A good example is the bright source Cygnus A, shown in Fig 4.8. In Cygnus A, the radio jet is just visible as it leaves the central source in opposite directions. The ends of the relativistic

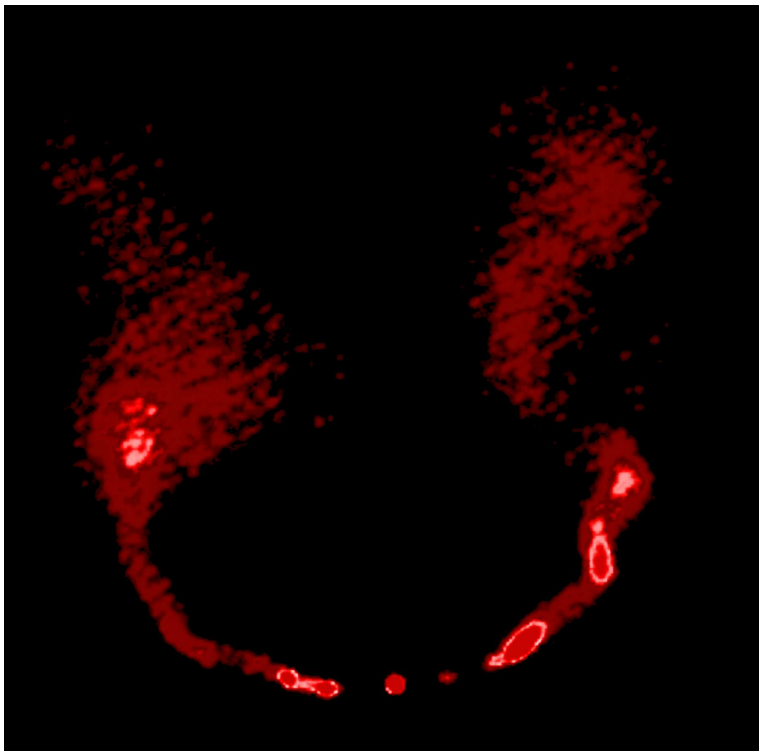

Figure 4.9: Radio continuum image of the archetypal head-tail source NGC 1265 (3C83.1). The image is 2 arcmin on a side. (Image courtesy of NRAO/AUI and O'Dea & Owen 1982)

jets are interacting with the intergalactic medium producing the two bright lobes. In radio continuum observations one commonly sees double sources that are these bright lobes at the end of such jets and not see either the jet or the galaxy that is their source (they are too faint to be seen). The DP Structure is unusual in that the radio jets are bright enough to see, though this is not that uncommon. The really strange thing about the DP Structure is the way the radio jets appear to be almost turning back onto each other.

One can understand why the jets have undergone such a radical change in direction by looking at the galactic environment that the DP Structure lies within. The structure lies close to the centre of a galaxy group. Galaxy 4, the likely source of the jets, would be moving with relatively fast velocity in the gravitational field of this group of galaxies, plowing through the intragroup ionised gas that builds up in such environments.

There are other radio sources that are interacting with a cluster/group environment that show some of the features of the DP Structure. These sources are known as head-tail sources, as they appear to have a bright source (the head) accompanied by tails of radio emission. These tails are the radio jets that are swept back by interaction with the intergalactic gas. The archetypal head-tail source is 3C83.1 (galaxy NGC 1265) which can be seen in Fig. 4.9. The galaxy NGC 1265 is located in the

Perseus Cluster and is moving through the cluster at a velocity of $\sim$2000 km s^{-1}. Twin radio jets are leaving the galaxy NGC 1265 (the small, central red object), in roughly opposite directions. After leaving the galaxy, the radio jets are bent backwards into the 'U' shape by the ram pressure of the intergalactic medium that the galaxy is travelling through. Head-tail sources have been found to occur in both rich clusters and poor groups despite such groups having less intragroup medium (Venkatesan et al. 1994).

The reason that the jets in the DP Structure appear to be almost joining back up onto each other is probably due to the orientation of the jets to the observer. The jets from the galaxy in the head-tail source 3C83.1 (Fig. 4.9) appear to have originally been pointing in directions roughly perpendicular to the observer in the direction into and out of the page. This gives rise to the 'U' shape tails seen when the jets interact with the intergalactic medium.

Now imagine changing the orientation of the source such that the two jets were perpendicular to the page, with one jet coming towards the observer and the other away. The two tails would then appear to be right on top of another. This is probably what is occurring in the DP Structure; the jets coming out of the galaxy are originally pointed almost straight at and directly away from the observer. The jets are then swept back with the interaction with the intergalactic medium into a similar 'U' shape to 3C83.1. However due to the orientation of the jets the 'U' shape appears much tighter so that the two tails appear to be almost joining up, though in reality one jet is foreground to the other.

The bending and twisting seen in other head-tail sources was explained by Icke (1981) as the precession of the jet beams combined with the interaction with the intergalactic medium. This and possible interactions with the two other optical galaxies that underlie the DP Structure are the likely cause of the other wiggles in the path traced by the two radio jets.

There is another possibility for the strange shape of the DP Structure that should noted. The structure could actually be two separate radio continuum emission sources that both lie along the same line of sight but are actually at different distances. In this case the two sources individual radio continuum emission are super-imposed on one another. As the DP Structure lies within the DP Group there are many galaxies that lie close together on the sky that could be sources of radio emission making this a distinct possibility. However the connected nature of the radio continuum emission would seem to suggest that this double source model is unlikely though it can not be ruled out. Higher resolution radio continuum imaging should aid in distinguishing between the single and dual radio continuum source models.

4.2 A possible gravitational radio arc in Abell 370

The second unusual object is a radio continuum source with an arc-like shape and is located near the centre of the galaxy cluster of Abell 370. As such, it could possibly

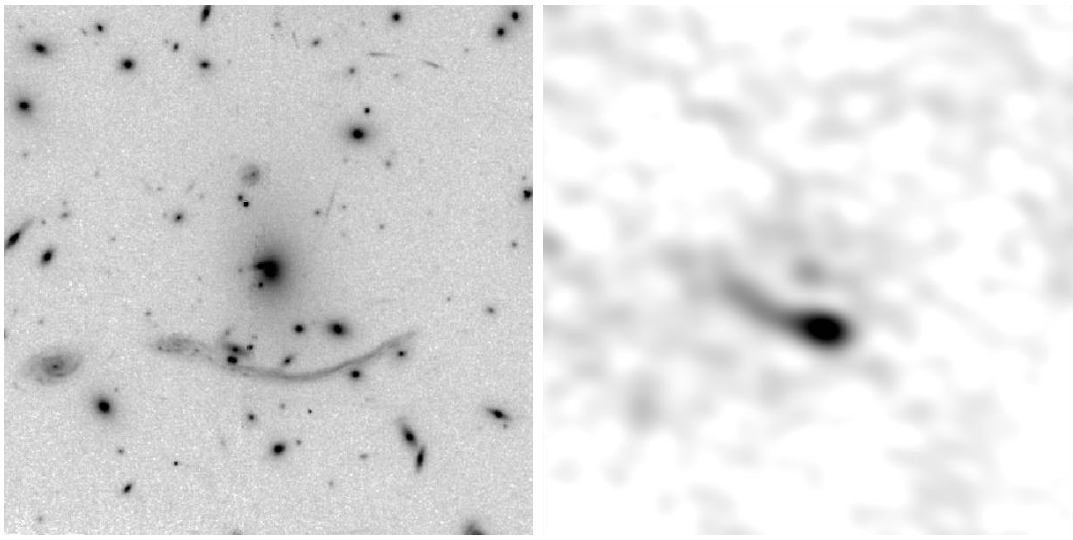

Figure 4.10: The left panel shows the optical *Hubble Space Telescope* image centred on the lower Declination of the two cD galaxies in the galaxy cluster, Abell 370. The right panel shows the radio continuum image of the same region. This image was observed at 1040 MHz and has a synthesised beam size (resolution) of ∼3.3 arcsec. The peak flux of the object is 490 μJy/Beam and the RMS noise is 20 μJy. Both images are 50 arcsec on a side. The darker the grey-scale in both image the brighter the optical/radio flux.

be created by gravitational lensing. Gravitational lensing occurs when light from a distant source is 'bent' by the gravity of a massive object between the source and the observer. The massive object acts like a lens by altering the shape of space around it, changing the path that the light will travel. Since gravitational lensing alters the shape of space it effects all wavelengths of light the same unlike normal lensing (e.g. through a glass lens). The massive, lensing object can be a large galaxy or the core of a galaxy cluster (more massive than a galaxy but also more extended) or a combination of both. If the source and lensing object are precisely aligned with the observer it is possible to produce an image of the source that appears as a complete ring around the lens known as an Einstein ring. If the lensing object is slightly misaligned with the observer, the source will instead form partial arcs around the lens; this is more commonly seen (Fort & Mellier 1994).

Abell 370 contains a giant, bright, optical arc that was the first identified gravitational lensing event by a galaxy cluster (Soucail et al. 1987). This optical gravitational arc is just a little below one of the two massive cD galaxies in the cluster (the cD galaxy at R.A. $02^{\rm h}39^{\rm m}53.1^{\rm s}$ Dec. $-01°34'56''$ J2000). This bright arc is lensed by the combined effects of both the massive cD galaxy and the galaxy cluster itself. This optical arc was so bright that it was possible back in 1986 to obtain a redshift for it. The redshift for the arc was at $z = 0.59$, showing that it was not contained in the cluster at $z = 0.37$ and hence likely a gravitational lensed object.

The left panel of Fig. 4.10 shows the *Hubble Space Telescope* (HST) image of the

region around the lower Declination cD galaxy in Abell 370 which includes the bright optical gravitational arc. This image was taken in 1995 using Wide Field/Planetary Camera II (WFPC II) though the F675W filter (centred ∼6750 Å, which is close to R band). The image is 50 arcsec on a side. Besides the bright optical arc, numerous other shorter and fainter gravitational arcs can be seen in this high resolution image. These are images of different background sources lensed by the cluster.

During a search for radio continuum emission from the Abell 370 galaxies studied in Chapter 3, an arc-like radio source was found within the cluster. This radio source was located just above the well known large optical gravitational arc and just below the nearby cD galaxy. The radio arc can be seen in the right panel of Fig. 4.10. The radio continuum grey-scale has been reversed from that used in Section 4.1.1 above as this made it easier to see the faint tail of the radio arc. The radio continuum image has a synthesised beam size of ∼3.3 arcsec and an RMS noise of 20 μJy. At the observed frequency of 1040 MHz, the peak flux of 490 μJy/Beam is located at R.A. $02^{\rm h}39^{\rm m}53.0^{\rm s}$ Dec. $-01°35'01''$ J2000. The total flux density of the object is between 1.9 to 2.5 mJy, depending on how one exactly defines the extent of the arc. From the head to the end of the tail the object is ∼9.6 arcsec long. The radio continuum emission from the cD galaxy can be seen above the arc. This point source has a peak flux of 148 μJy. The observed optical V band total magnitude for the cD galaxy is 18.3 from the ANU 40 inch observations. In the 1.4 GHz radio continuum survey of FIRST (Becker, White, & Helfand 1995) only the bright point-like head of the arc is seen and has a measured peak flux of 1.07 mJy.

The top panel of Fig. 4.11 shows the grey-scale optical image of this region overlaid with the radio continuum as contours. In the top panel the lowest radio continuum contour is 80 μJy which is 4 times the RMS noise of 20 μJy. As such one can see that the tail of the arc is significantly above the noise level though it is by no means a strong source. The good agreement between the optical and radio astrometry can be seen in the alignment of the optical and radio continuum emission for both the cD galaxy and another galaxy in the bottom left corner of the image. In this image one can clearly see that the radio arc lies above the bright optical arc. The relatively large width of the radio arc compared to the optical arc is likely due to the difference in resolution between the two images; the HST optical image has a resolution ∼0.1 arcsec while the radio image has resolution ∼3.3 arcsec. Higher resolution radio observations would probably find that the radio arc is quite a lot thinner than seen here.

The bottom panel of Fig. 4.11 shows the same image with the radio continuum in grey-scale and the optical overlaid as contours. This makes it easier to see the location of any optical counterparts to the radio arc. As one can now see there is a small optical object near the head of the radio arc, though it is offset somewhat from the centre of the radio head. This optical object does not have a measured redshift. With the large number of galaxies within this region of the cluster core of Abell 370, a chance alignment with an optical object is a significant possibility. Better resolution radio observations may shed light on whether this optical object is aligned with the radio arc.

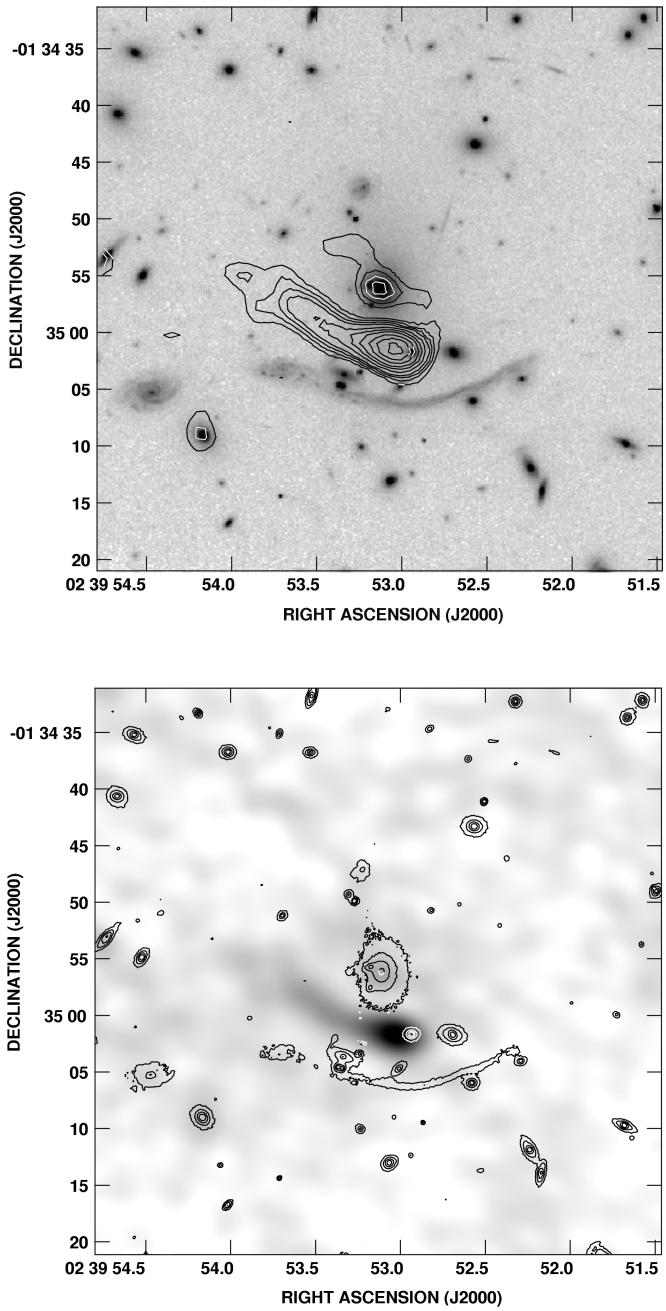

Figure 4.11: The top panel shows the region around the cD galaxy with the optical *Hubble Space Telescope* image as grey-scale and the GMRT radio continuum image as contours. The radio contour levels are 80, 100, 120, 140, 180, 220, 260, 320, 380, 460 μJy/beam. The bottom panel shows the same image except that now the radio is the grey-scale and the optical is shown as contours. Both images are 50 arcsec on a side.

Apparently shortly after the discovery of the bright optical arc in Abell 370, observations were done with the Very Large Array (VLA) to see if there were radio gravitational lensed objects in Abell 370. Nothing was found however, and this null result does not seemed to have been published (this information came from private communication with Mike A. Garrett). The reason for the successful detection of this radio arc in our data is probably due to the combination of the variety of $u - v$ baseline lengths of the GMRT observations as well as the advanced radio imaging techniques used. Abell 370 is almost equatorial (near 0° Declination) which causes problems in the radio imaging. Artifacts are produced around the brighter radio sources that take the form of narrow strips running north-south from the continuum sources. To remove these artifacts a complex procedure of self calibration and peeling was performed (see Section 3.3). Without this work it would be unlikely that the radio arc, which is a relatively faint structure, would be distinguishable in the data.

It is by no means certain that this radio arc is due to gravitational lensing. It is not impossible that it could be a radio jet within the cluster with a tail being bent by interactions with the intracluster medium. However the position of the radio arc between the cD galaxy and the bright optical arc is suggestive of a gravitationally lensed object as it is close to the caustic of the known strong gravitational lens. The shape of the radio arc also matches the general shape seen in the bright optical arc; they are both curving the same way. In order to prove that it is a gravitational lensed radio arc, modelling of the lensing system needs to be done to show that the shape of the arc is possible. One of the uncertainties that would go into this modelling would be the redshift of the radio continuum source being lensed. Deeper optical observations would be needed along with high resolution radio imaging to firmly identify any optical counterpart to the radio arc. Optical spectroscopic observations can then provide the objects redshift.

From the literature research I have done it appears that there are only a few radio gravitational arcs that have been found to date. The large survey of CLASS (Cosmic Lens All-Sky Survey) and JVAS (Jodrell Bank VLA Astrometric Survey) used VLA observations of 16503 sources to search for arcsec-scale lens systems. Using follow-up Very Long Baseline Interferometry (VLBI) on their candidates they found a total of 22 gravitational lens systems of which 2 appear to have some sort of radio arcs or partial Einstein rings (Browne et al. 2003). One of these objects is B1933+503 which was discovered by King et al. (1997). HST observations show a complete Einstein ring in the infrared to complement the substantial arc seen in the radio (King et al. 1998). In Fig. 4.12 the 5 GHz image made with the Multi-Element Radio-Linked Interferometer Network (MERLIN) of B1933+503 is shown. The image is ∼2 arcsec on a side with 40 milliarcsec restoring beam diameter (resolution). This is the best example of a radio gravitational arc in the literature that I could find. The gravitational lens for this system is a large galaxy located at the centre of the image. The scale of this gravitational arc is considerably smaller than the arc seen in Abell 370. However this is the scale of object that CLASS was searching for. As there appear to be few known radio gravitational arcs, further follow up on this object would appear to be scientifically interesting.

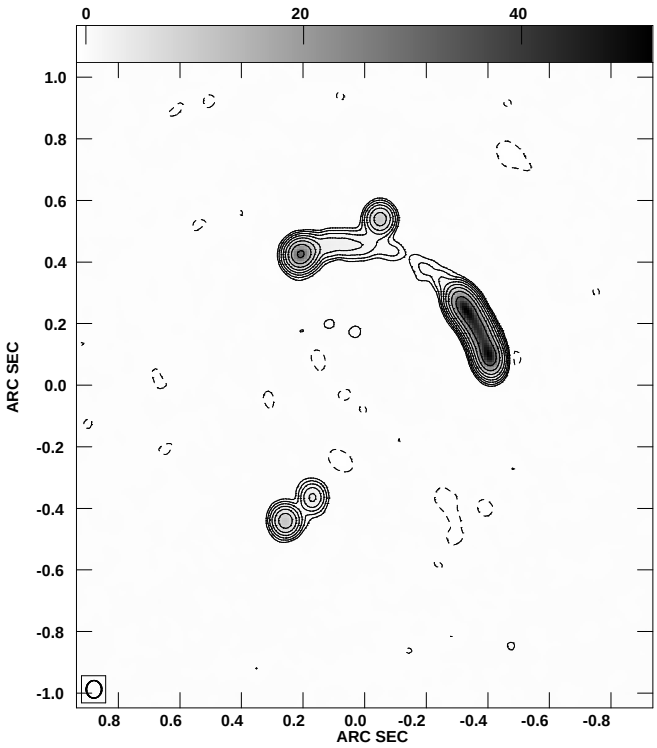

Figure 4.12: This figure shows the radio gravitational lens B1933+503 imaged at 5 GHz with MERLIN (King et al. 1997). The image is ∼2 arcsec on a side with 40 milliarcsec restoring beam diameter (resolution).

Chapter 5

H I Coadding Using SKA Pathfinder Telescopes

Measure what is measurable, and make measurable what is not so.

Galileo Galilei

5.1 Introduction

In this chapter I will show that the Australian SKA pathfinder telescope ASKAP and the South African SKA pathfinder telescope MeerKAT can be used to measure the coadded H I 21-cm emission signal from galaxies out to redshifts $z = 1.0$ using redshifts from the optical spectroscopic surveys of WiggleZ and zCOSMOS. As such, these SKA pathfinders should provide considerable insight into the gas supply available for star formation from redshift $z = 0$ to $z = 1$ (a look-back time of 7.7 billion years), the period over which there is an increase in the cosmic star formation rate density by a factor of 10 (Lilly et al. 1996; Madau et al. 1996; Hopkins 2004).

To directly measure the H I emission signal from individual galaxies at redshifts $z \sim 1$ in reasonable observing times will require the Square Kilometre Array (SKA), a planned future radio telescope with a square kilometre of collecting area (van der Hulst et al. 2004). The major promise of the SKA lies not only in its high sensitivity but also in its large field of view. This will enable the study of H I 21-cm emission from galaxies at significant redshifts in large volumes around the sky. The SKA pathfinders, ASKAP (being built in Australia) and MeerKAT (being built in South Africa), do not possess the large collecting area of the SKA but do have large fields of view. The larger field of view of these SKA pathfinders means that there are many more galaxies (particularly larger galaxies), which can be used in coadded H I observations, in a single telescope pointing compared to other existing radio telescopes such as the GMRT.

Another key advantage of these SKA pathfinders have over existing telescopes is that they are located in some of the quietest places on the planet with respect to radio frequency interference (RFI). This is important as observing H I 21-cm

emission beyond $z \sim 0$ involves observations in some of the most RFI contaminated radio frequencies including some used by the increasingly pervasive mobile phone ($\sim$900 MHz).

The specifications of the ASKAP and MeerKAT telescopes used here have come from various conferences and workshops including 'Science with MIRA' (2007), 'Deep Surveys of the Radio Universe with SKA Pathfinders' (2008), 'Synergies between ASKAP and Large Optical/IR Surveys' (2008) and 'ASKAP Extragalactic H I Science and Coordination Meeting' (2009), the paper by Johnston et al. (2007), and private discussion with the people involved in building them. Information on ASKAP has been easier to obtain and regularly updated while information on MeerKAT has been less readily available.

5.2 The SKA pathfinder telescopes

ASKAP stands for the Australian Square Kilometre Array Pathfinder. It is an Australian led project in collaboration with scientists and engineers in Canada, the Netherlands, United Kingdom and Germany. ASKAP will be built in the mid-west region of Western Australia at the Australian SKA candidate site (Johnston et al. 2007). The 'KAT' in MeerKAT stands for the Karoo Array Telescope, with 'meer' being the Afrikaan word for 'more' (the original KAT design received an upgrade when additional funds were made available by the South African government. A meerkat is also a small, fury mammal). MeerKAT will be built in the Karoo region of the Northern Cape Province which is remote and sparsely populated, with a dry climate. It is also the South African SKA candidate site. Both telescopes are planned to be finished sometime in 2012.

The expected telescope parameters for both telescopes can be found in Table 5.1. Both are radio synthesis telescopes using similar sized dishes of 12 m in diameter and covering similar frequency ranges around 1 GHz. The major difference between the telescopes is that ASKAP has a larger field while MeerKAT is more sensitive with more collecting area and lower system temperature.

ASKAP's larger field of view is due to its use of focal plane array technology to provide multiple beams (32) on the sky. This technology keeps the field of view the same size at all frequencies. However processing the data from so many beams is computationally intensive. This has meant that one can likely only use the 30 inner antennas (longest baseline 2 km) if one wants to observe with all 16384 spectral channels at least in the first few years of ASKAP operation. For radio continuum observations which use appreciably fewer channels all 36 antennas are usable. This limitation will disappear when computers are developed with sufficient power to process all the data that ASKAP produces.

MeerKAT is using standard 'single pixel' feeds, and as such, the primary beam size varies with frequency, becoming larger at lower frequencies (higher H I redshifts). ASKAP's field of view (comparing primary beam sizes) is $\sim$25 times larger than MeerKAT at 1420 MHz (H I at $z = 0$) and $\sim$6 times larger at 700 MHz (H I at

Telescope Parameter	ASKAP	MeerKAT
Number of Dishes	30 (36)	80
Dish Diameter	12 m	12 m
Aperture Efficiency	0.7	0.7
System Temperature (T_{sys})	50 K	30 K
Frequency range	700 to 1800 MHz	700 to 2500 MHz
Instantaneous bandwidth	300 MHz	512 MHz
Primary Beam Width:		
at 1420 MHz (H I $z = 0$)	30 deg^2	1.2 deg^2
at 700 MHz (H I $z = 1$)	30 deg^2	4.8 deg^2
Longest Baseline Length	2 (6) km	10 km
Number of Channels	16384 (2^{14})	16384 (2^{14})
Channel Width	18.31 kHz	31.25 kHz
Velocity Width per Channel:		
at 1420 MHz (H I $z = 0$)	3.9 km s^{-1}	6.6 km s^{-1}
at 700 MHz (H I $z = 1$)	7.7 km s^{-1}	13.2 km s^{-1}

Table 5.1: The expected telescope parameters for the SKA pathfinders of ASKAP and MeerKAT. The ASKAP parameters are accurate as of 5 May 2009 (from private communication with Simon Johnston and other ATNF staff). The MeerKAT parameters are accurate as of 27 July 2008 (from private communication with Justin Jonas, SKA South African Project Office).

$z = 1.0$). MeerKAT with its larger collecting area is ∼4 times as sensitive as ASKAP. Additionally MeerKAT has a larger instantaneous bandwidth (512 MHz compared to ASKAP's 300 MHz bandwidth).

For H I coadding experiments the frequency channel width needs to be smaller than the expected H I velocity width of the combined H I signal. Both telescopes have channel widths less than 30 km s^{-1} at all relevant frequencies (see Table 5.1). This is more than sufficient precision for coadding as the expected signal would be spread over more than 300 km s^{-1}(see Section 3.4). For H I coadding observations with these telescopes, the number of channels used could be reduced from the maximum by 2 to 4 times in order to decrease the considerable amount of data these telescopes generate that needs to be processed. However other scientific projects using the same frequencies may want the full spectral resolution such as H I absorption observations against strong radio continuum sources.

Fig. 5.1 shows the estimated ASKAP 5σ direct detections of H I 21-cm emission from galaxies between redshifts $z = 0.45$ to 1.0 from a year of observation (8760 hours) of a single pointing (this figure is adapted from Johnston et al. (2007)). The redshift range $z = 0.45$ to 1.0 is approximately what the 300 MHz instantaneous bandwidth of ASKAP can cover in a single observation (i.e. from 700 MHz at $z = 1.0$ up to ∼980 MHz at $z = 0.45$).

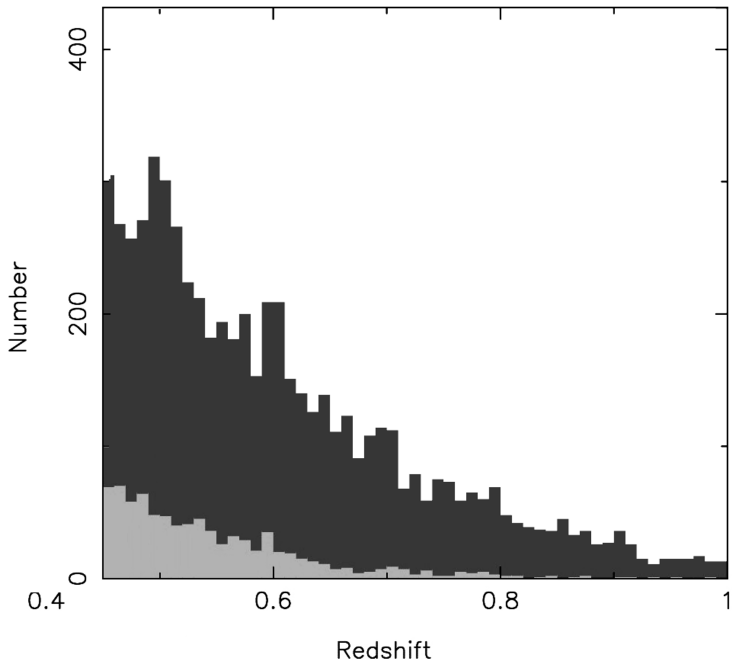

Figure 5.1: This figure shows the estimated ASKAP 5σ direct detections of H I 21-cm emission from galaxies between redshifts $z = 0.45$ to 1.0 from an observation of a year (8760 hours) of a single pointing. The light grey histogram is for a design of ASKAP with 30 dishes and $T_{sys} = 50$ K. The dark grey histogram is for a design of ASKAP with 45 dishes and $T_{sys} = 35$ K. For these estimates it has been assumed that there has been no evolution in the H I mass function. This figure is adapted from Johnston et al. (2007).

The two distributions here are for the so called 'Strawman' and 'Expansion' versions of ASKAP that were assessed by Johnston et al. (2007). The 'Strawman' version has 30 dishes and $T_{sys} = 50$ K and the 'Expansion' version has 45 dishes and $T_{sys} = 35$ K (~2.5 times as sensitive as the ASKAP current parameters). The parameters of ASKAP have since stabilised on the 'Strawman' configuration listed in Table 5.1. These H I direct detections estimates use the H I mass distribution of the nearby universe found in HIPASS Zwaan et al. (2005), making the assumption that there has been no evolution in the H I mass function. If there is evolution in the H I mass function the number of high H I mass galaxies may well be higher at redshift $z = 1.0$, increasing the number of galaxies detected compared to this estimate. However the exact nature of the evolution is unknown, providing the incentive for doing the observation.

Even with a year of observation (8760 hours) only an estimated ~70 galaxies are detected between z =0.95 to 1.0 using the 'Expansion' ASKAP version. These galaxies are likely to be strongly biased towards face-on systems that are easier to

detect with their narrower H I velocity widths. A year of time observing a single field will likely to take at least 3 years to complete and may be difficult to justify for the scientific return on the telescope time. A similar estimation of the H I direct detection of galaxies has not been made for MeerKAT. MeerKAT with its higher sensitivity should detect the same distant galaxy as ASKAP in $1/16^{\rm th}$ the time. However, once ASKAP begins to detect galaxies the number it will find will increase at a much faster rate than MeerKAT due to the larger volume it probes in a single pointing. With either telescope it will take extremely long observations of a single pointing to detect galaxies out to $z = 1.0$ and then only those with the highest H I flux densities (high H I mass, face on spiral galaxies).

Coadding the signal using optical redshift surveys will dramatically increase the number of galaxies for which an average H I mass can be determined. For coadding H I galaxies, it is preferable if the galaxies are unresolved by the synthesised beam of the telescope as one cannot see the individual galaxies to take into account their H I gas extent. A 30 kpc wide galaxy will be ∼9.1 arcsec across at $z = 0.2$ and ∼3.7 arcsec across at $z = 1.0$. The synthesised beam of both MeerKAT and ASKAP based on their longest baselines would not resolve a galaxy of this size for the majority of the lower frequency ranges (higher H I redshift ranges). Even larger galaxies of 60 kpc across in H I 21-cm emission will be unresolved by the pathfinders for the higher redshifts approaching $z = 1.0$. For the coadding estimates made in this chapter it has been assumed that galaxies are unresolved.

5.3 The optical redshift surveys considered for H I coadding

The optical surveys considered here for H I coadding are the WiggleZ survey for use with ASKAP and the zCOSMOS survey for use with MeerKAT. The main parameters of the two optical redshift surveys are listed in Table 5.2. Both surveys are still in progress so the data used here is only part of what the final surveys will contain. Both surveys will have been completed long before either ASKAP or MeerKAT become operational.

WiggleZ is an optical spectroscopic survey of 200,000 star-forming galaxies selected from a combination of GALEX ultraviolet and SDSS/RCS2 optical imaging. The main goal of the survey is the measurement of baryon acoustic oscillations in the galaxy clustering pattern at redshift between $z = 0.5$ and 1.0. This will provide an improved determination of the equation of state of dark energy. The survey is being carried out using the AAOmega spectrograph on the Anglo-Australian Telescope (AAT) and is expected to be completed in 2010. The survey comprises 7 fields each with minimum size of 100 deg^2. These large fields make the WiggleZ survey a good match to the field of view of ASKAP.

zCOSMOS is an optical spectroscopic survey undertaken in the COSMOS field using the VIMOS spectrograph on the VLT (Lilly et al. 2007). The COSMOS field is a 1.7 deg^2 field imaged by the Advanced Camera for Surveys (ACS) on the

Survey Parameter	WiggleZ	zCOSMOS bright
Instrument & Telescope	AAOmega on the AAT	VIMOS on the VLT
Target Selection	ultraviolet from GALEX	optical $I_{AB} < 22.5$
Survey Area	7 fields each with minimum size of 100 deg^2	the COSMOS field a single field 1.7 deg^2
Primary Redshift Range	$0.5 < z < 1.0$	$0.1 < z < 1.2$
Survey Timeline	2006 to 2010	2005 to 2008
Number z by survey end	~200,000	~20,000

Table 5.2: The parameters of the optical redshift surveys of WiggleZ and zCOSMOS.

HST and has been observed at many other wavelengths (Scoville et al. 2007). The primary goals of the zCOSMOS survey is to study the environments of COSMOS galaxies from the small scale of galaxy groups to the larger scale of the cosmic web and to provide spectroscopic information on the nature of the COSMOS galaxies. The relevant part of the survey for this work is the zCOSMOS bright survey. The targets for this survey are 20,000 galaxies with magnitude limit of $I_{AB} < 22.5$ that span the redshift range $z = 0.1$ to 1.2 across the whole 1.7 deg^2 field . The 1.7 deg^2 field of the zCOSMOS survey makes it a good match to MeerKAT's field of view.

5.4 The estimated observed coadded H I 21-cm emission signal

Estimates have been made of the coadded H I 21-cm emission signal that would be observed from galaxies in these optical redshift surveys using the SKA pathfinders. For these estimates the average H I gas mass that would be measured in redshift bins of width $\Delta z = 0.05$ has been considered. It has been assumed that all galaxies are at the luminosity distance of the centre of each redshift bin. This introduces only a small bias as the distance effects from galaxies at either end of the redshift bin will tend to cancel each other out.

As the galaxies are selected in the optical they are more likely to be 'edge-on' systems that have large H I velocity widths. This is because these galaxies are more common when considering randomly orientated galaxies, and they also tend to have higher optical surface brightnesses (see Section 3.4 for a detailed discussion of this selection effect). From the HIPASS survey (Meyer et al. 2004) a galaxy with H I mass $M_{HI} \sim 10^{10}$ $M_\odot$ (a large H I mass galaxy) has a maximum velocity width of $\sim$400 km s^{-1}, i.e. the value for an edge on system. When considering the velocity extent of the coadded H I signal, one must also factor in the error in the optical redshifts that will broaden out the signal. For the redshift catalogues considered this can be as large as 100 km s^{-1}. Considering these factors, the estimated H I coadded signal used in the modelled observations was assumed to span at most 600 km s^{-1}.

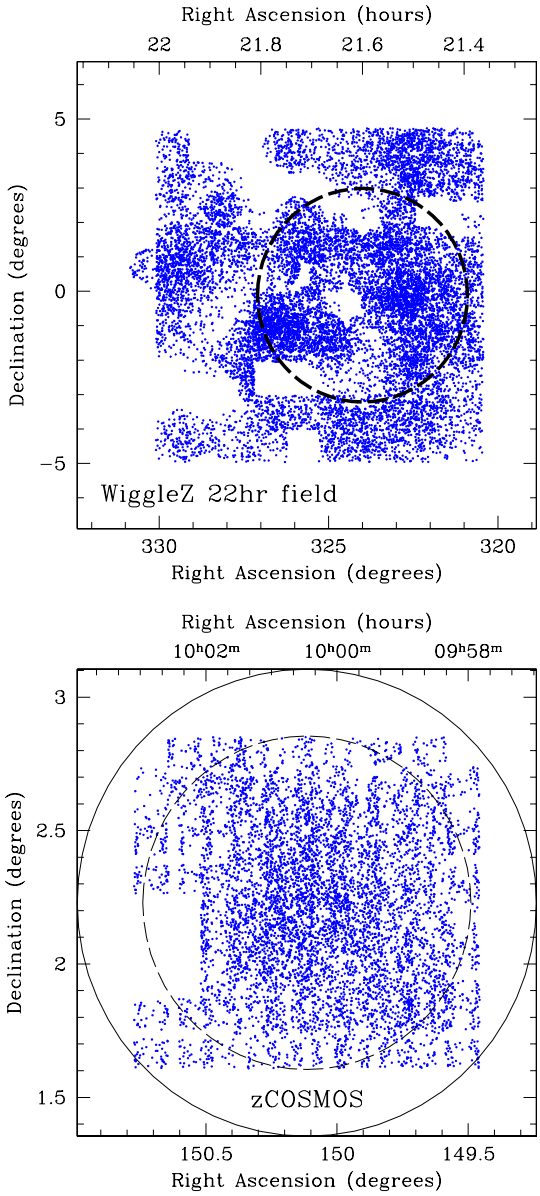

Figure 5.2: The top panel shows the state of the observations of the 22 hour WiggleZ field as of May 2009. The points are the 14,342 WiggleZ galaxies with redshifts between $z = 0.45$ to 1.0. The circle covers an area of 30 deg^2, the same area as the ASKAP field of view (though it may differ in shape). There are 7009 WiggleZ galaxies within the circle; these are the galaxies considered in the ASKAP simulation. The bottom panel shows the state of the observations of the zCOSMOS field as of March 2008. The points are the 7118 zCOSMOS galaxies between $z = 0.2$ to 1.0 and the figure is ∼78 arcmin on a side. The dashed circle is the MeerKAT primary beam size (FWHM) at 1420 MHz (H I at $z = 0$) with diameter 75 arcmin. The solid circle MeerKAT beam size at 1000 MHz (H I $z \sim 0.4$) with diameter of 105 arcmin. The MeerKAT beam size at H I redshift $z = 1.0$ has diameter of 149 arcmin which is larger than the size of the figure.

The uncertainty in the measured coadded H I 21-cm emission signal is approximately proportional to the square root of the velocity width used.

For calculating the ASKAP estimate a 30 deg^2 region from the WiggleZ survey was chosen and the galaxies with redshifts between $z = 0.45$ and 1.0 selected (the redshift range that ASKAP can cover in a single observation). The galaxies chosen are a subsample of the WiggleZ 22 hour field which is shown in the top panel of Fig. 5.2. This field is larger than the ASKAP field of view so a smaller region of this field which is well sampled with redshifts has been selected. There are 7009 WiggleZ galaxies in the chosen ASKAP pointing.

A circle covering an area of 30 deg^2 was used to select the galaxies. The actual ASKAP field of view is a complex shaped similiar to a square made up of multiple circles for the multiple beams of the focal plane array. The exact details of this field of view are still not fixed in the ASKAP design. However, the area on the sky is the same as that for the field of view used here and the number of galaxies in such an area on the sky for the WiggleZ survey should be similar. The chosen ASKAP field is not completely filled with WiggleZ observations as yet but will have been by the end of the survey. Redshifts in contiguous fields are necessary for the WiggleZ primary science objectives.

WiggleZ is targeting the brightest star-forming galaxies by selecting the galaxies in the ultraviolet. It is expected that these galaxies will contain the majority of the H I gas. This should be true if the star-formation H I correlation that is seen in the nearby universe continues to hold true at higher redshifts. It is known that this trend for galaxies appears to continue to hold true at $z = 0.24$ and $z = 0.37$ (see Section 2.4.3 and Section 3.7.1).

The zCOSMOS field was chosen for the MeerKAT estimate with galaxies selected between $z = 0.2$ and 1.0. This is the range of redshifts that MeerKAT can cover in a single observation using its instantaneous bandwidth of 512 MHz (i.e. from 700 MHz at $z = 1.0$ up to $\sim$1183 MHz at $z = 0.2$). The zCOSMOS field is shown in the bottom panel of Fig. 5.2. There are 7118 galaxies in chosen redshift range. Unlike the WiggleZ survey, the zCOSMOS survey does not have any constraint on the type of galaxy observed except for a simple I band magnitude limit. This means that many of the galaxies with redshifts are likely to be early-type galaxies that have little or no H I gas. The zCOSMOS sample is found to contain $\sim$65 per cent star-forming, blue, disk-dominated galaxies (Mignoli et al. 2008). As additional information was not avaliable it has been assumed that 65 per cent of the galaxies contain H I gas. As result 4627 galaxies are considered in this analysis.

Fig. 5.3 shows the estimate of the measured coadded H I signal using ASKAP targeting the selected WiggleZ galaxies. Fig. 5.4 shows the estimate using MeerKAT targeting the selected zCOSMOS galaxies. In each of these two figures the top panel is for 100 hours of telescope observations of the field and the bottom panel for 1000 hours ($\sim$10 per cent of a year).

The bottom part of each of these plots is the histogram of redshifts for the optical galaxies considered in each case. These histograms are broken up into 0.05 redshift bins. They range from $z = 0.45$ to 1.0 for the WiggleZ galaxies and from $z = 0.2$

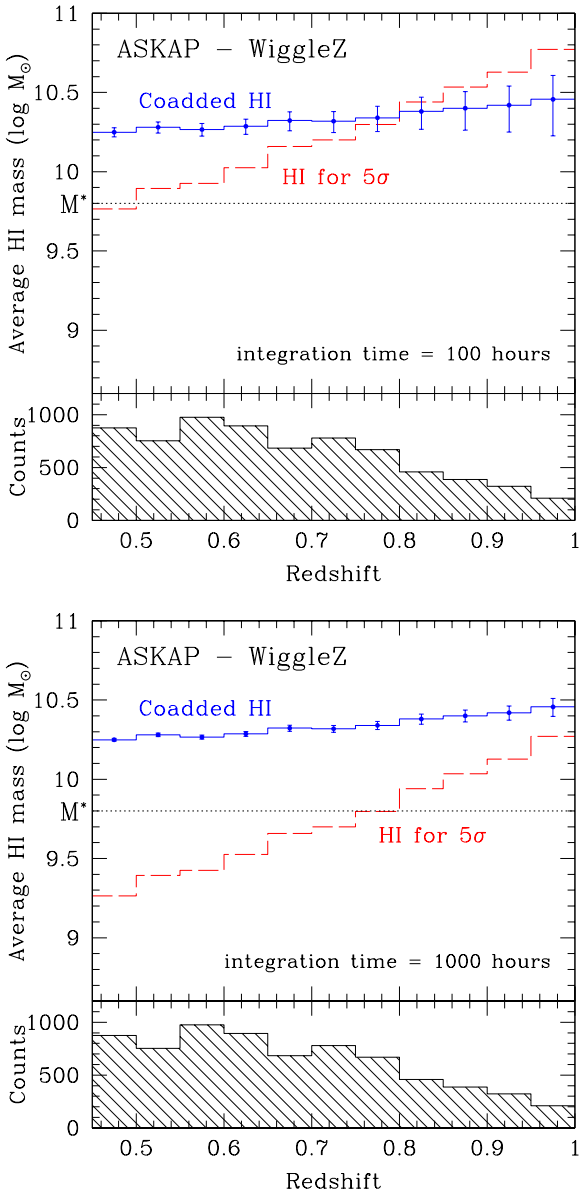

Figure 5.3: The panels show the estimated H I coadded signal that would be measured using ASKAP targeting the selected WiggleZ galaxies. The top panel is for 100 hours of ASKAP observations and the bottom panel for 1000 hours. The bottom part of each plot shows the histogram of the WiggleZ galaxies considered. This is broken up into 0.05 redshift bins from $z = 0.45$ to $z = 1.0$. The upper part of each plot shows the average coadded H I mass that would be measured for this number of galaxies. The dashed line shows the average H I gas mass required for this number of galaxies in order to make a coadded 5σ measurement; this is the minimum average amount of gas the galaxies can have and still be measurable with ASKAP. The solid line is the expected average H I gas mass for this number of galaxies assuming that they are the most gas rich galaxies in the volume. The error bars for this measured average are shown in the centre of the redshift bins. The dotted line is the value of M^*_{HI} at $z = 0$ (Zwaan et al. 2005).

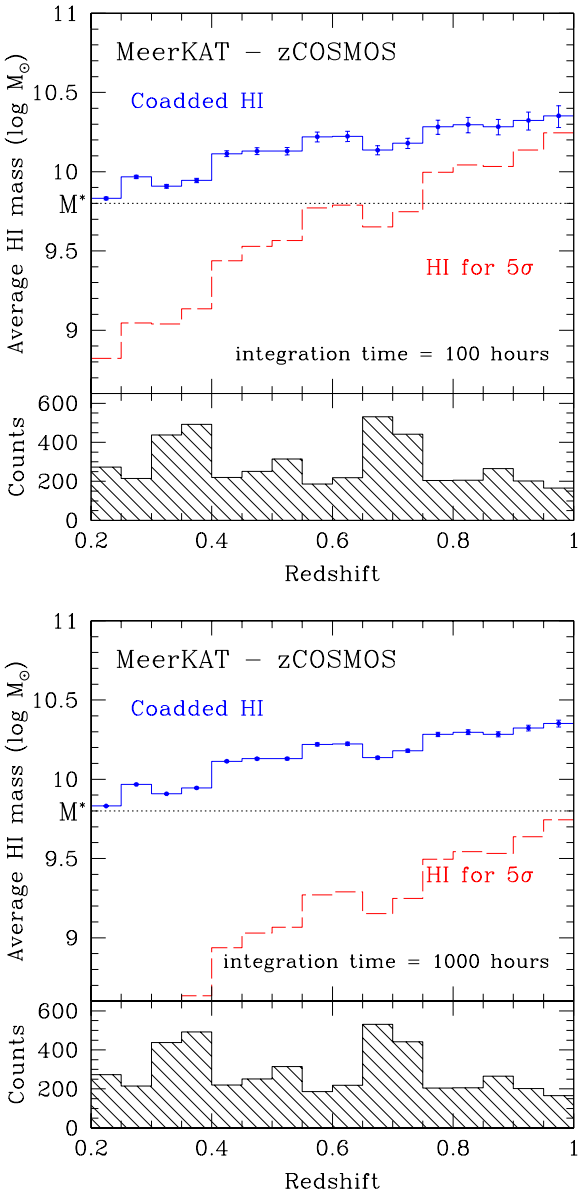

Figure 5.4: The panels show the estimated H I coadded signal that would be measured using MeerKAT targeting the selected zCOSMOS galaxies. The top panel is for 100 hours of MeerKAT observations and the bottom panel for 1000 hours. The bottom part of each plot shows the histogram of the zCOSMOS galaxies considered which is broken up into 0.05 redshift bins from $z = 0.2$ to $z = 1.0$. The upper part of each plot shows the average coadded H I mass that would be measured for this number of galaxies. The dashed line shows the average H I gas mass required for this number of galaxies in order to make a coadded 5σ measurement; this is the minimum average amount of gas the galaxies can have and still be measurable with MeerKAT. The solid line is the expected average H I gas mass for this number of galaxies assuming that they are the most gas rich galaxies in the volume. The error bars for this measured average are shown in the centre of the redshift bins. The dotted line is the value of M^*_{HI} at $z = 0$ (Zwaan et al. 2005).

to 1.0 for the zCOSMOS galaxies. The distribution shown in these histograms are quite different for the two surveys. For the WiggleZ galaxies there is a relatively smooth decrease in the number of galaxies detected with redshift. This is the expected distribution for a large magnitude limited sample as only the brighter galaxies will be detected at the higher redshifts. The distribution of the zCOSMOS galaxies is quite different with large increases in the number of galaxies seen in the redshift ranges from $z = 0.3$ to 0.4 and from $z = 0.65$ to 0.75. The smaller volume probed in the zCOSMOS survey means that cosmic variance is a considerable effect. The zCOSMOS survey at each redshift only samples a relatively small part of the cosmic web of galaxies as seen in redshifts surveys like the 2dF Galaxy Redshift Survey (Colless et al. 2001). This results in the survey selecting regions of high and low galaxy density at different redshifts. The volume that the WiggleZ galaxies cover at each redshift is sufficiently large that this variation has been smoothed out. The number of galaxies considered here from the two surveys are similar despite this volume difference. This is because the zCOSMOS survey includes galaxies down to a much fainter optical brightness than the WiggleZ survey.

Above the redshift histograms in each plot is plotted the average coadded H I mass that would be measured for this number of galaxies. The dashed line shows the average H I gas mass required for this number of galaxies in order to make a coadded 5σ measurement in 100 hours of observations for the plots on the top and 1000 hours for the plots on the bottom. This calculation is based purely on the number of galaxies and the integration time of the telescope; no information on the galaxies is included. This 5σ level gives one an idea of the minimum average H I gas content the galaxies studied need to have in order to make a useful scientific measurement. As MeerKAT uses single-pixel feeds, galaxies away from the primary beam centre do not receive the full sensitivity of the telescope. A correction has been included for this effect which raises the noise level in the estimated coadded H I mass measurements by $\sim$1.3 times. ASKAP using a focal plane array should be equally sensitive across is entire field of view so no correction is required. As expected the 5σ level reached by MeerKAT extends to lower H I masses than ASKAP for the same integration time because of its higher sensitivity.

The solid line in the plots is the expected average H I gas mass for this number of galaxies, assuming that they are the most gas rich galaxies in the volume. The H I masses of the galaxies are determined from the H I mass function of HIPASS at $z = 0$ (Zwaan et al. 2005) by assuming they are the most gas rich galaxies in the comoving volume probed by each redshift bin. This involves integrating the Schechter function for the comoving volume down in H I mass until the number of H I galaxies matches the number of galaxies with optical redshifts in each bin. The average H I mass can then be calculated for the galaxies. Due to the steepness of the Schechter function, the majority of the H I masses generated lie relatively close to the value of smallest H I mass galaxy included. As such, the estimated average H I mass is relatively robust to missing a few of the H I mass galaxies.

The expected error bars for this measured average are shown in the centre of the redshift bins on this solid line. These are determined from the telescope param-

eters and the length of the observation (either 100 or 1000 hours). These average H I estimates assume that there has been no evolution in the H I mass function with redshift. It is likely that any evolution will increase the average H I mass gas of the galaxies making the measurements easier to do. Both the WiggleZ redshifts considered and to a lesser extent the zCOSMOS redshifts do not contain all the redshifts for all the relevant high H I mass galaxies that lie within the volumes they probe. This makes the assumption that the galaxies sampled are the most gas rich galaxies in the volume less likely to be true. This will be less of a problem when the surveys are finished but this incompleteness will still be there at some level. Thus one could look at these estimates for the average H I mass as a lower limit to the likely true value that includes these missing galaxies. Despite this, these estimates are relatively insensitive to missing galaxies and galaxy evolution is likely to increase this value, the average H I mass calculated should be reasonable estimates.

Based on this analysis a 100 hour observation with ASKAP can make a 5σ measurement of the average H I mass of the WiggleZ galaxies considered out to redshift $z \sim 0.8$. With an observation lasting 1000 hours one can make measurements out to redshift $z = 1.0$ with greater than 5σ precision. However this is only quantifying the gas in the highest H I mass galaxies well above M^*_{HI} at $z = 0$ that are spread across the large volume probed. Using the above analysis a 100 hour observation with MeerKAT make a 5σ can measurement of the average H I mass of the galaxies out to redshift $z \sim 1.0$. In 1000 hours with MeerKAT, the precision is even higher, being $\sim 20\sigma$ at $z \sim 1.0$. This higher precision is despite the zCOSMOS galaxies being smaller H I galaxies than those in WiggleZ survey and is due to the higher sensitivity of MeerKAT. Nonetheless the galaxies from zCOSMOS are still quite H I massive since in the esitmate made they are all still above M^*_{HI} in gas mass. These estimates of the precision of these telescope measurements are not too dependant on the current parameters of either ASKAP or MeerKAT. Doubling the system noise for either telescope makes the 100 hour observations not as attractive but the 1000 hour observations still lead to measurements at greater than the 5σ level for all redshifts.

Due to the large area of the sky covered by WiggleZ it is possible to select many non-overlapping ASKAP pointings that are well covered by optical redshifts. This allows for a different observing strategy where instead of observing a single field for a long time, one spreads the observing time across multiple fields and coadd the H I emission signal from all the galaxies in all these fields. For example instead of observing 1000 hours on one pointing one might observe 100 hours on 10 ASKAP pointings. As long as the optical redshift distribution across each of the fields is similar the coadded H I signal from the single deep pointing and from the combination of the multiple pointings should be similar. The reason to observe multiple fields rather than one single deep field are:

- to increase the variety of galaxies observed. This avoids problems with cosmic variance in each redshift bin and allows for a greater range of subsamples for which the coadded H I signal can be examined.

- to avoid any systematic effects in the ASKAP data that may arise in very long single pointing integrations, e.g. incompelete removal of residual artifacts from radio continuum sources.
- to allow for easier scheduling of ASKAP telescope time by having a choice of pointings.
- to support other science with the observations that want to cover more area such as H I absorption studies.

The main reason to not observe multiple fields is the extra effort in obtaining optical redshifts for extra fields for no gain in coadded H I signal to noise for the same combined observing time. This is only an issue if the optical redshifts are not pre-existing and one has to go out and obtain them independently. There are no similar large area surveys which MeerKAT can take advantage of. However many current and planned deep redshifts surveys are ∼1 degree on the sky which is well matched to MeerKAT's field of view. Additionally, galaxy clusters at redshifts $z > 0.4$ cover less than 1 degree on the sky, and as such, are better matched to observations with MeerKAT.

5.5 The scientific significance of the surveys

In the previous section it has been established that it is possible in reasonable integration times using the SKA pathfinders ASKAP and MeerKAT to make coadded H I mass measurements out to redshift $z = 1.0$. The question now is what science one can do with this information.

The primary science goal of such observations would be to place constraints on the cosmic H I gas density with redshift as this is currently highly uncertain (see Section 1.2.2). The H I coadding using the SKA pathfinders will provide information on the high H I mass end of the galaxy distribution but will not provide much, if any, information on the smaller galaxies. As such, there will be a limit to the amount of information one can obtain on the cosmic neutral gas density especially at the higher redshifts. One will obtain a robust lower limit of the total H I gas density across the redshift range observed. Utilising the known H I mass function at $z \sim 0$ and the observed evolution in optical luminosity functions, one could create an estimate of the distribution of the low H I mass galaxies at these redshifts. This can then be used with the pathfinder observations to estimate the total cosmic H I gas density at the observed redshifts (see Section 6.2 for some thoughts on how the H I gas may be distributed at high redshift).

With the longer 1000 hour observations, there should be sufficient signal so that one could break the observed galaxies up into subsamples and so measure their coadded average H I mass. One can then examine how the H I gas distribution in galaxies varies in different galaxy density environments with redshift. One could examine other subsamples galaxies based on their observed star formation rate, on

their optical colour or optical magnitude. The observation can also be used to examine the star formation correlation with H I mass in galaxies during the period of extreme star formation activity in the universe at redshifts approaching $z = 1.0$. This should give an idea of the precise cause of the higher star formation rates seen at these higher redshifts. Stacking experiments to see if there is any H I gas in the non-star-forming, early-type galaxies in zCOSMOS may provide insight into the formation and evolution of these galaxies which are now seen to be generally gas poor.

The information on the velocity field of individual galaxies is lost when they are stacked. Trying to make a statistical measurement of the galaxies velocity width would be difficult. One would need to take into account the orientation of the galaxies with respect to the observer. Determining this in the optical imaging would be difficult as the galaxies subtend small angles and are optically faint. Additionally their optical redshifts not only have considerable random errors but also have systematic errors that may be difficult to untangle. The H I 21-cm signal from the gas in a galaxy can travel mostly unimpeded through the galaxy with minimal absorption. Dust in a galaxy obscures much of the optical light so that the light that is seen comes mostly from the surface of the galaxy. This may create a bias in the observed optical redshift so that it does not match up exactly with the centre of the H I gas velocity distribution. For example a galaxy may have a strong spiral arm which is moving in the direction of the observer and from which the main component of the optical redshift information comes from. This observed redshift would be substantially offset from the H I redshift. Identifying this type of effect in the optical would be difficult due to the small angular size of the galaxies at the higher redshifts. The possible bias in the optical redshift is taken care of in the H I stacking mass measurements by allowing the H I 21-cm integration velocity window to span a large width. This ensures that all the signal from the coadded galaxies is measured, at the price of a slightly higher noise level. This type of bias would make drawing any useful scientific information on H I velocity widths from stacked galaxies unlikely.

There may well be new larger optical redshifts surveys that one could use for H I coadding with these SKA pathfinders by the time they come online. Additional redshift measurements in these fields to probe optically fainter galaxies at these redshifts may not necessarily improve the signal to noise of the coadded H I mass measurements. This is because of the inclusion of increasing numbers of lower H I mass galaxies, as the low mass end of the H I mass function is probed. (see Section 1.3.2). What additional redshift measurements will do is provide for a larger range of subsamples of galaxies for which H I measurements could be made, increasing the possible science questions that can be addressed. The more subsamples one can break the data into and still have measurable H I signal, the closer one comes to having a measurement similar to what would be obtained from detecting the H I gas content of the galaxies individually.

Chapter 6

Conclusion

> There's two possible outcomes: if the result confirms the hypothesis, then you've made a discovery. If the result is contrary to the hypothesis, then you've made a discovery.
>
> Enrico Fermi

6.1 Summary of thesis results

The main focus of this thesis is the measurement of the gas content of the Fujita galaxies at $z = 0.24$ and the gas content of galaxies around the Abell 370 a galaxy cluster at $z = 0.37$. The Fujita galaxies are star-forming, field galaxies at $z = 0.24$ (a look-back time of ∼3 Gyr) that were selected to be Hα-emitting (see Chapter 2). The H I 21-cm emission signal from 121 of these galaxies was coadded to give a measurement of their average atomic hydrogen gas mass of $(2.26 \pm 0.90) \times 10^9$ M$_\odot$. This H I signal translates into into a cosmic density of neutral gas at $z = 0.24$ of $\Omega_{gas} = (0.91 \pm 0.42) \times 10^{-3}$ (an H I density = $(9.5 \pm 4.4) \times 10^7$ M$_\odot$ Mpc^{-3}). This value is consistent with previous measurements of the neutral gas density from damped Lyman-α measurements at a similar redshift. These observations also showed that the relationship between Hα luminosity and the restframe 1.4 GHz radio continuum emission in star-forming galaxies at $z = 0.24$ is consistent with the correlation found at $z = 0$. Additionally, the relationship between galaxy star formation rate and galaxy H I mass at $z = 0.24$ was shown to be consistent with the correlation found at $z = 0$. These two results suggest that the process of star formation in field galaxies is not significantly different 3 billion years ago from the present day, even though the star formation rate was ∼3 times higher.

Abell 370 is a large galaxy cluster at a redshift of $z = 0.37$, a look-back time of ∼4 billion years. 324 galaxies around this cluster were examined for H I gas (see Chapter 3). From coadding the H I 21-cm emission signals for all these galaxies, an average H I mass of $(6.6 \pm 3.5) \times 10^9$ M$_\odot$ is measured. Considering only the 105 optically blue galaxies an average H I mass of $(19.0 \pm 6.5) \times 10^9$ M$_\odot$ is measured. Abell 370 is found to have considerably more H I gas than Coma, a cluster

of similar size. The average H I mass measurements for galaxies around Abell 370 are ∼10 times higher than similar measurements made from galaxies around Coma. The measured H I density around the galaxy cluster Abell 370 is ∼8 times higher than around Coma. These results indicate that there has likely been substantial evolution in the gas content of clusters over the past ∼4 billion years. Despite the appreciable H I gas content of the Abell 370 galaxies, there is evidence that environmental effects reduce the gas content of the galaxies, similar to what is seen in nearby clusters. The galaxies close to the cluster core (within the R_{200} radius) have an average H I masses smaller by a factor of ∼3.5 than galaxies outside this region. The optically blue galaxies outside the hot, intracluster medium of the cluster core have a higher average H I gas mass than that found from the complete sample of blue galaxies around Abell 370. Although the galaxies around Abell 370 have high H I gas contents, they have similar galaxy properties to present day galaxies: the Abell 370 galaxies have normal H I mass to optical light ratios and have a similar correlation between their star formation rate and H I mass as found in nearby galaxies. The average star formation rate derived from [OII] emission and from de-redshifted 1.4 GHz radio continuum for the Abell 370 galaxies follows the correlation found in the local universe.

The reason that H I 21-cm emission could be detected in Abell 370 despite being at a higher redshift and having less observation time than the Fujita galaxies (GMRT observations of 63 hours vs. 80.5 hours) is primarily due to the difference in size between the galaxies in the two fields. The optically faintest of the Abell 370 galaxies is of order the same luminosity as the most luminous of the Fujita galaxies. The trend where galaxies with the most H I gas are optically luminous (Doyle et al. 2005) does not appear to have changed. The converse is not true; the most optically luminous galaxies do not necessarily have the most H I gas. In fact they may have none, or nearly none, as seen in the red galaxies around Abell 370 (Section 3.5.1).

In the GMRT observations of Abell 370 two unusual radio continuum objects were found (see Chapter 4). One is the 'DP Structure' which appears to be a head-tail source lying within a group of galaxies at redshift $z = 0.326$. Its strange shape is most likely due to a combination of: (1) the motion of the source through the intragroup gas bending the radio jets and (2) having an initial orientation of the radio jets almost aligned with the observers line of sight. The other unusual radio continuum source has an arc-like shape object and is located near the centre of the galaxy cluster Abell 370. This source could be a radio gravitational arc lensed by the cluster as it lies just above a major gravitational arc, long known from optical imaging.

In additional to making coadded measurements of the H I gas content of distant galaxies, work has been done to assess the prospects for using SKA pathfinder telescopes of ASKAP and MeerKAT to do similar observations (Chapter 5). Estimates of the coadded H I signal measurable using the ASKAP with the optical redshifts from the WiggleZ survey and similar estimates using MeerKAT and the optical survey zCOSMOS have been made out to redshift $z = 1.0$. These show that with only 1000 hours of observation one can make precise measurements of the average

H I mass of the coadded galaxies all the way out to to redshift z =1.0 with these telescopes.

6.2 Ideas on the evolution of gas in galaxies

In this section I present some thoughts on the evolution of gas in galaxies developed during the PhD. These ideas are an attempt to draw together the results of the thesis with the literature measurements of the cosmic H I density, cosmic star formation rate density and cosmic stellar mass density. Much of what is presented are only hypotheses. Possible experiments to test these hypotheses are outlined.

6.2.1 Gas for star formation

Both the Fujita galaxies at $z = 0.24$ and the galaxies around Abell 370 at $z = 0.37$ have measured gas contents that appear to be considerably more than that found in similar volumes in present day. Additionally the galaxies in these samples follow the same power law relationship between their star formation rate and their H I mass as seen in nearby galaxies by Doyle & Drinkwater (2006). This suggests that the observed higher star formation in these galaxies is due to their higher gas content. This result creates a problem: if the star formation rate in a galaxy is driven by its H I gas content, why does the cosmic H I gas density not increase dramatically like the cosmic star formation rate density?

The star formation rate density of the universe is seen to increase by ∼10 between the present time and $z \sim 1$ (see Fig. 1.5). The H I gas density of the universe is seen to rise by only at most a factor ∼2 between the present time and $z > 3$ (see Fig. 1.8). Indeed an almost constant cosmic H I density is consistent with much of the current data, especially with the large errors at low redshift. From these results one could naively suggest that there has been minimal evolution in the gas content of galaxies at least compared to the evolution seen in their star formation rate. However the relationship observed between star formation rate and a galaxy's H I mass would seem to suggest otherwise. This power law relationship is shown below:

$$\log(\mathrm{SFR}) = m \log(\mathrm{M_{HI}}) + b \tag{6.1}$$

$$\mathrm{SFR} = a\,(\mathrm{M_{HI}})^m \tag{6.2}$$

where SFR is the star formation rate of a galaxy, $\mathrm{M_{HI}}$ is the H I mass of that galaxy and m, b and a are fitted constants. Doyle & Drinkwater (2006) found that in nearby galaxies $m \sim 1.7$ and $a \sim 6.5\text{e-}17$. The work in this thesis has shown that this appears to be unchanged for galaxies at $z = 0.24$ and $z = 0.37$. To calculate the star formation rate density one sums up the star formation rates of the galaxies within a sufficiently large volume. Similarly the H I gas density is found by summing up the H I gas content of galaxies in a sufficiently large volume. These relationships are shown below:

$$\mathrm{SFRD} = \frac{\Sigma\,\mathrm{SFR}}{\mathrm{Vol}} \qquad\qquad \rho_{\mathrm{HI}} = \frac{\Sigma\,\mathrm{M_{HI}}}{\mathrm{Vol}} \tag{6.3}$$

where SFRD is the star formation rate density, SFR are the individual star formation rates of the galaxies in a volume of size Vol. Similarly ρ_{HI} is the H I density and $\mathrm{M_{HI}}$ are the individual H I mass of that galaxies in a volume of size Vol. Substituting equation 6.2 into the above gives:

$$\mathrm{SFRD} = \frac{a}{\mathrm{Vol}} \times \Sigma\,(\mathrm{M_{HI}})^m \tag{6.4}$$

This relationship shows that the star formation rate density is not directly proportional to the H I gas density but depends on how the H I gas is distribution among the galaxies. Due to the exponent in Equation 6.4, galaxies with high H I masses will contribute more to the star formation rate density than galaxies with lower H I masses than a simply ratio of their H I masses would initially suggest. This relationship can explain the apparent differences in the evolution of the star formation rate density and the H I gas density. To increase the star formation in the past all one requires is for there to be more high H I mass galaxies. By also having fewer low H I mass galaxies one can keep the H I gas density from rising significantly without diminishing the star formation rate density. That is, one can explain the substantial evolution in the cosmic star formation density and the minimal evolution in the cosmic H I gas density by postulating an evolving H I mass function.

To test whether an evolving H I mass function could produce a sufficiently high star formation rate density, a series of H I mass Schechter functions (Schechter 1976) were generated that spanned the relevant parameter space. The H I mass Schechter function has the form:

$$\Theta\left(\frac{\mathrm{M}}{\mathrm{M}^*}\right)\ \mathrm{d}\left(\frac{\mathrm{M}}{\mathrm{M}^*}\right) = \Theta^*\left(\frac{\mathrm{M}}{\mathrm{M}^*}\right)^{\alpha} \exp\left(\frac{-\mathrm{M}}{\mathrm{M}^*}\right)\ \mathrm{d}\left(\frac{\mathrm{M}}{\mathrm{M}^*}\right) \tag{6.5}$$

where M is the H I mass of individual galaxies and where M^*, α and Θ^* are the fitted Schechter function parameters. M^* is the characteristic H I mass, the point of change over between the power and exponential decline of the Schechter function. α is the low mass end slope and Θ^* is the normalisation of the function. One can calculate the H I density directly from the Schechter function as shown below:

$$\rho_{\mathrm{HI}} = \int_0^{\infty} \mathrm{M}\ \Theta\left(\frac{\mathrm{M}}{\mathrm{M}^*}\right)\ \mathrm{d}\left(\frac{\mathrm{M}}{\mathrm{M}^*}\right) \tag{6.6}$$

$$= \Theta^*\,\mathrm{M}^*\,\Gamma(\alpha+2) \tag{6.7}$$

where $\Gamma(\mathrm{x})$ is the gamma function. Similarly one can use the SFR–H I mass correlation to derive an estimate of the star formation rate density for a given Schechter function as shown below:

$$\mathrm{SFRD} = \int_0^{\infty} \mathrm{a}\,\mathrm{M}^{\mathrm{m}}\ \Theta\left(\frac{\mathrm{M}}{\mathrm{M}^*}\right)\ \mathrm{d}\left(\frac{\mathrm{M}}{\mathrm{M}^*}\right) \tag{6.8}$$

$$= a\,\Theta^*\,\mathrm{M}^*\,\Gamma(\alpha+m+1) \tag{6.9}$$

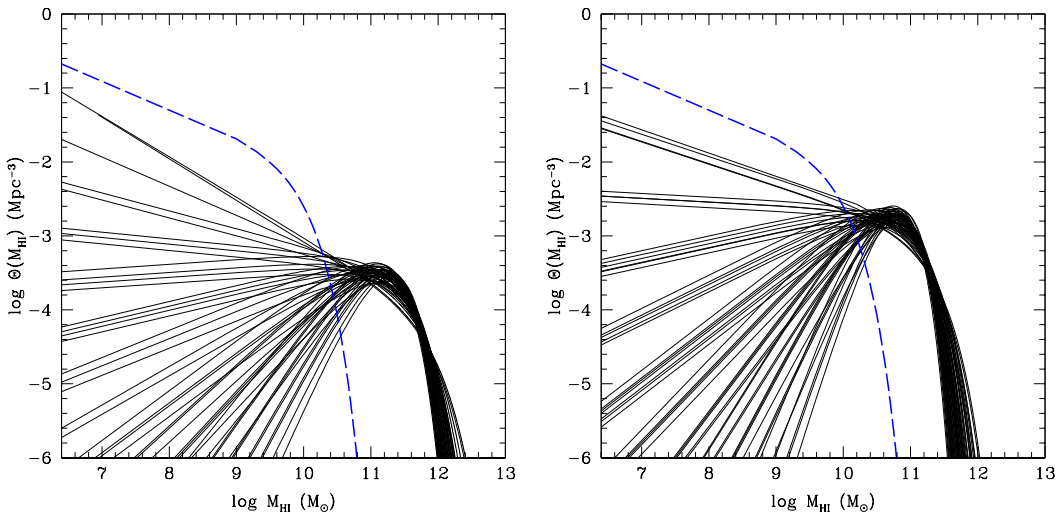

Figure 6.1: This figure shows a series of H I mass functions that all generate a star formation rate density equal to ±10 per cent of 0.3 $M_\odot$ yr^{-1} Mpc^{-3} (the approximate maximum SFRD observed). In the left panel all the H I mass functions sum to give an H I density equal to within ±10 per cent of the present day value (∼5.1 × 10^7 $M_\odot$ Mpc^{-3}), and in the right panel the H I mass functions all sum to within twice this value, ±10 per cent. The dashed line is the H I mass function found in the nearby universe ($z \sim 0$) in HIPASS (Zwaan et al. 2005).

where 'a' and 'm' are parameters of the SFR–H I correlation above. Calculating the star formation rate density using Equation 6.7 and the H I mass function found in the nearby universe ($z \sim 0$) in HIPASS (Zwaan et al. 2005) gives a SFRD of ∼0.0164 $M_\odot$ yr^{-1} Mpc^{-3}. This agrees well with the directly measured values at z ∼0 (see Fig. 1.5).

The set of generated H I mass Schechter functions that had a calculated H I density equal to within ±10 per cent of the present day value (∼5.1 × 10^7 $M_\odot$ Mpc^{-3}) were selected. The subset of these Schechter functions that had a calculated star formation rate density equal to ±10 per cent of 0.3 $M_\odot$ yr^{-1} Mpc^{-3} were chosen. This SFRD value is approximately the maximum star formation rate density value observed in the universe at redshifts around $z = 2$ to 3 (see Fig. 1.5). Some of the H I mass functions that are consistent with these conditions are shown in the left panel of Fig. 6.1. Also on this plot is the H I mass function found in the nearby universe ($z \sim 0$) in HIPASS (Zwaan et al. 2005). As can be seen the generated Schechter functions all have a lower normalisation Θ^* and substantially larger characteristic M^* than the $z \sim 0$ H I mass function. The higher M^* is necessary to produce a sufficient number of large H I mass galaxies that can produce the extra star formation required to raise the star formation rate density by a factor of almost 20 from that at redshift $z \sim 0$. The lower normalisation Θ^* is then required to keep the total H I mass density from increasing despite the addition of more high H I mass

galaxies. The low mass slope determined by α can vary greatly between the different H I mass functions. This indicates that neither the SFRD nor the H I density depend strongly on the number of low mass galaxies, unless there are enormous numbers of them.

The right panel of Fig. 6.1 shows some more generated Schechter functions that also have a calculated SFRD equal to ± 10 per cent of 0.3 $M_\odot$ yr^{-1} Mpc^{-3}. These H I mass functions were selected to have a calculated H I density equal to twice the present day value ± 10 per cent. This is the approximate maximum H I density value in the universe (see Fig. 1.8). As can be seen in the plot, the generated Schechter functions move closer to the $z \sim 0$ H I mass function with a lower M^* and higher Θ^*. Again, a wide range of α is consistent with the SFRD and H I density. What these two plots show is that by altering the distribution of H I gas across galaxies it is possible to produce a large star formation rate density in the universe without requiring a significant change in the H I density. However, they are only illustrations of an idea, and are not evidence that this evolution is occurring.

Possible observational evidence for an evolving H I mass function shape can be seen in 'downsizing', the phenomena whereby the largest galaxies are seen to form stars early in the universe and the smaller galaxies later. Downsizing is seen in the analysis of the stellar population of nearby galaxies which show that the majority of the stars in the more massive galaxies formed early in the universe (Heavens et al. 2004; Jimenez et al. 2005; Nelan et al. 2005; Thomas et al. 2005). Additionally, analysis of the star formation in distant galaxies has shown that the sites of active star formation shift from the more massive galaxies at the earliest times to less massive galaxies in later periods (Cowie et al. 1996; Guzman et al. 1997; Brinchmann & Ellis 2000; Kodama et al. 2004; Bell et al. 2005; Juneau et al. 2005). The phenomenon of downsizing can be seen as possible evidence for a change in the galaxy H I mass function shape. In particular the observed shift in the location of star formation matches what one would expected for the proposed evolution of the H I mass function.

This idea that evolution in the H I mass function can be used to explain the observed dramatic evolution in the cosmic star formation rate and the apparent minimal evolution in the cosmic H I gas density requires that galaxies at all redshifts follow the same SFR–H I mass relationship as observed at redshift $z \sim 0$. It is possible that this relationship could have been different in the past (although it was not found to significantly change at the redshifts examined in this work). One could imagine that in the past, when the distances between galaxies was less, that the higher rate of galaxy-galaxy interactions could cause considerable star formation activity in galaxies. This could result in galaxies to having higher star formation rates than the present day SFR–H I mass relationship would suggest based solely on their H I gas content.

The simplest way to vary the SFR–H I mass relationship is to change the values of the fitted constants 'a' and 'm' in the equation $\mathrm{SFR} = \mathrm{a}\,(\mathrm{M_{HI}})^{\mathrm{m}}$. To test this idea the $z \sim 0$ H I mass function was used with various different values of the SFR–H I mass constants 'a' and 'm' and the star formation rate density calculated. Some

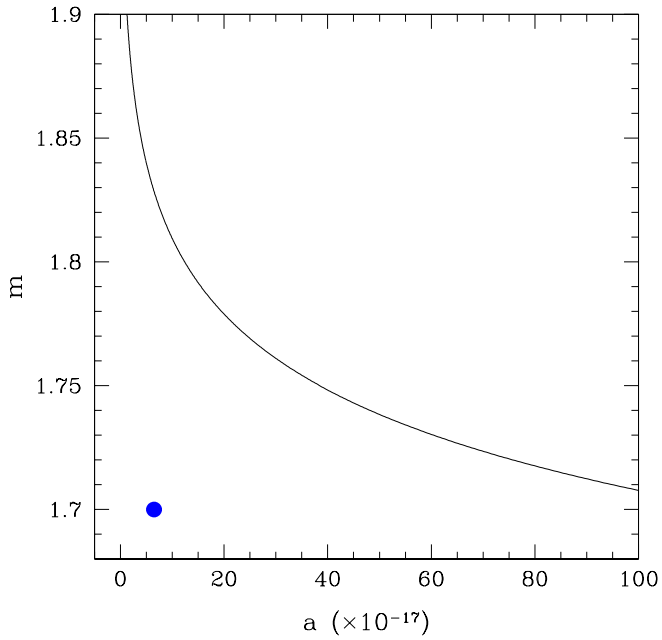

Figure 6.2: This figure shows the values of 'a' and 'm' from the galaxy star formation rate–H I mass correlation, SFR = $a\,(\mathrm{M_{HI}})^m$, that generate a star formation rate density of 0.3 $\mathrm{M_\odot\ yr^{-1}\ Mpc^{-3}}$ (the approximate maximum SFRD observed) from the $z \sim 0$ H I mass function (Zwaan et al. 2005). The Doyle & Drinkwater (2006) values for the present day 'a' and 'm' values are shown as the large point ($a = 6.5 \times 10^{-17}$ and $m = 1.7$).

of those pairs of 'a' and 'm' constants that produced a SFRD of 0.3 $\mathrm{M_\odot\ yr^{-1}\ Mpc^{-3}}$ are shown in Fig. 6.2. As one can see there is a smooth functional form to the allowed 'a' and 'm' values which continues beyond the range shown here. The Doyle & Drinkwater (2006) values for the present day are shown as the large point (a = 6.5×10^{-17} and m = 1.7). Only a small change in 'm' is required to increase the star formation rate density by the required factor ∼20 from the present value. Keeping 'a' unchanged, such an increase would require m = 1.83. A much larger change in normalisation 'a' value is required to achieve the same results. Keeping 'm' unchanged, such an increase would require a = 1.2×10^{-15}. So it is possible to produce a higher star formation rate density with minimal change in the H I density simply by changing the SFR–H I mass relationship. Again this is only an illustration of an idea and not evidence that this is occurring. One could imagine a more complex situation where the relationship between star formation rate and H I mass was not a simple power law in the past. Despite this, it is only important that the higher H I mass galaxies follow a power law SFR–H I mass relationship when considering the star formation rate density evolution, as these are the galaxies that are likely to dominate the measurements.

To experimentally test these two hypotheses, one needs to observe to higher red-

shifts, where the star formation rate density is higher and thus the dominant effect should be more noticeable. The observations using the SKA pathfinder telescopes proposed in Chapter 5 should be able to do this to redshift $z = 1.0$. To test whether there has been any evolution in the H I mass function one needs to see if there has been an increase in the number density of high H I mass galaxies at high redshift; these are also the easiest H I systems to detect and should be the most luminous, star-forming galaxies. Observations using ASKAP with the WiggleZ survey should provide a solid measure of this effect. Observations with MeerKAT with the zCOSMOS survey may provide evidence of changes in the H I mass function for lower mass systems, though cosmic variance may be an issue if only this single field is examined. To test whether there has been a change in the SFR–H I mass relationship one merely has to compare the SKA pathfinder measurements of the H I gas content of the observed galaxies with their measured star formation rates derived from either their optical or radio continuum properties. These observations should provide good constraints at the high H I mass galaxy end. It would not be unexpected if the observations showed that both effects occurred, that there has been evolution in the H I mass function as well as changes in the SFR–H I mass relationship.

6.2.2 Gas for stellar mass

Along side the issue of the dramatic evolution in the star formation rate density and the minimal evolution H I gas density there is another major, gas-related problem in the evolution of galaxies. This is the question of where does the gas that forms the stars in galaxies come from?

As can be seen in Fig. 1.6, the evolution of the cosmic stellar mass density, the total mass in stars today ($z = 0$) is $\sim 4 \times 10^8$ $M_\odot$ Mpc^{-3}. As seen in Fig. 1.8, the evolution of the cosmic neutral gas density, the total mass in H I gas at $z > 3$ (> 11 billion years ago) is $\sim 1.0 \times 10^8$ $M_\odot$ Mpc^{-3} and at $z = 0$ is $\sim 0.5 \times 10^8$ $M_\odot$ Mpc^{-3}. This is a decrease in the amount of H I gas density by $\sim 0.5 \times 10^8$ $M_\odot$ Mpc^{-3} which is insufficient to produce the total $\sim 4 \times 10^8$ $M_\odot$ Mpc^{-3} in stars. The molecular hydrogen (H_2) is found to have a density ratio of $\rho_{H_2}/\rho_{HI} = 0.81$ in the nearby universe (Fukugita, Hogan, & Peebles 1998). Molecular hydrogen at higher redshift is difficult to measure but from those few measurements it appears more likely that there is a lower ratio of H_2 to H I than a significantly higher one (Noterdaeme et al. 2008). So molecular hydrogen is unlikely to be the source of the missing matter to build the stars. Factoring in the neutral Helium (24 per cent by mass of hydrogen, i.e. a factor of ~ 1.3) increases the amount of neutral gas a little but does not account for all the gas needed to build all the stars observed. There is a total of $\sim 1.2 \times 10^8$ $M_\odot$ Mpc^{-3} available to build stars from neutral gas, assuming the same ratio of molecular H_2 gas to H I gas as found nearby, factoring in neutral Helium and adopting the unlikely scenario that star formation is 100 per cent efficient, that all the neutral gas is turned into stars. Even if this was the case this still leaves $\sim 2.8 \times 10^8$ $M_\odot$ Mpc^{-3} of stars to come from some other sources.

The only remaining source of gas available to provide the material for stars is

the ionised hydrogen (HII) of which there are vast amounts mainly located in the space between galaxies (Fukugita, Hogan, & Peebles 1998; Nicastro et al. 2005). Currently, an estimated 89 per cent of baryons are in this ionised gas, with at least 44 per cent of this ionised gas (39 per cent of all baryons) being more than a few hundreds of kpc from galaxies (Fukugita 2004). If this ionised hydrogen can accrete onto a galaxy and become sufficiently dense and cool to condense into H I gas it can fuel star formation in that galaxy. H I gas appears to be only a transitory state for hydrogen on its way to forming stars. It is assumed that at some point this condensation stops which then causes the star formation in the galaxy to halt. Whatever process causes the end of condensation is presumably the cause of the strong evolution seen in the cosmic star formation rate density. The source of this inflow of ionised gas to galaxies is either the space immediately surrounding a galaxy or more distant intergalactic space. These two models for where the condensing HII comes from I have labelled the 'reservoir' model and the 'accretion' model.

In the 'reservoir' model there is an envelope of ionised gas surrounding a galaxy that can flow into the galaxy over time and condense into H I gas. This is the model considered by Fukugita & Peebles (2006). Since this envelope of ionised gas is gravitationally bound to the galaxy, the expansion of the universe will not separate this gas from the galaxy. A galaxy would eventually use up the ionised gas component of this envelope that could condense to H I gas (that which is not too hot and/or diffuse). At this point star formation in that galaxy would soon end. Interactions in higher galaxy density regions could cause galaxies to use up this envelope faster by either driving this gas into the galaxies to condense faster or remove it from the halo of the galaxies entirely, i.e. the process of strangulation, (Larson, Tinsley, & Caldwell 1980; Diaferio et al. 2001). This would create the lack of current star formation and lack of gas seen in galaxies within the high density environments of nearby clusters. In this model, the cosmic star formation rate density decline is simply due to the decrease in the amount of ionised gas in the reservoirs of galaxies that can be used as fuel for star formation.

In the 'accretion' model, ionised gas moves from the intergalactic medium (IGM) onto a galaxy where it reaches a sufficient high density and low temperature to condense into H I gas. This accreted ionised gas would not have initially been gravitationally bound to the galaxy, unlike the ionised gas in the 'reservoir' model. This gas would have been slowly moving towards the galaxy gravitationally attracted by the mass of the galaxy and nearby large scale structure such as clusters, groups or filaments. The expansion of the universe with time would slow the rate at which this intergalactic ionised gas could accrete onto galaxies, reducing the rate of star formation in the galaxies.

The rate of gas replenishment by this mechanism would be related to the density of the intergalactic material. The density of intergalactic gas will be inversely proportional to the physical volume size of an element of comoving volume, i.e. the change in the size of universe due to the expansion. Fig. 6.3 shows the percentage change in the physical size of a comoving volume with redshift and look-back time. At $z = 0.37$, the redshift of Abell 370, a comoving volume element of the universe

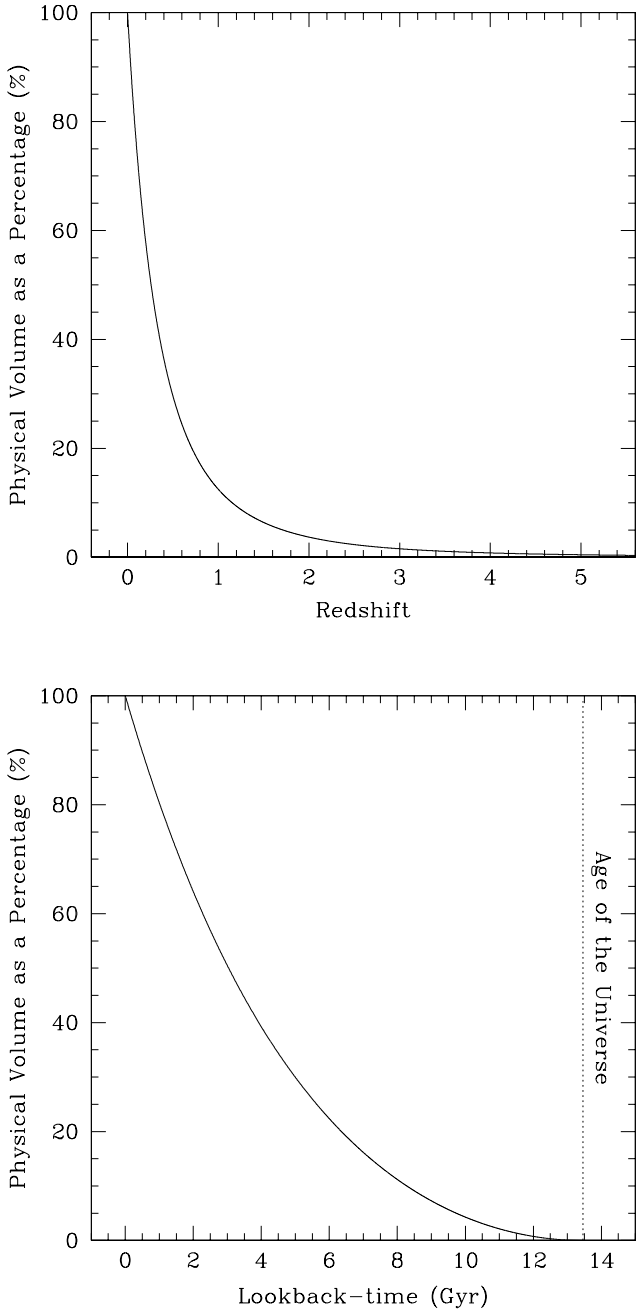

Figure 6.3: The change in the physical volume size of an element of comoving volume with redshift (top plot) and with look-back time (bottom plot). The change in volume is $\propto \frac{1}{(1+z)^3}$.

would have a physical volume that is ∼40 per cent its current size, an appreciable difference. The time period that shows the fastest growth in the physical volume size is for redshifts $z < 1.0$ onwards, the same time span where the dramatic decrease in the star formation rate density is seen. When the accretion rate drops to a low level, the rate of galaxy-galaxy interactions in the high galaxy density environments would quickly use up any H I gas remaining in the galaxies creating the H I gas poor clusters seen today. Galaxies in lower density regions with slower star formation rates and lower rates of galaxy-galaxy interactions would be able to retain their existing H I gas for longer.

Assuming no or minimal evolution in neutral gas density, then the gas that fuels star formation must, in effect, all come from ionised gas accreted onto galaxies. If one makes a number of assumptions, an interesting relationship between gas accretion and the star formation rate density can be derived for the time period $z < 1$. The rate of change of the density of gas in all galaxies in the universe can be represented as:

$$\frac{\mathrm{d}\rho_{\mathrm{gas}}}{\mathrm{dt}} = -\frac{\mathrm{d}\rho_*}{\mathrm{dt}} + \text{ inflow } - \text{ outflow } + \text{ merging } + \text{ recycling} \tag{6.10}$$

where $\frac{d\rho_*}{dt}$ is the star formation rate density, inflow is the rate at which gas accretes onto galaxies, outflow is the rate at which gas leaves galaxies mainly in winds, merging is the rate at which gas increases in galaxies due to galaxy-galaxy mergers and recycling is the amount of gas returned from stars either from their stellar winds or from their death throes (super novae, planetary nebulae, etc.). If one assume no evolution in gas, i.e. $\frac{d\rho_{gas}}{dt} = 0$, for at least the period $z < 2$ then:

$$\frac{\mathrm{d}\rho_*}{\mathrm{dt}} = \text{inflow } - \text{ outflow } + \text{ merging } + \text{ recycling} \tag{6.11}$$

The outflow rate from galaxies is likely to be related to the star formation rate as star formation likely provides the majority of the energy to drive out the gas (except possibly for galaxies with AGN). So it is assumed that outflow $\propto \frac{\mathrm{d}\rho_*}{\mathrm{dt}}$. Additionally, the outflow rate needs to somehow be related to the inflow rate or else the galaxies in the universe will either end up with no gas or vast amounts breaking the initial assumption of no evolution in gas density. It is assumed that merging is not a substantial component for galaxies at redshifts $z < 1.0$ (merging is seen to decrease with redshift; Conselice, Rajgor, & Myers 2008; de Ravel et al. 2009). Additionally, recycling is likely to be proportional to $\frac{d\rho_*}{dt}$ (Hopkins, McClure-Griffiths, & Gaensler 2008). Then, using these proportionalities:

$$\frac{\mathrm{d}\rho_*}{\mathrm{dt}} \propto \text{ inflow} \tag{6.12}$$

The 'accretion' model assumes that inflow is proportional to the density of the intergalactic medium which is inversely proportional to expansion of the volume of the universe $(1+z)^{-3}$, i.e. inflow $\propto (1+z)^3$. So then:

$$\frac{\mathrm{d}\rho_*}{\mathrm{dt}} \propto (1+z)^3 \tag{6.13}$$

So by making all these assumptions one has that the star formation rate density is inversely proportional to the volume change of the universe. The logarithm of the star formation rate density appears to be almost linear when plotted against the log(1+z) for redshifts from $z = 0$ to $z \sim 1.0$ (possibly a little higher). Linear fits to this region of the SFRD diagram by Baldry & Glazebrook (2003) find a slope of 3.44 and by Hopkins & Beacom (2006) find a slope of 3.28, both cutting off the data at redshift $z \sim 1.0$. Linear fits to the SFRD data of Hopkins (2004) (see Fig. 1.5) allow for a slope between ∼3.2 (cutting off at $z = 1.0$) and ∼2.7 (cutting off at $z = 2.0$). The fact that this slope is ∼3 could be evidence that the dilution of the IGM caused by the expansion of the universe is the dominant effect driving the decrease in star formation from redshift $z \sim 1.0$. If this is the case, then this relationship clearly breaks down somewhere above redshifts $z = 1.0$ as there is an observed levelling off of the cosmic star formation rate density. An explanation for this effect could be that at these high redshifts the rate of expansion of the universe is sufficiently small that it has minimal effect on the gas inflows and so it is other physical mechanisms that are the dominant influence on star formation. However as one approaches redshift $z \sim 1.0$, the change in the physical volume of a comoving element rapidly increases as seen in Fig. 6.3. Thus around this redshift the expansion of the universe would become the dominant influence on star formation in this model and the other effects would become less significant.

Both the 'reservoir' and 'accretion' model presented here probably play some role in supplying the gas needed to form the stellar mass in galaxies. Despite this, one model is likely to be the dominate cause of the dramatic decline in the cosmic star formation rate density. Distinguishing between models would likely require detailed simulation of galaxies based on their observed star formation and gas properties as a function of redshift. H I observations of the high density environment of clusters at high redshift may be useful in distinguishing between the models. This is because in the 'reservoir' model the reservoir of gas is likely to be disrupted by the higher number of galaxy-galaxy interactions (i.e. strangulation) potentially resulting in galaxies with lower H I masses. In the 'accretion' model, these high density regions would be sucking up all the surrounding gas in the IGM at a high rate leading potentially to galaxies with higher H I masses.

This thesis made progress in exploring the evolution of gas in galaxies by using the coadding technique to measure the H I 21-cm emission from distant galaxies. The ability to immediately compare the optical and H I gas observations of the galaxies that this technique provides allowed for useful insights into the properties of the galaxies especially in regards to their star formation. The H I measurements are still of low statistical significance, so future deeper observations using the GMRT are required to maximise the scientific return of this work. The future looks bright for the study of the evolution of gas in galaxies with the SKA pathfinders ASKAP and MeerKAT being built along with the prospect of the SKA on the horizon.

Appendices

Appendix A

The Technique of Threshold Flagging of Radio Data

> If we knew what it was we were doing, it would not be called research, would it.
>
> Albert Einstein

During the GMRT data reduction visibilities that exceeded a threshold set by the system noise statistics were flagged (see Section 2.2.2 and Section 3.3). This threshold flagging was performed separately on each day of GMRT observation. It was done after the initial self calibration with the bright radio continuum sources removed from the $u - v$ interferometer radio data. After the threshold flagging the bright sources were added back and the individual data sets from the different days were combined. In this chapter the details of the threshold flagging used will be discussed along with the potential biases that incautious use of this technique can produce.

A.1 Flagging data above an amplitude flux density threshold

Flagging is the process of editing radio interferometer data to remove bad quality data. Bad quality data is most often due to radio interference but can also be caused by undiagnosed equipment problems (often one does not know the exact cause of the spurious data). The editing of the bad data takes place in the $u - v$ database of the interferometer visibilities (this is what is actually recorded at the telescope). Identifying data to be flagged is mainly done on the amplitude properties of the interferometric data, rarely on the observed phases. With the H I coadding work done in this thesis it was critical to have only good quality data. This is because the signal being observed is fainter than the noise level (the data needs to be stacked to

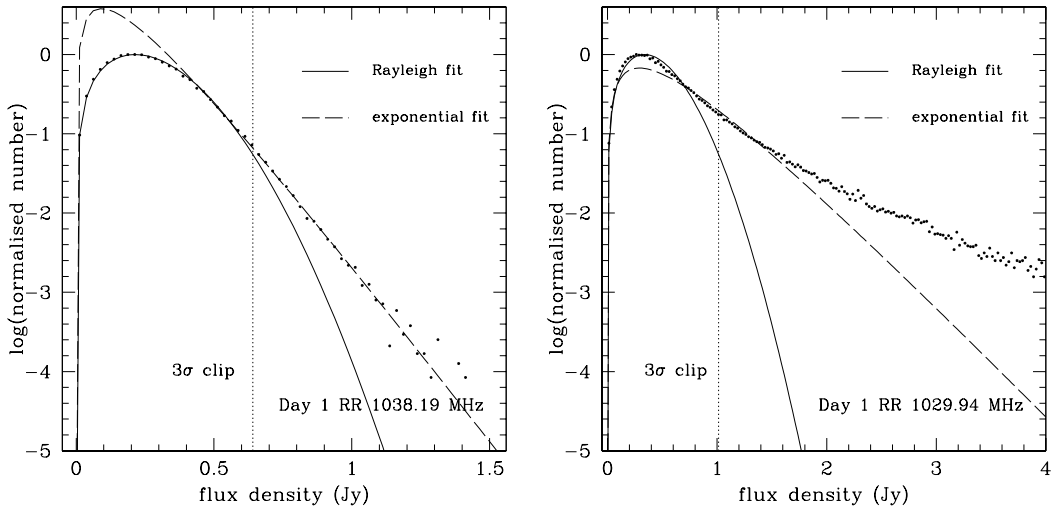

Figure A.1: The left panel shows the histogram of amplitude flux density from one channel of observed GMRT $u - v$ data. This is from the first day of the GMRT observations of Abell 370, the RR polarisation at a frequency of 1038.19 MHz RR polarisation. The number of visibilities (the y-axis) has been normalised so that the mode of the distribution is at a value of 1 and the $\log_{10}$ has then been taken. The Rayleigh fit and exponential fit to the data have been plotted on the figure (see text). The vertical dotted line labelled 3σ is the flux density threshold values used for this data. The right panel shows a similar histogram of $u - v$ data from the same radio observations but from the channel at a frequency of 1029.94 MHz. There was strong radio interference at this frequency that distorts the flux density distribution so that neither the Rayleigh distribution nor the exponential curve provide a good fit to the data.

see the desired signal). Even a small amount of spurious data can potentially create a significant bias in the final results.

A common practice in editing interferometer data is to flag visibilities in the residual $u - v$ data that have a flux density amplitude above a threshold (after the removal of the brightest continuum sources). These unusually high amplitude values are usually spurious data. This flagging must be done with care so that only abnormal values are removed. If one sets the amplitude flux density threshold too low one can create a biased data set with artificially low noise levels in the final reduced radio data cube. Outlined in this section is the method used to determine a reasonable amplitude flux density threshold in GMRT data so that the majority of the significant data is retained while excluding spurious data.

Usually an observed field of sky is mostly empty of strong radio signals so that the uncertainty in the measured amplitude flux densities are dominated by the system noise of the telescope. A Rayleigh distribution is the theoretical noise profile for such an amplitude distribution (Thompson, Moran, & Swenson 1986). The left panel of Fig. A.1 shows the $\log_{10}$ normalised histogram of the amplitude flux density values

of the first days GMRT observations of Abell 370 (∼8 hours in length) for a single frequency channel after the brightest radio continuum sources have been removed. A χ^2 fit of a Rayleigh Distribution was made to this data for the region 0 to $3\times$ the mode of the distribution. This Rayleigh Distribution has the form:

$$\mathrm{f(x)} = \frac{\mathrm{x}}{\sigma^2}\ \exp\left(\frac{-\mathrm{x}^2}{2\sigma^2}\right) \tag{A.1}$$

were σ is the mode of the distribution generated by this formula. For the lower flux density values the Rayleigh Distribution is a good fit but fails for higher flux density values. At these higher flux density values (∼$3\times$ the mode of the distribution) the profile is best fit by a curve of the form:

$$\mathrm{g(x)} = \alpha\,\mathrm{x}\ \exp(-\beta\,\mathrm{x}) \tag{A.2}$$

were α and β are fitting parameters. A χ^2 fit to this exponential distribution was made to the data in the left panel of Fig. A.1 for the region from $2\times$ the mode to $6\times$ the mode. As can be seen in the figure this function is a good fit to the data for this region. What this shows is that in this higher flux density region, the noise in the radio data no longer follows Gaussian statistics. These higher amplitude flux density values are the statistically discrepant values from spurious data that one would want to remove so that the data follows the expected normal distribution.

Based on the Rayleigh functional fit, a flux density threshold equal to 3σ has been used for the data. Using this threshold on a theoretically perfect Rayleigh distribution only 1.1 per cent of the data would be lost. However as the observed distributions above this level do not follow a Rayleigh distribution, what is being removed is dominated by non-normal high flux density amplitude noise. Application of the 3σ threshold for the well behaved channel seen in the left panel Fig. A.1 means that 1.8 per cent of the observed data is discarded. The effect of using this threshold across all channels of first day‘s Abell 370 data shifts the RMS flux density of the final data cube for that day's data down by only 0.03 mJy from the RMS level in the unflagged data of 0.30 mJy. Such a small shift is unlikely to distort the results and is probably due the removal of spurious structures in the final data cube.

The analysis of the noise distribution parameters on a channel-by-channel basis can be used to identify radio interference. The left panel of Fig. A.2 shows the RMS flux density vs. frequency in the final data cube made from the first days GMRT observations of Abell 370. This figure shows the expected RMS increases at the ends of the bandpass, which is a property of the receiving system. There is a spike in the RMS noise level at ∼1030 MHz and another smaller spike at ∼1034 MHz. An assessment of whether there is radio interference at these frequencies can be made using information from the Rayleigh fit to the visibility amplitude distribution. For a Rayleigh function the σ = mode of the distribution and $\sqrt{\frac{\pi}{2}}\ \sigma$ = mean of the distribution. From these two equations two different values of σ can be determined from the data. These two values can be calculated for each channel of the data and their difference taken.

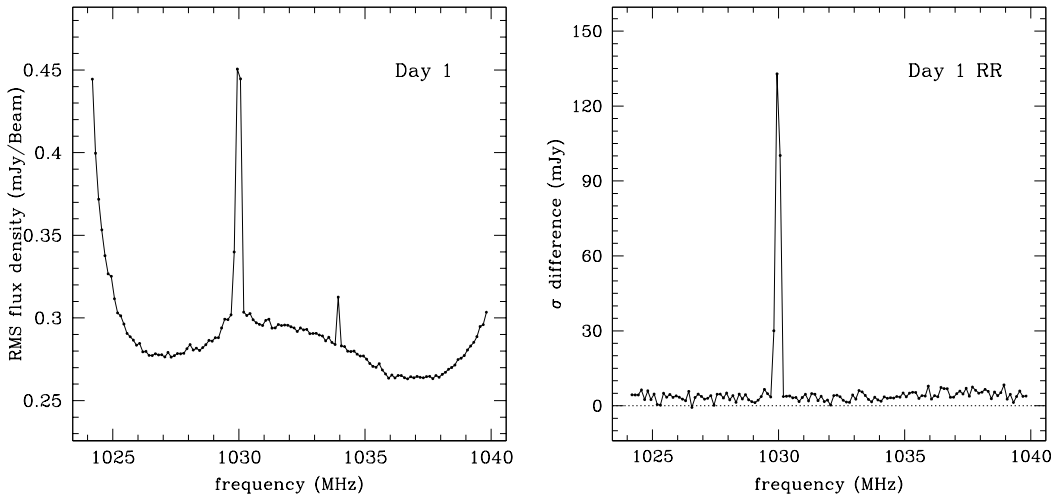

Figure A.2: The left panel shows the RMS flux density as a function of frequency for the lower sideband data cube made from the first day of GMRT observations of Abell 370. The right panel shows a plot of frequency versus the difference between the Rayleigh distribution σ calculated from the mode and the σ calculated from the mean in the u – v data for each channel. This σ difference shows whether the amplitude flux density distribution of a particular frequency channel is dominated by Gaussian noise (near zero difference) or non-Gaussian noise (large difference). A frequency channel dominated by non-Gaussian noise is an indication of some sort of radio interference.

The right panel of Fig. A.2 shows the plot of this difference vs. frequency for the data in left panel of Fig. A.2. For channels without major interference the value of the difference should be small (near zero). This shows that the channel is well described by a Gaussian noise distribution with only a few statistically discrepant high flux values. However, for channels affected by radio interference the difference is significantly above zero. This is because the σ calculated from the mean includes many high amplitude flux density values that do not fit on the normal distribution of the Rayleigh curve. This occurs at the data cube RMS spike at ∼1030 MHz which shows a similar spike in the u – v data difference plotted in the right panel of Fig. A.2. The histogram of the u – v data at this frequency is seen in the right panel Fig. A.1 and clearly shows the effect of the radio interference on the shape of the distribution (the effect of this strong RFI on the Abell 370 data is discussed in Section 3.4).

The peak at ∼1034 MHz in the final data cube RMS shows no corresponding peak in the u – v data σ difference plot. For the channel at this frequency there was significant problems with several antenna baselines in one polarisation. The problem values in this channel were flagged resulting in the removal of large quantity of interferometric u – v data. This heavy flagging caused the final data cube RMS at this frequency to increase relative to neighbouring frequency channels but the

noise in this channel became a normal noise distribution. Prior to this additional flagging, there was a peak in the $u - v$ data σ difference plot at this frequency indicating an unflagged problem. Using the sigma difference to find when one has successfully flagged the discrepant data is a useful application of this technique. (Note: The RFI at ∼1030 MHz was so extensive that all the channels affected had to be flagged.)

The other useful application of the threshold flagging technique is to find the time periods were particular antennas or baselines have a different and problematic response than the rest of the telescope. After the threshold flagging has been applied one can inspect the $u - v$ amplitude data to see where the data has been flagged. If a particular section of data is well behaved then the threshold flagging should flag only a few visibilities that are randomly distributed across the channels and across time. If there are large quantities of threshold flagged data for particular baselines or channels for certain time ranges then this is an indication of problem during that period. An example of this can be seen in Fig. A.3 which shows the output of SPFLG, an AIPS flagging task for a problematic GMRT baseline. Shown here is the amplitude flux density values from the baseline between antennas 18 and 19 for the RR polarisation on the first day of the Abell 370 observation data. The data shown here is from just after the threshold flagging has been performed but before the bright radio continuum sources have been added back. As such, the data removed by the threshold flagging can be seen as the black spots in the image. At the beginning of the observations this baseline shows little to no discrepant amplitude values. After the third scan though, there are more and more discrepant values seen with increasing time. This indicates a problem during this time and all this data for this period should flagged for this baseline. This method is good for finding problematic data that is difficult to find with other commonly used flagging techniques.

A.2 Analysis of the bias due to threshold-based flagging

The use of threshold flagging can lead to systematic biases in the final data cube. An example of this bias can be seen in Fig. A.4 which shows the radio continuum spectrum of one of the brighter source in the Abell 370 data cube. The left panel of Fig. A.4 shows the flux density vs. frequency of the continuum source before threshold flagging and the right panel Fig. A.4 shows the source after threshold flagging. The overall average flux density of the source has been slightly decreased after threshold flagging (not an unexpected result). However more concerning is the known radio interference peak at ∼1030 MHz has been transformed to what looks like an absorption trough after threshold flagging.

In this section the systematic biases created by threshold flagging are examined. This study simulates three different noise distributions;

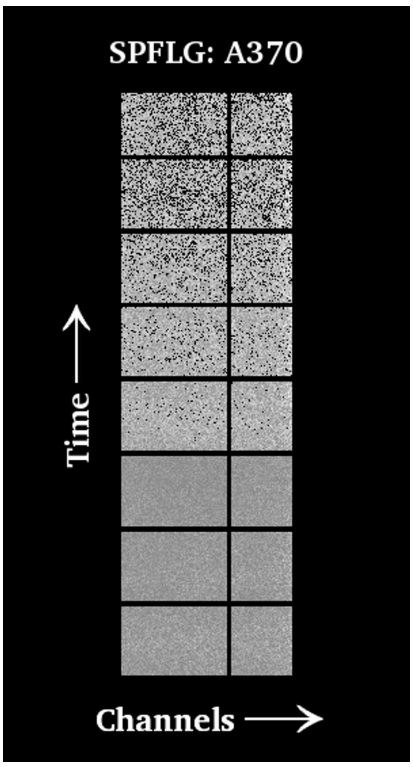

Figure A.3: An example image from the AIPS flagging task SPFLG showing a problematic GMRT baseline. This is the baseline of between antennas 18 and 19 for the RR polarisation from the first day of the Abell 370 observations. The grey-scale shows the amplitude flux densities for the different frequency channels (x-axis) at the different observed times (y-axis). The data shown here is from just after the threshold flagging has been performed but before the bright radio continuum sources have been added back. As such, the data removed by the threshold flagging can be seen as the black spots in the image. The long black line at constant channel corresponds to the flagged channels that were heavily RFI affected. The black lines at constant times are the gaps between individual scans on the source (phase calibration scans are usually done in these time intervals).

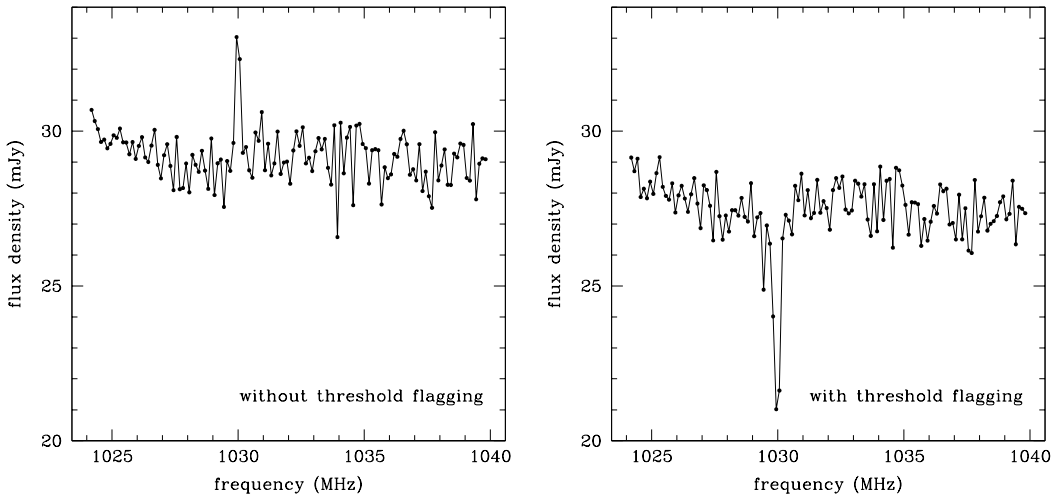

Figure A.4: The left panel shows the flux density vs. frequency of a radio continuum source in the Abell 370 data without any threshold flagging done on the data. The right panel shows the flux density vs. frequency of the same source after threshold flagging has been done on the data. There is significant RFI at ∼1030 MHz that appears as a spike in the left panel but as a dip in the threshold flagged data of the right panel.

1. a theoretical Rayleigh noise distribution.

2. the mildly distorted distribution of real GMRT spectral data (the distribution seen in the left panel Fig. A.1).

3. the severely distorted noise distribution of RFI effected GMRT radio data (the distribution seen in the right panel Fig. A.1 for the RFI at ∼1030 MHz in the Abell 370 observations).

In this work S_{TRUE} is the flux density of the modelled continuum source, S_{MEAS} is the measured flux density of the source after threshold flagging, and $S_{THRESHOLD}$ is the flux density level used in the threshold flagging. The complex visibilities of how an observed continuum source would appear were modelled. This was done by computing the combination of the visibilities due to the S_{TRUE} of the source with complex noise from one of the three distributions (amplitudes were generated from the distributions and a uniform distribution of phase was assumed). To simulate threshold flagging, the visibility values above an amplitude of $S_{THRESHOLD}$ were removed. This is followed by a calculation of the average real component of the visibilities which simulates the integration of the modelled source‘s flux density.

Fig. A.5 shows the results of the modelling with the ratio of S_{MEAS} with S_{TRUE} plotted as a function of the ratio of S_{TRUE} to the noise level σ. The parameter σ can be defined exactly for the theoretical Rayleigh noise distribution but for the

modelled GMRT data σ is experimentally determined from the Rayleigh fits to the distributions (see Fig. A.1).

Tests with a variety of threshold levels were performed on the theoretical noise distribution. When threshold levels are greater than $\sim 4\sigma$, there is very little bias and $S_{MEAS}/S_{TRUE} \approx 1$. As shown in Fig. A.5, more severe threshold levels at $S_{THRESHOLD} = 2$, 2.5, 3 and 3.5σ impose a bias on the ratio S_{MEAS}/S_{TRUE}. A reasonable, empirical fit to the functional dependence of this bias is:

$$\frac{S_{MEAS}}{S_{TRUE}} = 1 - \exp\left(\frac{{S_{THRESHOLD}}^{2.315}}{-4.3}\right) \tag{A.3}$$

This empirical fit only holds for $S_{TRUE} \ll \sigma$. The empirical fit in Fig. A.5 is the dashed line which becomes worse fit the closer S_{TRUE} approaches the value of σ.

The effect of threshold-flagging on data with less well-behaved noise distributions was modelled for a threshold of 3σ. This is shown as the dotted lines in Fig. A.5. The top line labelled 'GMRT' uses the noise distribution of real GMRT spectral data. The bottom line labelled 'GMRT+RFI' uses the RFI distorted noise distribution. The bias created by threshold flagging is stronger for realistic data than for a theoretical noise distribution and is particularly bad for the severely distorted noise distribution containing the radio frequency interference.

These results from the modelling relate to the flux density levels measured for the continuum source spectra shown in Fig. A.4. The source has a continuum strength $\sim$29.3 mJy when no threshold editing is applied (the left panel of Fig. A.4). Based on the modelling, threshold flagging at the 3σ level should reduce the measured flux density to $0.93\,S_{TRUE}$, $\sim$27.3 mJy, which is what is seen the right panel of Fig. A.4. For the more severely corrupted frequency channel, the modelling, suggests that the measured flux density should be reduced to $0.82\,S_{TRUE} = \sim$24 mJy; this is not as deep as the feature at 1030 MHz in the right panel of Fig. A.4. However at this frequency there is increased noise compared to the rest of the spectrum that is superimposed on the expected bias.

To avoid biasing the flux density measurements, threshold flagging must be applied to fully continuum-subtracted visibilities. Even sources whose integrated flux density are a tiny fraction of either the visibility noise level or the threshold, will have biased measurements, if present during the thresholding process. Care was taken in the GMRT data reduction to make sure to remove all the significant radio continuum sources before threshold flagging. If inadequate care is taken in adjusting the threshold level as a function of frequency, sources with strong astronomical spectral signals could have artificially induced features such as the weak absorption against continuum sources seen here. Distortions in the noise that vary with frequency do not have to be due to RFI but can also be due to astronomical effects such as the velocity spread of Galactic H I which can raise the relative system temperature several fold.

In conclusion, threshold flagging of radio is a useful method of removing spurious data but care must be taken not to removed too much data. Additionally the

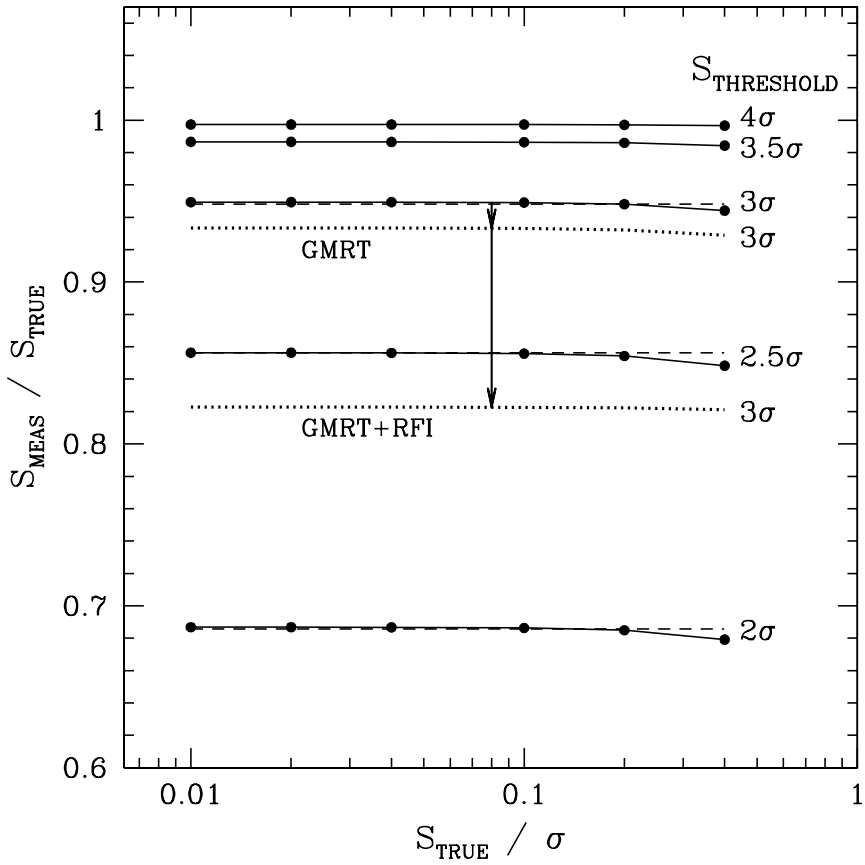

Figure A.5: This figure shows the modelled effect of different levels of threshold flagging on the measured flux density of a radio continuum source. The y-axis displays the ratio of the measured flux density after threshold flagging (S_{MEAS}) to the true flux density (S_{TRUE}). The x-axis displays the ratio of the source's true flux density (S_{TRUE}) with the noise σ in the modelled data. The filled dots linked by solid lines are the S_{MEAS}/S_{TRUE} for flagging thresholds of $S_{THRESHOLD} = 2$, 2.5, 3, 3.5 and 4σ for a theoretical ideal noise distribution. The dashed lines show the empirical relation fit to S_{MEAS}/S_{TRUE} (Equation A.3, which has no dependence on S_{TRUE}/σ). The dotted lines show the S_{MEAS}/S_{TRUE} ratio for the model using the two non-ideal noise distributions using a 3σ flagging threshold. The top line labelled 'GMRT' uses the noise distribution of real GMRT spectral data. The bottom line labelled 'GMRT+RFI' uses an RFI distorted noise distribution.

combination of RFI effected data with threshold flagging can lead to strange results that can easily be misinterpreted.

Appendix B

Calculating the H I Mass from the measured 21-cm emission

> When you can measure what you are speaking about, and express it in numbers, you know something about it; but when you cannot measure it, when you cannot express it in numbers, your knowledge is of a meagre and unsatisfactory kind: it may be the beginning of knowledge, but you have scarcely, in your thoughts, advanced to the state of science.
>
> William Thomson, Lord Kelvin

It is possible to directly calculate the H I mass of a cloud/galaxy of neutral atomic hydrogen (H I) given its observed flux density, velocity width and redshift/distance. Following the method outlined by Wieringa, de Bruyn, & Katgert (1992), the formula for this is derived. For this calculation it is assumed that the cloud of atomic hydrogen gas has a spin temperature well above the cosmic background temperature, that collisional excitation is the dominant process, and that the cloud is optically thin to electromagnetic radiation with wavelength of 21-cm.

For 21-cm line emission the emission coefficient (the energy emitted by a volume dV in time dt into a solid angle dΩ) is

$$j = \frac{h_p \, \nu_{21}}{4\pi} \, A_{21} \, \frac{3}{4} n_H \tag{B.1}$$

where h_p is Planck's constant, ν_{21} is the frequency of the emission (1420 MHz), A_{21} is the transition probability of the hydrogen spin-flip and n_H is the neutral atomic hydrogen number density. The factor of $\frac{3}{4}$ is due to the statistical weights of the two spin states with there being 3 times as many excited states as ground states.

The total power (energy emitted in time dt) of the 21-cm emission for a cloud of volume V with H I mass $\mathrm{M_{HI}}$ is

$$P = \int_{4\pi}\int_{V} j\, dV\, d\Omega \tag{B.2}$$

$$= \frac{3}{4}\, h_p\, \nu_{21}\, A_{21}\, \frac{\mathrm{M_{HI}}}{\mathrm{m_H}} \tag{B.3}$$

where $\mathrm{m_H}$ is the mass of a hydrogen atom ($\frac{\mathrm{M_{HI}}}{\mathrm{m_H}}$ is the total number of hydrogen atoms in the cloud).

If the cloud is located at a redshift z with a corresponding luminosity distance d_L, then the total flux (the energy passing through an area dA in time dt) that will be measured is

$$S = \frac{P}{4\pi d_L^2} \tag{B.4}$$

$$= \frac{3}{4}\, h_p\, \nu_{21}\, A_{21}\, \frac{\mathrm{M_{HI}}}{\mathrm{m_H}}\, \frac{1}{4\pi d_L^2} \tag{B.5}$$

The frequency of the 21-cm emission observed at Earth from a galaxy at redshift z

$$\nu = \frac{\nu_{21}}{(1+z)} \tag{B.6}$$

If the cloud has a velocity distribution with width ΔV, the frequency width $\Delta\nu$ of the 21-cm emission signal will be

$$\Delta\nu = \frac{\nu}{c}\, \Delta V \tag{B.7}$$

$$= \frac{\nu_{21}}{c\,(1+z)}\, \Delta V \tag{B.8}$$

where c is the speed of light.

The average flux density S_ν (the energy at averaged over the emission profile passing through a unit area per unit time) from the cloud will be

$$S_\nu = \frac{S}{\Delta\nu} \tag{B.9}$$

$$= \frac{S}{\Delta V}\, \frac{c\,(1+z)}{\nu_{21}} \tag{B.10}$$

$$= \frac{3}{16\pi}\, \frac{c\, h_p\, A_{21}}{\mathrm{m_H}}\, \frac{,\mathrm{M_{HI}}\,(1+\mathrm{z})}{d_L^2\, \Delta V} \tag{B.11}$$

Rearranging this equation gives

$$\mathrm{M_{HI}} = \frac{16\pi}{3}\, \frac{\mathrm{m_H}}{c\, h_p\, A_{21}}\, \frac{S_\nu\, d_L^2\, \Delta V}{(1+z)} \tag{B.12}$$

The constants in this equation are:

$m_H = 1.67 \times 10^{-24}$ g
$c = 3.00 \times 10^{10}$ cm s^{-1}
$h_p = 6.63 \times 10^{-27}$ erg s
$A_{21} = 2.85 \times 10^{-15}$ s^{-1}

Other important conversion values are:

1 $M_\odot = 1.99 \times 10^{33}$ g
1 Jy $= 10^{-23}$ erg s^{-1} cm^{-2} Hz^{-1}
1 Mpc $= 3.09 \times 10^{24}$ cm

Substituting for these values gives

$$\left(\frac{M_{HI}}{M_\odot}\right) = \frac{236}{(\ 1+z\ )}\left(\frac{S_v}{\text{mJy}}\right)\left(\frac{d_L}{\text{Mpc}}\right)^2\left(\frac{\Delta V}{\text{km s}^{-1}}\right) \tag{B.13}$$

This equation allows one to take the measured 21-cm emission flux density S_v averaged across the velocity width ΔV and with the measured redshift z and luminosity distance d_L calculate the total mass of neutral atomic hydrogen M_{HI} in a cloud/galaxy.

Appendix C

Spectral Lines

All truths are easy to understand once they are discovered; the point is to discover them.

Galileo Galilei

Spectral Line	Wavelength
Lyman-α	1215.7 Å
[OII]	∼3727 Å
[OII] doublet	3726.0 Å
[OII] doublet	3728.8 Å
Ca K	3933.7 Å
Ca H	3968.5 Å
Hδ	4101.7 Å
G–band	4304.4 Å
Hγ	4340.5 Å
Hβ	4861.3 Å
[OIII]	4958.9 Å
[OIII]	5006.8 Å
Mg	5175.3 Å
Na	∼5894 Å
[NII]	6548.0 Å
Hα	6562.8 Å
[NII]	6583.5 Å
[SII]	6716.4 Å
[SII]	6730.8 Å
H I	21.106 cm

Table C.1: Useful Spectral Lines

Appendix D

Stories from the PhD

> A learning experience is one of those things that says, 'You know that thing you just did? Don't do that.'
>
> Douglas Adams

In this appendix I discuss some of the various problems (challenges?) I faced during the preparation of this thesis and how they were overcome. Various lessons were learnt from vanquishing these problems. I have included this in the thesis to provide insight into the journey that is a PhD.

One of the biggest lessons learnt is the speed at which astronomy changes. When I started my PhD in 2004 the best research suggest that the cosmic neutral gas density at high redshift was $\sim$5 times higher than the current value. Within only a couple of years this changed to being only a factor $\sim$2 higher (see Section 1.2.2). The lesson I learnt was that to be successful in research you need to constantly keep up to date on the latest developments or be left in irrelevancy.

In late 2005 I was working on getting the maximum number of redshifts from the 2dF AAT optical observations of the Fujita galaxies (see Section 2.2.1). Roberto De Propris had already found many redshifts in the observations while we were still at the telescope. We had observed many of the Fujita galaxies multiple times with different 2dF configurations. I was trying to combine these spectra from different runs to create higher signal to noise spectra in which additional redshifts could be found. The optical spectra were basically noise with emission lines popping out, i.e. no optical continuum. Unfortunately the then current version of the 2DFDR software could not combine such noisy spectra. So I used IRAF to combine the spectra but this meant that I could no longer use RUNZ to search the spectra for redshifts (it would not accept the modified files). So I again use IRAF to do the redshift search which proved much slower. In the end I picked up only a handful of additional redshifts for months of work; the return was not proportional to the effort. The lesson I learnt is to keep your analysis as simple as you can unless the reward for the extra effort is sufficient for the additional time that will be consumed.

The first lesson one gets on the flagging of bad data from radio observations is to flag the data once, then do it again, then go and flag some more and then just

to be safe flag some more. The importance of this lesson was learnt the hard way when I was working on the GMRT data for the Fujita galaxies (see Section 2.2.2). There was a strange result from the initial H I emission stacking which was still unsolved by the time I presented my midterm in 2006. The stacked H I signal for the bright L(Hα) galaxies (high star-forming galaxies) was positive; the stacked H I signal for the faint L(Hα) (low star-forming galaxies) was also positive; however the stacked H I signal for the medium L(Hα) (mid star-forming galaxies) was negative which made no sense. The cause of the problem was eventually tracked to several unflagged unusually high amplitude baselines in the Upper Sideband of the GMRT radio data. Once this discrepant data was flagged and the data reprocessed the current results were found, including the correlations in the data similar to those for nearby galaxies. Making sure one removes all discrepant data (flags it) is critically important particularly if you are looking for a signal that is below the noise level of your data.

When dealing with the data for the Fujita galaxies the importance of having good astrometry (positional information) was made clear. In 2005 I was searching for the reason why I was not getting any H I emission signal in my stacked data. There were multiple reasons for this and I eventually found them all. The most difficult to find was a discrepancy between the coordinates I had for the galaxies and the location of the galaxies in the Subaru optical imaging. The reason for this difficulty is that this discrepancy appeared to be semi-random. Eventually, many months later after solving most of the other issues, I worked out what was happening. The Right Ascension and Declination coordinates had been measured correctly from the imaging. Before the coordinates had been converted from decimal format to degrees/hours, minutes and seconds, the numbers had been rounded to the $4^{\rm th}$ decimal place, e.g. R.A. 161.2665678 degrees convert to 10.751124519 hours, then rounded to 10.7511 hours, then converted to $10^{\rm h}45^{\rm m}03.960^{\rm s}$. While this only led to a rounding error $\pm 0.18''$ in Declination, it caused a rounding error of $\pm 2.7''$ in Right Ascension as this was measured in hours (a factor of 15 different). The seeming random offset in the positions I had discovered was this rounding error. Once this was understood the problem was it was easily solved. After the problems with the optical, I of course was concerned about the radio astrometry, so I checked the positions of radio continuum objects in the field with those in FIRST Survey (Becker, White, & Helfand 1995). There was a difference but it was a simple offset and easily corrected for (see Section 2.2.2). When it came to working with the Abell 370 data I applied what I had learnt and checked both the optical and radio astrometry carefully. Of course this time there was no problem with either data set.

One particularly annoying problem occurred when calculating the K-corrections of the optical magnitudes of the Abell 370 galaxies at the end of 2007 and beginning of 2008 (see section 3.2.2). After performing the K-correction the galaxies ended up too blue; the reddest galaxies (the giant ellipticals) were as blue as the most blue nearby galaxies. I went to a fellow student Brad Tucker for help and he used a program KCORRECT (Blanton & Roweis 2007) to perform the K-corrections. However the problem still persisted. Brad checked the KCORRECT code and found some bugs

when it converting from Vega to AB magnitudes. After fixing this and rerunning the KCORRECT the problem was still there. Eventually we brought in the big gun, Brian Schmidt (Brad's supervisor) and he manage to track down the problem as poor photometric calibration; the standard star fields used for calibration of the optical imaging were not photometric (not unusual for Siding Springs). Eventually based on information from Brian and others, Mike Pracy used a clever way to calibrate the optical imaging data using stars in the field compared against their 2MASS J and K observed magnitudes. For stars there is linear relationships between $J - K$ colour and optical$-J$ colour which can be used to calibrate the optical magnitudes. The advantage of this method is that you are calibrating from your actual science imaging itself and calibrating using standards stars in a field in a different part of the sky and which were observed only sporadically. With the calibration fixed and a little more help from Brian, the current reasonable K-corrected optical magnitudes for the Abell 370 galaxies were finally produced. The lessons I learnt here are the importance of accurate calibration and also the importance of finding the right person to turn to for help.

The final lesson learnt during the PhD is not to make definite plans and expect everything to necessarily follow the schedule. This was dramatically demonstrated when I became unwell in mid-November 2008, shortly before I planned to submit my thesis. I would not return to work on the thesis for nearly 6 months at the end of April 2009. Unexpected events can throw carefully constructed plans into chaos. The trick is to adapt to the changing circumstance; the delay in my PhD submission meant that I was still in Australia when the ASKAP proposals for large surveys were due making it easier to engage in that process.

Overall, the main lessons learnt during the PhD can be summarised by these two 'laws'.

> Hofstadter's Law:
> "It always takes longer than you expect, even when you take Hofstadter's Law into account."

> Parkinson's law:
> "Work expands so as to fill the time available for its completion."

Appendix E

The Joy of AIPS

> Truth is stranger than fiction; fiction is obliged to stick to possibilities, truth isn't.
>
> Mark Twain

During my PhD I made extensive use of AIPS (Astronomical Image Processing System) software for the data reduction of the GMRT radio observations. The good thing about AIPS is that it works and works well. However after years of dealing with AIPS I feel that it is only fair that I introduce to you the reader some of its strangeness.

First AIPS is old. It has existed since at least the 1970's possibly longer (its exact origin appears to have been lost in the mists of time). Now there is nothing inherently bad about old software but in the case of AIPS many of its features are relics from a different era of computing. When you first run AIPS from a terminal it opens three additional windows: a TV window, a message window and a graphics window. These multiple windows are a legacy of AIPS past. The TV window was an actual television on which your data and images would be displayed. This was necessary as the computer monitor you were working on would have had a monochrome display. The graphics window produces plots that could appear on a monochrome display. When working with the TV window you are limited to using four keyboard keys 'A, B, C & D' to directly manipulate the data on the screen in addition to your mouse. This comes from the time when your TV window was an actual television monitor which only had four buttons connected to it.

Another notable feature of AIPS is its manual. This is known as the AIPS cookbook which is put out by the National Radio Astronomy Observatory (NRAO). The authors of this 'cookbook' have an obsession with bananas as if they themselves were apes. Each of the chapters of the AIPS cookbook ends with a recipe involving bananas.

Some of examples of the recipes include:

- banana bran muffins
- banana caramel pie
- banana curried chicken
- banana daiquiri
- banana dream pizza
- banana relish
- banana–rhubarb crisp
- chicken salad with banana mayonnaise and grapes
- Columbian fresh banana cake with sea foam frosting
- cranberry banana bread
- cream of banana soup
- curried bananas
- Mexican chicken vegetable soup with bananas
- orange gingered bananas
- roasted turkey quesadillas with banana

All the recipes in the AIPS Cookbook are real recipes that you can make and eat. Despite this strangeness the AIPS manual is one of the better written manuals that I have used.

AIPS has two basic types of commands 'tasks' and 'verbs'. Tasks are separate programs which are started from within AIPS and receive their input parameter from AIPS. Tasks do most of the actual heavy computational work in data reduction and analysis. Verbs are commands that are actually compiled into AIPS and tend to be used only for less computational activities. Yes AIPS verbs are 'doing words'. If having commands called verbs was not strange enough the input parameters for verbs are called 'adverbs'. The input parameters to the tasks are also called adverbs for no particular reason.

For some reason all AIPS tasks have names limited to 5 letters. This condition does not apply to either verbs or adverbs. It is likely a legacy of some limitations with computers when AIPS was first written. However this 5 letter limit continues to this day and leads to some unusual names. There is the task SQASH (yes it is missing the U) which collapses several planes in a data cube to one plane. There is the task SMOTH which smooths image data. And there is the task SPLAT which is like SPLIT only different (I am still not exactly sure how).

The verbs even without the 5 letters restriction have some unusual names. One of these is KLEENEX (clean and exit) which kills all AIPS windows and exits AIPS (if you just use 'exit' command the TV window, message window and graphics window remain open once you leave AIPS).

Finally there is the command name in AIPS that is my favourite, a verb called STALIN. This verb is unusual in that when you try and get information on it within AIPS.

Using the AIPS help command on STALIN gives:

```
> help stalin

Help on STALIN in AIPS version 31DEC04
STALIN
You are not allowed to know.
```

That is all you get. However there is also an 'explain' option in AIPS that gives more detailed information on an AIPS task or verb than the 'help' command (this can be many pages of additional information for some of the more important tasks). Using the 'explain' command on STALIN gives:

```
> explain stalin

STALIN
Type:  Verb
Use:  STALIN allows the user to delete selected lines from the
history file of an image or uv data set.  The lines may be
deleted as ......
```

Additionally running STALIN on the command line in AIPS gives:

```
> stalin

3748 messages have been shipped to Siberian salt mine
```

So the STALIN command erases history, in particular the information that AIPS writes to the headers of FITS files when ever it modifies that file. I needed this command because I kept reprocessing my data while I experiment with the data reduction. Eventually the FITS headers of the original raw data files had so much AIPS junk that I had trouble with some commands when handling the headers. So I used STALIN to remove the history of my past data reduction runs and only kept the information from the most recent run.

That brings us to the end of this joyful journey with AIPS and also to the end of this thesis.

Bibliography

Baldry I. K., Glazebrook K., 2003, Constraints on a Universal Stellar Initial Mass Function from Ultraviolet to Near-Infrared Galaxy Luminosity Densities, ApJ, 593, 258

Baldwin J. A., Phillips M. M., Terlevich R., 1981, Classification parameters for the emission-line spectra of extragalactic objects, PASP, 93, 5

Balogh M., Eke V., Miller C., et al., 2004, Galaxy ecology: groups and low-density environments in the SDSS and 2dFGRS, MNRAS, 348, 1355

Balogh M. L., Morris S. L., Yee H. K. C., Carlberg R. G., Ellingson E., 1999, Differential Galaxy Evolution in Cluster and Field Galaxies at $z \sim 0.3$, ApJ, 527, 54

Balogh M. L., Schade D., Morris S. L., et al., 1998, The Dependence of Cluster Galaxy Star Formation Rates on the Global Environment, ApJ, 504, L75

Basilakos S., Plionis M., Kovač K., Voglis N., 2007, Large-scale structure in the HI Parkes All-Sky Survey: filling the voids with HI galaxies?, MNRAS, 378, 301

Becker R. H., White R. L., Helfand D. J., 1995, The FIRST Survey: Faint Images of the Radio Sky at Twenty Centimeters, ApJ, 450, 559

Bell E. F., 2003, Estimating Star Formation Rates from Infrared and Radio Luminosities: The Origin of the Radio-Infrared Correlation, ApJ, 586, 794

Bell E. F., McIntosh D. H., Katz N., Weinberg M. D., 2003, The Optical and Near-Infrared Properties of Galaxies. I. Luminosity and Stellar Mass Functions, ApJS, 149, 289

Bell E. F., Papovich C., Wolf C., et al., 2005, Toward an Understanding of the Rapid Decline of the Cosmic Star Formation Rate, ApJ, 625, 23

Bessell M. S., 1990, UBVRI passbands, PASP, 102, 1181

Bessell M. S., Castelli F., Plez B., 1998, Model atmospheres broad-band colors, bolometric corrections and temperature calibrations for O - M stars, A&A, 333, 231

Blanton M. R., Roweis S., 2007, K-Corrections and Filter Transformations in the Ultraviolet, Optical, and Near-Infrared, AJ, 133, 734

Boesgaard A. M., Steigman G., 1985, Big bang nucleosynthesis - Theories and observations, ARA&A, 23, 319

Bravo-Alfaro H., Cayatte V., van Gorkom J. H., Balkowski C., 2000, VLA H I Imaging of the Brightest Spiral Galaxies in Coma, AJ, 119, 580

Briggs F. H., 1990, The space density of low-profile gas-rich galaxies at the present epoch, AJ, 100, 999

Brinchmann J., Ellis R. S., 2000, The Mass Assembly and Star Formation Characteristics of Field Galaxies of Known Morphology, ApJ, 536, L77

Broeils A. H., Rhee M.-H., 1997, Short 21-cm WSRT observations of spiral and irregular galaxies. HI properties., A&A, 324, 877

Browne I. W. A., Wilkinson P. N., Jackson N. J. F., et al., 2003, The Cosmic Lens All-Sky Survey - II. Gravitational lens candidate selection and follow-up, MNRAS, 341, 13

Butcher H., Oemler A., 1984, The evolution of galaxies in clusters. V - A study of populations since Z approximately equal to 0.5, ApJ, 285, 426

Calzetti D., 1997, Reddening and Star Formation in Starburst Galaxies, AJ, 113, 162

Carlberg R. G., Yee H. K. C., Ellingson E., et al., 1997, The Average Mass Profile of Galaxy Clusters, ApJ, 485, L13

Catinella B., Haynes M. P., Giovanelli R., Gardner J. P., Connolly A. J., 2008, A Pilot Survey of H I in Field Galaxies at Redshift z ˜ 0.2, ApJ, 685, L13

Cayatte V., van Gorkom J. H., Balkowski C., Kotanyi C., 1990, VLA observations of neutral hydrogen in Virgo Cluster galaxies. I - The Atlas, AJ, 100, 604

Chengalur J. N., Braun R., Wieringa M., 2001, HI in Abell 3128, A&A, 372, 768

Chung A., van Gorkom J. H., Kenney J. D. P., Vollmer B., 2007, Virgo Galaxies with Long One-sided H I Tails, ApJ, 659, L115

Cole S., Norberg P., Baugh C. M., et al., 2001, The 2dF galaxy redshift survey: near-infrared galaxy luminosity functions, MNRAS, 326, 255

Colless M., Dalton G., Maddox S., et al., 2001, The 2dF Galaxy Redshift Survey: spectra and redshifts, MNRAS, 328, 1039

Condon J. J., 1992, Radio emission from normal galaxies, ARA&A, 30, 575

Condon J. J., Cotton W. D., Broderick J. J., 2002, Radio Sources and Star Formation in the Local Universe, AJ, 124, 675

Conselice C. J., Rajgor S., Myers R., 2008, The structures of distant galaxies - I. Galaxy structures and the merger rate to z ˜ 3 in the Hubble Ultra-Deep Field, MNRAS, 386, 909

Cortese L., Minchin R. F., Auld R. R., et al., 2008, The Arecibo Galaxy Environment Survey - II. A HI view of the Abell cluster 1367 and its outskirts, MNRAS, 383, 1519

Couch W. J., Sharples R. M., 1987, A spectroscopic study of three rich galaxy clusters at Z = 0.31, MNRAS, 229, 423

Cowie L. L., Songaila A., Hu E. M., Cohen J. G., 1996, New Insight on Galaxy Formation and Evolution From Keck Spectroscopy of the Hawaii Deep Fields, AJ, 112, 839

Croton D. J., Springel V., White S. D. M., et al., 2006, The many lives of active galactic nuclei: cooling flows, black holes and the luminosities and colours of galaxies, MNRAS, 365, 11

De Propris R., Colless M., Driver S. P., et al., 2003, The 2dF Galaxy Redshift Survey: the luminosity function of cluster galaxies, MNRAS, 342, 725

De Propris R., Colless M., Peacock J. A., et al., 2004, The 2dF Galaxy Redshift Survey: the blue galaxy fraction and implications for the Butcher-Oemler effect, MNRAS, 351, 125

de Ravel L., Le Fèvre O., Tresse L., et al., 2009, The VIMOS VLT Deep Survey. Evolution of the major merger rate since z ˜ 1 from spectroscopically confirmed galaxy pairs, A&A, 498, 379

Diaferio A., Kauffmann G., Balogh M. L., et al., 2001, The spatial and kinematic distributions of cluster galaxies in a ΛCDM universe: comparison with observations, MNRAS, 323, 999

Dickinson M., Papovich C., Ferguson H. C., Budavári T., 2003, The Evolution of the Global Stellar Mass Density at $0 < z < 3$, ApJ, 587, 25

Doyle M. T., Drinkwater M. J., 2006, The effect of local galaxy surface density on star formation for HI selected galaxies, MNRAS, 372, 977

Doyle M. T., Drinkwater M. J., Rohde D. J., et al., 2005, The HIPASS catalogue - III. Optical counterparts and isolated dark galaxies, MNRAS, 361, 34

Dressler A., 1980, Galaxy morphology in rich clusters - Implications for the formation and evolution of galaxies, ApJ, 236, 351

Dressler A., Oemler A. J., Couch W. J., et al., 1997, Evolution since Z = 0.5 of the Morphology-Density Relation for Clusters of Galaxies, ApJ, 490, 577

Dressler A., Oemler A. J., Poggianti B. M., et al., 2004, Studying the Star Formation Histories of Galaxies in Clusters from Composite Spectra, ApJ, 617, 867

Drory N., Bender R., Feulner G., et al., 2004, The Munich Near-Infrared Cluster Survey (MUNICS). VI. The Stellar Masses of K-Band-selected Field Galaxies to z˜1.2, ApJ, 608, 742

Eisenstein D. J., Hu W., 1998, Baryonic Features in the Matter Transfer Function, ApJ, 496, 605

Elbaz D., Daddi E., Le Borgne D., et al., 2007, The reversal of the star formation-density relation in the distant universe, aap, 468, 33

Farouki R., Shapiro S. L., 1981, Computer simulations of environmental influences on galaxy evolution in dense clusters. II - Rapid tidal encounters, ApJ, 243, 32

Fasano G., Poggianti B. M., Couch W. J., et al., 2000, The Evolution of the Galactic Morphological Types in Clusters, ApJ, 542, 673

Fontana A., Salimbeni S., Grazian A., et al., 2006, The Galaxy mass function up to z =4 in the GOODS-MUSIC sample: into the epoch of formation of massive galaxies, A&A, 459, 745

Fort B., Mellier Y., 1994, Arc(let)s in clusters of galaxies, aapr, 5, 239

Fujita S. S., Ajiki M., Shioya Y., et al., 2003, The Hα Luminosity Function and Star Formation Rate at z $\sim$ 0.24 Based on Subaru Deep Imaging Data, ApJ, 586, L115

Fukugita M., 2004, Cosmic Matter Distribution: Cosmic Baryon Budget Revisited, in IAU Symposium, Vol. 220, Ryder S., Pisano D., Walker M., Freeman K. (eds.), Dark Matter in Galaxies, p. 227

Fukugita M., Hogan C. J., Peebles P. J. E., 1998, The Cosmic Baryon Budget, ApJ, 503, 518

Fukugita M., Peebles P. J. E., 2006, Massive Coronae of Galaxies, ApJ, 639, 590

Gómez P. L., Nichol R. C., Miller C. J., et al., 2003, Galaxy Star Formation as a Function of Environment in the Early Data Release of the Sloan Digital Sky Survey, ApJ, 584, 210

Gallego J., García-Dabó C. E., Zamorano J., Aragón-Salamanca A., Rego M., 2002, The [O II] λ3727 Luminosity Function of the Local Universe, ApJ, 570, L1

Gallego J., Zamorano J., Aragon-Salamanca A., Rego M., 1995, The Current Star Formation Rate of the Local Universe, ApJ, 455, L1

Gavazzi G., Boselli A., Donati A., Franzetti P., Scodeggio M., 2003, Introducing GOLDMine: A new galaxy database on the WEB, A&A, 400, 451

Gavazzi G., Boselli A., van Driel W., O'Neil K., 2005, Completing H I observations of galaxies in the Virgo cluster, A&A, 429, 439

Gavazzi G., O'Neil K., Boselli A., van Driel W., 2006, H I observations of galaxies. II. The Coma Supercluster, A&A, 449, 929

Georgakakis A., Hopkins A. M., Sullivan M., et al., 2003, The Phoenix Deep Survey: X-ray properties of faint radio sources, MNRAS, 345, 939

Gunn J. E., Gott J. R. I., 1972, On the Infall of Matter Into Clusters of Galaxies and Some Effects on Their Evolution, ApJ, 176, 1

Guzman R., Gallego J., Koo D. C., et al., 1997, The Nature of Compact Galaxies in the Hubble Deep Field. II. Spectroscopic Properties and Implications for the Evolution of the Star Formation Rate Density of the Universe, ApJ, 489, 559

Haarsma D. B., Partridge R. B., Windhorst R. A., Richards E. A., 2000, Faint Radio Sources and Star Formation History, ApJ, 544, 641

Hashimoto Y., Oemler A. J., Lin H., Tucker D. L., 1998, The Influence of Environment on the Star Formation Rates of Galaxies, ApJ, 499, 589

Haynes M. P., 2008, Conference Summary: HI Science in the Next Decade, ArXiv e-prints, 806

Haynes M. P., Giovanelli R., Chincarini G. L., 1984, The Influence of Envirionment on the H I Content of Galaxies, ARA&A, 22, 445

Haynes M. P., Giovanelli R., Herter T., et al., 1997, 21 CM H1 Line Spectra of Galaxies in Nearby Clusters, AJ, 113, 1197

Heavens A., Panter B., Jimenez R., Dunlop J., 2004, The star-formation history of the Universe from the stellar populations of nearby galaxies, Nat, 428, 625

Hogg D. W., Cohen J. G., Blandford R., Pahre M. A., 1998, The O II Luminosity Density of the Universe, ApJ, 504, 622

Hopkins A. M., 2004, On the Evolution of Star-forming Galaxies, ApJ, 615, 209

Hopkins A. M., Beacom J. F., 2006, On the Normalization of the Cosmic Star Formation History, ApJ, 651, 142

Hopkins A. M., McClure-Griffiths N. M., Gaensler B. M., 2008, Linked Evolution of Gas and Star Formation in Galaxies Over Cosmic History, ApJ, 682, L13

Icke V., 1981, Kinematic evidence for precessing beams in 3C 129, ApJ, 246, L65

Jimenez R., Panter B., Heavens A. F., Verde L., 2005, Baryonic conversion tree: the global assembly of stars and dark matter in galaxies from the Sloan Digital Sky Survey, MNRAS, 356, 495

Johnston S., Bailes M., Bartel N., et al., 2007, Science with the Australian Square Kilometre Array Pathfinder, Publications of the Astronomical Society of Australia, 24, 174

Juneau S., Glazebrook K., Crampton D., et al., 2005, Cosmic Star Formation History and Its Dependence on Galaxy Stellar Mass, ApJ, 619, L135

Kashikawa N., Shimasaku K., Yasuda N., et al., 2004, The Subaru Deep Field: The Optical Imaging Data, PASJ, 56, 1011

Kauffmann G., White S. D. M., Heckman T. M., et al., 2004, The environmental dependence of the relations between stellar mass, structure, star formation and nuclear activity in galaxies, MNRAS, 353, 713

Kennicutt R. C., 1998a, Star Formation in Galaxies Along the Hubble Sequence, ARA&A, 36, 189

Kennicutt R. C., Jr., 1983, The rate of star formation in normal disk galaxies, ApJ, 272, 54

Kennicutt R. C., Jr., 1998b, The Global Schmidt Law in Star-forming Galaxies, ApJ, 498, 541

Kewley L. J., Geller M. J., Jansen R. A., 2004, [O II] as a Star Formation Rate Indicator, AJ, 127, 2002

Kim A., Goobar A., Perlmutter S., 1996, A Generalized K Correction for Type IA Supernovae: Comparing R-band Photometry beyond z=0.2 with B, V, and R-band Nearby Photometry, PASP, 108, 190

King L. J., Browne I. W. A., Muxlow T. W. B., et al., 1997, Multifrequency radio observations of the gravitational lens system 1938 + 666, MNRAS, 289, 450

King L. J., Jackson N., Blandford R. D., et al., 1998, A complete infrared Einstein ring in the gravitational lens system B1938 + 666, MNRAS, 295, L41

Kodama T., Yamada T., Akiyama M., et al., 2004, Down-sizing in galaxy formation at z˜ 1 in the Subaru/XMM-Newton Deep Survey (SXDS), MNRAS, 350, 1005

Lah P., Chengalur J. N., Briggs F. H., et al., 2007, The HI content of star-forming galaxies at z = 0.24, MNRAS, 376, 1357

Lah P., Pracy M. B., Chengalur J. N., et al., 2009, The HI gas content of galaxies around Abell 370, a galaxy cluster at z = 0.37, mnras, 399, 1447

Larson R. B., Tinsley B. M., Caldwell C. N., 1980, The evolution of disk galaxies and the origin of S0 galaxies, ApJ, 237, 692

Lewis I., Balogh M., De Propris R., et al., 2002, The 2dF Galaxy Redshift Survey: the environmental dependence of galaxy star formation rates near clusters, MNRAS, 334, 673

Lilly S. J., Fèvre O. L., Renzini A., et al., 2007, zCOSMOS: A Large VLT/VIMOS Redshift Survey Covering $0 < z < 3$ in the COSMOS Field, ApJS, 172, 70

Lilly S. J., Le Fevre O., Hammer F., Crampton D., 1996, The Canada-France Redshift Survey: The Luminosity Density and Star Formation History of the Universe to Z approximately 1, ApJ, 460, L1

Lopes P. A. A., de Carvalho R. R., Gal R. R., et al., 2004, The Northern Sky Optical Cluster Survey. IV. An Intermediate-Redshift Galaxy Cluster Catalog and the Comparison of Two Detection Algorithms, AJ, 128, 1017

Madau P., Ferguson H. C., Dickinson M. E., et al., 1996, High-redshift galaxies in the Hubble Deep Field: colour selection and star formation history to $z \sim 4$, MNRAS, 283, 1388

McGaugh S. S., Schombert J. M., Bothun G. D., de Blok W. J. G., 2000, The Baryonic Tully-Fisher Relation, ApJ, 533, L99

Meyer M. J., Zwaan M. A., Webster R. L., et al., 2004, The HIPASS catalogue - I. Data presentation, MNRAS, 350, 1195

Mignoli M., Zamorani G., Scodeggio M., et al., 2008, The zCOSMOS redshift survey: the three-dimensional classification cube and bimodality in galaxy physical properties, ArXiv e-prints

Moore B., Katz N., Lake G., Dressler A., Oemler A., 1996, Galaxy harassment and the evolution of clusters of galaxies., Nature, 379, 613

Moore B., Lake G., Katz N., 1998, Morphological Transformation from Galaxy Harassment, ApJ, 495, 139

Nelan J. E., Smith R. J., Hudson M. J., et al., 2005, NOAO Fundamental Plane Survey. II. Age and Metallicity along the Red Sequence from Line-Strength Data, ApJ, 632, 137

Nicastro F., Mathur S., Elvis M., et al., 2005, The mass of the missing baryons in the X-ray forest of the warm-hot intergalactic medium, Nat, 433, 495

Niklas S., Klein U., Wielebinski R., 1997, A radio continuum survey of Shapley-Ames galaxies at λ 2.8cm. II. Separation of thermal and non-thermal radio emission., A&A, 322, 19

Norberg P., Cole S., Baugh C. M., et al., 2002, The 2dF Galaxy Redshift Survey: the b_J-band galaxy luminosity function and survey selection function, MNRAS, 336, 907

Noterdaeme P., Ledoux C., Petitjean P., Srianand R., 2008, Molecular hydrogen in high-redshift damped Lyman-α systems: the VLT/UVES database, A&A, 481, 327

O'Dea C. P., Owen F. N., 1982, High Resolution VLA Observations of the Head-Tail Radio Source in NGC 1265, in Bulletin of the American Astronomical Society, Vol. 14, Bulletin of the American Astronomical Society, p. 935

Ota N., Mitsuda K., 2004, A uniform X-ray analysis of 79 distant galaxy clusters with ROSAT and ASCA, A&A, 428, 757

Pascual S., Gallego J., Aragón-Salamanca A., Zamorano J., 2001, Hα emitting galaxies and the star formation rate density at z =˜ 0.24, A&A, 379, 798

Percival W. J., Baugh C. M., Bland-Hawthorn J., et al., 2001, The 2dF Galaxy Redshift Survey: the power spectrum and the matter content of the Universe, MNRAS, 327, 1297

Pérez-González P. G., Rieke G. H., Villar V., et al., 2008, The Stellar Mass Assembly of Galaxies from z = 0 to z = 4: Analysis of a Sample Selected in the Rest-Frame Near-Infrared with Spitzer, ApJ, 675, 234

Perley R. A., Dreher J. W., Cowan J. J., 1984, The jet and filaments in Cygnus A, ApJ, 285, L35

Perlmutter S., Aldering G., Goldhaber G., et al., 1999, Measurements of Omega and Lambda from 42 High-Redshift Supernovae, ApJ, 517, 565

Pimbblet K. A., 2003, At the Vigintennial of the Butcher-Oemler Effect, Publications of the Astronomical Society of Australia, 20, 294

Pimbblet K. A., Smail I., Kodama T., et al., 2002, The Las Campanas/AAT Rich Cluster Survey - II. The environmental dependence of galaxy colours in clusters at z˜0.1, MNRAS, 331, 333

Poggianti B., 2004, Evolution of galaxies in clusters, in Dettmar R., Klein U., Salucci P. (eds.), Baryons in Dark Matter Halos. SISSA, Proceedings of Science, http://pos.sissa.it, p.104.1.

Poggianti B. M., 1997, K and evolutionary corrections from UV to IR, Astronomy and Astrophysics, Supplement, 122, 399

Poggianti B. M., Desai V., Finn R., et al., 2008, The Relation between Star Formation, Morphology, and Local Density in High-Redshift Clusters and Groups, ApJ, 684, 888

Poggianti B. M., Smail I., Dressler A., et al., 1999, The Star Formation Histories of Galaxies in Distant Clusters, ApJ, 518, 576

Pozzetti L., Bolzonella M., Lamareille F., et al., 2007, The VIMOS VLT Deep Survey. The assembly history of the stellar mass in galaxies: from the young to the old universe, A&A, 474, 443

Pracy M. B., Lah P., Colless M., et al., 2009, A spectroscopic catalogue of the galaxies in Abell 370, in preparation

Prochaska J. X., Herbert-Fort S., Wolfe A. M., 2005, The SDSS Damped Lyα Survey: Data Release 3, ApJ, 635, 123

Prochaska J. X., Wolfe A. M., 2009, On the (Non)Evolution of H I Gas in Galaxies Over Cosmic Time, ApJ, 696, 1543

Quilis V., Moore B., Bower R., 2000, Gone with the Wind: The Origin of S0 Galaxies in Clusters, Science, 288, 1617

Rao S., Briggs F., 1993, Neutral Hydrogen in Galaxies at the Present Epoch, ApJ, 419, 515

Rao S. M., Turnshek D. A., 2000, Discovery of Damped Lyα Systems at Redshifts Less than 1.65 and Results on Their Incidence and Cosmological Mass Density, ApJS, 130, 1

Rao S. M., Turnshek D. A., Nestor D. B., 2006, Damped Lyα Systems at z<1.65: The Expanded Sloan Digital Sky Survey Hubble Space Telescope Sample, ApJ, 636, 610

Richstone D. O., 1976, Collisions of galaxies in dense clusters. II - Dynamical evolution of cluster galaxies, ApJ, 204, 642

Riess A. G., Filippenko A. V., Challis P., et al., 1998, Observational Evidence from Supernovae for an Accelerating Universe and a Cosmological Constant, AJ, 116, 1009

Roberts M. S., Haynes M. P., 1994, Physical Parameters along the Hubble Sequence, ARA&A, 32, 115

Rudnick G., Rix H.-W., Franx M., et al., 2003, The Rest-Frame Optical Luminosity Density, Color, and Stellar Mass Density of the Universe from z = 0 to z = 3, ApJ, 599, 847

Rybicki G. B., Lightman A. P., 1986, Radiative Processes in Astrophysics. Wiley-VCH, 1986, pp. 400. ISBN 0-471-82759-2.

Sato Y., Cowie L. L., Kawara K., et al., 2004, Faint 6.7 Micron Galaxies and Their Contributions to the Stellar Mass Density in the Universe, AJ, 127, 1285

Schade D., Croom S., Boyle B., et al., 2001, AGN Host galaxies: HST at z ˜ 0.1 and Gemini at z ˜ 2, in Márquez I., Masegosa J., del Olmo A., et al. (eds.), QSO Hosts and Their Environments, p. 215

Schechter P., 1976, An analytic expression for the luminosity function for galaxies., ApJ, 203, 297

Schlegel D. J., Finkbeiner D. P., Davis M., 1998, Maps of Dust Infrared Emission for Use in Estimation of Reddening and Cosmic Microwave Background Radiation Foregrounds, ApJ, 500, 525

Schmidt B. P., Suntzeff N. B., Phillips M. M., et al., 1998, The High-Z Supernova Search: Measuring Cosmic Deceleration and Global Curvature of the Universe Using Type IA Supernovae, ApJ, 507, 46

Scoville N., Aussel H., Brusa M., et al., 2007, The Cosmic Evolution Survey (COSMOS): Overview, ApJS, 172, 1

Smail I., Edge A. C., Ellis R. S., Blandford R. D., 1998, A statistical analysis of the galaxy populations of distant luminous X-ray clusters, MNRAS, 293, 124

Solanes J. M., Manrique A., García-Gómez C., et al., 2001, The H I Content of Spirals. II. Gas Deficiency in Cluster Galaxies, ApJ, 548, 97

Soucail G., Mellier Y., Fort B., Mathez G., Hammer F., 1987, Further data on the blue ring-like structure in A 370, A&A, 184, L7

Spergel D. N., Bean R., Doré O., et al., 2007, Three-Year Wilkinson Microwave Anisotropy Probe (WMAP) Observations: Implications for Cosmology, ApJS, 170, 377

Spergel D. N., Verde L., Peiris H. V., et al., 2003, First-Year Wilkinson Microwave Anisotropy Probe (WMAP) Observations: Determination of Cosmological Parameters, ApJS, 148, 175

Springel V., White S. D. M., Jenkins A., et al., 2005, Simulations of the formation, evolution and clustering of galaxies and quasars, Nat, 435, 629

Stark D. P., Bunker A. J., Ellis R. S., Eyles L. P., Lacy M., 2007, A New Measurement of the Stellar Mass Density at z˜5: Implications for the Sources of Cosmic Reionization, ApJ, 659, 84

Storrie-Lombardi L. J., Wolfe A. M., 2000, Surveys for z>3 Damped Lyα Absorption Systems: The Evolution of Neutral Gas, ApJ, 543, 552

Sullivan M., Mobasher B., Chan B., et al., 2001, A Comparison of Independent Star Formation Diagnostics for an Ultraviolet-selected Sample of Nearby Galaxies, ApJ, 558, 72

Swarup G., Ananthakrishnan S., Kapahi V. K., et al., 1991, The Giant Metre-Wave Radio Telescope, Current Science V.60, No.2/Jan25, P. 95, 1991, 60, 95

The National Radio Astronomy Observatory , 31-DEC-2008 and ealier, AIPS Cookbook

Thomas D., Maraston C., Bender R., Mendes de Oliveira C., 2005, The Epochs of Early-Type Galaxy Formation as a Function of Environment, ApJ, 621, 673

Thompson A. R., Moran J. M., Swenson G. W., 1986, Interferometry and synthesis in radio astronomy. New York, Wiley-Interscience, 1986, 554 p.

Toomre A., Toomre J., 1972, Galactic Bridges and Tails, ApJ, 178, 623

Tresse L., Maddox S. J., 1998, The H alpha Luminosity Function and Star Formation Rate at Z approximately 0.2, ApJ, 495, 691

van der Hulst J. M., Sadler E. M., Jackson C. A., et al., 2004, From gas to galaxies, New Astronomy Review, 48, 1221

Venkatesan T. C. A., Batuski D. J., Hanisch R. J., Burns J. O., 1994, Why do head-tail sources exist in poor clusters of galaxies?, ApJ, 436, 67

Verheijen M., van Gorkom J. H., Szomoru A., et al., 2007, WSRT Ultradeep Neutral Hydrogen Imaging of Galaxy Clusters at z ˜ 0.2: A Pilot Survey of Abell 963 and Abell 2192, ApJ, 668, L9

Verheijen M. A. W., 2004, Galaxy evolution in dense environments: a concise HI perspective, in IAU Colloq. 195: Outskirts of Galaxy Clusters: Intense Life in the Suburbs, p. 394

Wieringa M. H., de Bruyn A. G., Katgert P., 1992, A Westerbork search for high redshift H I, A&A, 256, 331

Wu X.-P., Xue Y.-J., Fang L.-Z., 1999, The L_X-T and L_X-σ Relationships for Galaxy Clusters Revisited, ApJ, 524, 22

Zwaan M. A., 2000, Ph.D. thesis, Atomic hydrogen in the local universe, PhD Thesis, Groningen: Rijksuniversiteit, 2000 152 p. Proefschrift, Rijksuniversiteit Groningen, 2000

Zwaan M. A., Briggs F. H., Sprayberry D., Sorar E., 1997, The H i Mass Function of Galaxies from a Deep Survey in the 21 Centimeter Line, ApJ, 490, 173

Zwaan M. A., Meyer M. J., Staveley-Smith L., Webster R. L., 2005, The HIPASS catalogue: $\Omega_{\rm HI}$ and environmental effects on the HI mass function of galaxies, MNRAS, 359, L30

Zwaan M. A., Staveley-Smith L., Koribalski B. S., et al., 2003, The 1000 Brightest HIPASS Galaxies: The H I Mass Function and Ω_{HI} , AJ, 125, 2842

Zwaan M. A., van Dokkum P. G., Verheijen M. A. W., 2001, Hydrogen 21-Centimeter Emission from a Galaxy at Cosmological Distance, Science, 293, 1800

If A equals success, then the formula is: A = X + Y + Z. X is work, Y is play, Z is keep your mouth shut.

Albert Einstein